Master's Thesis

Compatibility of C_4F_7N/CO_2 And Epoxy & Optical PD Characteristics Of The Gas

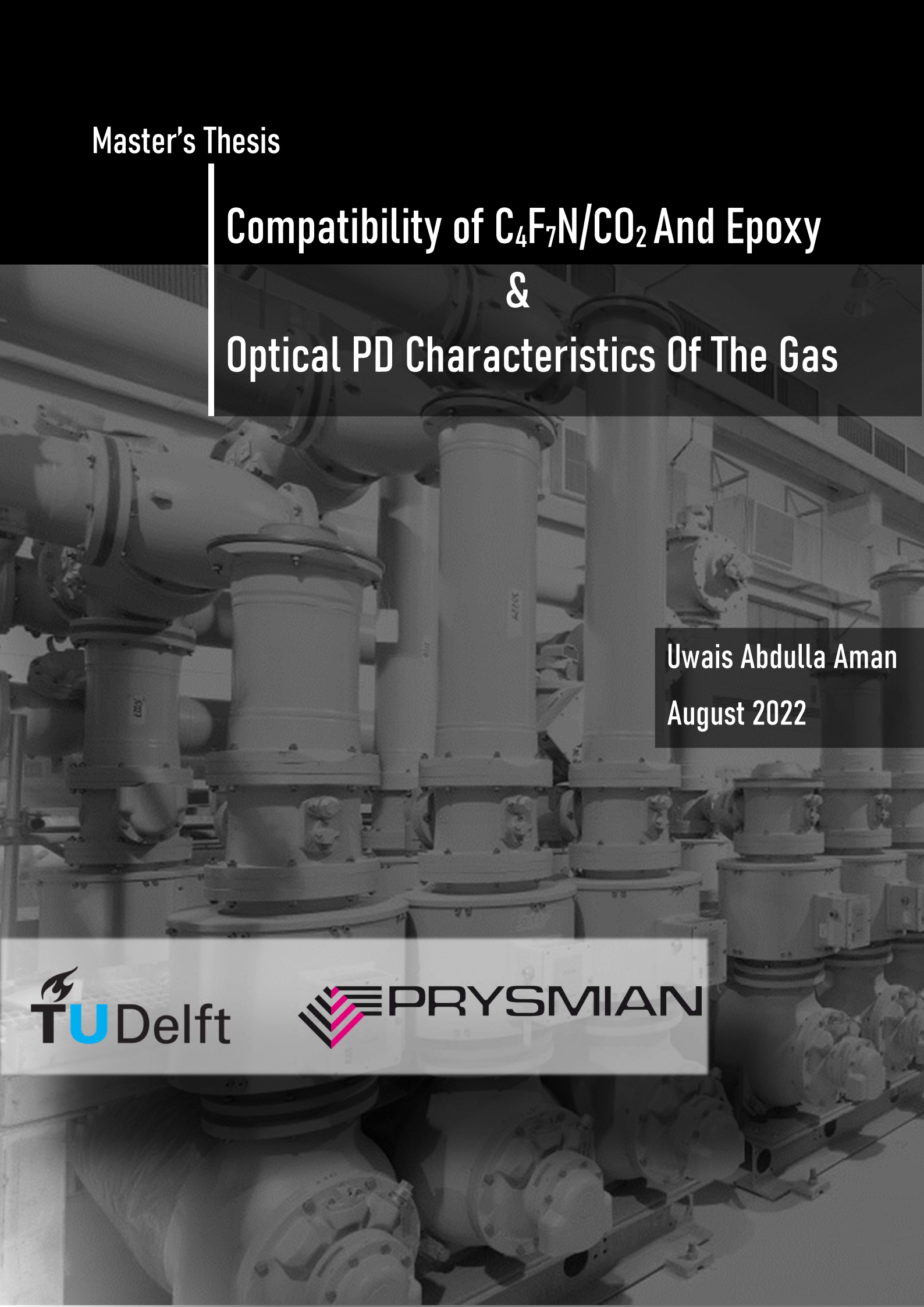

Uwais Abdulla Aman

August 2022

TU Delft

PRYSMIAN

Compatibility Of C_4F_7N/CO_2 And Epoxy

&

Optical PD Characteristics Of The Gas

By

Uwais Abdulla Aman

To obtain the degree of Master of Science in Electrical Engineering,
at the Delft University of Technology

To be defended publicly on Friday, August 26, 2022, at 15:00

Student Number:	5369630	
Project Duration:	December 1, 2021 – August 26, 2022	
Supervisors:	Dr. Ir. Mohamad Ghaffarian Niasar Dr. Ir. Riccardo Bodega	
Thesis Committee:	Prof. Ir. Peter Vaessen	TU Delft
	Dr. Ir. Mohamad Ghaffarian Niasar	TU Delft
	Dr. Ir. Milos Cvetkovic	TU Delft
	Dr. Ir. Riccardo Bodega	Prysmian Group

This thesis is under embargo till December 2023

An electronic version of this thesis is available at *http://repository.tudelft.nl/*

Prysmian Group

TU Delft Delft University of Technology

Acknowledgement

This thesis would not have been possible without the generous support and assistance of numerous individuals. First and foremost, I am deeply indebted to my supervisors, **Dr. Ir. Mohamad Ghaffarian Niasar** and **Dr. Ir. Riccardo Bodega**, for exposing me to this exciting research topic and providing me with the chance to complete my master's thesis in collaboration with Prysmian Group. Throughout the thesis, their consistent encouragement, eye-opening questions and valuable comments at weekly sessions inspired and guided me in the right direction and helped me build up a researcher's mindset both from the perspective of academia and industry.

I would like to thank all the colleagues at Prysmian Group, Netherlands, especially the R&D Department and NWC, for supporting my research at TU Delft and providing us with all the necessary equipment and raw materials. Also, their insightful remarks and expert guidance in technical areas helped 'Click-Fit' my theoretical knowledge with practical aspects during the projects in Prysmian. It was a privilege to work for a prestigious company filled with friendly people. I would also like to thank people from the gas and epoxy provider for all the technical help and for providing the test items right on time

I would like to extend my gratitude to my thesis committee chair **Prof. Peter Vaessen**, who, with his inspiring experience, made the HV lectures engaging. I would also like to thank **Dr. Ir. Milos Cvetkovic** for taking the time to be part of my thesis committee. A big thanks to **Ir. André Lathouwers** for sharing his knowledge of alternative gases and the industrial aspects.

I am highly grateful to the TU Delft HV lab manager **Dr. Luis Castro Heredia,** for providing the freedom to do research, trusting me with all the HV equipment and giving me valuable recommendations and guidance throughout the experimental stages. My highest gratitude to **Mr. Wim Termorshuizen** and **Ing. Paul Van Nes** for always being willing to help me in my thesis. The technical and non-technical discussions with you both always gave more insights into reality. I would like to thank **Mr. Geert Jan Kamphuis** for sharing his knowledge of optics and helping with experiments on optical PD detection.

Thanks to **Mr. Christian Mier Escurra** for being curious about the project and thereby giving advice throughout. Studying HV courses would not be the same without my beloved friends **Ashutosh, Ayan, Hassan, Nitish and Ravi**. The conversations and humour we shared over lunch, parties, and last-minute submissions will be memories I cherish for the rest of my life. Thanks to all my friends in Delft for their immense help throughout the last two years at TU Delft.

Finally, no amount of thanks can justify the support that I received from my **family members**. I want to thank my beloved **parents** and **grandparents**, whose love, prayers and guidance are with me in whatever I pursue. I want to thank my late **valyuppa** and **valyumma**, who nurtured me into who I am now; I am sad that they will not see me graduate.

Uwais Abdulla Aman

Delft, August 2022

Executive Summary

SF_6 has been the primary dielectric medium in electrical power applications for many years, notably in high voltage gas-insulated equipment. Governments have pursued emission reductions from Gas insulated equipment, recognizing that SF_6 has an extremely long atmospheric lifetime and significant global warming potential. The electrical power industry has responded to this environmental concern by incorporating SF_6-free technologies to an expanding range of applications that formerly used SF_6, such as in gas-insulated switchgear and gas-insulated lines or bus bars.

Because of its lower impact on global warming and excellent dielectric strength, fluorinated nitrile (C_4F_7N)/CO_2 mixture is a potential SF_6-alternative gas in HV Gas-Insulated Systems. Laboratory accelerated thermal ageing experiments on material compatibility were performed to assure long-term physical and chemical stability at the interface between C_4F_7N/CO_2 gas mixture and epoxy resin with different fillers. As there are no standards for accelerated ageing for this novel gas, the ageing test is performed based on the recommendations of CIGRE. The compatibility of gas and solid insulating materials in contact was assessed based on the changes in insulation performance after ageing. Before and after ageing experiments, such as AC and LI flashover tests, visual inspection, FTIR of epoxy samples and breakdown strength of the gas were analysed and compared.

The optical detection of partial discharge (PD) is a critical method for determining the insulating quality of equipment. Moreover, the PD of different gases correspond to distinct multispectral characteristic distributions, but the current investigation is limited to SF_6. As a result, this research offers a solution to identify the optical PD spectrum of the novel alternative gas C_4F_7N/CO_2. Based on the finding, the research is extended to use it in fluorescent fibres for PD detection in Gas Insulated Systems. The selection of fluorescent fibres and sensors is analysed, and tests are performed to produce PRPD patterns from the optical sensor output. Investigations on the Correlation between electrical and optical PD detection methods were also performed.

Finally, the Industrial perspective on eliminating SF_6 is presented based on the author's work at Prysmian. The different HV cable network components that use SF_6 for testing, its test voltages and waveforms are identified and based on the electrical field calculations, suitable alternatives are proposed. Functionality tests with synthetic air in real network components are carried out to validate the calculations. Further, an experimental study for using compressed air in network components testing is carried out.

Contents

List of Abbreviations

SF_6	Sulphur Hexa Fluoride	LI	Lightning Impulse
GIS	Gas Insulated Switchgear	SPMD	swarming partial micro discharges
GIL	Gas Insulated Line	PDIV	Partial Discharge Inception Voltage
GWP	Global warming potential	VIS	Visible
BW	Bandwidth	HFCT	High Frequency Current Transformer
PFC	Perfluorocarbons	PRPD	Phase Resolved Partial Discharge
C4F7N	2,2,3,3,4,4,4-heptafluorobutanenitrile or NOVEC 4710	EMI	Electromagnet Interference
CAS	Chemical Abstracts Service Number	PMT	Photo Multiplier Tue
TRL	Technology Readiness Level	SiPM	Silicon Photo Multiplier
Ppm	Parts per million	EPDM	ethylene propylene diene monomer
ODP	Ozone Depletion Potential	PRSV	Peng–Robinson Stryjek–Vera Equation
SIS	Solid Insulation Switchgear	UV	Ultraviolet
AIS	Air Insulated Switchgear		
RMU	Ring Main Unit		
HV	High Voltage		
PD	Partial Discharge		
SNR	Signal to Noise Ratio		
IR	Infra Red		

1. Introduction

1.1 Motivation

“Since childhood, studying how global warming could lead to climate change, I understood how the ecosystem works in syzygy and how we humans affect the whole cycle. My yearning is devoted to joining in the rally of the new generation of optimists looking forward to renovating the world back to green by contributing the insights from this research.“

Since the introduction of GIS in the late 1960s, SF_6 has become the favourite insulating and arc quenching medium, thanks to its remarkable characteristics. Since then, the percentile of gas-insulated high voltage equipment such as GIS, GIL, and high and medium voltage breakers increased annually due to its advantages, mainly compactness, which directly influences land requirement, land cost and visual impact. However, SF_6 has the significant drawback of presenting a GWP of 23,500 times higher than CO_2 and a lifetime in the atmosphere of around 3200 years, according to IPCC Assessment Report 5 from 2014 [1]. The long lifetime of SF_6 makes its emission almost "irreversible" [2]. Due to these properties, it is designated as one of the six potent greenhouse gas listed in the Kyoto Protocol of 1997. Of the 8000 tonnes of SF_6 produced annually, approximately 80% of this is consumed by the energy industry for use in switchgear [3]. However, in this context, it is essential to note that the contribution of SF_6 to global warming emissions is estimated at only 0.1% [4].

Owing to the long life in the atmosphere and the GWP concern, even this small contribution is significant for electric power industry stakeholders. Many efforts were put forward across the industry to minimise and better manage the use of SF_6. Subsequently, international regulations such as the Kyoto Protocol have been made to limit its emissions across several industries. However, despite all these regulatory actions, the SF_6 concentration is rapidly increasing, as shown in Figure 1.1, and it is to be noted that the rate of increase also grows continuously.

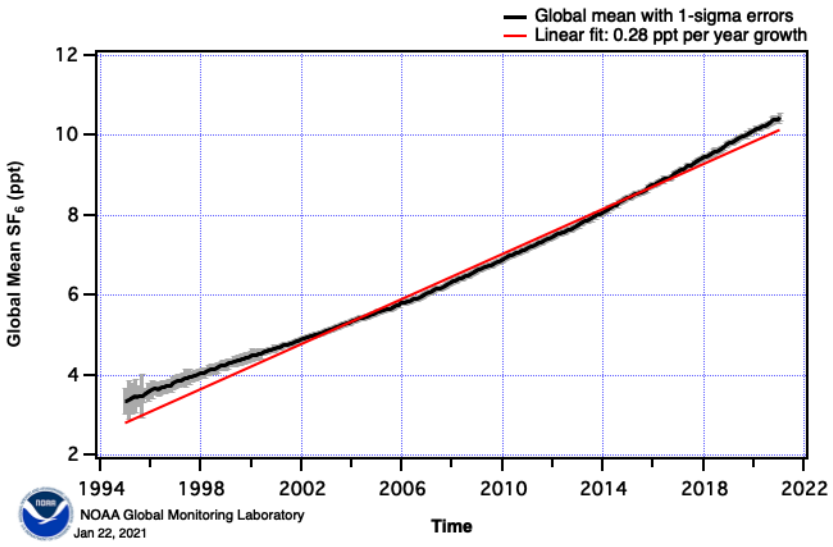

Figure 1.1: *Evolution of SF_6 concentration in the atmosphere [97]*

The two main reasons for this are [2]:

- Installation of new SF_6 insulated electrical equipment
- Multiple types of very old equipment are reaching their end-of-life without a proper SF_6 recycling unit.

Universities, gas-insulated HV equipment manufacturing companies, and utilities cooperated and intensified the search for better alternatives since the beginning of the last century. The driving motivation for the SF_6 alternative is the reduction of greenhouse gas emissions during the full life cycle of the switchgear. Most of these solutions use gas mixtures instead of a single gas as normally used with SF_6. The alternative gases are mainly composed of a specific amount of fluorinated compound and the rest with air components (such as N_2, O_2, or CO_2).

The most feasible solution for a utility will be to replace SF_6 and use the alternative gas in the Gas-insulated system (i.e., to retrofit the system) to reduce the use of SF_6 equipment population. However, the effects of applying alternative gases may differ and need to be recognised. The present IEC and IEEE standards for switchgear aim at the application of SF_6 and are therefore not fully transferable to non-SF_6 gases or gas mixtures [5]. So far, the best alternative is the fluoronitrile C_4F_7N (2,2,3,3,4,4,4-heptafluorobutanenitrile or NOVEC 4710) - CO_2 mixture, marketed as g^3 (Green Gas for Grid) by GE. A detailed study of whether it is feasible to retrofit a gas-insulated system with alternative gas must be thoroughly analysed before using it in the switchgear.

Working in collaboration with the world leader in High Voltage cables and their network components, Prysmian's sustainability policies was well understood. The organisation's sustainable policy, together with the EU green policy, has compelled the Prysmian Delft R&D team to eliminate SF_6 used during HV cables network components testing, which further led to the feasibility study of using Synthetic air (80% N_2 + 20% O_2) and dry air for network components testing.

1.2 Scientific Gap

During the extensive literature review as part of the research, the following scientific gaps were addressed which need more clarification:

- The compatibility of the novel gas C_4F_7N/CO_2 mixture and different materials of Gas-insulated systems such as epoxies has hardly been addressed.
- No general standards are defined on how material compatibility for materials in contact with alternative gases must be tested. However, CIGRE WG B3.45 recommends specific ageing parameters. Literature shows no compatibility studies based on this.
- Compatibility study of C_4F_7N/CO_2 with epoxies having different fillers (Quartz filled and Al_2O_3) are not yet studied.
- The breakdown strength of the alternative gas after interaction between epoxy and gas at elevated temperature is not studied before.
- LI flashover test over the epoxy surface after ageing with the alternative gas is not yet known, as observed during the literature survey phase.

- The knowledge of the novel gas C_4F_7N/CO_2's optical partial discharge characteristics for various defects is minimal.
- The study on the usage of fluorescent fibres for detecting partial discharge in this novel gas is limited.

Thus, with the following research gaps, it seems that if this research can answer some of them, it will be possible to deliver an answer to one of the most critical questions for utilities and manufacturing companies – Whether retrofitting gas-insulated systems with alternative gas is a solution to reduce GWP and how new trends in PD detection can be applied to alternative gases. Hence, in the next section, the research questions are formulated, which the author will try to solve through the extensive research done in chapters 4 to 6.

1.3 Research Questions

This research at TU Delft ESP Lab, in collaboration with Prysmian Group, for nine months targets to solve the following research questions:

1. What is the compatibility of the novel alternative gas C_4F_7N/CO_2 mixture and epoxy with different fillers, and is retrofitting a solution from this point of view?
2. What are the optical PD characteristics of the C_4F_7N/CO_2 mixture considering different defects in a gas-insulated system?
3. Is it technically feasible to use Siemens clean air (80% N_2 + 20% O_2) and dry air for network components HV routine testing?

These proposed questions have been addressed in this thesis, and the interpretations are discussed in chapter 7 with future recommendations to elaborate the study.

1.4 Research Methodology

This section will outline the approach used to achieve the aforementioned goals and research objectives. Figure 1.2 presents a comprehensive overview of this.

The first step starts with a literature study focusing on the previous works and gathering knowledge related to each research question. The next step is identifying the proper test setup requirement and performing initial calculations for the experimental study. Identifying the bottlenecks in the study, solving them one by one, and analysing them in between lead to a proper test setup for each research question. After this phase, tests were performed, and the results were analysed. The possible reasons were identified as per the literature studies. Finally, future scopes in the field of these research questions were identified and presented.

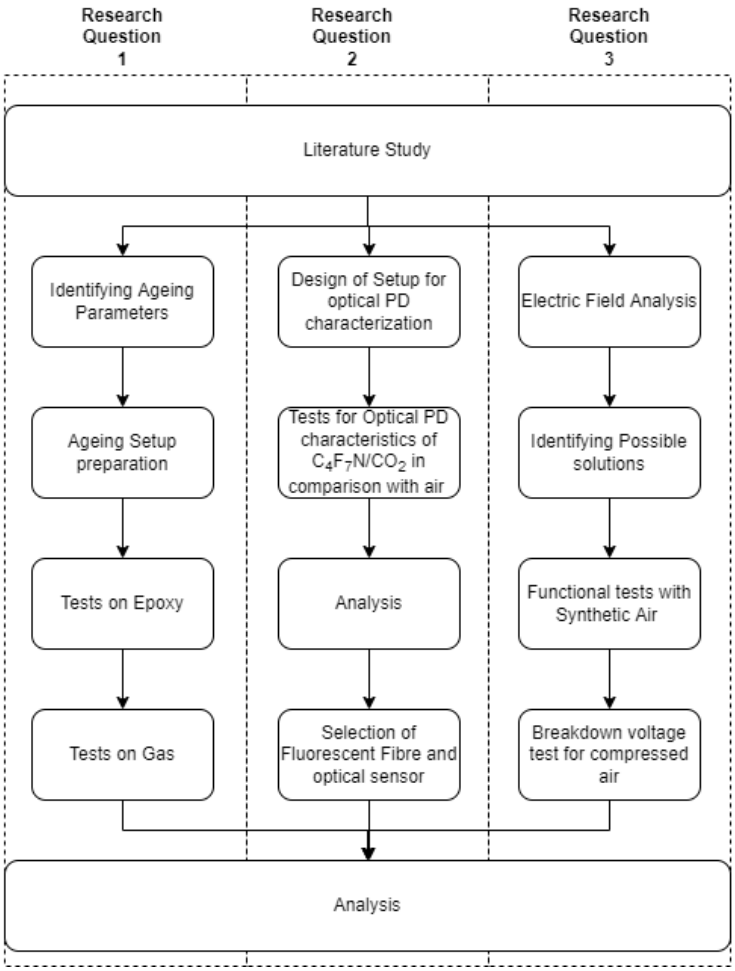

Figure 1.2: *Work Division*

1.5 Outline of Chapters

This thesis report contains seven chapters with the following structure:

- **Chapter 2: Background Knowledge**

Throughout this research, an intensive literature review has been conducted to determine the research gap and formulate the research question. Chapter 2 discusses the state of art literature regarding alternative gases, PD measurement techniques and gas breakdowns. First, background information on different SF_6 alternatives giving primary importance to gaseous dielectric is presented. Then, what is the importance of accelerated ageing was studied. Third, different PD activities that could occur in a gas-insulated system and the prevailing PD measuring techniques are discussed. Finally, Prysmian's sustainability policies and how gaseous dielectrics break down under high voltages are investigated.

- **Chapter 3: Materials & Alternative Gas Qualification**

This chapter deals with the need for ageing, reviews existing standards and guides on ageing test methods, and previous research with compatibility of alternative gas C_4F_7N on EPDM and electrode materials. Then the recommendation as per CIGRE to qualify a material or gas to use as an alternative gas is presented.

- **Chapter 4: Compatibility Of C_4F_7N/CO_2 & Epoxy Under Accelerated Thermal Ageing**

This chapter comprises the selection of the alternative gas and epoxy, experimental setups, conditions considered, and experimental results obtained towards solving the research question 'Compatibility of C_4F_7N/CO_2 and epoxy under accelerated thermal ageing'. The reasoning for the anomalies identified after the experiments is also presented.

- **Chapter 5: Optical Partial Discharge Characteristics of C_4F_7N/CO_2**

This chapter describes the novel C_4F_7N/CO_2 alternative gas's optical PD characteristics and the devices and sensors utilized. The technique and criteria used to pick optical sensors are presented. The technique for employing the optical sensor, as well as its location, is also discussed. The selection of fluorescent fibre based on the optical PD characteristics of the gas is presented. Finally, tests and analyses of optical PD measurement using fluorescent fibre are presented.

- **Chapter 6: Alternative Gases For Network Components Testing**

This chapter comprises of author's work at the R&D Department of Prysmian Group Delft. First, an introduction to HV cable network components and the study strategy is explained. In the initial study of all the cable network components developed by the Prysmian Group, the components that undergo testing in SF_6 and the different tests and the test setup are studied in detail. Then non-homogeneity factor or Schweiger factor is introduced along with electrical field calculations of all the network components. Based on the study, verification test results of synthetic air used for testing two important network components are presented. Finally, test results of air from 2 compressors are studied for reference.

- **Chapter 7: Conclusions and Future Scope**

Chapter 7 summarizes the insights from the preceding chapters, allowing us to address the research questions methodically. It also discusses prospective research areas not covered in the current study and should be expanded.

2. Background Knowledge

2.1 Review of SF_6 gas alternatives

This session will summarise the available literature on SF_6 alternatives solely for HV insulation and arc interruption applications.

2.1.1 SF_6 As Gaseous Dielectric And Its Environmental Concerns

SF_6 has been the best gaseous dielectric and was widely used in the power industry. The first industrial use of SF_6 as an insulation gas ages to the 1930s. Industrial production of SF_6 increased with the growth of electrical applications after World War II. This led to the massive use of SF_6 in MV and HV equipment in the 1960s and 1970s [2].

The critical properties of SF_6 that attract utility companies and manufacturers to use in their gas-insulated systems as both electrical insulator and electrical interrupter are tabulated in Table 1 [3].

SF_6 as an electrical insulator	**SF_6 as an electrical interrupter**
High Dielectric Strength: 2.5 – 3 times higher than air under the same conditions.	Electronegative gas
High Thermal stability	High Thermal Stability
High Density	Self-healing property
Low heat transfer	Negligible interruption by-products
Non-toxic	Non-toxic
Chemically inert: high molecular recombination after PD	Chemically inert: high molecular recombination after arcing
Reduced switch gear footprint	Non-flammable
Low boiling point: -64°C	Fast arc-quenching: due to its strong molecular structure
	Low arc time constant

Table 2.1: *SF_6 key properties for a utility application*

These unique properties of SF_6 have made it possible to be one of the best gaseous dielectrics and helped in relatively compact designs. Despite the numerous advantages it brings to the power industry, SF_6 has been globally recognised as a potential Global Warming Potential (GWP) gas, or Green House Gas (GHG), with a GWP of 23,500 (literature [6], [7] suggests GWP as 23,900) that of CO_2 and a lifetime of 3200 years in the atmosphere [1]. As a result, SF_6 was

designated as one of the most GWG in the Kyoto Protocol of 1997, which paved the governments taking control measures to eliminate the usage of SF_6. For the power industry, this means that the utilities should responsibly operate their gas-insulated systems.
In the European Union, the actions on behalf of this development are as follows:

- The F-gas regulation from 2014 (EU 517/2014) states that there are no restrictions on SF_6 use in electrical equipment. However, training, labelling, and reporting are mandatory [8]. Intentional SF_6 release is prohibited, and recovery after use is mandatory. Leakages should be minimised and measured.
- European Commission, in September 2020, published a report which will allow the replacement of SF_6 in switchgear [9].
- At the end of 2019, the European Commission announced the Green Deal, aiming for climate neutrality and zero net emissions of greenhouse gases in 2050.
- In 2020, an open consultation process was conducted, and it was decided to commission a draft proposal for the updated F-gas regulation, which shall be published at the end of 2021.
- On 5th April 2022, the Commission made a legislative proposal to update the F-gas Regulation. Due to the F-gas Regulation, the EU's F-gas emissions are expected to be cut by two-thirds by 2030 compared to 2014 levels [10].

2.1.2 SF_6 Alternatives: Selection Criteria And Current Solutions

Even though the environmental impact of SF_6 has been acknowledged and quantified for decades, there existed significant difficulty in finding an alternative that matches the technical performance of SF_6 and can provide the same compact solution to serve the current applications. Since the last century, universities and manufacturers have intensified the hunt for SF_6 alternatives as a consequence of the protocols.

A potential alternative gas should be compliant with the following strict criteria [11] [12]:

- Physical and chemical:
    - High electric strength: To prevent all undesired electrical discharge phenomena and breakdown in the equipment during its in-service life duration, typically 30 to 50 years when subjected to operating voltages and overvoltage stresses.
    - Good arc quenching capability (optional): high thermal conductivity, fast gas Recovery, self-healing, non-flammability, and high heat dissipation
    - Low boiling point and high vapour pressure at operating and ambient temperature
    - Compatibility with existing switchgear materials
    - Market availability
- Health and safety:
    - Low toxicity
    - No flash point
    - No harmful decomposition products
    - Easy gas handling during maintenance works

- Environmental
    - Low GWP
    - No ozone depletion potential (ODP)
    - Minimal environmental impact
    - Similar SF_6 footprints

Breakdown measurements in typical electrode configuration (homogenous, quasi-homogeneous, and strongly inhomogeneous) with standard voltage waveforms (AC, DC, Lightning Impulse, or Switching Impulses) is the conventional way to identify and characterise a potential dielectric gas. Multiple breakdown experiments under various conditions have to be carried out to obtain a complete characterisation of the gas, as breakdown is a statistical phenomenon. The sparks occurring during the breakdown mechanism damage the electrodes and require repeated changing of the electrode; hence is a time-consuming and resource-intensive process. Hence preliminary studies such as quantum-chemical screening of molecules, swarm parameter measurement of suitable gases from the screening process, and finally, prediction of breakdown behaviour (only holds for homogenous fields) of the most promising candidates are carried out [13].

Finding an SF_6 alternative is a multi-criterion optimisation challenge. Apart from the GWP and high dielectric strength requirement, the optimisation must be performed by taking into account the typical operating conditions of the application: maximum pressure, minimum operating temperature, and any other nontechnical requirement considered necessary. A possible process is shown in figure 2.1.

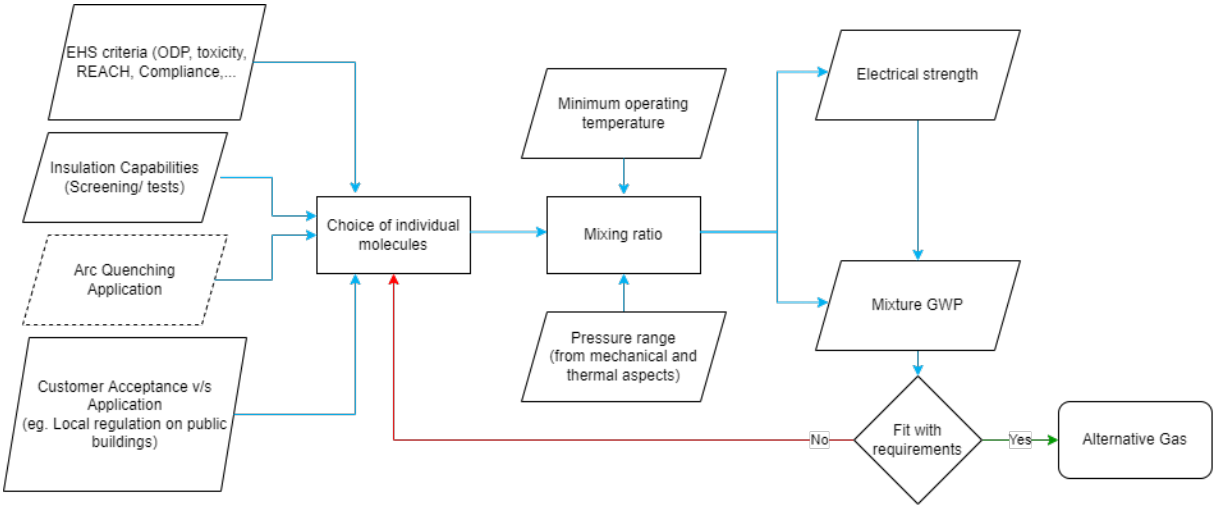

Figure 2.1: *SF_6 alternative mixture estimation process*

From an initial assessment of the available gases, the following gas family was concluded to have the most significant potential to use as an SF_6 alternative:

1. **Perfluorocarbons (PFC):**

   From a technical point of view, the first and foremost criteria an alternative gas should comply with is the high dielectric strength, which requires a vital attaching gas. Some candidates from these investigations are from the PFC family, such as CF_4, C_3F_8, C_4F_{10}, C_3F_6, C_2F_6, and C_4F_8. However, these gases are toxic, chemically reactive, and environmentally

damaging (in the range of 5000-12000) with low vapour pressure and decomposition products from gas discharge that are extensive and unknown [14]. Table 2.2 outlines the dielectric strength and GWP of a selection of PFCs [11]. Hence gas mixtures are today's research focus.

2. Hydrofluoroolefins:
The compounds of interest in this family are HFO1234ze and HFO1234yf. Experimental results show that these compounds had a dielectric strength of 80% compared to SF_6 and a low GWP (<10). However, due to their flammability property and leaving carbon residue during gas decomposition, these compounds were deemed unsuitable for switchgear applications [15].

3. Fluorooxiranes:
Research on C_4F_8O (member of the Fluorooxiranes family) shows that the compound has superior dielectric strength (relative to SF_6), low boiling point (0°C), and low toxicity. However, the conclusion was that the GWP was too high compared to the mixture's technical benefits. Some compounds in this family have responded similarly to fluoroketones. Nevertheless, the molecular structure is different, so this compound is more stable under solar radiation, having a lifetime of 38 years and a GWP of 4100.

4. Fluoroketones:
C_5FK and C_6FK are of interest in this gas family. Research has shown greater dielectric strength and low GWP when compared to SF_6. However, the problem with these compounds lies in the property of having a high boiling point. Hence, mixing with buffer gas is required to maintain a gaseous state at operating temperatures [11].

5. Fluoronitriles:
C_4F_7N has shown promising results, having twice dielectric strength as SF_6, a reduced GWP of 2100 (literature [16] suggests the GWP-100 year as 1490), and a low boiling point of -4.7°C [17]. This compound was explicitly developed in partnership with 3M™, commercially available under the designation of 3M™Novec™ 4710 Dielectric Fluid. This particular gas was used in this research, and more information about the gas will be covered in sections 2.1.3 and 2.1.4.

PFC	Dielectric strength (% of SF_6)	GWP
CF_4	40%	7390
C_3F_8	88%	8830
C_4F_{10}	120%-130%	8860
C_4F_8	125%	10300
C_2F_6	78%	12200

Table 2.2: *Relative dielectric strength of PFC (Compared to SF_6)*

Fluoroethers and Hydrochlorofluoroolefins have also been investigated, but these gases were not determined as suitable alternatives for various reasons [18]. Using computational

methods, Cyanoketene (OCCHCN) has been theoretically studied as a potential alternative to SF_6 in literature [19]. However, there is no evidence of the gas being tested to confirm the findings from the report. Table 2.3 summarises the critical characteristics of these gases considered above as a pure medium.

	SF_6	**CO_2**	**C5-FK**	**C4-FN**	**HFO1234zee**
CAS Number	2551-62-4	124-38-9	756-12-7	42532-60-5	1645-83-6
Boiling Point (°C)	-64	-78.5	26.5	-4.7	-19
GWP	23900	1	< 1	2100	6
ODP	None	None	None	None	None
Flammability	None	None	None	None	Yes
Dielectric Strength (relative to SF_6)	1	0.3	1.4	2	0.8-0.9
Toxicity (ppm)	1000	5000	225	65	800
Potential Insulator	-	✓	✓	✓	✓
Potential Interrupter	-	✓	✕	✓	✕
TRL	9	8-9	7	6	3
References	[20] [21] [22]	[23] [24]	[25] [26]	[18] [27]	[18] [28] [29]

Table 2.3: *Properties of pure medium alternative gases*

Apart from these gases, manufacturers and developers have researched other paths to identify alternative mediums. This will be briefly investigated in section 2.1.3.

From a technical point of view, a low boiling point was one of the bottlenecks researchers had significant difficulty with, as this will ensure the medium remains gaseous within typical operating temperature ranges without condensing.

SF_6 by-products are investigated to be harmful to various degrees; hence, multiple policies support maintenance workers in identifying and protecting themselves from these compounds. Similarly, the alternative should have minimal toxicity where it can be handled safely, and a short-term exposure is not harmful.

Investigating any alternative gas should look beyond its technical characteristics and assess it holistically. CIGRE brochure by WGB3.45 describes the needs for adaption or new requirements for the safe, reliable, and sustainable application of non-SF_6 gases and gas

mixtures in gas-insulated switchgear. Paper 0819 from CIRED 2017 also presented the critical variables outside technical capabilities that impact the viability of a compound used as an SF_6 alternative for switchgear. The summary of their outcome is shown in figure 2.2 [30].

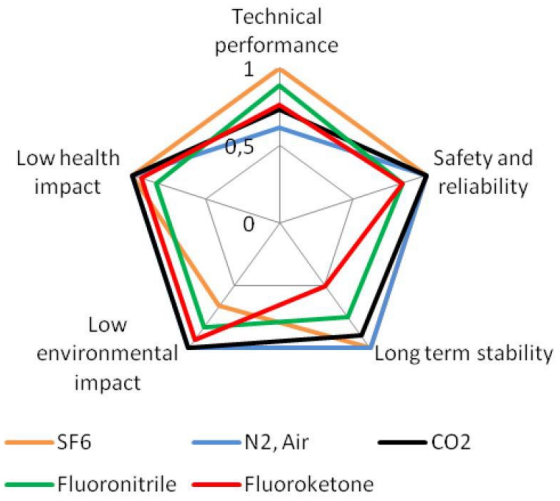

Figure 2.2: *Outcome of holistic assessment of SF_6 alternative [30]*

2.1.3 Commercially Available SF_6 Alternative Solutions

Manufacturers of gas-insulated systems have investigated various other paths to identify alternative mediums. The following paragraph will summarise the commercially available solutions:

1. **Solid Insulation Switchgear (SIS):**

   Companies such as Schneider, Toshiba, Hitachi, Eaton, Meiden, and others have investigated the possibility of developing solid-insulation, Vaccum interrupting solutions up to 145kV. In this design, epoxy resins are moulded over the live part and then covered with an earthed conductive layer. Manufacturers claim this technology to be highly reliable and have reduced routine maintenance requirements. SIS presents an advantage over AIS by protecting the equipment from external or environmental interference and also limits the possibility of a Line to Line fault.

   Moreover, hybrid solutions in GIL, such as a hybrid of solid insulation and gaseous solutions, have also been proposed. Here, epoxy resin acting as the solid insulation covers the live part, provides a steep electric field gradient, and thus reduces the electric stress. The spacing between the solid insulation and enclosure is further provided by the gaseous insulation such as dry air, N_2, or CO_2. Even though it is a promising solution, these sources of insulation may require an increased physical footprint than SF_6 [3].

2. **Airplus:**

   ABB collaborated with 3M™ to produce a gas mixture branded ‘Airplus’, a mixture of Novec™ 5110 (C5-FK) and dry air for MV levels; CO_2 and dry air as a buffer for HV applications. As with other pure gases, adding fluorine increases the dielectric strength

but at the cost of increased boiling point. Hence, it is needed to add a buffer gas. The mixing ratio usually is <15 mol% of C5, and the rest is dry air, O_2, or CO_2 depending on the application [31]. This mixture is commercially available within a specific product portfolio of ABB RMU advertised as SafeRing Airplus, which can operate at 24kV with a 630 A rating [32]. Since November 2015, these have been in the field and have provided consistent results with the behaviour expected from previous work [33]. The gas details are as mentioned in column 4 of Table 2.3.

3. g^3- Green Gas for Grid:

Novec™ 4710 fluid is the first to incorporate all essential qualities into a single composition. The structure of the Novec™ 4710 fluid molecule allowed for the optimal combination of attributes with no significant sacrifice in any of them. Because pure Novec™ 4710 dielectric Fluid liquefies at low temperatures, it cannot replace SF_6 independently. Further research revealed that the optimum answer was to combine it with CO_2 to produce a gas mixture appropriate for disconnector and circuit breaker applications [17]. In collaboration with 3M™, GE dubbed 'g^3—green gas for grid' the resulting mixture.

4. Clean Air:

Synthetic air (marketed as Siemens CleanAir) is a mixture of approximately 20% O_2 and 80% N_2 and is mainly used in switchgear in combination with the vacuum switching technology up to 145 kV from Siemens [34]. It can only be liquefied at temperatures lower than -183°C and is also stored at room temperature in a homogeneous state under high pressure (> 200 bar) [31]. GWP of this gas is 0. This gas is used to replace SF_6 at Prysmian during the experimental stage, and further results on this will be dealt with in chapter 6.

Solid insulations are often a mixture of solid material and ambient air. The most common use for solid insulation is in medium-voltage equipment. However, this solution cannot be deployed in challenging environmental circumstances such as humidity and pollution because the electrical field stays in the ambient air due to lower permittivity.

The screened insulation technology adds an extra conductive shield layer to all insulating elements' exterior surfaces. As opposed to GIS, electric fields are restricted within the solid insulating material rather than in the ambient air, making the switchgear immune to the most severe climatic operating conditions. This technique has long been employed in bushings, cable accessories, and transformers. However, the production procedures of solid-insulated components remain complicated and require precise quality controls to achieve partial discharge suppression. Even the tiniest air inclusions must be avoided since they accelerate the ageing process and cause the working medium to fail after a few months to years of service.

The limitations of all solid insulation solutions include most likely decreased heat dissipation away from conductors, related manufacturing complexity, and expense, which increases with

system voltage. In addition, unlike (most) gaseous insulation, solid insulation does not self-restore following an electric breakdown.

The other mode of insulation is Liquid insulation like oil, which was previously utilized in circuit breakers but is now mostly reserved for transformer applications, despite the fact that commercially available fluid insulated MV switchgear is limited. The primary drawbacks of oil over SF_6 are its weight, flammability dangers, particularly in the event of an internal arc fault, and environmental effect. However, the current shift to synthetic esters may reduce the environmental and flammability hazards compared to oil.

Vacuum insulation is frequently used in vacuum interrupters for switching purposes, with rated voltages reaching 145 kV. Switching using single vacuum interrupters is now viable up to 245 kV, with the possibility of serial connection for greater voltages. The electric strength of the vacuum is not proportional to distance and is restricted by electron field emission on contacts. This is a technological constraint for fully vacuum-insulated GIS, particularly in HV applications. Furthermore, the effort required to guarantee the ultra-vacuum tightness of such massive systems is significant.

Hence, solid, liquid, and vacuum modes of electrical insulation for higher voltages are ruled out.

2.1.4 g^3: A Potential Solution

As mentioned in section 2.1.3, a blend of C_4F_7N and buffer gas, marketed as g^3, is a potentially promising solution as an alternative to SF_6. The systematic name of the C4-FN is 2,3,3,3-tetrafluoro-2-(trifluoromethyl)-propane nitrile, described by the formula $(CF_3)_2CFCN$. The molecular structure of this compound is shown in figure 2.3 [2]. There are many pilot projects with this promising gas to understand the reliability further.

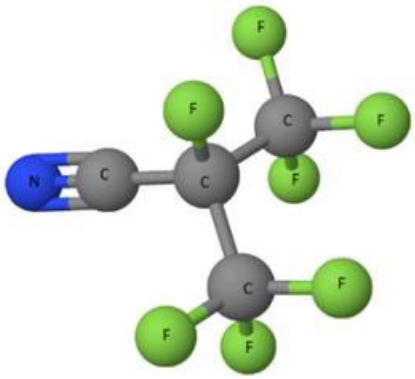

Figure 2.3: *3D Representation of C4-FN [2]*

N_2 and CO_2 are buffers for MV and HV level applications, respectively. O_2 is often used as a further component to reduce soot production in case of arcing or switching operations in switchgear. The mixing ratio is often less than 10 mol% C4, and the rest buffer gas [31]. This mixture is found to have a similar performance as SF_6 at ambient conditions and has been tested for current quenching capability.

Following are the characteristics of this novel gas:

1. **Swarm parameters: effective ionisation coefficient:**

Ionisation is an essential factor in the breakdown of gases. The effective ionisation coefficient of a C4-FN/CO_2 mixture was studied by H.Nechmi *et al.* [35] utilising a steady-state Townsend (SST) experiment with two plane electrodes of aluminium (surface roughness: 0.1µm) with a Bruce profile, which provided a uniform electric field. Initial electrons were produced by a Vaccum UV light source aimed at the centre of the cathode. Ionisation current is determined from the measurements of ionisation current and voltage applied at the electrode for different gas densities and electrode gap distances. Figure 2.4 compares the effective ionisation coefficient in pure SF_6 and different mixtures of C4-FN/CO_2. E/N is the density normalized limiting field strength (E being the electric field and N the gas density)

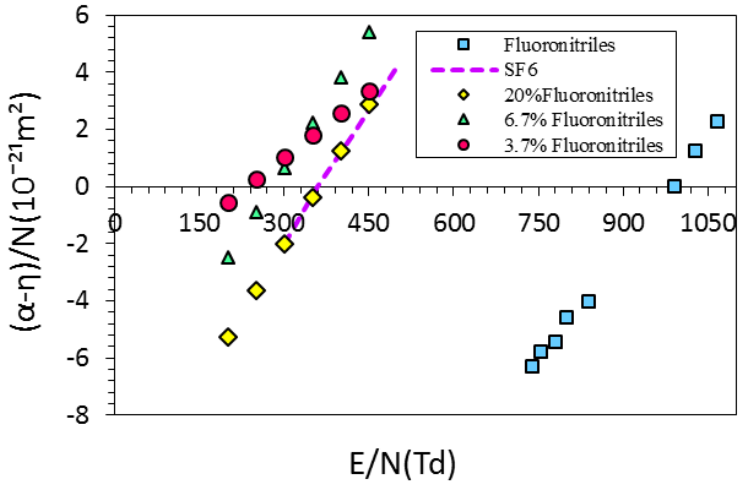

Figure 2.4: *Density-reduced effective ionisation coefficient, (α-η)/N, as a function of E/N for the C4-FN/CO_2 mixtures and SF_6 [35]*

2. **Electrical Breakdown Strengths:**
   a. **AC breakdown strength:**

Considerable research on the electrical breakdown strength of this gas mixture has been investigated and reported in recent years.

A round-robin electric test campaign within the framework of WG D1.67 performed in 14 different High Voltage laboratories has studied the effect breakdown strength of this alternative gas in detail. This campaign investigated pressure influence for 5% C4-FN and 5% O2 mixture in CO2 for AC breakdown in a uniform arrangement. Figure 2.5 (a) shows the results [2].

The authors of [36] investigated this gas mixture's power frequency breakdown characteristics under various nonuniform electric fields (f=1.05 to f=22.5). The results of this study are presented in figure 2.5 (b-f). They also investigated the breakdown strength for different mixing ratios.

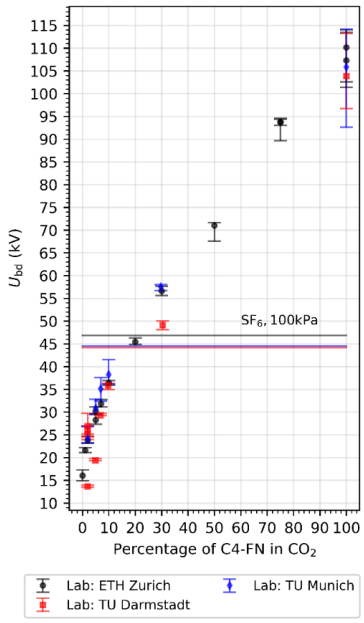

(a)

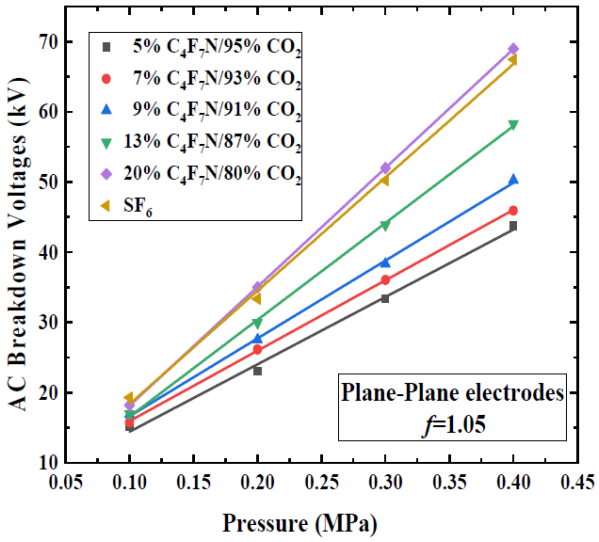

(b)

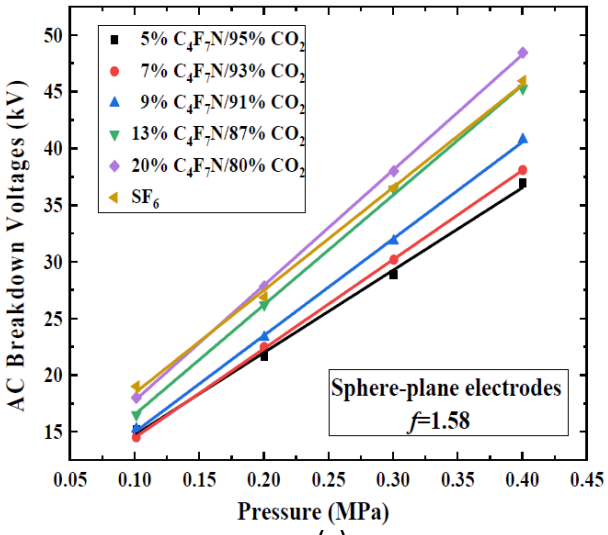

(c)

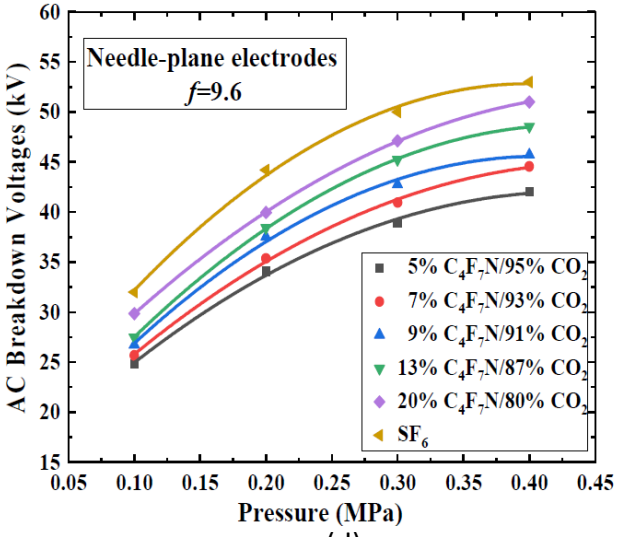

(d)

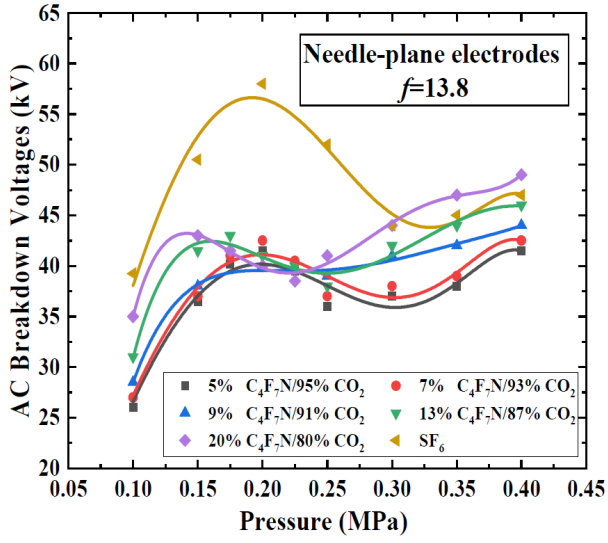

(e)

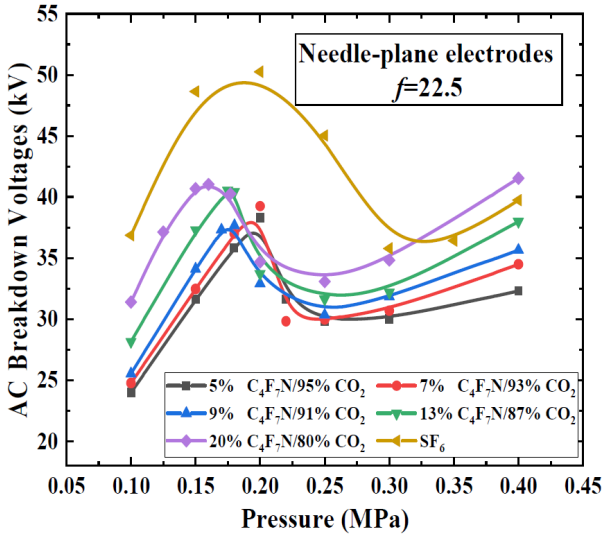

(f)

Figure 2.5: *(a) Pressure v/s AC BDV in a uniform electric field in (b) f=1.05 (c) 1.58 (d) f=9.6 (e) f=13.8 (f) f=22.5 [2] [36]*

b. Lightning Impulse Breakdown Voltage

LI breakdown voltage characteristics and polarity effect in 9% C4-FN and 91% CO_2 were investigated by the authors of [37]. The LI positive and negative breakdown voltage for the sphere plate electrode configuration is presented in figure 2.6

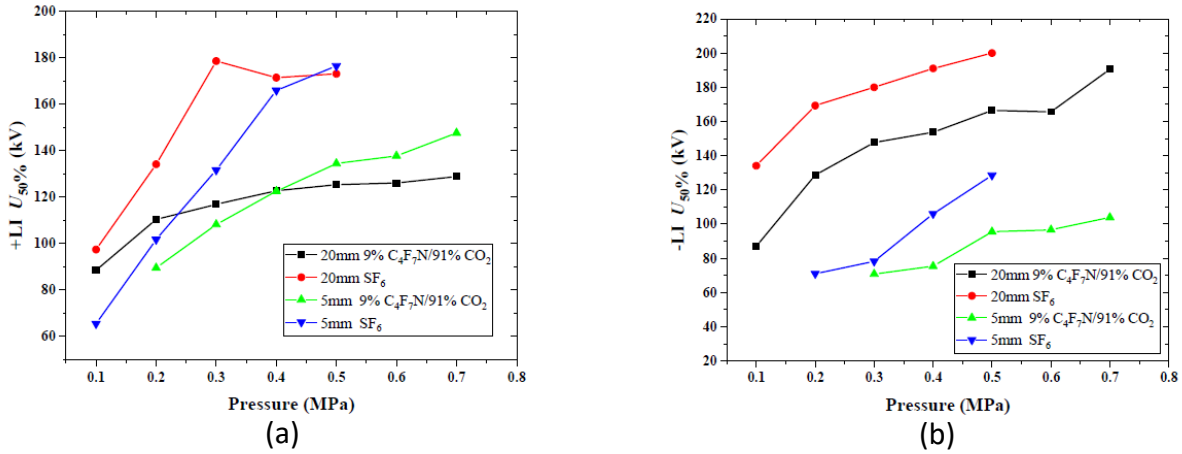

Figure 2.6: 50% breakdown voltage of sphere-plate electrode C_4F_7N/CO_2 and SF_6

3. GWP:

The GWPs of the gas mixtures are computed in line with EU 517/2014 F-gas regulation by adding the weight fractions of the constituent components multiplied by their respective GWPs, i.e. 1 for CO_2 and 2090 for fluoronitrile. To avoid liquefaction at the equipment's lowest operating temperature, the molar fraction of the fluoronitrile compound is chosen based on its saturated vapour pressure. A mixture having 4mol% of fluoronitrile is typically suitable for -30°C, whereas 6mol% or 10mol% is suitable for -25°C or -10°C, respectively. The GWPs of those three mixes are 327, 462 and 690, correspondingly [17].

4. ODP:

Organic compounds with no halogen atoms other than fluorine have been found not to affect the stratospheric ozone layer. As a result, because 3M™ Novec™ 4710 Dielectric Fluid contains no halogen other than fluorine, its atmospheric deterioration does not affect the stratospheric ozone layer and is not considered ozone-depleting. CO_2 does not affect the stratospheric ozone layer since it is halogen-free. Thus the gas mixture also has a 0% ODP [17].

5. Information on Toxicology:

Because the LC_{50} (Lethal concentration, 50% of test population) of pure fluoronitrile gas is much above 20,000 ppm, the aforementioned gas combinations are considered harmless under CLP regulation 1272/2008 and do not require additional labelling. Additional toxicity measurements performed following current interruption tests show that a heavily arced C_4F_7N/CO_2 mixture is less harmful than heavily arced SF_6 under the same conditions [17].

2.2 Ageing Aspects Of Gas Insulated Systems

Gas-insulated HV systems like GIS and GIL are designed for a lifetime of 30 years or more. Utility companies anticipate these gas-insulated systems to last up to 50 years. During this lifespan, maintenance work should be minimised. The gas-insulated HV region is expected to function without maintenance operations, particularly for MV switchgear. As a result, most current MV GIS gas compartments are constructed as sealed pressure systems (IEC 62271-200:2011 - 3.118.2) [38], requiring no maintenance during their lifespan. Hence, when there is a transition to alternative gases, the alternative shall not corrode the switchgear unit, reducing its useful lifetime beyond that of the presently deployed units.

There is extensive experience with the influence of oxygen and humidity on the ageing of air-insulated equipment, and established ways to suppress ageing mechanisms such as corrosion of electric contacts are known and reported, for example, in IEC/TR 60943. Furthermore, test techniques for ageing rubber or plastic materials in the air are well recognised and documented in specialised standards such as ISO 11346(2014): 'Rubber, vulcanised or thermoplastic- estimation of a lifetime and maximum temperature of use.' CIGRE WG B3.45 in the report 'Application of non-SF_6 gases or gas-mixtures in medium and high voltage gas-insulated switchgear' describes the exemplary test procedures and additional ageing mechanism in non-SF_6 gas or gas mixture, mainly containing fluorinated compounds with low GWP.

When considering the detrimental impact of gas on the material or vice-versa during its lifetime, the influence must be limited to a manageable level. The interaction of gases and materials must be explored and understood for this. As a result, materials or gases may or may not be certified for use with certain gases or gas mixes. This study is of significant importance as this might differ from the known experiences with SF_6 or air as insulation gas. The literature on prospective alternatives to SF_6 is not as extensive as the research on SF_6 characteristics. The industry recognises that such inquiries are still in their early stages and that further research is needed [21]. Additionally, these studies will help to predict the lifetime or to quantify the impact at the end of the lifetime of the gas-insulated system filled with alternative gas [5].

There could be four possible principal mechanisms of ageing during the lifetime of a gas-insulated HV system, and they are [5]:

- Gas decomposition due to limited stability.
- Gas decomposition due to material incompatibility.
- Material ageing due to incompatibility with the gas and its decomposition products.
- Gas decomposition due to electric arcing.

Each of the following is briefly discussed in sections 2.2.1-2.2.3. Chapter 3 will elaborate on gas decomposition due to material incompatibility and material ageing due to incompatibility with the gas. This is the basis of the first research question mentioned in section 1.3.

2.2.1 Insulating Gas Or Gas Mixture - Stability

It is a prerequisite for insulating gas or gas mixture that the gas should be stable throughout the lifetime of the gas-insulated HV system for a reliable operation. This means that the gas

should be stable throughout its lifetime without additional influence such as contact with materials, electrical stress, or discharges.

The gas molecules or the various components of a gas mixture must be chemically stable even without external influence to be used in the gas-insulating system. When a molecule decomposes, it may no longer qualify as an insulating medium, and the resultant molecules may have inferior insulation qualities. Decomposition products include, for example, two or more fragments of the original molecule or a novel combination produced from molecule fragments with or without interaction with other enclosed gases (in the case of a gas mixture). These decomposed products may have quite distinct physical or chemical characteristics. Furthermore, the chemical interactions of the components of a gas mixture must be understood and researched.

CIGRE WG B3.45 recommends ageing experiments in closed containers at elevated temperatures for extended periods to show the chemical stability of an insulation gas or insulation gas combination. It also suggests that since humidity might affect the outcome, ageing testing should be done in the real switchgear under the permissible maximum humidity environment. After a certain period, the concentration of the gas components must be within acceptable limits, and the number of decomposed products must be less than specified limits. Furthermore, the main decomposed products should be identified and tested for toxicity and corrosiveness. These ageing tests must be done without desiccants and in containers with minimal risk of reacting with any gas mixture component [5].

Homogeneity of the alternative gas mixture is also essential for a reliable operation of GIS or GIL, as the dielectric performance depends on the mixing ratio and homogeneity of the mix. The chosen mixing ratio must be location and time-independent in GIS or GIL to ensure this. The prospect of component separation overtime must be ruled out. Suppose the mixture's components are filled sequentially; for example, one component after the next, there should be knowledge of how long it will take under specified conditions before the gas mixture is homogeneous and when acceptable attributes are attained. Ideally, this should be done without additional methods, such as fans and heaters, inside the gas chamber, even though they are required to enforce evaporation or homogeneity at temperatures below the condensation temperature [5].

Low temperatures like those encountered during transportation may condense one or more gas mixture components. This is permissible as long as the process is reversible and the condensed gas is dissipated once the minimum operating temperature is reached. To recover gas mixture homogeneity, a knowledge of how long the equipment must be held at the minimum operating temperature or above after transportation, below the minimum operating temperature is essential. Additionally, CIGRE WG B3.45 recommends a temperature cycle test if transportation below the minimum operating temperature is permitted. For this, pressure and concentration should be measured in different areas of the compartment during and after the test.

2.2.2 Compatibility Of Insulating Gas Or Gas Mixture And Gas Insulated System Materials

GIS or GIL comprises several compartments mainly for gas handling and monitoring. Each compartment not only comprises metals but also contains many different materials, which are at least partly in contact with the insulation gas. These can be metals, polymers, surface treatments, grease, oil, desiccants etc.

The HV switchgear or transmission line's technical functionality is linked to an appropriate electrical design and the stable mechanical, thermal, and dielectric properties of the materials used over the whole lifetime of the equipment. With SF_6 as a dielectric medium, literature and experience show that the gas and materials cover all those requirements. The industry recognises that such inquiries are still in their early stages and that further research is needed for alternative gases [21].

Ageing processes may occur due to the interaction of the employed materials and one or more components of the insulating gas mixture. The interaction may modify the qualities of the material, but it may also affect the quality of the insulation gas.

Both impacts (impact of gas on material and material on gas) must be explored. It must be determined whether the influence on the material and the gas is acceptable or if the interaction is too strong. If there is a compatibility issue, the material must be replaced with an alternate material with more excellent gas compatibility and equivalent physical qualities.

Finally, the aggregate of contributions from all used materials in the utilised quantity must have a restricted influence on the insulating gas, and none of the materials may suffer unacceptable reductions in material qualities, which are necessary for the technical performance of the equipment. Moreover, Since utility companies look forward to retrofitting SF_6 with alternative gas in their GIS/GIL, this analysis is of significant importance, giving a qualitative idea of whether retrofitting is a solution.

There has been many standards and guidelines describing ageing test procedure and analysis to find compatibility between gas and materials. CIGRE WG B3.45 has studied those existing techniques and discussed the aspects of those tests that can be adopted for non-SF_6 gases and gas mixtures. Based on this recommendation, the experiments for solving research question 1 are carried out. Further details on compatibility, a review of existing standards, and guides on the ageing test method, an example of compatibility test with C_4F_7N/CO_2 mixture and EPDM O-rings and electrode materials will be covered in Chapter 3.

2.2.3 Insulating Gas Or Gas Mixture – Decomposition Due To Arcs And Discharges

Studies have shown that gases may decompose due to electrical arcs and discharges and can damage their electrical, chemical, and toxicological properties. New Insulating gases or gas mixtures also have the potential to be decomposed due to arcing and discharging in the gas. Decomposed gas products might also impact materials and impure insulation medium compatibility, as discussed in section 2.2.2. Electrical discharges in switchgear have varying energy levels (hence varying decomposition levels) that may be classified into the classes listed below:

1. High-energy arcs:

High-energy arcs mainly occur in gas circuit breakers having the highest arc energies (mainly used in HV applications (>52kV)). Gas load breaker switches, used in MV applications (which also uses gas to quench the arc), has arc energy level significantly lower as there are no short circuit currents but only rated currents that are to be interrupted.

In both cases, the gas is heated to high temperatures and converted into plasma. During this condition, some of the gas components may decompose by the thermal destruction of the molecules. After thermal destruction, the gas may or may not recombine as this depends on the gas chemistry. Arc energy, the volume of gas affected, duration, temperature attained in the region by the arc, and the insulation gas composition plays a vital role in determining the level of decomposition [5].

Performing a type-test or verification test can help in quantifying the decomposition. Gas sample analysis such as GC-MS before and after the test will show how much the gas has decomposed. The decomposition rate per unit arc energy [mol/MJ] is an excellent universal factor for demonstrating the intrinsic gas characteristic.

2. Low energy arcs:

In this case, no-load or short circuit currents are interrupted; instead, the charged busbars or cables (which have voltage applied) are disconnected. Small capacitive or inductive currents cause repetitive low-energy arcs between the disconnectors' opening and closing contacts. Because of the slow operation speed, the arc duration can be substantially longer than in devices designed for quick current interruption. Bus transfer currents (in the case of a double bus) in the range of some kilo Amps and earthing switches that are sometimes required to interrupt electrostatic and electromagnetic induced currents in the range of ten to some hundred amps are to be interrupted.

CIGRE WG B3.45 advises that a representative test series of operations be performed to get the decomposition rate per unit stress, e.g. [mol/operation], utilising representative capacitances and inductances, and gas samples to be taken before and after the tests. The overall impact can then be estimated by utilising the maximum number of permitted operations. If any solid decomposition products are formed due to arcing, performing a gas dielectric test before and after switching is advisable [39].

3. Partial Discharges (PD):

PDs in the gaseous dielectric are most important when considering the overall lifetime of an HV gas-insulated system. Many defects in a GIS/GIL, such as metal protrusion, floating electrodes, and surface discharges, can occur. These all have high chances of decomposing the insulating gas or component of the gas mixture, which might degrade the insulation properties of the alternative gas. Gas analysis before and after PD will give a quantitative result of the decomposition. Duration of PD application might also influence the result, as seen from experimental results in the literature. By this, the manufacturer of the GIS/GIL

with alternative gas can ensure that the possible appearance of PD does not limit the operation under normal conditions.

Solid decomposition products can also be produced by PD. These may deposit on the surface of the electrode and will significantly affect insulation strength [5]. Moreover, carbon traces could also form and shorten the gap between conductors, eventually leading to a short circuit of the carbon bridge. This is considered to have a significant effect on the lifetime of the gas-insulated system.

Decomposition product due to PD of the gas C_4F_7N/CO_2 mixture utilised in this research will be addressed in Chapter 5.

2.3 Partial Discharges In Gas Insulated System and Detection Techniques

As Gas Insulated HV systems like GIS and GIL are becoming widely utilised in power systems, their safety directly impacts the overall reliability of the power grid. GIS insulation ageing will worsen with time, posing a severe hazard to the safe operation of the electrical grid. In a long-term operation, there are often multiple defects inside a GIS, generating a unique pattern of PD signals [40]. The long-term impact of these defects has a damaging effect, primarily on organic insulation systems, degrading the electrical properties of the insulation or the insulation systems, as mentioned in section 2.2.3. This can lead to electrical breakdown and blackout [41].

2.3.1 PD Origins In GIS / GIL and 'abc' Equilant Diagram

Partial discharge in gas-insulated systems refers to the partial breakdown of electrical discharge, which might occur near the high-voltage conductor or elsewhere. The reasons for GIS/GIL PD vary, and the damage to the equipment varies greatly depending on the type of partial discharge. As a result, different forms of PD in GIS/GIL must be distinguished so an appropriate measure can be planned and executed.

Because GIS has a complicated structure, internal defects may occur throughout the manufacturing, moving, and installation processes. Internal defects include high-voltage (HV) conductor protrusions, free metal particles, floating potential, insulator-metal pollution, and insulator gap [42]. Figure 2.7 depicts the numerous faults in GIS.

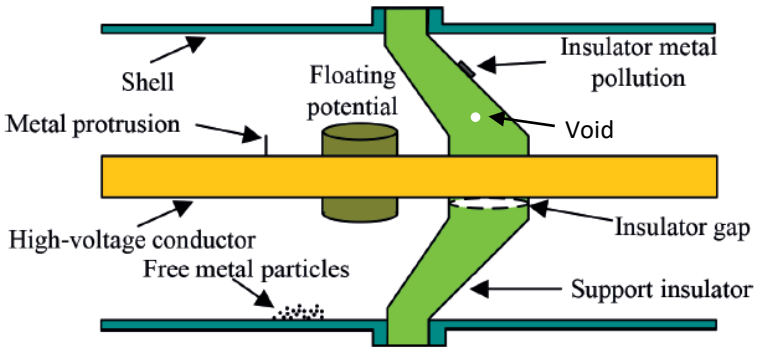

Figure 2.7 *GIS Internal Insulation-defects [43]*

- **Metal Protrusion Defects:**

  Metal protrusion defects arise from protruding elements inside GIS, such as HV conductors. These protrusions, like free-metal particles, are typically produced during the assembly, installation, or operation. Because of the sharp tip of the protrusions, the electric field is distorted, resulting in a high electric field. The strong electric field will generate a stable PD at the rated operating voltage, but it may produce a breakdown and a GIS fault at some overvoltage.

  The discharge characteristics of the protrusion on the HV conductor and the inner wall of the shell vary. Protrusions on the HV conductor often discharge in the negative half-cycle of the power frequency. In contrast, protrusions on the shell's inner wall typically discharge in the positive half-cycle of the power frequency. Some little protrusions will be ablated during long-term discharge and will not jeopardise GIS insulation. Larger protrusions, on the other hand, will persist for a long time and compromise GIS operating insulation [43].

- **Free Metal Particles Defect**

  One of the most common reasons for insulation failure is free-metal particle defect in GIS/GIL. Metal parts may rub against each other during the assembly, installation, or operating process, resulting in loose metal particles. These metal particles will move due to the electric field forces because of their tiny size. If the particle movement range is broad enough, conductive channels or arc tunnels can emerge between the HV conductor and the shell, causing catastrophic damage to the GIS. Many factors influence path formation, including applied voltage, particle shape and size, and particle position [43].

- **Insulator Gap Defect:**

  Insulator gap defects in GIS are most common on basin-type insulators (epoxy insulators), which can be divided into two groups. One kind is caused by internal epoxy resin bubbles that form throughout the production process. In this case, during operation, PD will occur in these bubbles under a high electric field, resulting in slow insulation degradation of the basin-type insulator and potentially significant insulation breakdown.

  The other kind is due to electric force in long-term operation. Mechanical vibration can cause connection loosening of basin-type insulators and HV conductive rod connections. Then an insulator gap defect arises and induces PD, causing the basin-type insulator's insulating characteristics to deteriorate [43].

- **Insulator Metal Pollution Defect:**

  The Insulator surface occasionally adsorbs metal particles that migrate due to the electric field force. Some particles may not appear harmful at first, but their mobility enhances the discharge and eventually induces the PD owing to mechanical vibration caused by electrostatic force.

Some particles will not migrate due to intense adsorption. Insulator surface pollution defects are caused by particles stuck to the insulator surface. These fixed metal particles have the following properties: charges collect on their surface, and these surface charges can occasionally increase the distortion of the electric field, resulting in PD. The particle-induced discharge will damage the surface of the insulator, resulting in surface tree markings. It may eventually lead to significant insulation breakdown and flashover [43].

The above defects can also occur in a GIL. Insulation problems produced by poor contact and metal particle defects account for a greater share, as shown in figure 2.8.

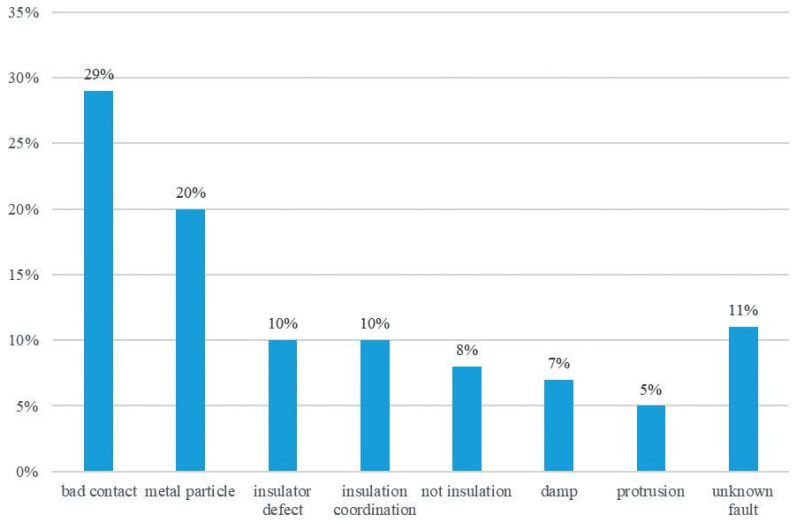

Figure 2.8: *Statistics of GIS defects [43]*

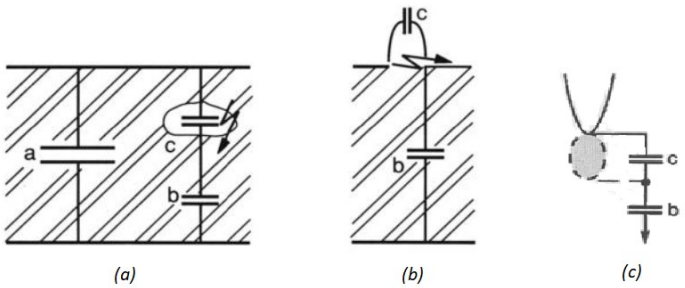

Figure 2.9: *Equivalent circuit of (a) Internal (b)Surface (c) Corona discharge [44]*

Knowing how PD takes place is essential. This can be explained using the well-known abc equivalent circuit diagram shown in figure 2.9. The voltage and current behaviour during internal (bubble in epoxy insulator defect), surface (Insulator metal pollution defect), and the corona (metal protrusion defect and/or free metal particle defect) can be understood by the equivalent circuit depicted in figure 2.9 (a), (b) and (c) respectively. The capacitance 'c' represents the void or defect in the insulation, capacitance 'b' represents the part of the insulation in series with the void, and 'a' represents the void-free healthy section of the insulation parallel to the fault.

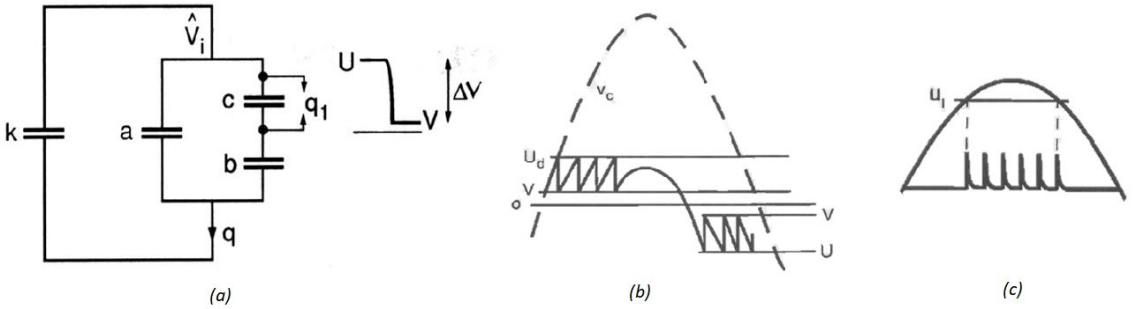

Figure 2.10: (a) Model representation of partial discharge; Recurrent Discharge in (b) void or surface (c) Corona [44]

When an AC voltage is supplied to an insulator with a void (represented by capacitance c in figure 2.9 (a)) or applied to an insulator with metal pollution defect (surface discharge) (illustrated by capacitance c in figure 2.9 (b)), a recurring discharge phenomenon occurs, as shown in Figure 2.9 (b). In corona, recurrent discharge, as shown in figure 2.10 (c), occurs. A discharge will occur if the AC voltage supplied to the sample is larger than the breakdown voltage U_d. If the voltage rise is continuous and the breakdown voltage is always exceeded, discharge happens, and the repeated pattern develops. Regarding corona, as illustrated in Figure 2.9 (c), the number of discharges grows rapidly with an increase in voltage while the amplitude remains relatively constant. As a result, the corona pattern distinguishes itself from other partial discharges. It is important to remember that actual instances are less stable than the abc model. The value of U_d is not the same for the positive and negative parts of the period, and there may be several discharge channels. As a result, discharges will develop along the sine wave with uneven size and behaviour.

The charge (commonly represented in pico coulombs, pC), which describes the amount of the discharge, is the key parameter for assessing PD activities. The direct charge value from a cavity, surface or corona discharge cannot be estimated while measuring, but the apparent charge determined is a fair representation of the intensity of the discharge, providing good information on energy dissipation and dimension of the discharge site.

2.3.2 PD Detection Methods

Due to the adverse effects described in section 2.2.3 caused by PD, detecting PD early and mitigating the cause is essential. The insulation defects mentioned in section 2.3.1 will induce local electric field distortion in the insulation medium at the operational voltage. When the local electric field approaches the critical breakdown field strength of the insulation, PD is induced, resulting in a significant number of charged particles. These Charged particles will move, recombine, and adhere in an electric field, resulting in a pulse current and accompanied by visual, electrical, thermal, and auditory phenomena. Consequently, PD detection may now be performed utilising acoustic, chemical, and optical signals in addition to electrical signals with suitable sensors. PD may be quantified in the GIS/GIL by effectively detecting these signals [43]. Digital PD measurement methods are employed for quality assurance during type testing in factories, on-site testing, and online monitoring during the service life of HV equipment. An overview of existing PD detection methods is illustrated in figure 2.11. and details of them are described below:

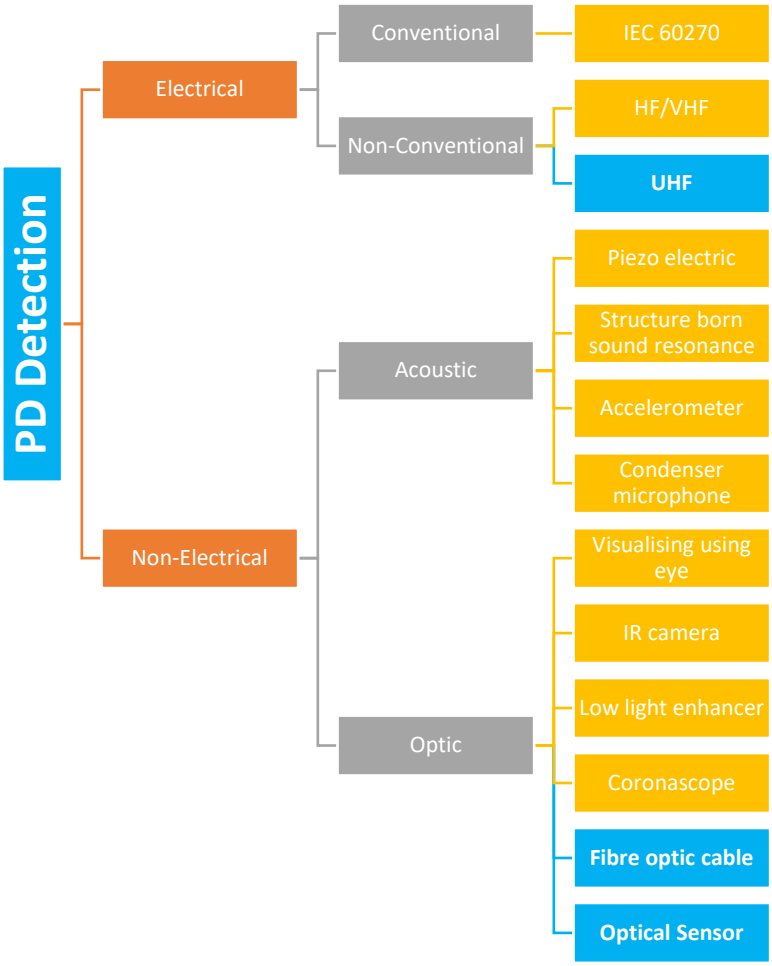

***Figure 2.11**: PD Detection Methods - Overview*

1. Conventional Electrical Method (IEC 60270)

This is the state-of-the-art conventional method of detecting PD. Figure 2.12 depicts the corresponding circuit diagram for the detection of PD in the IEC 60270 method. It consists of the test object C_a, the coupling capacitor C_k, the measurement system with the input impedance Z_{mi}, the coupling device (CD), the connecting cable (CC), a high voltage source and impedance Z between the supply unit and test item. A resonant circuit extending discharge current pulses in the time domain is usually employed in the external impedance, making detection easier [45].

The following are the major requirements for using this circuit:

- The cable's end should be correctly terminated; otherwise, a signal loss may occur.
- The high voltage supply should not contain any PD.
- An impedance or filter should be present to limit noise or interference on the supply side.
- To attain the entire PD signal, the coupling capacitor should have a suitably low level of partial discharges and a capacitance larger than or equal to that of the test item.
- Before measuring, the circuit should be calibrated with a step generator ΔV in series with a small capacitor or calibrator. To calibrate the measuring system, a known

quantity discharge is injected into test item C_a and measured using the connected system. This step is critical to ensure that the instrument correctly measures the charge during the experiment.

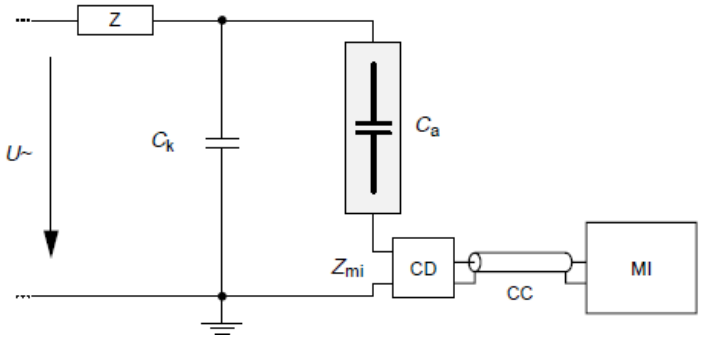

***Figure 2.12**: Standard PD circuit Diagram as per IEC 60270*

CD, CC, and MI in figure 2.12 stand for connection device, transmission system (which might be a cable or an optical cable), and a measurement instrument (oscilloscope). CD is intended to improve the signal sensitivity obtained from the PD source and is often a quadrupole. Upon accurately capturing the PD pulse with the appropriate equipment described above, PD pattern recognition and analysis could be done using time or frequency domain approaches [46].

2. Non-Conventional Electrical PD Detection

This detection is based on the fact that PD pulses consist of up to hundreds of MHz energy frequencies. As a result, an HF/VHF/UHF PD detection system is used to detect partial discharges in an unconventional electrical manner. We lose some data in the classical detection method, making it harder to reduce most noise in the lower frequency region. As sampling rate and signal processing speed improve, PD detection with a larger frequency spectrum can be measured. It yields results with reduced noise or a high signal-to-noise ratio. As a result, the usage of these unconventional approaches is rapidly increasing, particularly for field measurements in power cables, network components, GIS, and transformers.

Non-traditional electrical PD detection may be divided into three categories based on its operating frequency range:

- High Frequency (HF) - 3 to 30 MHz
- Very High Frequency (VHF) - 30 to 300 MHz
- Ultra-High Frequency (UHF) - 300 MHz to 3 GHz

To capture PD, the concept utilised here is to detect the high-frequency signal generated during a PD activity. The primary tools required are PD sensors, triggering components, a spectrum analyser or oscilloscope, and a computer equipped with PD analysis software. The circuit is identical to the IEC 60270 method, where the test item is connected in parallel to coupling capacitors, except that high-frequency capacitive or inductive sensors

are used instead of a quadrupole or coupling device. The PD pulses occur in a very brief period, with pulse width and rise time in the nanosecond range. Consequently, PD pulses with energies ranging from tens to hundreds of megahertz are generated. The PD signal collected is then sent to the spectrum analyser or oscilloscope via coaxial wire and amplifier. On the processing side, the electrical signals from the spectrum analyser are stored, and the software will be able to produce Phase Resolved PD Pattern (PRPD), which is the number of PD pulses as a function of phase. PRPD patterns can be used as an identification tool to detect the type of defect in the test object.

In this research, High-Frequency Current Transformer (HFCT) is employed along with optical sensors for comparison purposes. The details of the test setup will be explained in Chapter 5.

3. Chemical PD Detection

PD actions can be monitored chemically by analysing the insulating material's chemical composition variation. It is typically seen in GIS and transformers, where the dielectrics are gas and liquid, respectively. It is based on the idea that anytime PD actions occur, an arc is generated, resulting in high temperatures, and the insulating begins to break down into various chemicals that may be hazardous to the equipment (The case of effects of chemical decomposition is explained in section 2.2.3. Depending on the media, there are two basic methods for doing chemical PD analysis: high-performance liquid chromatography (HPLC) and dissolve gas analysis (DGA). Fuel-cell detectors, Gas Chromatography – Thermal Conductivity Detector (GC-TCD), Gas Chromatography-Mass Spectroscopy (GC-MS), and hydrogen-oil detectors can also be employed.

4. Acoustic PD Detection

This non-conventional and non-electrical method of PD detection is based on the fact that PD activities initiate wave pressure in the insulation medium [47]. GIS, GIL, transformers, cable accessories, instrument transformers, and other applications are the most common.

Sound propagates through a medium using wave motion, i.e., the propagation of local disturbance through the medium. This is the basic principle behind acoustic PD detection. It operates in the frequency range of 10 Hz to 500 kHz. As a result of PD activities, when mechanical changes occur within the insulating medium, wave motion and pressure wave are produced, which may be detected by an appropriate sensor and recorded and analysed using a typical data acquisition system. There are several ways of detecting PD activities in the acoustic domain, as represented in figure 2.11.

Piezoelectric sensors are the most commonly used acoustic PD detection domain. They are typically used in GIS and transformers. The sensors can be mounted on the body of the HV equipment for detection and monitoring purposes. The timing of arrival of the acoustic signal is commonly used to estimate PD location. Acoustic PD detection is extensively used on HV equipment having huge capacitances because its sensitivity does not vary with test

object capacitance. This approach is the most intriguing for on-site measurements since it has some intrinsic properties and strong immunity to noise and interference when performed in a shielded system. The disadvantage is the complexity of pressure wave propagation in an insulating medium, where signal path and attenuation are almost unpredictable [48].

5. Optical PD Detection

Light radiation is constantly present during the whole process of PD, from initial ionisation to extinction is the basis of optical PD detection. As a result, the light emitted throughout the process can be considered the most intrinsic nature of the PD, and optical detection can be regarded as the most intuitive method for studying fundamental properties of discharges, such as discharge morphology, discharge energy, PD pulse, and excitation spectra [49]. Ultraviolet, visible, and infrared radiations can be detected along with an electrical discharge during PD activity [50]. The emission spectrum of the emitted light is affected by the surrounding dielectric medium and must be considered when choosing an optical detecting system. This is validated in literature [51]; the authors mention, “The PD of the different gases will be different correspond to different multispectral characteristic distribution.”

Optical PD detection methods were performed only in HV laboratories for a very long time due to the complex setup and space requirement. Nowadays, thanks to better manufacturing processes for optical sensors, there are sensors available that are smaller in size, have higher sensitivity, and are incredibly resistant to electromagnetic and noise interference. Companies like Vogl electronic GmbH have developed optical-based PD monitoring techniques. However, these studies and techniques are limited to SF_6 dielectric medium. Further studies on how technically feasible it is to detect the PD using optical methods in alternative gaseous have to be carried out as the utility companies are looking forward to replacing SF_6 with an alternative gas. This research will focus on optical detection in C_4F_7N/CO_2 mixture.

As depicted in Figure 2.11, there are several methods for monitoring light during PD activities, including the eye, IR camera, low light enhancer, fibre optic cables, corona scope, optic-acoustic technique, and, most importantly, employing an optical sensor. Coronascopes are commonly used for exterior insulation such as bushing and can readily detect corona. An eye can also easily perceive some light at high voltage equipment in the dark. The optic-acoustic approach is one of the oldest and most widely used methods for detecting PD, integrating optics and acoustics physics. Optical PD detection in alternative gas was of interest in this research as it has the highest immunity to electromagnetic interference compared to all other PD monitoring techniques [49]. Optical PD monitoring can also be expected to be the state of art PD detection method in Gas Insulated Systems of the future. Table 2.4 shows the advantages and disadvantages of different PD detection methods. The following section will summarise the past research in the field of detection of PD using optics.

PD detection method / Parameters	Advantages	Disadvantages
Electrical	• Determining PD's intensity, cause, kind, and location is possible. • Measurement of high precision	• Electromagnetic interference • Relatively expensive
Chemical	• High SNR and immune to noise • Provides essential information on dielectric • Easily measurable in laboratories	• No information about PD source, intensity, type of PD • Not applicable for on-site PD measurement
Acoustical	• PD localisation possible • Noise immunity • Relatively low cost	• Low sensitivity • Not advisable for continuous PD measurement
Optical	• Best immunity against noise and EMI • High sensitivity • PD localisation possible	• Night Vision is required for most of the optical sensors [48] • Cannot detect internal discharges in solid material

Table 2.4: *Advantages and disadvantages of different PD detection methods*

2.3.3 Past Researches In Optical PD Detection

This section is dedicated to previous studies that employed optical PD detection techniques with various setups and mediums. This helped to analyse the research gap and what setup has to be used for experiments.

1. **Lens, Fibre Cable, and Optical Sensor Combination**

A combination of lens, fibre cable, and optical sensor was used to detect the light emitted due to the PD activity in literature [50] and [52]. The block diagram of detection and the experimental setup is shown in figures 2.13 (a) and (b), respectively.

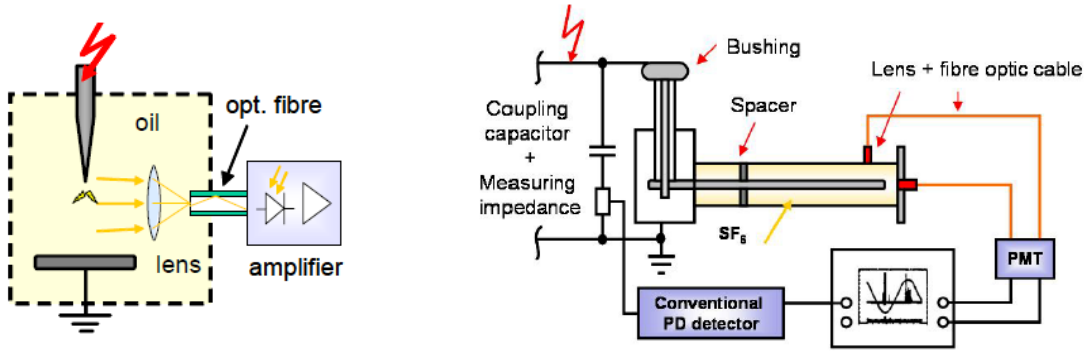

Figure 2.13: *Block dagram and experimental setup used in literature [50] and [52]*

A lens having a specific focal length was used to focus the optical fibre and the PD source. The optical fibre and lens assembly enable the collection of emitted PD light and guide the light to the detector. The detector used here is a photomultiplier. As seen in the experimental setup, the optical sensor's orientation and position are critical because they should be focused on the PD source to record the light emitted PD activity. As a result, the lens may be installed at various locations throughout the equipment. The distance between fibre optic – lens and lens- PD source should be varied per the lens equations. This optical sensor will convert optical signals to electrical signals and can thus be used to display on an oscilloscope and enables post-processing of data to obtain PRPD patterns etc.

2. Utilising Fluorescent Fibre Cable and Optical Sensor

Fluorescent fibre may also be employed for PD optical detection. The fluorescent fibre for PD detection works on the following principle: the fluorescent fibre core is blended with a trace of fluorescent material that is selectively absorbent of particular wavelengths for optical signals. The fluorescent fibre working principle and selection procedure is discussed in Chapter 5.

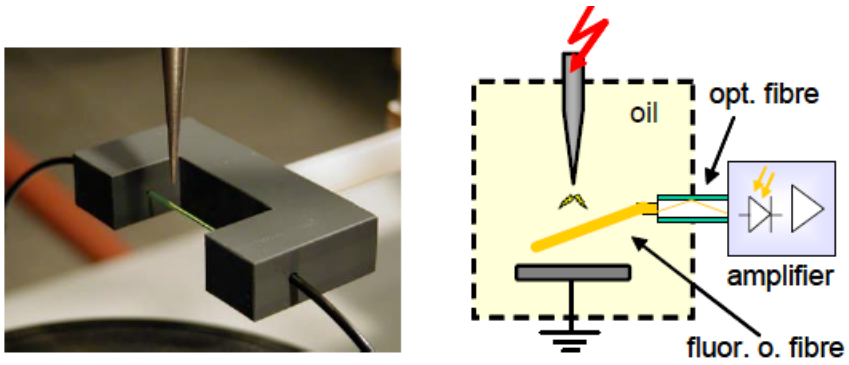

Figure 2.14: *Fluorescent fibre and block diagram representation of setup used in literature [53]*

Utilising fluorescent fibre for PD detection is researched in the literature [52], [50], [54], [53] and [55]. Figure 2.14 depicts a systematic representation of this method. It operates on the same sample premise as described in the previous section. To capture the light emission, the fluorescent fibre optic cable is put right in the centre where the PD will occur. The light travels across the fibre's surface, enters the core via this fibre, and finally reaches the end of the fibre. The illuminated tip of the fluorescent fibre (optical signal) is delivered to the optical sensor and then to the oscilloscope at the other end. Using a fluorescent fibre optic allows for direction-independent light connection [48].

This way of detecting PD can be utilised in Gas Insulated Systems. Hence, in this research, PD detection using optical fibre in the gaseous dielectrics, including alternative gas C_4F_7N/CO_2, is carried out and discussed in detail in Chapter 5.

3. Direct Measurement Using Photomultiplier

Direct measurements utilising optical sensors are the most straightforward method of detecting PD by optical methods. The use of an optical sensor for PD detection is not popular, but some study has been done in the past, and as a consequence, the PMT (Photomultiplier) is the common sensor that has been utilised in the majority of the research done in this sector. Moreover, SiPM (silicon Based Photomultiplier) sensors were also investigated for PD detection in literature [49].

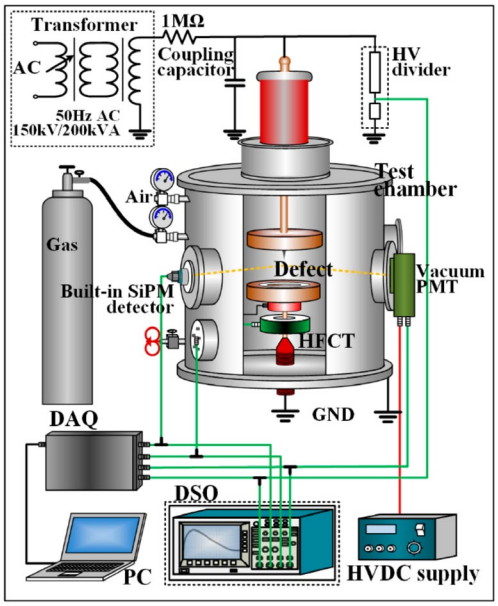

Figure 2.15: *Synchronous PD measurement system used in literature [49]*

Figure 2.15 shows the synchronous PD measurement system used in literature [49]. The system utilised two optical sensors in a confined and dark environment, PMT and SiPM. The optical sensor's output is fed directly into the oscilloscope for analysis. The optical detector is used in tandem with the standard electrical detector. This is necessary to clarify any correlation between optical system measurements and conventional measuring system results.

In the master research thesis at TU Delft by Sweta Kumari, the author has researched the feasibility of using optical PD in HV cable termination in collaboration with Prysmian Group. The research used a direct measurement utilising PMT and lens to collect PD light waves and showed successful results.

4. Optical Interferometric PD Detection In Oils

This technology, also known as Mach-Zender interferometers, is based on a merge of acoustic and optical physics. This is based on fibre optics essential interferometers such as fibre Michelson and Mach-Zender interferometers and is one of the earliest acoustic detection technologies [56]. A partial discharge creates an acoustic wave in the insulation medium’s sonic and ultrasonic range. This pressure wave will distort the fibre cable in the presence of optic fibre. As a result, the fibre's mechanical stress, strain, and optical transmission properties will vary [57].

The experimental setup is shown in figure 2.16. The primary fibre employs a single fibre mode and a laser. A beam splitter and a fibre coupler divide the light from a source into two fibres with equal intensity of 3 dB. The first fibre is known as the reference fibre and the second as the sensing optical fibre coil. The lights in the two coils are recombined at the end by transmission using a Mach-Zender interferometer or reflection using a Michelson interferometer to form interference signals. The reference optical fibre coil contains the original light source, while the sensor optical fibre coil is kept close to the PD source and is permitted to be disturbed by the PD-induced acoustic wave. When a long fibre is utilised for sensing, the essential fibre interferometer has a high sensitivity; when an acoustic wave strikes the detecting fibre optic sensor coil, the phase of the optical signal changes in comparison to the reference sensor coil. In the end, the detector will transform the light source from the sensor coil into an electrical signal (through an optoelectronic transducer), which may then be amplified before being analysed with a digital oscilloscope.

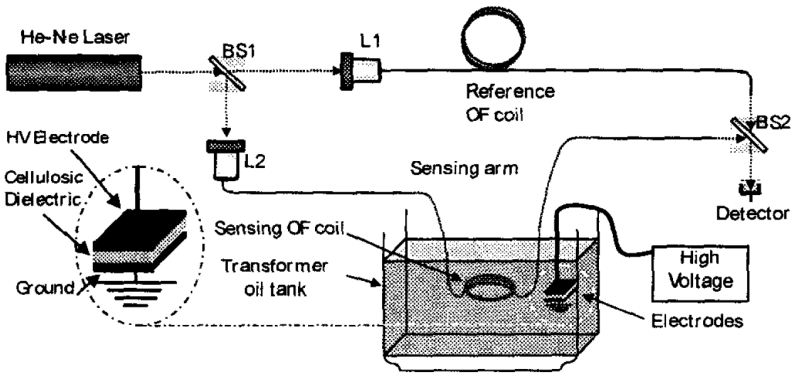

Figure 2.16: *Experimental setup of the optical fibre interferometric detection of PD [56]*

In the laboratory, this technique may be used for the transformer. The intricacy of the test setup and the need for a laser and a good acoustics source make it challenging to apply in a real-world context.

5. Fabry-Perot Interferometer

The Fabry-Perot interferometric sensor has been utilised for various purposes, including detecting waves emitted by a PD source. This method is based on the previously discussed optical interferometric technology. In this case, a Fabry-Perot cavity with two reflecting surfaces is used as the sensing device.

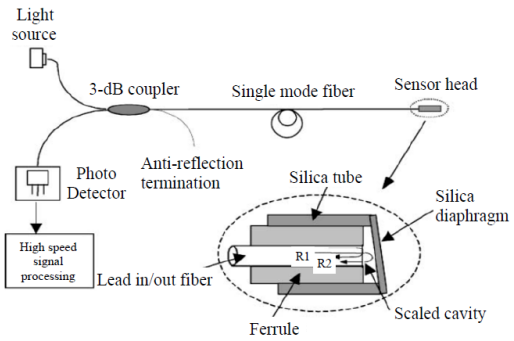

Figure 2.17: *Illustration of the principle behind the Fabry-Perot Interferometric sensor [58]*

The Fabry-Perot interferometer sensor, as shown in Figure 2.17, is built with a silica diaphragm and signal mode fibre at the sensor lead. The LED light source's output is linked to a 2x2 coupler. This coupler's output is fed into a single-mode fibre, which is attached to the sensor head, while the other arm leads to the photodetector. Initial reflection is caused by the split end of the fibre. The remaining light is transmitted from the fibre end and reflected off at the silica disk, as seen in the magnified view of the sensor in Figure 2.17.

Several previous investigations have shown that this sort of sensor is suitable for detecting the acoustic signal caused by the PD in transformers or GIS.

2.4 Prysmian's Policy On Sustainability And SF_6 Usages

This section covers the background knowledge gained towards solving the question proposed by the Prysmian Group R&D team at Delft and is linked with the third research question mentioned in Chapter 1, section 1.3.

Prysmian Group has been the world leader in the energy and telecom cable industry since its birth in 1879. Headquartered in Milan, this multinational corporation each year manufactures thousands of miles of underground and submarine cables, network components systems for power transmission and distribution, and medium and low voltage cables for the construction and infrastructure sectors. It has the broadest range of services and know-how in the business.

Prysmian proposed two new strategic aspirations in 2021 that will lead the Group's medium-term actions: the Climate Change Ambition and the Social Ambition. Linking Social Ambition with Environmental Objectives is a fundamental component of Prysmian's ESG identity, alongside the Group's intention to actively contribute to the energy transition, promote the transition towards a more equal, diverse, inclusive, and prosperous working environment, actively and positively impact the development of the communities and societies in which we are present.

The Climate Change Ambition aims to position the Group as a critical technology participant in the low-carbon energy transition. As depicted in figure 2.18, The climate plan embraces "science-based" objectives that are in line with the standards of the Paris Agreement, which aims for net-zero emissions from internal operations (Scopes 1 and 2) by 2035 and by 2050 from the value chain (Scope 3). Prysmian received approval for its aims from the Science-Based Target Initiative (SBTI) in September 2021, an organisation created in 2015 to assist corporations in establishing emission reduction objectives in line with the Paris Agreement objectives [59].

2.4.1 SF_6 Emission Origins & Regulatory Rules

Network components in a cable system help in bridging two places or two power equipment. They are one of the most crucial components in the power system network. Due to accuracy in fine details requirement, Cable network components such as power cable terminations are comprised of complex designs and hence require more careful development. Many iterations are to be carried out to bring out a single product. Moreover, the network component must operate at a safe limit and withstand all the stresses it is exposed to, including the high stresses during testing.

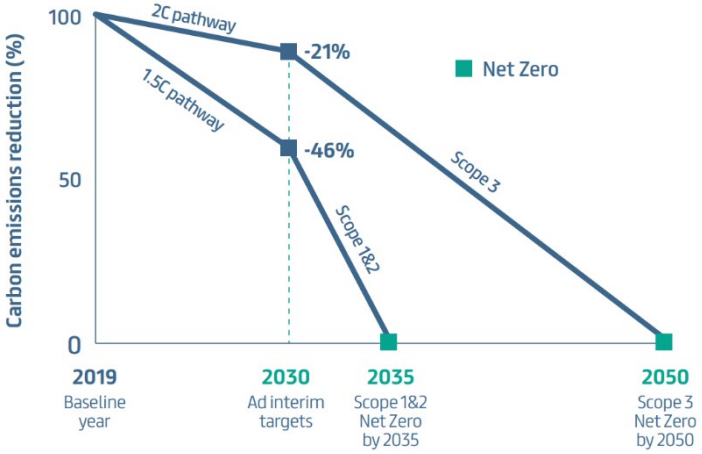

Figure 2.18: *Prysmian's net-zero climate ambition [58]*

Prysmian produces various HV cable components rated for multiple operating voltages. All the network components undergo routine testing to provide a quality product to their customers. Apart from that, factory acceptance and special tests are also carried out in a sample to further verify the reliability and quality. Each product family has its test setup and voltages as per the norms. The test setup and test stresses are detailed in chapter 6.

Since enormous stresses must be withstood during the test voltages, most components are tested with the help of SF_6 as an insulating medium. During routine testing, multiple components are filled with SF_6 and tested one by one with a risk of leakages. As per the Prysmian sustainability report of 2019, from all the factories of Prysmian, it is estimated that emissions from network component gas leakages were 35, 021 t CO_2 eq in 2019. This increased in the year 2020 to 56,134 t CO_2 eq. In 2021, the emissions were at a high of 61,970 t CO_2 eq.

Considering this, Prysmian undertook a thorough analysis to examine the potential originating from the energy transition process, including favourable conditions resulting from more strict greenhouse gas emission reduction legislation. The project was carried out by evaluating four International Energy Agency scenarios (STEPS, APS, SD, and NZ), demonstrating how the cable market will play a critical role in reaching the expected goals of the ecological-energy transition. The Group identified that it is already committed to 'Reducing SF_6 in the cable testing phase and lead reduction/substitution for insulating sheaths' [59]. Under Scope 1&2, the Group aims to phase out SF_6 emissions.

The first step toward reducing SF_6 emissions was actively monitoring the SF_6 leakages, giving adequate training to testing personnel and recovering SF_6 to the maximum after testing. Since products are tested one after the other, leakages are inevitable, and an alternative solution is required. This search for alternative solutions leads to the research question proposed by the Prysmian Delft R&D team.

A plan was proposed to solve the research question and is detailed in Chapter 6. As part of the initial study, it was found that it was much more feasible to use an alternative gas to replace SF_6 than dry-type setups. The test stresses in the component being tested have to be evaluated first, and a thorough knowledge of how breakdowns happen in gas medium has to be studied.

2.4.2 Breakdown In Gas

Because gas molecules can be ionised by light, radioactive radiation, or even cosmic radiation, a gaseous dielectric always includes electrons. Several electrons occur between the electrodes, which recombine if there is no electric field. In the presence of an electric field, electrons are propelled in the direction of the field.

The mean free path in low-pressure gas is limited to part of a millimetre; hence, electrons will collide with the gas molecules. The gain in kinetic energy during this collision is

$$W = eE\lambda = e\frac{E}{p} \qquad \textit{Eq, 2.1}$$

Where E is the field strength and p is the gas pressure. An electron colliding with a gas molecule can be an elastic or inelastic collision. When an elastic collision occurs, it may change direction and accelerate till another collision. However, the gas atom is excited to a higher energy state during an inelastic collision. Since this is a non-stable state and the atom falls back to its primary state, radiating photons. At a higher energy state of an atom, there is a possibility that the collision will lead to the liberation of an electron from gas molecules and finally having two electrons. This multiplication of electrons is known as ionisation and is the most critical factor for initiating gas breakdown.

A coefficient is introduced known as the ionisation coefficient α, which is the average number of ionisations per cm in the field direction. This also equals the number of new electrons per cm in the field direction. The coefficient is proportional to the number of collisions taking place per cm. This is also proportional to the gas pressure. As the pressure increases, the number of electrons available for collision increases.

$$\alpha :: p \qquad \textit{Eq, 2.2}$$

Moreover, α depends on the kinetic energy of colliding electrons,

$$W = eE\lambda \qquad \textit{Eq. 2.3}$$

Combining equations 2.2 and 2.3 leads to

$$\alpha = pf\left(\frac{E}{p}\right) \qquad \textit{Eq. 2.4}$$

The general expression for many gases is

$$\alpha = Ap.e^{-\frac{Bp}{E}} \qquad \textit{Eq. 2.5}$$

Where A and B are constants depending on the gas type and temperature.

Ionisation factor α or ionisation efficiency as a function of E/P for Argon is shown in figure 2.19. It has a maximum, below which there are no sufficient amount of molecules to have optimal ionisation, and above the maximum, the mean free path between the molecules is too small to gain sufficient energy.

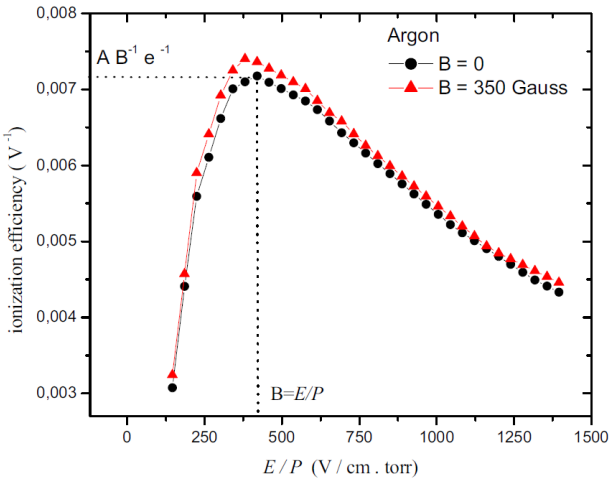

Figure 2.19 Ionisation factor vs E/P for Argon [60]

The repeated ionisation of gas molecules causes a multiplication of the number of electrons, termed Avalanches. If N_0 number of electrons leave the cathode, the number of electrons at a distance x from the cathode can be calculated as

$$N_x = N_0 e^{\alpha.x} \qquad \textit{Eq. 2.6}$$

As can be derived from equation 2.5, the number of electrons increases exponentially, hence the term avalanche. Avalanches do not cause a breakdown but cause leakage current.

- **Townsend Mechanism**

As per the Townsend mechanism, a feedback process that requires releasing the new electron is required for breakdown. There are two feedback mechanisms:

1. Feedback by γ process
   - After ionisation, the electric field accelerates positive ions that remain in the avalanche and flow towards the cathode.
   - When an ion collides with the cathode, there is an γ chance that an electron will be expelled from the cathode.
   - The order of magnitude of γ relies on the velocity of the ion and, as a result, on the field strength E and the material of the cathode.
   - Secondary electrons are formed in this manner, and they trigger new avalanches.
   - These fresh avalanches create new secondary electrons, and the series goes on.
   - The series will explode, and a very large number of electrons are created, so the gas breaks down.
2. Feedback by photons
   - Photons emitted by excited atoms in the gas reach the cathode and produce photoelectrons.
   - These photons move in every direction, and only a part of them reaches the cathode. The gas also absorbs a part of these photons.
   - The photons that reach the cathode release an electron upon reaching the cathode.

This mechanism is only valid up to about 1atm x 5mm. For larger distances, the breakdown mechanism changes and can be explained as per the streamer mechanism.

- **Streamer Mechanism**

There are fundamental differences when the pressure x distance exceeds 5atm mm. In this case, the time to breakdown is far shorter than derived from the Townsend mechanism. The breakdown voltage no longer depends on the cathode material; the breakdown channel is sharp and narrow. To explain this, around 1940, Raether, Meek and Loeb independently proposed the Streamer Theory of Breakdown in Gases.

The theory postulates that the space charge formed in the avalanche starts to affect the electric field if the avalanche surpasses a critical length. The breakdown mechanism is as follows:

- 75% of all space charge is situated in 8% only of the avalanche length, and 95% of the space charge is situated within 18% of the length. Moreover, the positive ions are way too slow compared to electrons. As a result, the positive ions are still at the spot where they were formed when the electrons have vanished. Hence positive space charges are formed.
- The large space charge formed starts to affect the electric field in the gap.
- If more than 10^8ions are present, and the electric field is greatly enhanced so that extra ionisation and the creation of photons takes place.
- Photons cause ionisation in adjacent gas atoms so that new avalanches are formed that amalgamate with the space charge of the original avalanche
- The space charges reach out, and a streamer builds up from the anode towards the cathode, causing a breakdown.

The breakdown voltages are affected by several parameters, which have to be taken care of when choosing a gaseous dielectric:

1. Pressure
2. Temperature
3. Humidity
4. Dust
5. Electrode surface
6. Air current

Out of these, the humidity effect of breakdown voltage is crucial when choosing dry air as an insulating medium. The effect is caused by the attachment of electrons to water molecules so that the electron multiplication is impeded.

Chapter 6 discusses the validation tests done in Prysmian with synthetic air (80%N_2 and 20% O_2) on network components, and different Schweiger value with breakdown strength in air is carried out.

3. Materials & Alternative Gas Qualification

This chapter deals with the need for ageing, reviews existing standards and guides on ageing test methods, previous research with compatibility of alternative gas C_4F_7N on EPDM and electrode materials, and the recommendation as per CIGRE to qualify a material or gas to use as an alternative gas.

3.1 Introduction

GIS and GILs are one of the power grid's most expensive components and are expected to have a lifetime of more than 40 years. These components of GIS are mainly made of metal, but it also contains various other materials that are at least partially in touch with the insulation gas. Typical materials include:

- Polymers: Elastomers (rubber), Epoxy resin and thermoplastic materials
- Metals: Stainless steel, Copper, Aluminium, Zinc, Silver, Brass, Tungsten, metallic coating and alloys.
- Surface treatments: Metallic coating, wet paints or powder agents
- Desiccants: Molecular sieves or other types
- Oil and Grease: Contact grease, Mechanical grease

The materials that are in touch with another material should be compatible to assure that there is no possible degradation during the lifetime.

3.2 Material Compatibility Tests Objective And Possible Incompability Consequences

A gas-insulated system's technical functioning is linked to a good design and the mechanical and dielectric qualities of the materials employed throughout the equipment's lifetime. During the lifetime, ageing processes caused by the combination of the employed materials and one or more components of the insulating gas or gas mixture may occur. This contact may modify the characteristics of the material itself, but it may also affect the quality of the insulation gas.

The impact of insulating gas or gas mixture on the material and the material on the gas must be researched for all materials utilised. It must be determined whether the influence on the material and the gas is acceptable or if the interaction is too strong, and the material must be replaced with an alternate material with more excellent gas compatibility and equivalent physical qualities.

Finally, the aggregate of contributions from all used materials in the utilised quantity must have a restricted influence on the insulating gas, and none of the materials may suffer unacceptable reductions in material qualities, which are necessary for the technical performance of the equipment.

This information will help the utility companies to retrofit their gas-insulated system with an alternative gas. An idea of whether materials and gas are compatible will also help

manufacturers of the gas-insulated system move with the trend. Moreover, manufacturers of cable components such as HV cable to GIS termination can also yield information from this study.

If there is a compatibility issue between gas and material, the following consequences, as mentioned in table 3.1, might occur [5].

Material	Possible failure mode	Consequence
Polymers – Thermoplastic, thermoset	**Chemical reaction**	**Increased brittleness, risk of cracking, reduced strength, loss of dielectric performance**
Polymers - elastomers	Chemical reaction	Swelling, reduced elasticity, extraction of softener, change in tensile strength, elongation and hardness
Metals	Surface Corrosion	Particle generation, increased friction, gas leakage, increased resistance
Surface treatments (paint, passivation)	Chemical reaction	Particle generation, reduced adhesion
Desiccant	Absorption of the gas in addition to humidity	Reduction of dielectric performance
Grease and oil	Chemical reaction	Separation of components, loss of function as a lubricant
All materials	Decomposition of the gas	Loss of dielectric performance

Table 3.1: *Possible consequences of material incompatibility with gas*

3.3 Existing Standards And Guidelines On Ageing Test Procedures

Only ageing could depict the compatibility of gas and materials. However, ageing throughout the lifetime is a time-consuming process. Hence accelerated ageing with the help of elevated temperature and thereby increasing the chemical reaction is the way to get fast results on compatibility.

Over the past years, there has been some standardisation for this ageing test. However, no particular ageing mechanisms are addressed in standards (except T&D Europe Guide and IEEE PES Report) to qualify alternative gas and gas mixtures for gas-insulated equipment. This section overviews the prevailing test procedures and CIGREs recommendation on what aspects of those tests can be adopted for novel alternative gas or gas mixtures. Following are the prevailing test procedures and their primary scope [5]:

1. **IEC 60505 (2011) - Evaluation And Qualification Of Electrical Insulation Systems:**
   This standard offers the foundation for calculating the ageing of electrical insulation systems (EIS) under electrical, thermal, mechanical, and environmental stresses or combinations of these (multifactor stresses).

2. **IEC 60216-1 (2013): Electrical Insulating Materials – Thermal Endurance Properties – Part 1: Ageing Procedures And Evaluation Of Test Results**
   This standard defines the general ageing conditions and processes for determining the thermal endurance properties of electrical insulating materials or mixtures of such materials. An Arrhenius relationship between material property change (ageing) and temperature is assumed in the implementation of this standard.

3. **T&D Europe (2016) "Technical Guide To Validate Alternative Gas For SF6 In Electrical Equipment"**
   The proposed test sequence with electrical equipment or mock-ups is designed to demonstrate that no major degradation in dielectric performance, tightness, or resistance of the main circuit occurs.

4. **ISO 2578 (1993): Plastics –Determination Of Time Temperature Limits After Prolonged Exposure To Heat**
   This standard provides the concepts and processes for assessing the thermal endurance qualities of polymers subjected to extreme temperatures for extended periods.

5. **ISO 11346 (2014): Rubber, Vulcanised Or Thermoplastic —Estimation Of Lifetime And Maximum Temperature Of Use**
   This International Standard provides the concepts and processes for determining the thermal endurance of rubbers based on prolonged exposure to high temperatures.
   In this case, the calculation of thermal endurance is exclusively dependent on the change in chosen attributes caused by periods of exposure to increased temperatures.

6. **DIN 7795 (2015): Measuring Compression Set Of Elastomers In Hot Water**
   This standard describes the equipment and technique for measuring the compression set of elastomer seal rings in hot water between 70 and 80 IRHD (IRHD = International Rubber Hardness Degree).

7. **IEC 60300-3-1 (2003): Dependability Management – Part 3- 1: Application Guide Analysis Techniques For Dependability – Guide On Methodology**
   This section of IEC 60300 overviews frequently used dependability analysis approaches. It outlines the standard methodology, its benefits and drawbacks, data input, and other requirements for employing various techniques.
   This standard is designed to give the required knowledge for selecting the most appropriate analysis techniques by providing an introduction to various methodologies.

8. **IEEE Power & Energy Society Technical Report PES-TR64 Of May 2018: Impact Of Alternate Gases On Existing IEEE Standards**
   Type testing should be done not only at the lowest pressure level. But also with the lowest mixture proportion to replicate end-of-life conditions. In chapter 4.2 on compatibility, the discussion focuses on the stability of the gas when exposed to material or components as used in HV or MV equipment.

CIGRE recommends a testing procedure for alternative gases compiling the prevailing compatibility testing standards. The methods for compatibility can be divided into the following two cases:

1. **There are no or very few chemical interactions predicted between the insulating gas and the materials:**

The goal of the test is to show that the expectation is valid and that chemical reactions and decompositions are insignificant. In this scenario, a suitable test process is an integral test, which covers the complete design in a single test. There are different ways how this can be done.

One way will be to use a whole compartment of a GIS for this, containing all materials in the correct quantities and depicting the product's design. Alternatively, smaller compartments containing various material samples might be utilised to accelerate ageing, understanding that the ratio of gas volume to material surface in GIS may not match the real scenario (preferably more material in smaller volumes). Humidity conditions, as in real cases, should be considered. The gas compartment must be filled with the insulating gas or gas mixture and kept at a high temperature. Care should be given in selecting the right temperature to avoid an extra ageing impact that deviates from the actual circumstances of the insulating gas during service. The maximum permissible temperature, particularly for polymers, must be addressed. A temperature of 100°C is a reasonable compromise for accelerated ageing.

2. **Chemical interactions of the insulating gas with materials are known or anticipated:**

If there is an expectation of incompatibilities, CIGRE recommends testing the interaction of materials and gas in a defined procedure, as shown in figure 3.1.

The initial test (STEP 1) focuses on the material's influence on the new gas or gas combination. The chosen material will come into touch with the new insulating gas or gas combination during the test. During ageing, additional chemicals and decomposition products are created due to chemical interactions or breakdown of the insulating gas molecules.

The Arrhenius equation shows that temperature is the driving force in most chemical processes. The reaction rate of most chemical reactions at normal temperature doubles every 10°C. It is evident that Increasing temperatures will result in quicker chemical reactions, resulting in observable quantities of breakdown products. However, this approach has limitations since some chemical reactions do not begin below certain temperatures and the findings are deceptive if these temperatures are surpassed.

As per CIGRE, using an ***ageing temperature of 100°C*** appears to be a reasonable balance between the desired acceleration of the ageing process and the unintended influence of the temperature itself on the material properties, regardless of the gas. The test duration required to have decomposition products which can be quantified depends on many factors. The main factor is the gas mixture, but also the compatibility of the materials. Short durations may result in inaccurate measurement; extended durations are more accurate but time-intensive. Based on previous experience with examined gas mixtures, including fluoroketones *or* ***fluoronitriles, a length of 4 to 8 weeks*** allowed for the initial distinction of compatibility levels.

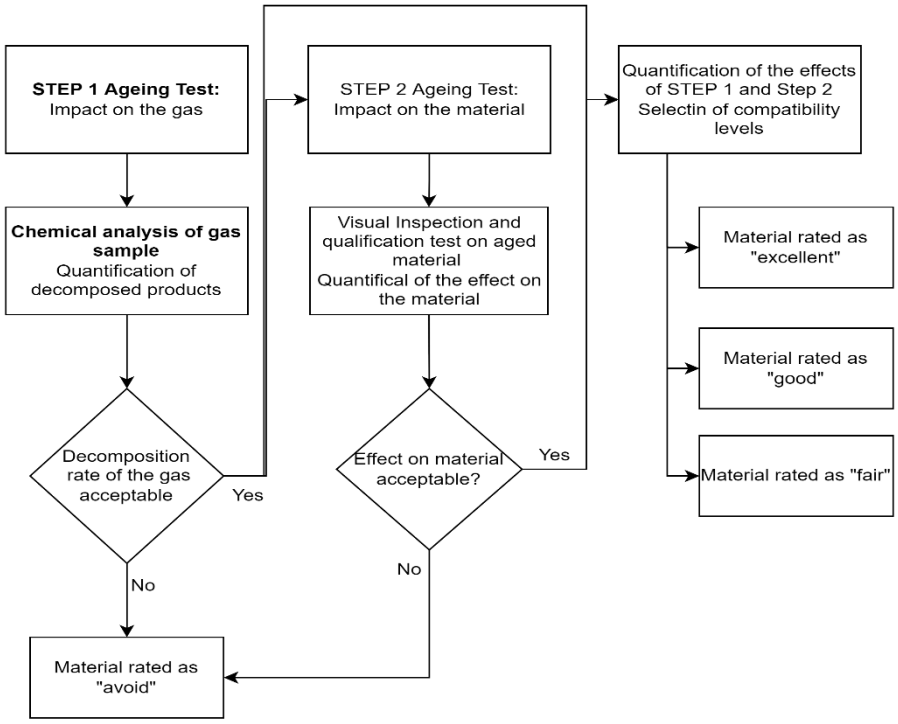

Figure 3.1: Material qualification procedure as per CIGRE

Gas sampling and the analysis of the gas sample using the method of GCMS, FTIR, and breakdown test can be performed to analyse the compatibility of material on gas.

Step 2 deals with the impact of the gas on the material. There is a chance that during the ageing process, the various ingredients in the test container will create breakdown products. The test container must be chosen (or produced) in a way that only compatible materials are used. Otherwise, it may have a detrimental and deceptive effect on the test findings. Stainless steel encapsulation materials are suggested. When seals are necessary to close the container, an appropriate sealing material must be chosen. The case of incompatibility issue with EPDM O-ring and C_4F_7N/CO_2 alternative gas mixture is addressed in section 3.4. The seal should not be greased (this is not necessary for static seals), or suitable grease should be used. Industrial autoclaves might also be an alternative.

It is advised that a pressure sensor or manometer be installed to record the pressure's evolution over time. A slowly decreasing pressure might indicate a leak. Because of the high

temperature, considerable gas loss by permeation through the seal is to be expected. This can vary greatly depending on the components of the gas combination.

Polymer degradation is determined by the decline of their characteristics. The rate of deterioration of these qualities, i.e., the rate of degradation reaction, changes with temperature. Temperature increases often cause an increase in reaction rate, which is related to a rise in the reaction rate constant (k). The Arrhenius equation describes the link between the rate constant and temperature as:

$$k(T) = A \cdot e^{\frac{E_a}{RT}} \qquad \textit{Eq. 3.1}$$

Where A is the pre-exponential factor, E_a Is the activation energy, R is the gas constant, and T is the absolute temperature. Equation 3.1 can be further derived into lifetime represented as a function of the temperature [61]:

$$ln(t) = \ln\left(\frac{1}{A}\right) - \frac{E_a}{R} \cdot \frac{1}{T} \qquad \textit{Eq. 3.2}$$

Accelerated ageing by application of temperature will increase the chemical reaction between the gas and the materials. Hence, to accurately measure the influence of the gas on the material throughout the whole lifetime of the GIS/GIL equipment, Arrhenius life estimation and the right temperature obtained from Arrhenius curves has to be considered.

3.3.1 Qualification Test On Aged Material

The following are some tests that may be used to certify aged materials:

- Real components aged in the tests mentioned above can be utilized for applicable type tests or qualification tests under type test circumstances, such as dielectric tests, interruption tests, mechanical endurance tests, or short-time current (STC) testing. The content should be qualified if these tests are passed.
- When testing a whole physical component is not practicable, representative test objects can be developed, and functional parameters can be tested on these test objects. These tests should be evaluated in a comparative manner, that is, by comparing non-aged material samples and aged samples. Additional information can be obtained if the results are compared with those aged in air or SF_6 (reference ageing). Furthermore, the emphasis should be on dielectric and mechanical efficiency.
- Seals, for example, may need special testing. Elongation until the break or other parameters is an example of the test.
- Corrosiveness is another significant factor to evaluate in the material test. Visual inspection provides a preliminary suggestion, but another testing may be necessary to rule out detrimental influence.

3.3.2 Material Rating

Once the tests are done, a material can be rated as in table 3.2 [5].

Rating	Effect	Details
Excellent	Negligible	Negligible gas decomposition and negligible material effect
Good	Minor	The gas decomposes slowly and has little influence on the substance.
Fair	Moderate	Moderate gas decomposition and/or low influence on the material
Avoid	Severe	Substantial gas decomposition and/or significant material effect

Table 3.2.: Possible material compatibility rating

3.3.3 Lifetime Impact Of Material On The Insulation Gas

As long as any decomposition of the insulation gas is induced by any substance in contact with the gas, there may be an influence on the insulation gas's and/or equipment's lifetime. This is just one conceivable process that leads to the consumption of the original gas or gas components over time, among other impacts. The influencing factors of used materials in real GIS/GIL equipment are:

- The primary influencing aspect is the dielectric performance of the insulating gas or gas mixture during the equipment's lifespan. This is the direct impact in which the breakdown may result in the reduction of a dielectrically significant insulating gas component, lowering the dielectric withstand of the gas mixture.
- Another element that might be considered is the formation of solid decomposition products. They can considerably influence dielectric performance, especially in the case of conductive breakdown products. Because the effects vary depending on the design, tests must be carried out on actual equipment.
- As an indirect influencing factor, the impact of breakdown products caused by material incompatibility or arcing may decrease lifetime.

Moreover, the impact of gas decomposition on the lifetime is also essential. The impact of parameters like duration of the ageing, temperature, the ratio between material surface or volume and gas, ratio between surface and volume of the material and humidity (in the material, bound on the surface or in the gas) on certain common materials to determine whether they are relevant or not is essential.

Lifetime estimation using the Arrhenius law can be examined; however, this is greatly dependent on the chemical reaction processes. The parameters, however, form a multidimensional matrix in which it is difficult to perform tests for every potential combination, even if only a few distinct parameters are chosen for each effect. In such cases, the Design of Experiments (DoE) technique can be utilized to minimize the number of experiments.

3.4 Addressed Compatibility Issue of C_4F_7N/CO_2 And GIS Materials

In previous years, researchers started to check the compatibility between the novel alternative gas C_4F_7N/CO_2 with the common materials found in GIS.

3.4.1 Compatibility between C_4F_7N/CO_2 And EPDM

Ethylene Propylene Diene Monomer (EPDM) is commonly used as a gasket material in SF6-filled HV equipment, and the combination of its specific material properties and gasket design allows, for example, GIS to be tight with sufficient reliability throughout its lifetime and to meet the maximum allowed leakage rate of 0.5% per compartment per year as specified in IEC 62271-203. However, the compatibility of C_4F_7N/CO_2 and EPDM gas mixture must be studied for applying the gas in GIS/GIL.

Because the fluoronitrile molecule is bigger than SF_6, there is no problem with penetration. However, CO_2 is the primary component of the gas mixture, and CO_2 molecules are smaller than SF_6 molecules; penetration through polymeric materials, particularly gasket materials, has been thoroughly tested for compatibility by the researchers in literature [62], [63], [64] and [17].

The gas permeability of elastomer material used for gaskets used in GIS/GIL was tested using the differential-pressure technique in line with ISO 2782-1:2012. The penetration rate is tested at room temperature on 2mm thick elastomer samples. The test cell is made up of a low-pressure side and a high-pressure side that is separated by an 80mm sample under test. The low-pressure cup side is filled with N_2 at 1 Bar absolute, while the high-pressure cup side is filled with the test gas at 5 Bar absolute, such as SF_6 or CO_2 or a C_4F_7N/CO_2 mixture alternative gas.

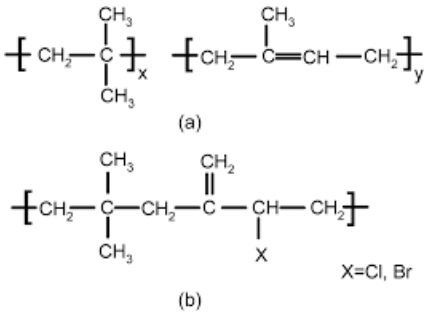

Figure 3.2: Molecular structure of (a) Butyl (b) halogenated butyl rubber

Butyl rubber is known to be impermeable to low molecular weight gases like CO_2 and air components. Butyl is an isobutylene-isoprene copolymer with a low proportion of isoprene (0.5% to 3%), as shown in figure 3.2(a). Copolymerization with isoprene produces some double bonds, allowing it to be vulcanized by sulfur-based chemicals. Pure butyl is known to be ozone sensitive due to the double bonds in the isoprene chain, which prohibits its widespread usage in high voltage equipment. To address this issue, halogenated butyl rubber, as shown in figure 3.2 (b), was chosen in the study since it has no double bonds on the main molecular chain and is not ozone sensitive.

Temp [°C]	Permeation rate coefficient $[cm^2 \cdot bar^{-1} \cdot S^{-1}]$			
	C_4F_7N/CO_2		SF_6	
	EPDM	CIIR-BIIR	EPDM	CIIR-BIIR
20	$2 \cdot 10^{-8}$	10^{-9}	$4 \cdot 10^{-9}$	$7 \cdot 10^{-11}$

Table 3.3: Permeation rate coefficient of EPDM and CIIR-BIIR in SF_6 and C_4F_7N/CO_2 alternative gas mixture [17]

The penetration rate of EPDM and halogenated butyl (CIIR-BIIR) vs SF6 and the $C_4F_7N_2/CO_2$ combination is shown in Table 3.3. The tests' findings reveal that the C_4F_7N/CO_2 gas combination's penetration rate is five times greater than EPDM's. In contrast, the penetration rate of CIIR-BIIR to the C_4F_7N/CO_2 combination was lower than the reference value, guaranteeing appropriate electrical equipment in compliance with the current standard for SF_6-filled equipment.

Moreover, the following conclusions were also mentioned regarding the compatibility of EPDM and C_4F_7N/CO_2 mixture [63]:

- When EPDM is subjected to a C_4F_7N/CO_2 environment at temperatures of about 80°C, it decomposes, releasing various distinctive byproducts such as C_3F_6, CF_3H, and C_2F_5H. The EPDM surface was also found to be severely damaged at this temperature. Fluorine buildup occurs throughout the contact as well.
- C_4F_7N adsorption and dissociation are caused by interactions between C_4F_7N and EPDM defects and particles. The CN group's N atom tends to create new bonds with EPDM. Furthermore, the F atom attached to the central C atom of C_4F_7N might react with EPDM particles to produce C_4F_6N and establish additional FC bonds with EPDM.
- At temperatures above 70°C, EPDM rubber is incompatible with the C_4F_7N/CO_2 gas mixture. Hence, It is essential to modify EPDM or locate another appropriate rubber to be utilized as the O-ring for C_4F_7N/CO_2 in engineering applications.

During the course of this thesis, gas providers, manufacturers and utility companies shared experiences with Nitrile Butadiene Rubber (NBR) and C_4F_7N/CO_2. From this, it was understood that NBR is compatible with novel alternative gas.

3.4.2 Compatibility Between C_4F_7N And Electrode Materials

The authors of the paper [65], developed a gas-solid interfacial reaction platform, and thermal ageing studies of C_4F_7N/CO_2 gas mixture with copper and aluminium at different interface temperatures were performed. The composition of the C_4F_7N/CO_2 and the structure and element content of metal materials were investigated and studied. The gas-solid interfacial mechanism was addressed, and the compatibility of the C_4F_7N/CO_2 gas mixture with copper and aluminium was examined. The conclusions were:

1. At 220°C, a C_4F_7N/CO_2 gas mixture might react with copper, producing C_3F_6 and causing severe corrosion on the metal surface. The colour of the copper surface rapidly deepens as the interface temperature rises, and a massive number of crystalline particles are formed. CuO, CuF_2, and fluorine buildup on the metal surface were observed.
2. At high temperatures, the interaction of the C_4F_7N/CO_2 gas mixture with aluminium did not decompose the gas insulating medium or severely corrode the aluminium surface. Aluminium's morphology does not alter considerably, and its compatibility is excellent.
3. The compatibility of C_4F_7N/CO_2 gas combination with copper is weaker than that of aluminium, and the high temperature generated during overheating fault

circumstances would enhance the contact of the gas mixture with copper, endangering the service life and safety of the equipment.

4. To avoid copper corrosion in GIS applications using this alternative gas, anti-corrosion treatment will be required. Moreover, temperature monitoring should also be improved to minimize severe corrosion caused by overheating issues.

3.5 Summary

The technical operation of a gas-insulated system is tied to proper design and the mechanical and dielectric qualities of the materials used throughout the equipment's lifetime. Ageing processes caused by the combination of the utilized materials and one or more components of the insulating gas or gas mixture may occur during the lifetime. This contact may change the material's properties itself or may even also change the quality of the insulating gas.

Only ageing could depict the compatibility of gas and materials. However, ageing throughout the lifetime is a time-consuming process. Hence accelerated ageing with the help of elevated temperature and thereby increasing the chemical reaction is the way to get fast results on compatibility.

There are no existing standards to test the compatibility of C_4F_7N/CO2 alternative gas with the materials of gas insulated systems. However, CIGRE WG B3.45 has derived compatibility test parameters from the existing SF_6 standards. Based on this, a temperature of 100°C and an ageing time of 4-8weeks are suggested for this alternative gas. This will be the basis of the ageing test performed in the next chapter.

4. Compatibility Of C_4F_7N/CO_2 & Epoxy Under Accelerated Thermal Ageing

This chapter comprises the selection of gas and epoxy, experimental setups, conditions considered, and results of the experiments towards the research question 'Compatibility of C_4F_7N/CO_2 alternative gas mixture and epoxy under accelerated thermal ageing'. The reasoning for the anomalies found after the experiments are also addressed.

4.1 Ageing Setup

4.1.1 Choice Of Gas And Its Properties

The alternative gas C_4F_7N/CO_2 mixture was utilised in this research. This alternative gas was chosen because of its high potential as an SF_6 alternative. During the course of the literature study, it was understood that this promising solution had research gaps that needed to be solved and addressed to be finally used as an alternative. Hence, the research trend in gaseous dielectric systems is this novel gas.

As mentioned in section 2.1.4, a mixture of less than 10 mol% C_4F_7N and the rest CO_2 is termed g^3. Moreover, during the literature study stages, it was understood that many companies are pilot testing this gas mixture which comprises 3mol% to 9mol% of C_4F_7N. So an average of this concentration was considered. Hence, 5mol% C_4F_7N and 95mol% CO_2 were utilised for all the experiments. ***This gas will be termed 'test gas' in the proceeding sections.*** O_2 was not considered in the mixture as the study focuses more on the dielectric property and not the arc quenching capability. O_2 needs to be added to the mixture only to reduce soots produced in case of arcing or switching operations in switchgear.

The gas was obtained as per the requested mixture from the reputed gas dealer DILO. As per the datasheet received, the gas had the properties as tabulated in Table 4.1. Concentration data are in mole fraction of the component (equal to parts per mole). The analytical accuracy gives the uncertainty of the content of a specified component as a product of the stand uncertainty and the coverage factor (k=2).

Component	Nominal value [%]	Analytical value [%]	Analytical accuracy
2,3,3,3-tetrafluoro-2-(trifluoromethyl) propane nitrile [C4-FN]	5.00	4.99	± 3% rel
Oxygen [O_2]	0.00	0	± 3% rel
Carbon dioxide [CO_2]	Rest		

Table 4.1.: *Mixture concentration of the gas*

The obtained gas's pressure, temperature and volume can be approximated using the Ideal gas law and are presented in *appendix A*. However, applying ideal gas for test gas will cause a certain error at higher pressures and low ambient temperatures. Hence, two assumptions are

used to calculate partial pressure and liquefaction temperature. First, the intermolecular interaction of C_4F_7N and CO_2 is ruled out. The total pressure is considered to be the sum of the partial pressures of C_4F_7N and CO_2. Second, the mixed gas's liquefaction criterion is examined, such that when any of its components achieves its saturation vapour pressure, the mixed gas liquefies. The cubic equation is a popular, ideal gas correction equation widely used. It can illustrate the pressure, volume, and temperature correlations between liquid and gas states. The Peng–Robinson cubic equation of state with the Stryjek–Vera modification (PRSV) equation is a cubic equation that is more accurate than the Redlich–Kwongand and Peng-Robinson equations. As a result, the equation of state is determined based on the PRSV equation, with a and b as the two parameters, as indicated in Equation 4.1, where b represents the adjustment for molecule volume and the second term of the PRSV equation represents the correction for intermolecular interaction [66].

$$p = \frac{RT}{V_m - b} - \frac{a(T)}{V_m(V_m + b) + b(V_m - b)} \quad \textit{Eq. 4.1}$$

Where,

$$a(T) = a_c\alpha(T_r) = 0.457235\frac{R^2T_c^2}{p_c}\alpha(T_r) \quad \textit{Eq. 4.2}$$

$$b = 0.077796\frac{RT_C}{p_c} \quad \textit{Eq. 4.3}$$

$$\alpha(T_r) = \left[1 + k\left(1 - \sqrt{T_r}\right)\right]^2 \quad \textit{Eq. 4.4}$$

$$k = k_0 + k_1\left(1 + \sqrt{T_r}\right)(0.7 - T_r) \quad \textit{Eq. 4.5}$$

$$k_0 = 0.378893 + 1.4897153\omega - 0.1713184\omega^2 + 0.0196554\omega^3 \quad \textit{Eq. 4.6}$$

$$T_r = \frac{T}{T_c} \quad \textit{Eq. 4.7}$$

Here, p is the pressure of the gas, V_m is the molar volume, R is the ideal gas constant ($8.31446262\ m^2\ kg\ s^{-2}\ K^{-1}\ mol^{-1}$), T_c is the critical temperature, P_c is the critical pressure, ω is the acentric factor and k_1 is the pure compound parameter. For C_4F_7N, T_c is 112.778°C and T_p is 25.028 Bar [27].

The concentration of C_4F_7N in the mixture significantly affects the dielectric strength of the mixture. The breakdown strength of 5mol% C_4F_7N and 95mol% CO_2 compared to SF_6, 5mol%C5-PFK 95mol% CO_2, air, and pure CO_2 in a homogenous electric field with a 2.5mm gap distance is as shown in figure 4.1.

It can see that the dielectric strength is almost 175% times that of air by adding only 5mol% C_4F_7N into CO_2. Literature studies on the breakdown in this gas show that when the concentration of C_4F_7N is between 15% and 20%, the dielectric strength is comparable to SF_6.

Moreover, since the gas is mainly indented to reduce GWP, this gas aspect of the gas mixture is also of importance. Literature [67] has analysed this for this particular gas mixture concentration, as shown in Table 4.2. The liquefaction temperature for the mixture concentration is shown in figure 4.2.

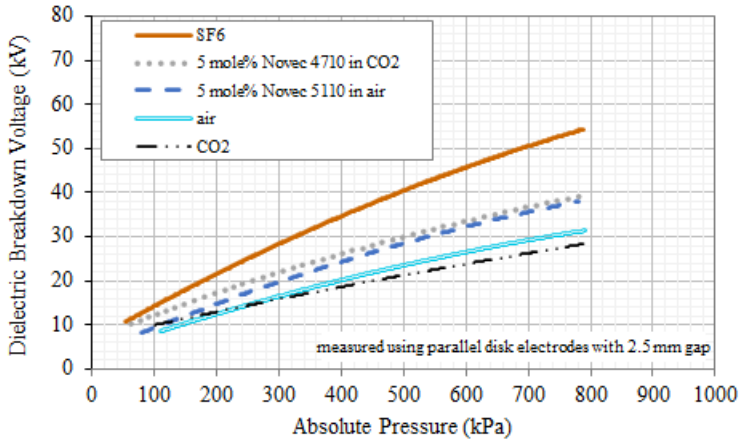

Figure 4.1: Dielectric breakdown voltage of 5mol% of C_4F_7N and 95mol% CO_2 compared to other gases

Gas	100% SF_6	5mol% C_4F_7N / 95mol% CO_2
Pressure (bar)	4	6
GWP of the gas mixture	23500	398
GWP reduction relative to SF_6	-	98.3%
GHG content (kg CO_2e/m^3)	553929	4969
GHG emission reduction from discrete emission with respect to SF_6	-	99.1%

Table 4.2: Climate performance of 5mol% C_4F_7N/95 mol% CO_2 compared to SF_6

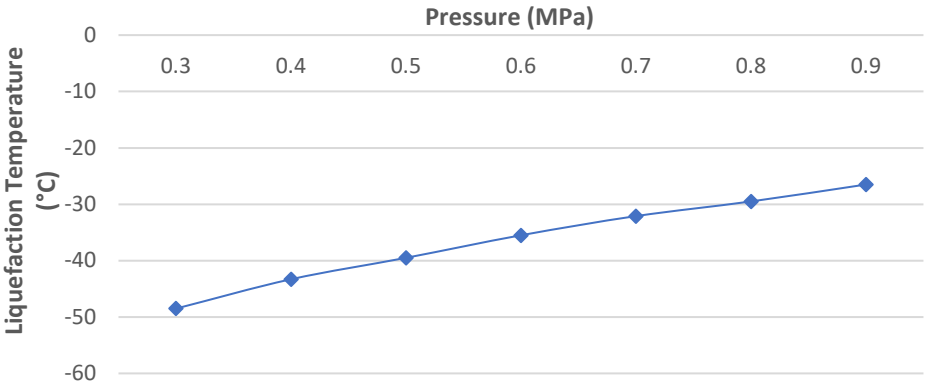

Figure 4.2: Liquefaction temperature of 5mol%C_4F_7N/95mol% CO_2

4.1.2 Epoxies – Uses, Types And Samples Used

Epoxies are used as spacer insulators in Gas Insulated Systems. However, these epoxies contain certain fillers instead of bare epoxy resin. Inorganic elements applied to organic resin insulation in varied quantities provide some control over certain physical and electrical qualities.

In the power industry, inorganic fillers such as aluminium nitride (AlN), boron nitride (BN), silicon dioxide or silica (SiO_2), aluminium oxide or alumina (Al_2O_3), titanium oxide or titania (TiO_2), silicon carbide (SiC), and zinc oxide (ZnO) are commonly incorporated into electrical

insulating polymers to achieve and improve specific electrical, mechanical, and thermal properties. For example, the resistance of nanocomposites to partial discharges and electric treeing permits the development of novel insulation systems with increased electrical breakdown strength. Aside from electrical qualities, mechanical strength and thermal conductivity are significant in some applications, such as the insulation systems of big electrical machinery and high ampere rated gas-insulated lines.

During the course of this thesis literature study, it was found that Quartz filled and Al_2O_3-filled samples are typically used in GIS and GIL, respectively. Quartz-filled epoxies were found in the GIS-cable termination. Literature has shown that Al_2O_3-filled epoxies are widely used in GIL as spacers. Hence, these filler types of epoxy samples were considered in the study.

Quartz-filled (BXH) and Al_2O_3-filled (ITH) types of epoxy samples were obtained from a leading epoxy resin insulators and parts manufacturer for the high-voltage transmission industry in the EU. Table 4.3 depicts the critical specification of the epoxies obtained. The mechanical and electrical strengths of both the epoxies are mentioned in *Appendix B*.

Code	**SiO_2**	**Al_2O_3**	**Unit**	**Measurement Standard**
Resin Type	Solid epoxy resin based on Bisphenol A	Solid epoxy resin based on Bisphenol A		
Hardener	Phthalic anhydride PSA	Anhydride		
Filler	Quartz LM-10	Al_2O_3		
Processing	Conventional gravity casting process (under vacuum)			
Loss Factor (Tan δ)	2.2	0.5-0.7	%	IEC 60250, 50 Hz, 25°C
Dielectric Constant (ϵ_r)	4.1	4.99	-	IEC 60250, 50 Hz, 20°C

Table 4.3: *Material specification of the samples used in the test*

Cylindrical as well as epoxy sheets of both types were utilised for the study. The dimensions of the samples are mentioned in figure 4.3.

As per the manufacturer, to produce the cylindrical samples uniformly, quickly and efficiently, the samples were cast inside tubes with an inner diameter of 20mm. The author thoroughly checked the samples for defects, and only good samples were selected for the experiments and ageing purposes.

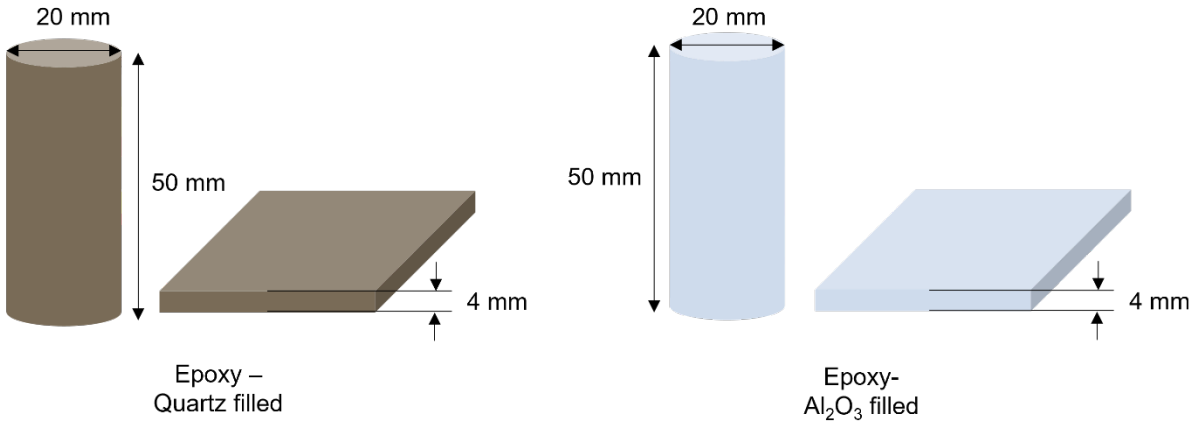

Figure 4.3: *Epoxy sample dimensions*

4.1.3 Ageing Chambers

As per the CIGRE recommendation, the ageing container or chamber must be chosen in such a way that only compatible materials are used. Otherwise, it may have a negative, misleading effect on the test results. Also, when seals are necessary to pressure tight the container, an appropriate seal material must be chosen.

Two separate chambers were utilised to age the two different filler epoxy samples. A stainless steel chamber with a volume of approximately 12 litres (as shown in figure 4.4 (a)) and a GIS-cable termination (as shown in figure 4.4 (b)) provided by Prysmian were utilised. The GIS-cable termination is made of epoxy with quartz filler. The cable end of the termination is used as the chamber, which has a volume of approximately 8 litres. The end can be sealed with a flange.

O-rings were utilised between the flange and the chamber to seal the pressure. As mentioned in section 3.4, O-rings must be given special care when used with alternative gases. Only compatible material O-rings are to be used.

(b) *(b)*

Figure 4.4: *Ageing chambers (a) stainless steel chamber (b) GIS-cable termination*

In the initial phase of the experiment, a test with EPDM O-ring and the stainless steel chamber filled with test gas at 100°C was conducted. This resulted in gas entirely escaping from the

chamber. A clear understanding of whether leakage happened due to the compatibility issue of EPDM and test gas or some other leakages is unknown. However, the ageing was repeated.

In order to ensure there were no leakages in the chambers, they were pressurised with dry air to 6 $Bar_{(abs)}$ for a day. A digital manometer was used to monitor the pressure. Both chambers were found to be pressure tight.

Moreover, the datasheets of the couplings equipped with the chamber were also referred to ensure they could withstand the ageing temperature and were found to be resistant. The stainless steel chamber had a DILO DN20 coupling, and the GIS-cable termination chamber was equipped with a DILO DN8 coupling.

4.2 Ageing Parameters and Preparation

As recommended by CIGRE (covered in section 3.3), an ageing temperature of 100°C and a duration of 744 hours (1 month) were considered. The pressure of the gas was selected to be 6 $Bar_{(abs)}$ based on the information obtained that most companies are pilot testing the gas at a pressure normally ranging from 3 $Bar_{(abs)}$ to 9 $Bar_{(abs)}$. An average of 6 $Bar_{(abs)}$ was hence selected.

40 cylindrical samples along with multiple sheets of both quartz and Al_2O_3-filled epoxies were well cleaned with Isopropyl alcohol. However, the samples were not treated to remove the humidity within the epoxy, if any, after manufacturing (During manufacturing, the samples were treated under vacuum (see appendix B)). Both the chambers were also cleaned with Isopropyl alcohol to remove any grease or contaminants if present. They were kept in a clean area to further dry and prevent dust and contaminants.

Because the chambers in this experiment are composed of various materials, care was taken to prevent the undesirable influence of chamber material on the test gas and epoxy samples. Epoxy with quartz filler was put in GIS-cable termination as the sample, and the chamber is made of the same material, quartz. If epoxy with Al_2O_3 filler is used in the GIS-cable termination chamber, it will result in a mixed interaction between the two distinct filler types and test gas, making it difficult to determine the reason for compatibility issues if any.

Taking this into account, the samples were put into the chamber one by one to ensure that each sample surface would be in touch with the gas during ageing. It also ensures that the ratio of gas volume to epoxy is good enough. The chambers were then sealed by applying a small amount of silicone grease around the O-ring and tightening with suitable nuts and bolts. Silicone grease is often used for lubricating and maintaining various rubber parts, such as O-rings, without expanding or softening the rubber, although silicone rubber is contraindicated owing to these qualities. On non-metal-metal contact surfaces, this grease works effectively as a corrosion inhibitor and lubricant.

We are interested in analysing the interaction between dry alternative gas mixture and epoxies. Hence, care should be taken to make the ageing gas free from all contaminants. The hose and fittings used to vacuum and fill the gas should also be free from contaminants and moisture. This can be ensured to a great extent by flushing the hose and fittings using dry N_2. Moreover, DILO advises using steel hoses and maybe even a special reducer due to some

degrading properties of the test gas as C_4F_7N can be a little corrosive, and CO_2 damages some EPDM sealing material used in the reducers.

Once the chambers were sealed with the flanges, they were vacuumed. This ensures that the ageing gas mixture does not contain traces of any other gas element (mainly components of ambient air, as the chambers were exposed to ambient air before sealing) apart from the test gas mixture. This also makes the chambers humid-free. The epoxies will then only be subjected to interact with the test gas during ageing. Chambers were vacuumed to a pressure of 0.3 mbar and were left for a few minutes under this condition to remove the residual humidity. DILO SF_6 mobile handling machine, as shown in Figure 4.5, was used for this purpose.

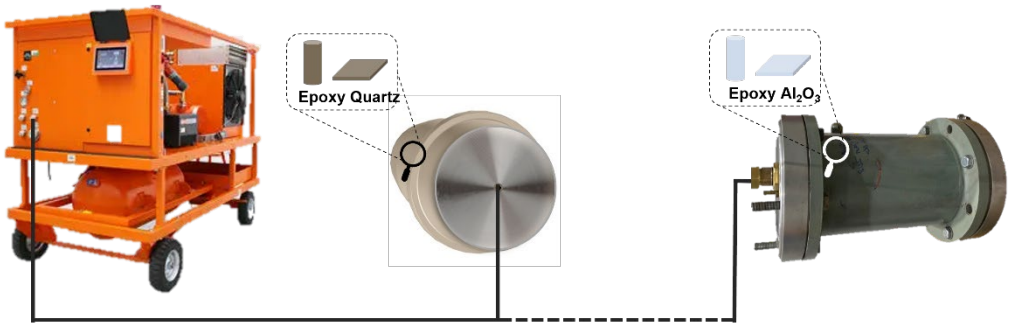

Figure 4.5: *Vacuuming process using DILO SF_6 mobile handling machine*

Upon Vacumming, the chambers were filled with the test gas, 5mol% C_4F_7N / 95%CO_2 mixture to a pressure of 6 $Bar_{(abs)}$. The chambers were then placed in the BINDER BD 400 oven for thermal ageing, as in figure 4.6. Along with the chamber, cylindrical samples were placed in the oven to see if heat affected the sample. This will aid in determining the change in epoxy physical characteristics (if any) was caused by interaction with the test gas or simply by heat application. The ovens were set to a temperature of 100°C.

Figure 4.6: *BINDER BD 400 and the chamber with epoxy inside the oven*

Both temperature and pressure are critical in the ageing process. Hence, these parameters are to be monitored. The chamber temperature was monitored using a T-type thermocouple connected to a RS 1314 Dual Thermometer, as seen in figure 4.7 (a). The pressure was monitored on alternative days with a digital manometer, as shown in figure 4.7 (b).

(a) *(b)*

Figure 4.7: *(a) Thermometer and (b) manometer used*

The samples were kept in the oven for 1 month, and care was taken to monitor any leakages that could happen due to overpressure or wear and tear of sealants on heat application.

The primary scientific goal of this research question is to understand and have explicit knowledge of what happens when the epoxy comes into touch with this novel gas and to determine whether the gas and epoxy are compatible. Multiple after-ageing tests must be performed to provide an answer to this.

4.3 After Ageing Visual Inspection

After the ageing procedure, both the samples were visually inspected for changes. Both the samples had a shiny surface upon ageing. Epoxy with Al_2O_3 filler showed a yellowing on the surface. However, the Al_2O_3-filled epoxy sample left in the oven for the same ageing period with air did not show any characteristic difference. Figure 4.8 shows the colour difference observed. To verify whether the colouration was in the bulk of the material, epoxy aged in gas was cut into a section. It was found from the cut section that there was no characteristic colouration inside the epoxy. The colouration was only on the surface. These comparisons demonstrate that the yellowing is caused due to interaction with the gas at elevated temperatures rather than the influence of temperature.

The occurrence of yellowing on the surface was also addressed previously in the literature where different gases were used. As per the literature, three possible reasonings are possible:

- Photo-oxidation
- Epoxy leaching
- Thermo-oxidative reaction

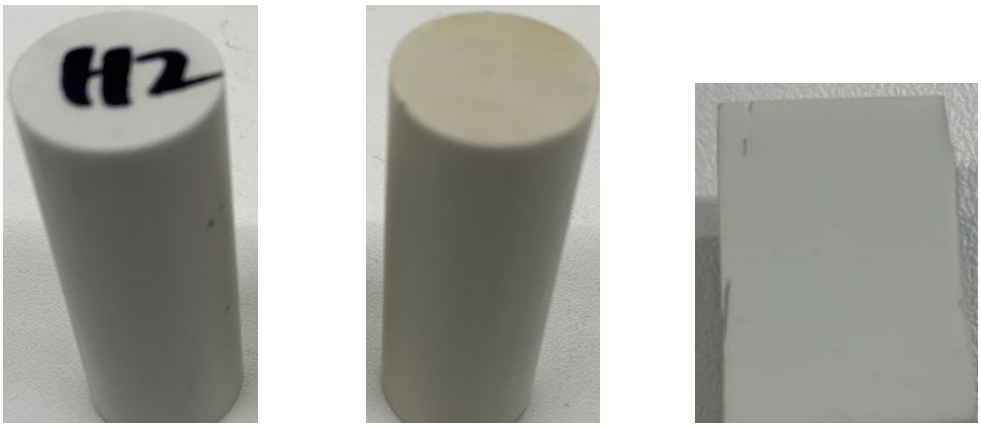

Figure 4.8: *Epoxy with Al_2O_3 filler (a) aged in oven with ambient air (b) aged in gas (c) cutsection of epoxy aged in gas*

Due to photo-yellowing (via the photo-oxidation mechanism), light exposure can cause the yellowing of epoxy. According to a study [68], epoxy does not change colour in a vacuum when exposed to high temperatures. The photo-degradation of the amine hardener, the degradation of the amine epoxy network via various pathways, the degradation of additives or accelerators, and the presence of impurities have all been linked to the phenomenon of epoxy yellowing. The amine epoxy network may degrade due to chain scission, crosslinking between segments, and thermal and photo-oxidation of the main chains or side groups. However, the sample in this thesis did not use amine as a hardener and was not exposed to light in the chamber. Hence, this reasoning can be discarded.

Bisphenol A and epichlorohydrin are two commonly reported epoxy leaching compounds. The difference in concentration of these chemicals inside the resin and the aqueous environment is expected to be the driving force behind this process. However, as per the test gas supplier, the gas is dry, and also, prior to ageing, the humidity was removed in the test chamber by vacuuming for extended periods. Hence, this reasoning can also be discarded.

The molecular mechanism of epoxy thermo-oxidation is complicated, and the precise degradation chemistry is still being researched [68]. Carbonyl formation, double bond creation, and amide production are all common processes during oxidation. Yellowing occurred due to the thermo-oxidative carbonyl formation was addressed in literature [68]. According to the literature, the thermo-oxidative carbonyl is generated in the carbon-carbon backbone of epoxy by the nucleophilic radical attack. Four specific reactive sites were discovered to be responsible for thermo-oxidation. Three of the four sites were associated with carbonyl production. This might be the possible reason for yellowing here. The cut section of epoxy may have been preserved from oxidation, resulting in a lighter colour.

Moreover, the literature suggests that the ageing temperature has a much more significant effect on the yellowing and is a common observation and the colour change was irreversible with unaffected morphological change. According to the research, Yellowing may also be prevented or delayed by adding phenolic antioxidants such as inhibited phenols.

4.4 AC Flashover Test

As the gas is in direct contact with the epoxy surface, we can expect some change in surface morphology if the gas interacts with epoxy. The electrical way to investigate the epoxy's interfacial insulation properties after in contact with the test gas is to perform surface flashover voltage under power frequency AC, as this is the operational voltage waveform the epoxy will be subjected to during its lifetime in GIS or GIL.

Flashover voltages are highly impacted by insulator size, shape, **surface condition**, triple junction geometry, and particle contamination. These impacting parameters on surface flashover along solid dielectrics in compressed SF_6 were examined in the papers [69] and [70].

Moreover, surface flashover is influenced by surface charges, created mainly by electron collisions on the insulator surface and the energy gap between the surface layers [71]. So AC flashover tests will also help in analysing whether there is any change in the surface upon ageing.

4.4.1 Electrode Design

In practice, the highest tangential electrical field on the insulator's surface has been widely adopted as the design criterion for gas-insulated equipment. This is also why the flashover test is of higher priority in this thesis.

Because there is only a tangential electrical field on the surface of the cylindrical insulator sample under a uniform electric field, the impact of the tangential electrical field can be investigated with clarity for the flashover test. Electrodes should be designed in such a way that they give a homogenous field. Here, the electric field will be parallel to the sample cylindrical surface and constant at any location.

The electrodes are made in such a way that the cylindrical epoxy samples will fit tightly in between the electrodes well. It also ensures perfect contact between epoxies and the electrodes where the potential is applied.

Schwaiger factor (or field factor as detailed in chapter 6) has been introduced to measure the degree of homogeneity of the electrode configuration. Schwaiger factor is the ratio between a geometry's maximum and average electric field. For a homogenous field, the Schwaiger factor is 1. Here, we are interested in the field factor, which is the ratio of maximum and the average electric field along the surface of the epoxy sample. Simulations were done using COMSOL® to ensure the geometry provides a homogeneous field.

The dimensions of the electrode configuration used are shown in figure 4.9. A 50mm x 20mm cylindrical sample, as discussed in section 4.1.2, is placed between two identical electrodes with a curvature radius of 4mm.

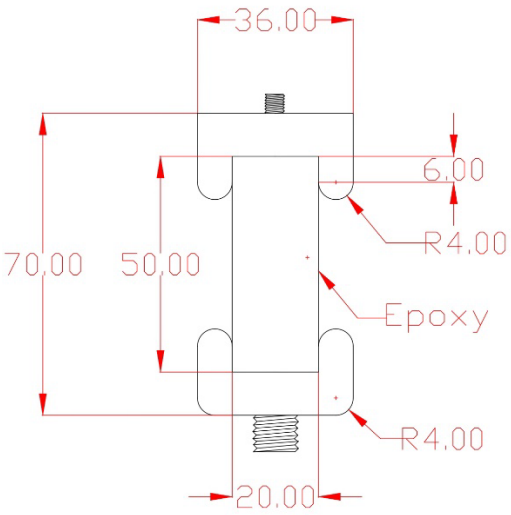

Figure 4.9: *Dimensions of the electrode used*

Figure 4.10 and 4.11 presents the simulation results of the electrode using electrostatic physics in COMSOL®. The maximum electric field occurs at the triple point where the electrode, epoxy, and gas come together. In this case, the tangential field factor along the epoxy is 1.02.

The electrodes were lathed from stainless steel. This material is utilized as it is a strong metal that significantly reduces pitting during testing and allows easy polishing. Before a new series of tests, the electrodes were thoroughly re-polished to eliminate pittings (crates) to ensure consistent results. 'Jokisch heavy-duty cutting oil alpha 93' and P400 sanding paper were used to remove the crates. For the final polish, 'Brasso' copper gloss was used.

The electrode and epoxy are placed in a miniature 'spacer-and-gas' model explained in the next session. The electrodes also meet the requirements of the standard ASTM D149-20 [72]: Standard Test Method For Dielectric Breakdown Voltage and Dielectric Strength of Solid Electrical Insulating Materials at Commercial Power Frequencies.

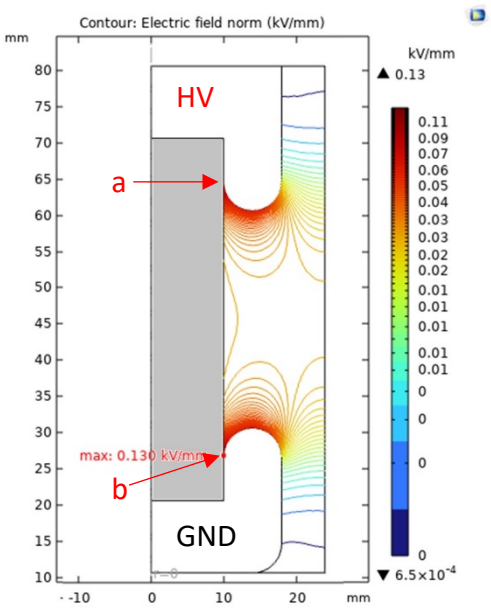

Figure 4.10: *Electric field distribution in the gas medium at 1kV.*

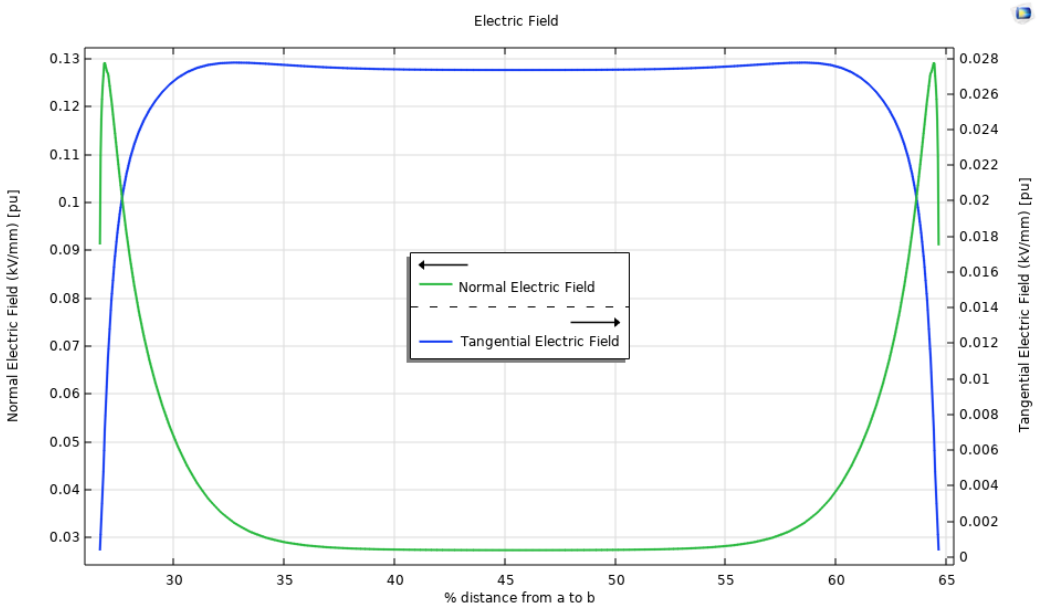

Figure 4.11: *Normal electric field and tangential electric field distribution on the sample from a to b at 1kV*

4.4.2 Spacer-And-Gas Cell

To conduct the flashover test in the test gas, epoxy and the electrodes should be placed inside a test cell. A cell designed for the project of [73] was utilised for this purpose. This miniature 'spacer-and-gas' test cell is a vessel of 60ml and can withstand a pressure of 6 $Bar_{(abs.)}$. The test cell with electrodes and epoxy to be tested is presented in figure 4.12. An O-ring on both sides of the plexiglass is also used to make the test cell gas and pressure tight. This construction will be placed inside a GIS for applying high voltage explained in the forthcoming session.

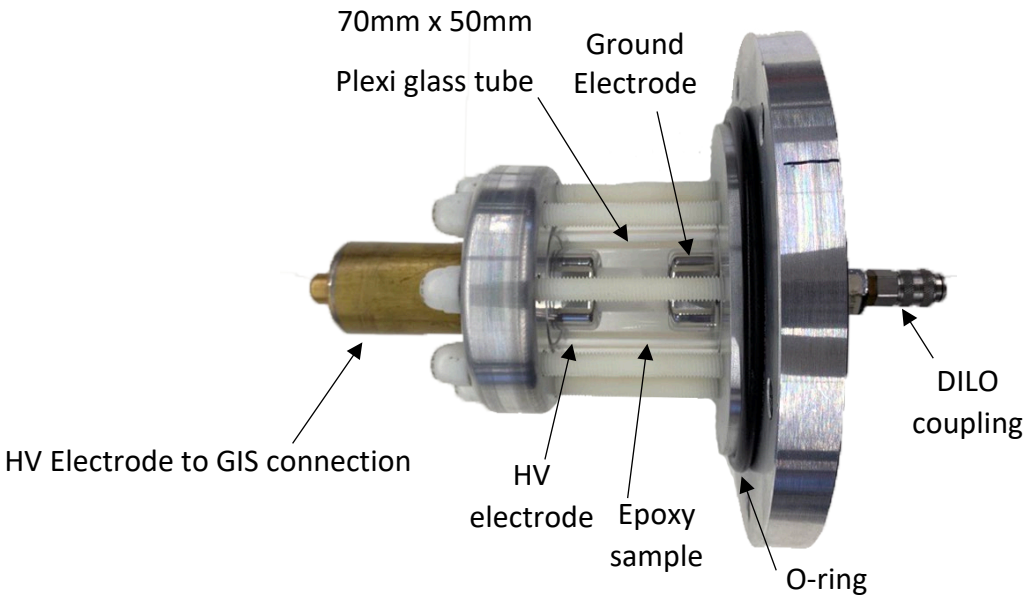

Figure 4.12: *Spacer-and-Gas test cell*

The electrodes were polished and cleaned with alcohol before placing them in the test cell prior to each test. The Plexiglass tubing was also cleaned with alcohol to prevent any grease or solid byproducts (if any) during flashover tests. Because grease protects from pinching, breaking, and cutting of O-ring and helps in seating it perfectly, silicon grease was utilised. The test cell is then tightened using nylon nuts and thread rods. Care was given to tightening the nuts equally, to have an equal and adequate tightness on all the sides of the cell and to keep the gas pressure intact. This was made sure using a dial torque wrench.

After the miniature spacer-and-gas test cell was assembled, the cell was vacuumed to a pressure of 0.3 mbar. Then the required gas was filled to the test pressure.

4.4.3 GIS Setup

The surface flashover experimental platform was a 220-kV gas-insulated switchgear system. Figure 4.13 depicts the major components of this surface flashover experimental platform. Connected to the GIS is an HV bushing. To prevent internal breakdown, the bushing was filled with 3 Bar SF_6. The test cell is placed inside the test chamber where it connects the HV connecting rode of GIS to the test cell and thereby to the electrode and sample to be tested.

Upon mounting the test cell to the GIS, the volume of GIS was vacuumed to a pressure of 0.3mbar and then filled with a dielectric gas as follows:

- For an expected low voltage of flashover (ie. Usually, for test gas pressure of 1 Bar(absolute), clean air (relatively humid free) at a pressure of 6 $Bar_{(abs.)}$ from the compressor was used.
- For expected higher flashover voltage, SF_6 at 3.5$Bar_{(abs.)}$ was used as the dielectric medium inside the GIS.

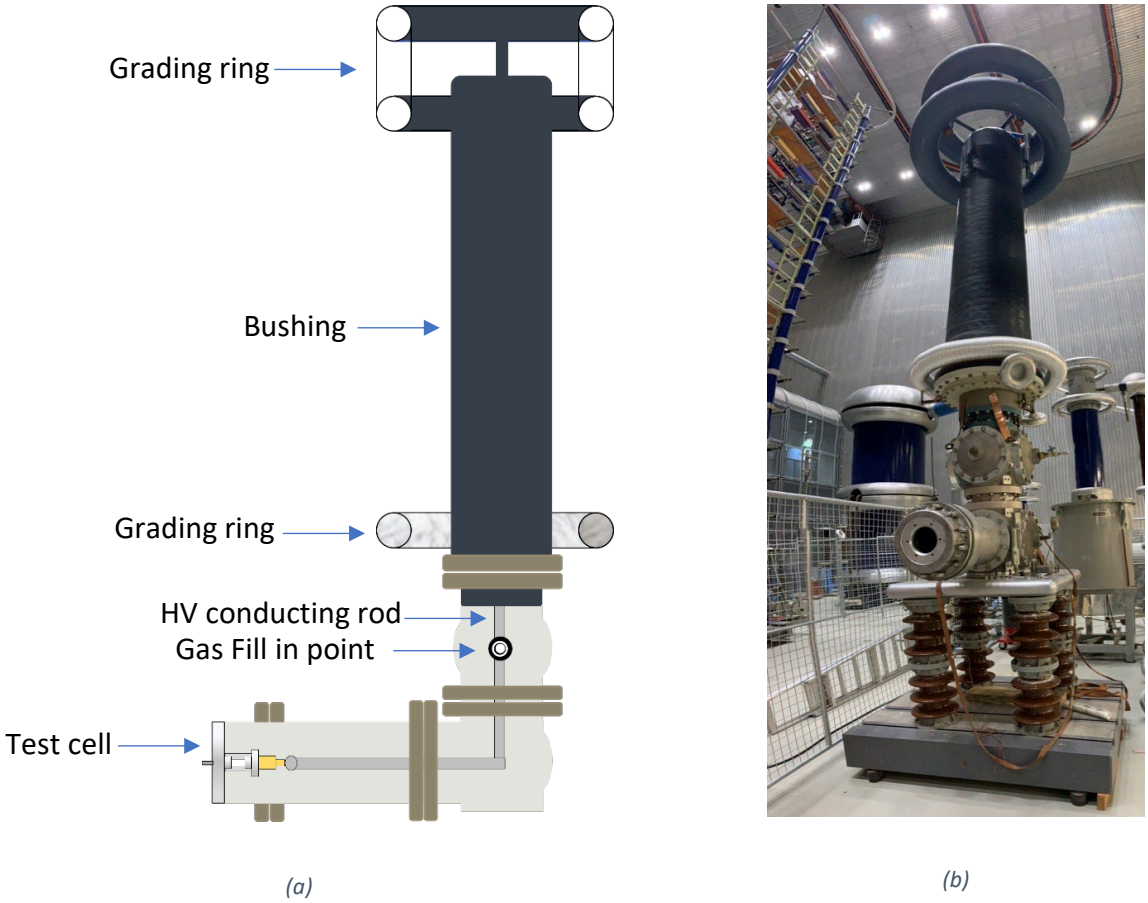

Figure 4.13: *(a) Model of GIS setup with Test cell mounted (b) GIS setup*

4.4.4 HV AC Generation And Connection Diagram

A single-phase power transformer having a maximum capacity of 200kVA was utilized to provide the electrode with the requisite HV AC voltage at power frequency. The schematic of the test setup is shown in figure 4.14. The high voltage terminal of the power transformer was connected to the GIS (thereby to the test cell) and a voltage divider. A voltage regulator was connected to the low voltage side of the power transformer to regulate the HV output. The power transformer was rated for 200kV. An RLC circuit puts the transformer in resonance, limiting the current during breakdown or flashover. Moreover, a fast-tripping circuit triggered by a current transformer connected to the earth circuit trips the circuit from continuous current flow. These combinations aid in performing multiple breakdowns or flashover tests in one sample, limiting the damage to the sample.

The voltage divider (point 8 in figure 4.14) was rated for a maximum voltage of 300kV and has a scale factor of 2114. The voltage divider is connected to HAEFELY Digital Measuring Instrument DMI 551. The protection resistor connecting the HV terminal to the GIS (point 6 in figure 4.14) is 4.8kΩ. The test setup used here follows the standard of ASTM D149-20 [72].

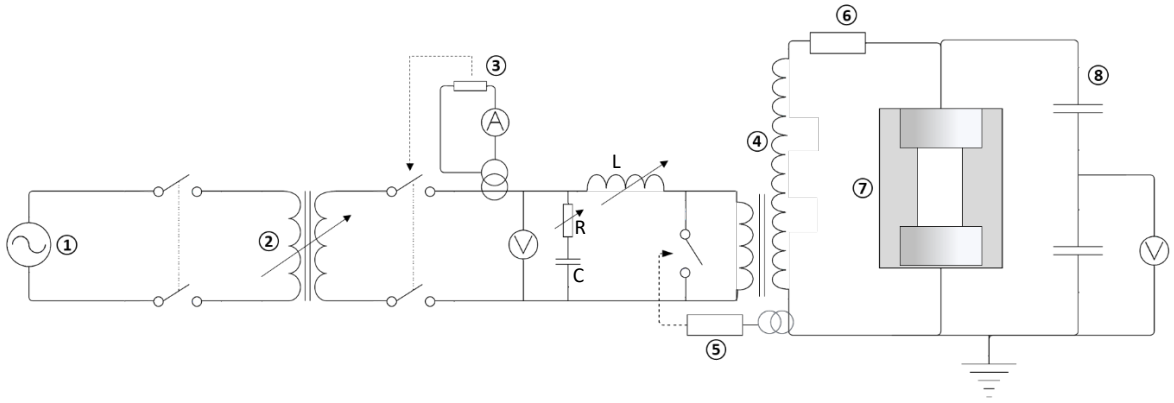

Figure 4.14: High Voltage AC Generation Setup: 1. 220V 50Hz AC Grid; 2.Autotransformer; 3. Current Limiter; 4.HV transformer; 5.High Speed Tripping Circuit; 6. Damping Resistor; 7.Test cell; 8.Capacitive Voltage Divider

4.4.5 Test procedure

The electrodes were polished and conditioned as mentioned in section 4.3.1 prior to each test. Furthermore, non-aged epoxy samples, electrodes and each component of the test cell were cleaned with ethyl alcohol. The dry epoxy samples were fitted between the electrode as indicated in Figure 4.11, ensuring there is no clearance between the electrodes and samples. The test cell was then evacuated to a pressure of less than 0.3 mBar. The test cell was then pressurised with the test gas or reference gas (SF_6) at the required test pressure. Care was taken to ensure that the pressure did not deviate from the intended. The test cell was then connected to the GIS setup for applying HV after being pressurized with the required gas. The GIS was filled with the dielectric medium, as mentioned in section 4.3.3.

For the 50-Hz AC flashover testing, the test voltage was raised to 75% of the expected flashover voltage at a rate of 5 kV/s as the voltage regulator was controlled manually. Then, the voltage was raised until flashover at a rate of 0.1 kV/s as per the Slow Rate-of-Rise Test method in ASTM D149-20 standard [72]. The peak value of the voltage was recorded. The minimum time interval between two consecutive tests was 10 minutes. This allows sufficient recombination time for the insulating gas. After six flashovers on a single sample, it was changed to a fresh sample to remove the impact of insulator damage, as flashover creates traces that remain on the insulator's surface and might cause insulator degradation. After the test, the electrodes and samples were investigated to check whether the number of traces was equal to the number of flashover trips observed during testing. This allowed in verifying that the flashover occurred along the epoxy and not anywhere inside the GIS.

AC Flashover voltage tests in both quartz and Al_2O_3-filled epoxy were conducted in SF_6 for reference apart from the test gas 5%C_4F_7N/95%CO_2. Aged samples were tested only in the test gas.

4.4.6 Experimental Results

Figure 4.15 shows the AC flashover voltage of Al_2O_3 expoxy – aged and non-aged, and Figure 4.16 shows the AC flashover results obtained for Quartz filled epoxy. The medians of the flashovers at each pressure are considered for the graph. The maximum and minimum flashover voltages obtained during the tests are also shown in the figure.

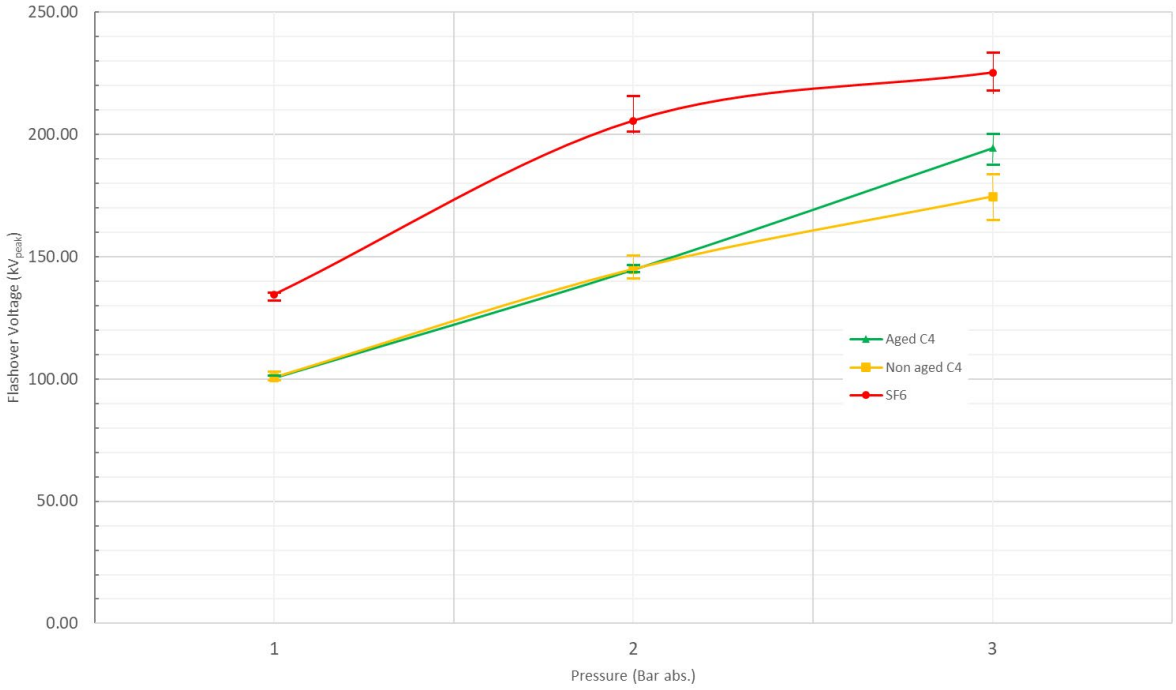

Figure 4.15: *AC Flashover voltage for Al_2O_3 filled epoxy*

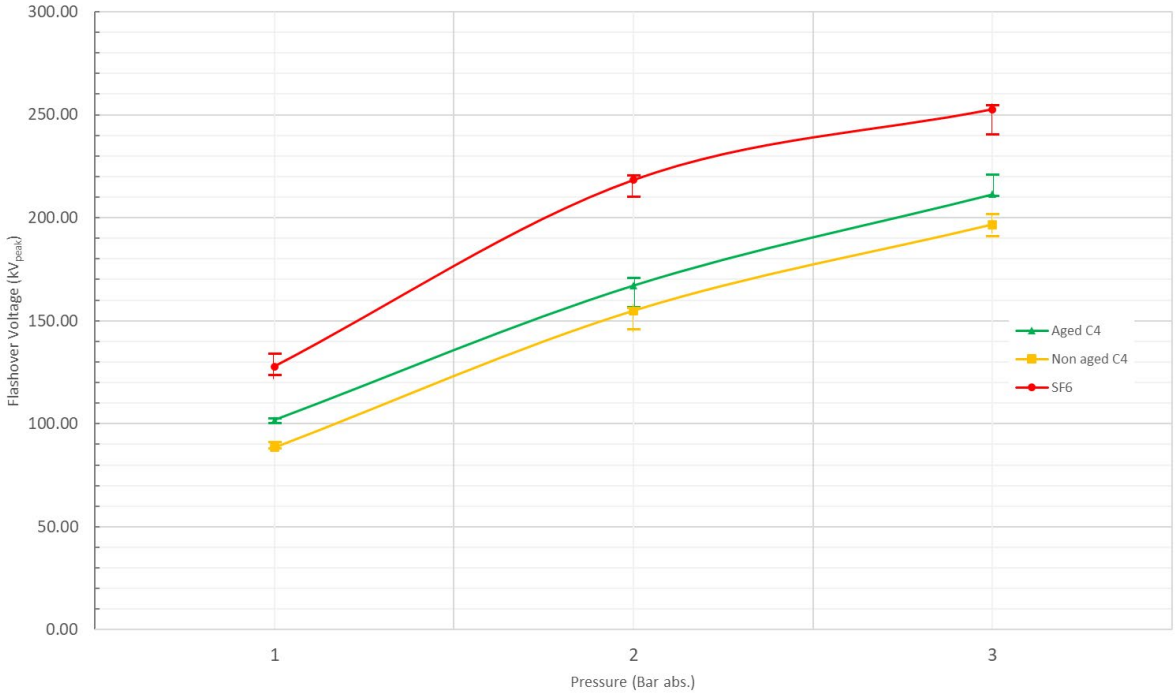

Figure 4.15: *AC Flashover results obtained for Quartz filled epoxy*

The following are observed:

- The flashover voltage increases with an increase in pressure for both the epoxy materials.
- The flashover voltage seems more linear in the test gas C_4F_7N/CO_2 case than SF_6.
- The flashover voltage of quartz is higher than that of its counterpart Al_2O_3, filled with epoxy

- When comparing the aged and non-aged samples, we could see no change in flashover voltage for Al_2O_3-filled epoxy. However, the flashover voltage tends to have increased in the case of quartz-filled epoxy.

These observations must be investigated further based on the LI+ flashover voltage test results.

The experimental results can be fitted into the following equation,

$$V_{fAC} = a(10P)^b \qquad \textit{Eq. 4.8}$$

Where V_{fAC} Is the AC flashover voltage, P is the pressure in the absolute bar a, and b are the constants explained as in table 4.4.

Constant	Al_2O_3 Filled			Quartz filled		
	SF_6	Non- aged	Aged	SF_6	Non- aged	Aged
a	45.7	31.7	25.2	30.7	16.7	21.93
b	0.469	0.502	0.601	0.6197	0.725	0.666

Table 4.4: *Fitting result constants*

4.5 Positive Lightning Impulse Flashover Test

Surface flashover is a complex phenomenon with multiple dominant factors. The dominant elements for causing the surface flashover process changes under different voltage waveforms, and the mechanism of the surface flashover development stage are still in disagreement [74] [75]. One crucial factor is the solid properties of the insulation material [71]. Here, as we are interested in analysing the insulation property change, AC flashover alone will not completely give the flashover characteristics of insulating material. Hence, the lightning impulse test is of importance.

Lightning Impulse(LI) tests on the samples are performed to ensure the insulation level is sufficient to withstand overvoltages induced by lightning strikes. The LI test can be positive polarity (LI^+) or negative polarity (LI^-). However, a LI^+ could give less breakdown or flashover strength compared to a (LI^-). From a physics point of view, the reason for the different breakdown strengths is that during (LI^+), at the positive electrode, the avalanches expand in the direction of the point and form a natural extension of the electrode. However, during a (LI^-), the avalanches fan out from the negative electrode and electrons are expelled to lower field regions [76]. Consequently (LI^+) can be regarded as the weakest failure possible during LI.

As per the standards such as IEC 60060-1:2010, “a standard lightning impulse is a full lightning impulse having a front time of 1.2μs and a time to half-value of 50μs. It is described as a 1.2/50 impulse”.

4.5.1 Experimental Platform

The experimental setup is the same as the AC flashover setup mentioned in sections 4.3.1, 4.3.2 and 4.3.3, except for the generation, connection and test procedure as explained in the next section.

4.5.2 LI Voltage Generation, Connection Diagram and Test Procedure

The schematic of the test loop used in this paper is shown in Figure 4.14, and the block diagram is presented in Figure 4.17. The circuit includes a HAEFELY ten-stage Marx Generator that could collectively output 1 MV impulse voltage, a 1200kV resistive voltage divider, GIS setup, and Generator controller GC223 connected to HiAS 744 Impulse analysing system and software unit. R_1 and R_2 were 300Ω each. R_f is the front resistance which determines the front time, and R_t is the tail resistance which governs the time to half-value. Capacitor C_p is 0.001μF capacitor rated at 700kV connected across the load and is used to improve the waveform. The voltage waveform adhered to the IEC 60060-1:2010 standard [77]. The test setup gave a LI^+ waveform, as shown in figure 4.19.

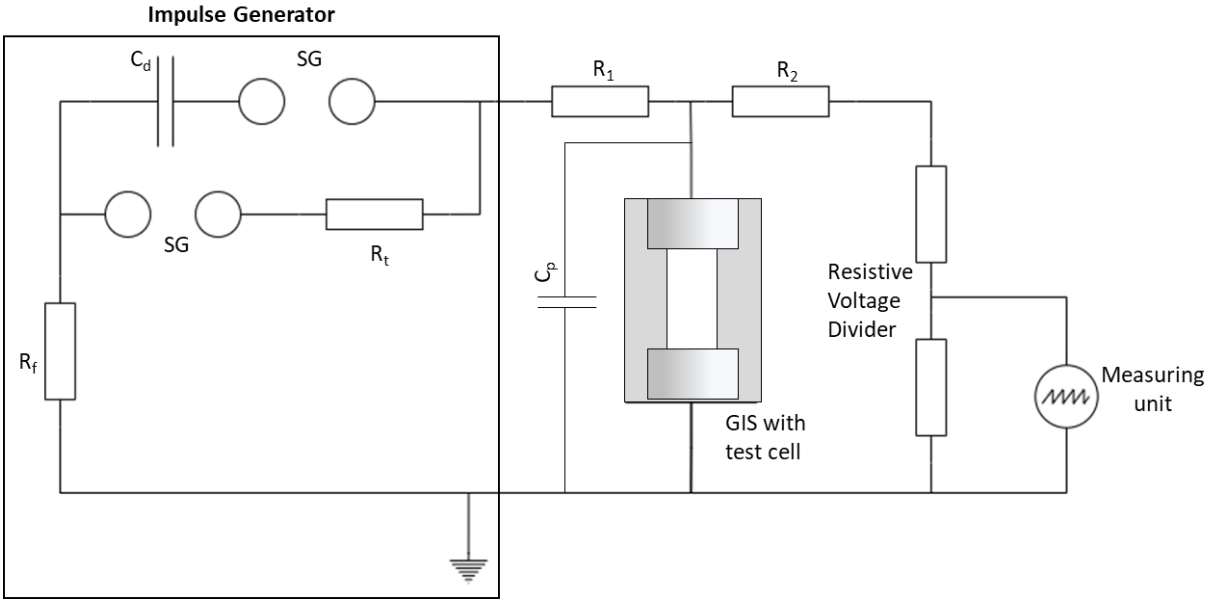

Figure 4.16: Schematic of the Impulse generator setup; C_d is the discharge capacitance, R_t is the tail resistance, R_f is the front resistor, C_f is a capacitor connected in parallel with the load

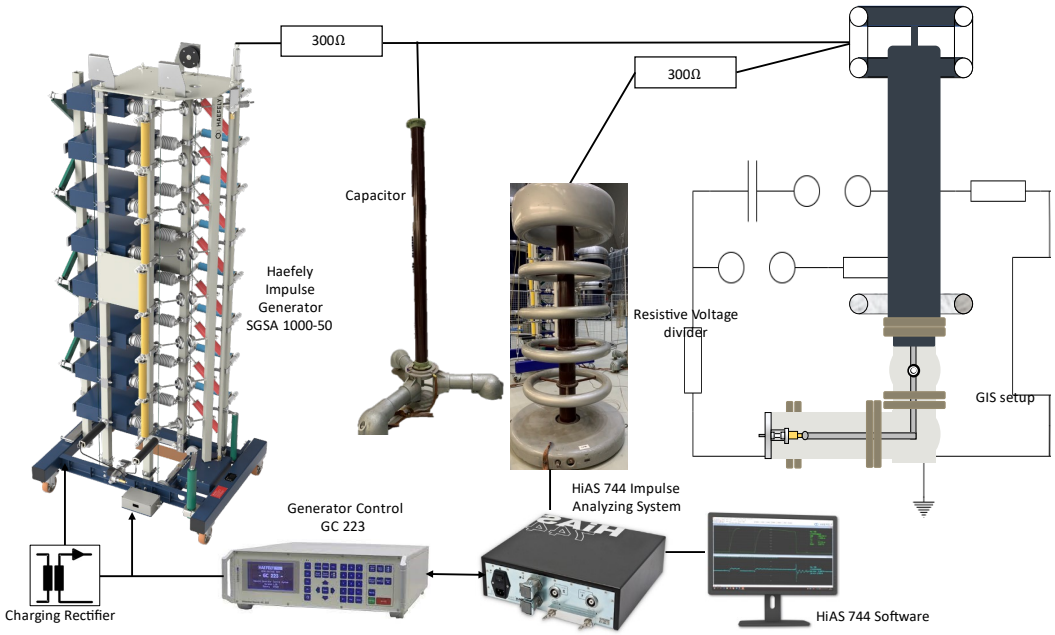

Figure 4.17: Connection Diagram for LI^+flashover test

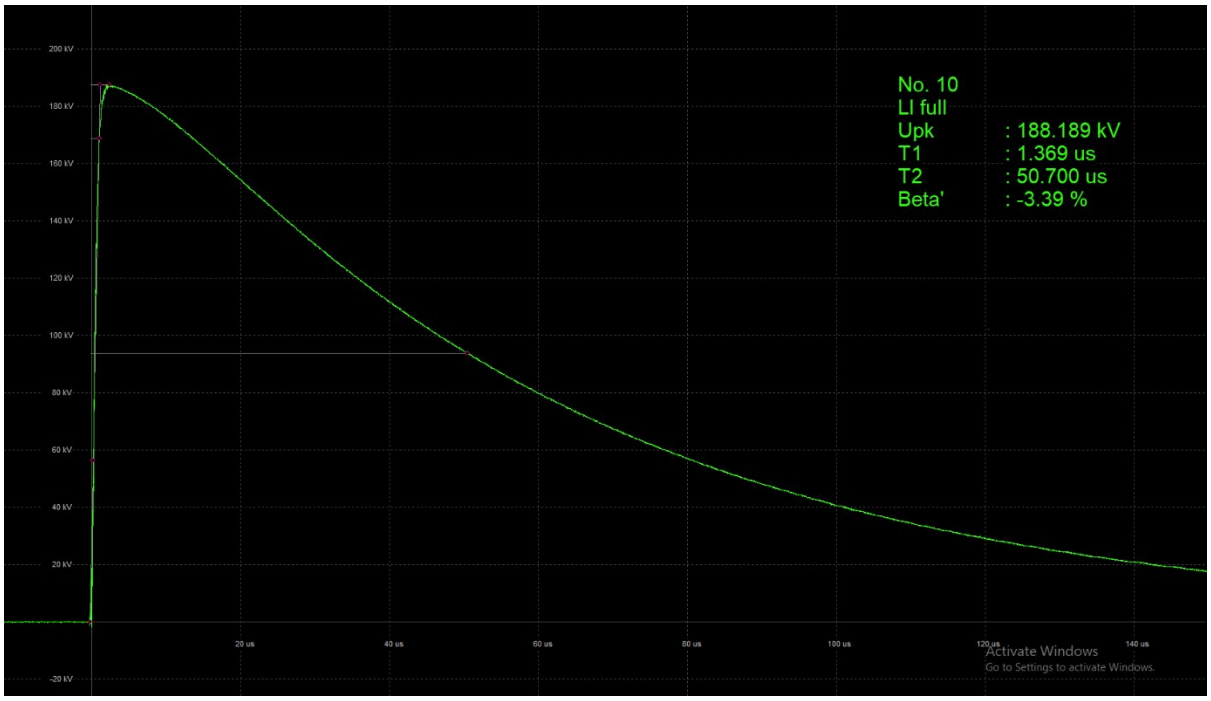

Figure 4.18: *LI⁺ waveform applied to the samples*

The preparation of electrodes and test cells before each test is similar to the steps followed during the AC flashover test. For the LI⁺ flashover testing, every impulse began at around 50% of the expected breakdown voltage and was raised in steps of 5 kV. During a flashover, the peak value of the voltage and the chopping time was recorded. After a certain amount of sample testing, the chopping time helped understand whether the flashover occurred in the sample or elsewhere. The minimum time interval between two consecutive tests was 10 minutes. This allows sufficient recombination time for the insulating gas. After five flashovers on a single sample, it was changed to a fresh sample to remove the impact of insulator damage, as flashover creates traces that remain on the insulator's surface and might cause insulator degradation. After the test, the electrodes and samples were investigated to check whether the number of traces was equal to the number of flashover trips observed during testing.

LI⁺ Flashover voltage tests in both quartz and Al_2O_3-filled epoxy were conducted in SF_6 for reference apart from the test gas 5%C_4F_7N/95%CO_2. Aged samples were tested only in the test gas.

4.5.3 Experimental Results

Upon LI⁺ tests, the results obtained for Al_2O_3-filled epoxy and quartz-filled epoxy are shown in Figures 4.20 and 4.21, respectively. The median of flashovers at each pressure is considered in the graph. The maximum and minimum of the flashover voltages are also shown.

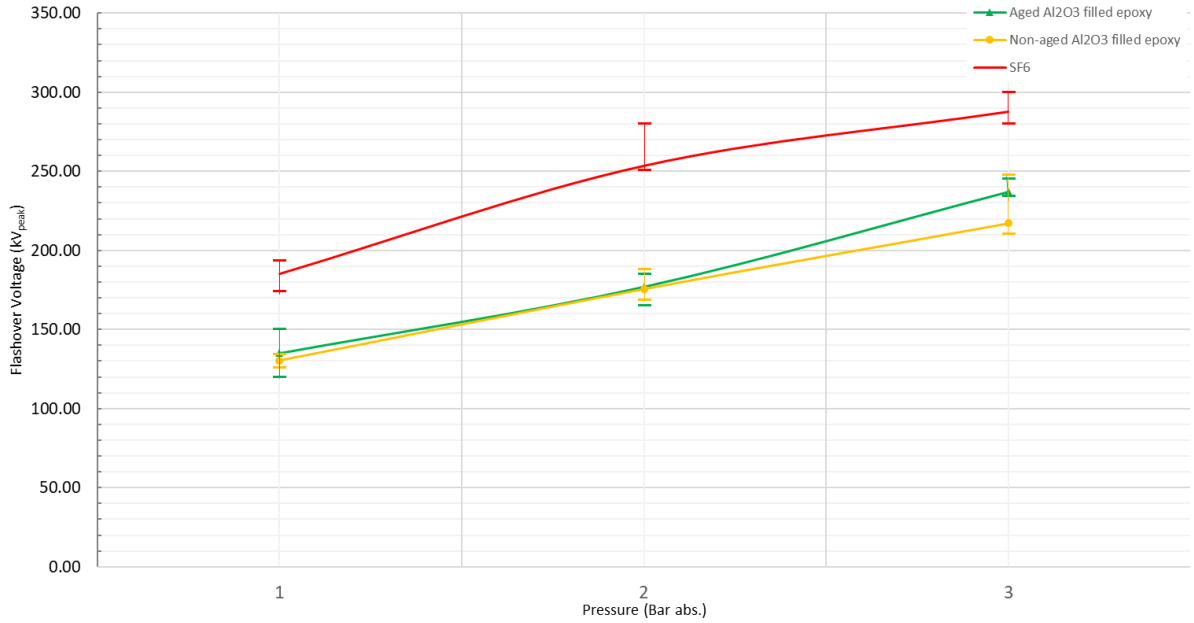

Figure 4.19: *LI⁺flashover voltage for Al_2O_3 filled epoxy*

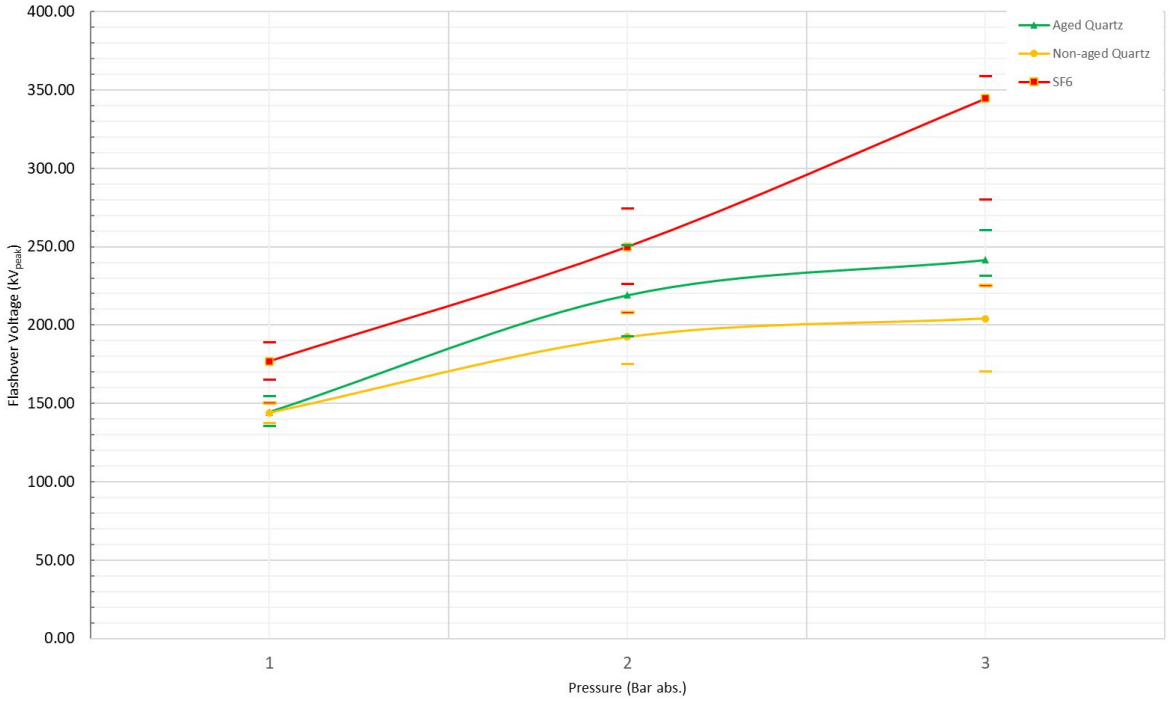

Figure 4.20: *LI⁺Flashover voltage for quartz-filled epoxy*

The following are observed:

- The flashover voltage increases with an increase in pressure for both the epoxy materials.
- The flashover voltage of quartz is higher than that of its counterpart Al_2O_3, filled with epoxy

- When comparing the aged and non-aged samples, we could see no change in flashover voltage for Al_2O_3-filled epoxy. However, the flashover voltage tends to have increased in the case of quartz-filled epoxy.
- A standard deviation of above ten was observed for each sample above 2 bars.

These observations are similar to that of AC flashover voltage, and the possible reasonings are investigated in the following section.

The experimental results can be fitted into the following equation,

$$V_{fLI^+} = a(10P)^b \qquad \textit{Eq. 4.9}$$

Where V_{fLI^+} Is the positive lightning impulse flashover voltage, P is the pressure in the absolute bar a, and b are the constants explained as in table 4.5.

Constant	Al_2O_3 Filled			Quartz filled		
	SF_6	Non- aged	Aged	SF_6	Non- aged	Aged
a	73.6	42.6	41.5	43.7	69.5	49.3
b	0.401	0.469	0.513	0.608	0.317	0.467

Table 4.5: *Fitting result constants*

4.6 Analysis

This part is dedicated to identifying the cause of the results obtained based on the LI^+ and AC flashover tests.

4.6.1 Visual Inspection

Traces of flashover remained on both the insulator's surface after both AC and LI^+ tests. The intensity of the traces increased with an increase in pressure. At higher pressures, we have higher flashover voltages. This is more visible in the case of Al_2O_3-filled epoxy due to its light colour nature. However, no significant changes were seen with gas change for almost the same flashover voltages. Figure 4.22 shows the flashover traces left on the epoxy at 3 bar AC flashover in C_4F_7N/CO_2. It is interesting to note that the flashover traces are random, multipath and wormhole, as explained in the works of literature. Traces remaining on the insulator's surface might cause insulator degradation.

Figure 4.21: *Flashover traces at 3 bar in C_4F_7N/CO_2*

Figure 4.22: *Crates on the electrode after LI tests*

Craters were found on both electrodes at 'the triplepont', as seen in figure 4.23. The maximum roughness of 10 µm is necessary to ensure the craters do not influence the breakdown strength [78]. The higher the energy discharge, the more significant the crater on the electrodes. Therefore, the electrodes were carefully re-polished after a series of tests, and the number of flashovers in the tests was limited to gas pressure levels above 3 bars. The crates were deeper in the case of LI due to their high energy discharge. No significant changes in the craters formed between SF_6 and C_4F_7N/CO_2 were observed for the similar flashover voltage.

White powders were found on the surface of electrodes and on the sample for both SF_6 and C_4F_7N/CO_2 gases. These powders are most likely Aluminium Fluorides from a flashover [73]. More powders were found during the AC tests than during the impulse tests. The more extended period of partial discharge under AC before a complete flashover is most likely the cause.

Standard deviations increased with an increase in pressure. More deviations were found during LI^+ tests. This might be because big craters formed on the electrodes at a higher pressure and hence higher voltages, contributing to the increased electric field and decreased flashover voltage.

4.6.2 Flashover voltages

The sections will give the hypothetical reasoning to the following questions:

- Why does C_4F_7N/CO_2 show better linearity than SF_6?
- Why is flashover in SF_6 higher than that at C_4F_7N/CO_2?
- Why is the flashover voltage increase with aged quartz as observed in both AC and LI^+ tests?

Surface flashover is more complex than gap breakdown. The insertion of the spacer not only distorts the electric field due to permittivity differences, but its surface also accumulates and stores charge. Research is still proceeding to understand the actual mechanism during a flashover. However, there is widespread agreement that the surface flashover process can be divided into two stages; The first stage is the initiation stage, during which an electron swarm is generated as a result of the triple junction, conducting particulates, static charges, or electric field distortion. When there are enough free ions, propagation occurs across the entire surface, known as the second flashover stage.

Although calculating the result of surface flashover or breakdown effect for realistic surface defects is impossible, a figure of merit based solely on gas properties was defined by [79], to indicate the relative effect of surface defects. It gives a relationship between surface defects and breakdown voltage. The surface flashover voltage of the C_4F_7N/CO_2 mixture is more linear than that of SF_6, which may indicate that the C_4F_7N/CO_2 mixture has a high figure of merit than SF_6. A similar trend and reasoning were observed in the literature [66] for C_4F_7N/CO_2. Microdischarges generate initiating electrons, lowering the surface flashover voltage. Furthermore, in surface flashover tests, the flashover discharge dispersion of the C_4F_7N/CO_2 mixture is smaller than that of SF_6; this phenomenon was also observed in the tests of literature [66]. This could imply that the C_4F_7N/CO_2 mixture is more resistant to field distortion than SF_6.

It was observed that flashover is higher for SF_6 compared to the test gas C_4F_7N/CO_2 gas mixture. The gas mixture shows a flashover voltage of almost 70% of that of SF_6. It is to be noted that the gas utilised here has a concentration of 5mol% of C_4F_7N and the rest 95% CO_2. This mixture has lower electron capturing capability and hence lower breakdown than SF_6. During flashover, the electrons are injected from the triple point, and when SF_6 is used, due to its higher electronegativity compared to the gas mixture, the electrons can readily attach to SF_6 molecules than the mixture gas. A C_4F_7N concentration of around 15-20% in CO_2 is required to reach the same flashover voltage.

Based on the literature understanding of [80], the hypothetical reason why quartz-filled epoxy showed a higher flashover upon ageing is explained as follows. Before ageing, epoxy with the SiO_2 particles will be evenly distributed in the bulk of the epoxy resin. Traps in the epoxy can be divided into electron traps and hole traps. Hole traps attract the positive charges, and electron traps the negatively charged electron. As the sample was thermally aged, the SiO_2 filler particles in the bulk of the material might have migrated towards the surface layer of epoxy resin. This migration of fillers can form traps on the surface of the epoxy resin. The carriers' charges could get trapped in these deep traps, which could not easily escape. These traps could then form a dense electron region, prevent electron injection from an electrode or limit the movement of electrons. Hence, it would need higher voltages to cause flashovers in the aged sample. This reasoning must be verified using tests like dielectric spectroscopy in the GHz range to understand what is happening at the macromolecular levels. However, this is considered not to be the gas's effect but the temperature.

Another hypothesis would be based on the literature [71] information that the internal capture energy levels, composed of localized traps and recombination centres, can be well described by the band structure of solid materials. The band gap of the insulating material should be large, and valence electrons in valence bands should not be quickly excited to empty bands. However, the insulating material's band gap width is influenced by crystal defects, particularly on the surface, which can narrow the band gap width by introducing trap energy levels. The introduced trap energy levels may influence the de-trapping and trapping of electrons, which may further influence the flashover development process [71]. While ageing at higher temperatures, there might have been a crystal defect in the epoxy, which had increased the flashover voltage.

4.7 FTIR Measurement

To detect the surface composition of chemical elements and morphology changes of epoxy before and after ageing with the gas, Fourier Transform InfraRed spectroscopy measurements were tried. The instrument on which measurement was tried was Nicolet iS50 FT-IR from the 3mE department, as shown in figure 4.24.

Figure 4.23: *FTIR measuring instrument*

Since it was hard to detect the characteristic peaks of both samples with the Pottasium Bromide (KBr) detector, a trial with the MCT (Mercury-Cadmium-Telluride) detector cooled with liquid Nitrogen was also tried for high accuracy. Both transmission method and reflectance method were utilised. However, no characteristic peaks were found. The plate samples were thick enough not to transmit IR; hence transmission mode did not work out. Since both types of epoxy samples did not reflect the incident IR ray, the reflectance mode was also ruled out. It was realised that the samples utilised in this study were not optimum for this purpose. However, it is considered that with ATR (Attenuated Total Reflection), it might be able to get some characteristic peaks in the samples. Due to the lack of ATR component at the study moment, the measurement was not further carried out.

Research by the authors of [80] on the interaction of epoxy resin with C_4F_7N at 160°C showed that no new substance was found on the sample surface, as seen in figure 4.25. It was also found that the filler was more on the epoxy surface due to high temperature.

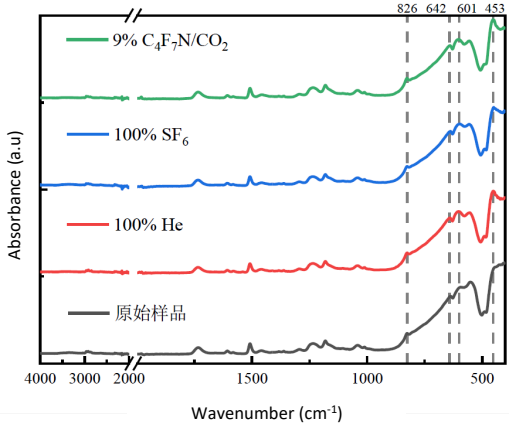

Figure 4.24: *FTIR results at 160°C by authors of [80]*

4.8 Breakdown Test On Aged Gas

As the gas was in contact with the epoxy, the chances of gas being contaminated cannot be ruled out. An AC breakdown test on the aged gas was done to verify whether the gas had undergone any change. A small test cell with rod-plane electrodes with a gap distance of 5mm was utilised for the study. The radius of the rod was 2mm. The test setup was similar to the one used for the AC flashover test in section 4.4. The test cell was cleaned with ethanol and vacuumed to 0.3mBar prior to each test. The electrodes were polished after each set of tests. Figure 4.26 shows the results obtained.

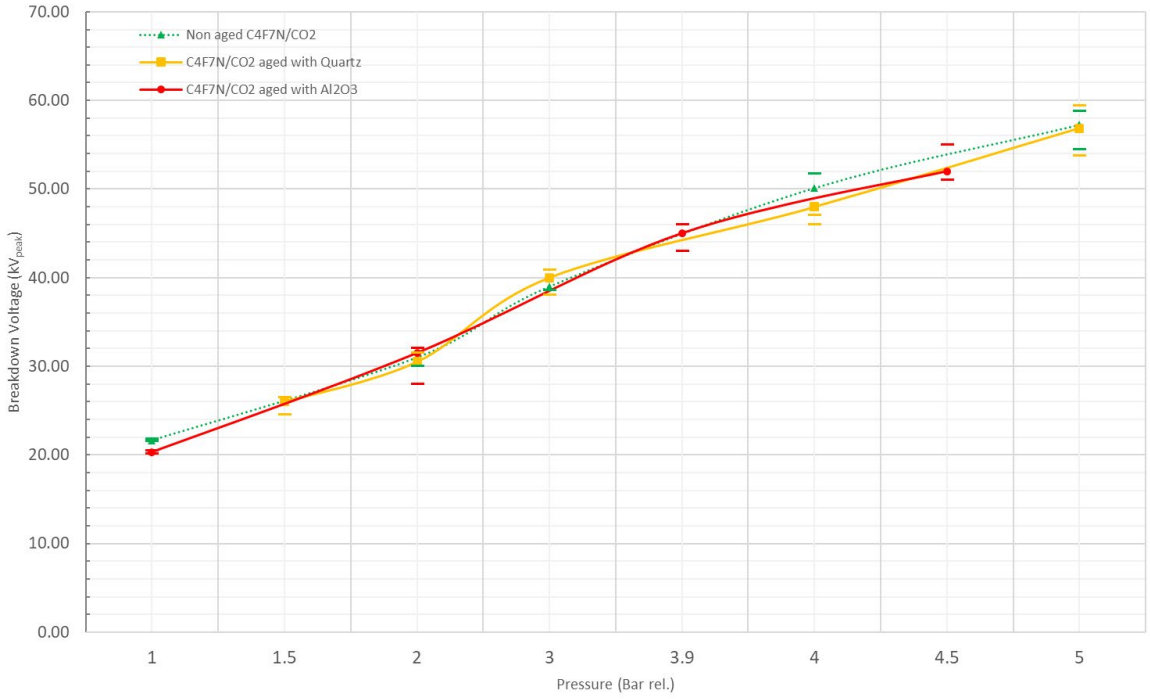

Figure 4.25: *Breakdown test in aged gas*

It is found that there is no change in AC breakdown strength of the aged gas in both quartz and Al_2O_3-filled epoxies. However, whether the gas is in the actual state, is there any additional substance in the gas, or whether the gas has decomposed after ageing has to be studied further with Gas Chromatography-Mass Spectroscopy (GC-MS) analysis.

However, it is worth noting that the discharge dispersion of the gas breakdown appears smaller than the AC surface flashover. In contrast to gas breakdown, surface flashover has several characteristics, such as surface charges that may generate more significant discharge dispersion.

4.9 Conclusion

The electrical experiments performed on the sample and the gas have shown no significant compatibility issue with C_4F_7N/CO_2, with the epoxies having different fillers. The reason why Quartz-filled epoxies showed improved flashover characteristics has to be verified by more experiments. There could be a possibility that the epoxy shows good properties for a short period and might degrade later. Prolonged ageing tests could only study this. Moreover, different concentrations of the gas might affect the epoxy, which has to be investigated

further. Gas chromatography-mass spectroscopy has to be done to analyse the byproducts after the ageing process.

However, from the point of the recommended ageing conditions and the electrical tests conducted, epoxies and the alternative gas 5%C_4F_7N/95%CO_2 show no compatibility issues and retrofitting the GIS with 6 bar absolute may not cause any long-term problems.

4.10 Summary

Electrical tests of AC flashover and LI^+ flashover were conducted on the samples and the gas to check for compatibility issues. The mixture of 5mol%C_4F_7N/95mol% CO_2 at 6Bar absolute was found to be compatible with epoxy and vice versa. Al_2O_3-filled epoxies showed yellowing on the surface after ageing, which may be due to a thermo-oxidative reaction of the gas. It was understood that yellowing was only a surface phenomenon, not a bulk phenomenon. Flashover left white powders on the electrode, which might be due to the formation of Aluminium Fluoride, as seen in SF_6. The surface flashover voltage of the C_4F_7N/CO_2 mixture is more linear than that of SF_6, which may indicate that the C_4F_7N/CO_2 mixture has a high figure of merit than SF_6. Quartz-filled epoxy showed good flashover characteristics compared to non-aged, which may be attributed to the migration of SiO_2 fillers to the epoxy's surface due to high temperature, creating traps and increasing the flashover voltage. Another hypothetical reason, as per the literature, could be due to a change in the bandgap of the insulating material due to crystal defects during temperature application. However, this has to be further studied with dielectric spectroscopy tests. Tests like FTIR and Scanning Electron Microscopy tests are to be further carried out to check the surface conditions of the epoxy. Detailed gas chromatography tests must be conducted to analyse the gas's decomposition products, if any.

5. Optical Partial Discharge Characteristics of C_4F_7N/CO_2

This chapter describes the novel C_4F_7N/CO_2 alternative gas's optical PD characteristics. The technique and criteria used to pick optical sensors are presented. The technique for employing the optical sensor, as well as its location, is also discussed. The selection of fluorescent fibre based on the optical PD characteristics of the gas will be presented. Throughout the testing process, the electrical method of PD detection is utilised for comparison purposes. Finally, the relationship between PD and light intensity is summarised.

5.1 Introduction

Gas Insulated Systems such as GIS and GIL are replacing the conventional air-insulated substation. Moreover, the novel dielectric gases that could replace SF_6 also attract more and more utilities in moving toward Gas Insulated Systems. However, the defects in such insulation systems are inherent and crucial for the system's lifetime. PD's caused by these defects significantly lower the insulating system's breakdown strength, particularly during impulse overvoltage circumstances [81].

PD activity can not only raise the local temperature of the gas but can also generate high-energy electrons. The thermal deterioration of the gas will occur as the local temperature rises, and the byproducts may not be compatible for further use as an insulation medium. Due to the electron impact process, gas molecules will be ionized, dissociated, and recombined. The following are the primary reactions in the C_4F_7N gas [82]:

$$C_4F_7N \longrightarrow (CF_3)_2CN + CF$$

$$(CF_3)_2CF \longrightarrow (CF_3)_2C + C$$

$$CF_3CFCN \longrightarrow CN + CF_3CF$$

$$CF_3CF \longrightarrow C - F_3 + F$$

$$CF_2 \longrightarrow CF + F$$

The decomposition of CO_2 is as follows:

$$CO_2 \longrightarrow CO + O$$

$$CO_2 + O \longrightarrow CO + O_2$$

$$CO + O_2 \longrightarrow CO_2 + O$$

Optical detection of partial discharge is free from interference and has been a research interest for different insulation mediums and HV equipment. The optical PD characteristics of Sf_6 are studied in depth by the authors of [81]. It was understood that corona light emission in SF_6 produces distinctive spectra related to a complex process of ionization, excitation, and

recombination during discharges. However, it is also mentioned that the PD characteristics in different gases will differ and correspond to the different multispectral optical characteristic distributions. The literature on the optical PD characteristics of the alternative gas C_4F_7N/CO_2 is limited. Hence, the focus of this research question will be to solve them. The optical PD Characteristics of this alternative gas will be compared with the experimental results obtained for air.

Understanding the PD optical characteristics of gas gives a solid background of the spectrum of light emitted during a PD activity. However, an appropriate sensor to detect the PD light is required. Fluorescent fibres are introduced for the same. The optical spectrum of PD activity in the gas must first be studied to choose an appropriate fluorescent fibre and sensor. However, before proceeding to the characteristics and detection methods, it is essential to know how PD emits light.

5.1.1 PD Light Origin

When PD occurs, the free electrons collide with the molecules of the medium, resulting in ionization. Because the number of electrons and ions in the gas that has been ionized are the same at the macroscopic level, we may consider the PD region a type of plasma [83]. Line radiation, recombination radiation, and bremsstrahlung (German: “breaking radiation” or “declaration radiation”) are the three types of PD radiation [84]. The radiation's power is as follows:

1. Line radiation:

$$I_{pq} = \frac{1}{4\pi}\int n(q)\cdot A(p,q)\cdot h\nu(p,q)\cdot dx \qquad \textit{Eq. 5.1}$$

Where I_{pq} is the radiation intensity between energy levels p and q; $n(q)$ is the electron density; $A(p,q)$ is the probability of transition of the atom and $h\nu(p,q)$ is the energy of a photon with h as Planck's constant and ν as the optical signal's frequency.

2. Recombination radiation and bremsstrahlung:-
   The recombination radiation's power:

$$W = \frac{1.73\cdot 10^{-51}\cdot N_i\cdot N_e\cdot Z^4}{(n^3\cdot(\sqrt{kT_e})^3)\bar{g}}\cdot e^{\frac{E_n-h\nu}{kT_e}} \qquad \textit{Eq. 5.2}$$

   And, the power of the bremsstrahlung is given by:

$$W = \frac{6.37\cdot 10^{-53}\cdot\ N_i\cdot N_e\cdot Z^2}{\sqrt{kT_e}\cdot\bar{g}}\cdot e^{-\frac{h\nu}{kT_e}} \qquad \textit{Eq. 5.3}$$

   Where W is the radiation power, $\bar{g}$ is the radiation's gaunt factor; the unit of kT_e is electron volt; N_i is the ion density, measured in m^3; N_e is the density of electrons, measured in m^3; Z is the atomic coefficient; n is the ions recombination to level n; h is the Planck constant, and ν is the optical signal's frequency.

We can see from Eqs. 5.1 to 5.3 that the three types of radiation are all connected to the energy of the photons.

The primary gaseous discharge types caused by insulation defects in summarised in literature [81] according to their intensities, features and optical and current detectabilities. This is tabulated in Table 5.1. The applied electric field's intensity significantly impacts the transitions from one discharge type to another. The weakest discharges are caused by charge carrier emissions from insulator surfaces and conductors accompanied by the electroluminescence phenomenon. These discharges are distinguished by extremely low and quasi-continuous currents, which the standard pulsed PD measurement techniques fail to detect. In highly sensitive laboratory tests, an additional class of relatively low-intensity discharges, such as Townsend discharges and swarming pulsive micro discharges (SPMD), can be seen when the applied electric field increases. At relatively high electric field settings, streamer, leader, and spark discharges are the most prevalent in insulation systems [81].

Discharge type	**Intensity**	**Feature**	**Detectability**	
			Current	**Optical**
Field electron emission	10^{-10}, …10^{-5} A/m^2	continuous	No	No
glow	~10 A/m^2	continuous	No	Yes
Townsend, SPMD	~100 μA	pulsed, ~100ns	Yes	Yes
streamer	~mA, >10 pC	pulsed, ~100ns	Yes	Yes
leader	~0.1, …~10 A	pulsed, 0.01 … 1ms	Yes	Yes
spark	~0.1, …~10 A	pulsed, 0.001 … 1ms	Yes	Yes
partial arc	~1, …~10 A	pulsed to continuous, 0.1 … 1s	Yes	Yes

***Table 5.1**. Gaseous discharge types generated by insulation faults are summarized based on their intensities, characteristics, and detectability.*

5.2 Partial Discharge Optical Spectrum Measurement- Test Setup

Ionization, excitation, recombination, cathode photoionization, and secondary electron emission are all discharge-related phenomena accompanied by photon emission and absorption. These happen at different optical spectrums based on the PD defect and dielectric medium. During discharge events, a certain number of photons produced by the aforementioned processes escape from the active zone. The relative light intensity can be used to detect these photons. The wavelength of this photon emitted can be measured using a spectrophotometer. The following sections will detail the optical spectrum measurement test setup for different gases with different PD defects.

5.2.1 Considered PD Defects And Test Cell

Insulation defects caused by design, manufacture, and assembly are dispersed at various locations in gas insulated systems. As mentioned in section 2.3.1, there are broad types of PD defects that could occur in a GIS or GIL. Considering the critical PD defects and the contribution of the electric field to discharge excitation, three typical models were considered for testing. A metal protrusion fixed on a conductor depicting corona PD (Figure 5.1 (a)), a metal particle on an insulator surface depicting surface discharge (Figure 5.1 (b)) and a floating metal particle in the vicinity of an electrode representing floating potential electrode (Figure 5.1(c)).

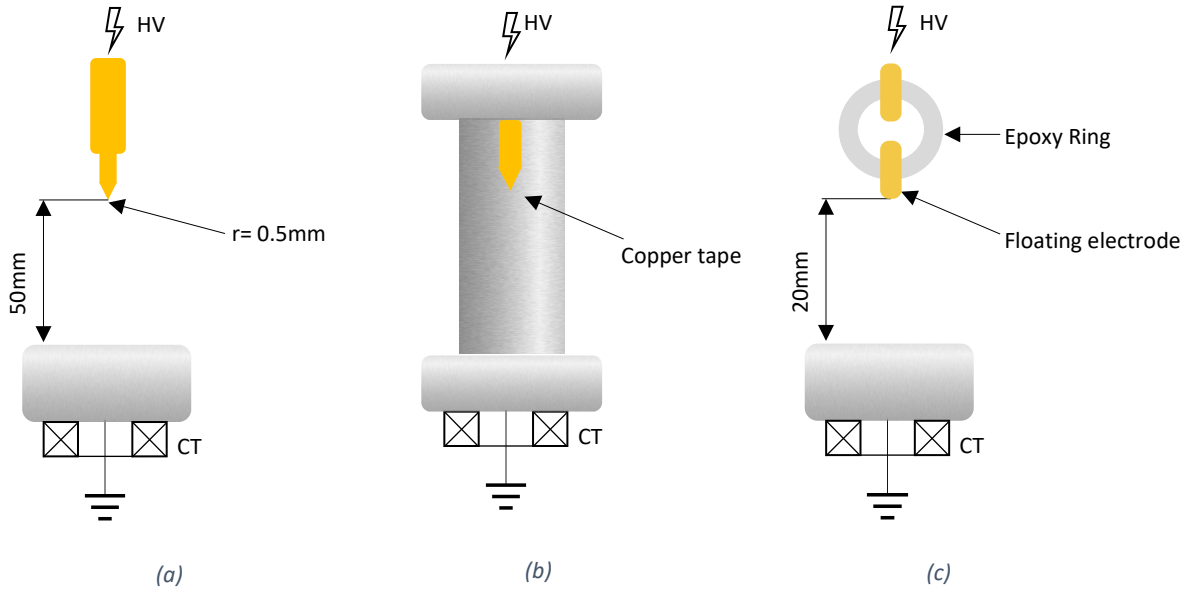

Figure 5.1: *Configuration of PD defect models: (a) metal protrusion fixed on a conductor depicting corona PD (b) metal particle on an insulator surface depicting surface discharge (c) floating metal particle in the vicinity of an electrode representing floating potential electrode*

The artificial defects were installed inside a test cell, as shown in figure 5.2. The test cell comprises a Plexi glass sandwiched between two epoxy flanges. The test cell could withstand a maximum pressure of 5Bar$_{(rel.)}$ and flashover voltage of 80kV RMS.

Figure 5.2: Test cell with protrusion fixed on a conductor depicting Corona

To fill the cell with the test gas, the cell was first cleaned thoroughly with ethanol and then vacuumed to a pressure of 0.3mBar. The test gas was then filled at a pressure of 1Bar$_{(abs.)}$ to minimise the PD inception voltage.

5.2.2 Selection Of Optical Spectrometer And Its Specification

An optical spectrometer (spectrophotometer, spectrograph, or spectroscope) is a device that measures light characteristics throughout a specified portion of the electromagnetic spectrum. In short, it enables in measuring of the wavelength spectrum of light. An optical spectrometer to capture the optical PD emission should have the following capabilities:

- Low Light power level should be high: This is essential for picking any light recognition detector. It should be able to capture even the weak corona.
- Spectral range: The PD source generates light radiation of a specific wavelength. This wavelength changes depending on the medium, here gas. So the optical spectrometer should be active in the optical PD bandwidth.
- It should have Signal to Noise ratio
- The sampling rate and integration time should be high enough to capture the spontaneous PD pulses.

Based on the literature studies on optical detection in SF_6 and air, PD in this medium occurs in the Near Infrared to Visible region of the optical spectrum. Moreover, as CO_2 is the main constituent of the alternative gas C_4F_7N/CO_2 gas mixture, studies show that the optical emission spectrum ranges from around 220nm to approximately 600nm. However, since the alternative gas is a mixture and PD is a process of Ionization, excitation, recombination, cathode photoionization, and secondary electron emission, we cannot assure that the spectrum of PD will be in this range. However, as a rough estimate, this was taken into consideration.

Based on the availability of optical spectrometers at TU Delft, the AvaSpec-3648, as shown in Figure 5.3, from the company Avantes, was utilised. AvaSpec-3648 is a Fiber Optic Spectrometer built on the AvaBench-75 symmetrical Czerny-Turner design and has a 3648 pixel CCD Detector Array. A fibre optic SMA entry connector, a collimating and focussing mirror, and a diffraction grating are the main components of this spectrometer. Applications in the 200-1100nm range are possible thanks to a selection of 16 distinct gratings with varying dispersion and blazing angles. The AvaSpec-3648 has a 16-bit AD converter and a USB2.0 high-speed interface. The AvaSpec- 3648 is ideal for measuring high-resolution applications and has an extensive dynamic range owing to the 10sec electronic shutter. The important specification of this model is presented in Table 5.2 [85].

Figure 5.3: *Avantes 3648 Spectrometer and internal construction [85]*

Property	Value
Optical Bench	Symmetrical Czerny-Turner, 75 mm focal length
Wavelength range	200 – 1100 nm
Resolution	0.025 -20 nm, depending on configuration
Stray light	< 0.1%
Sensitivity (AvaLight-HAL, 8 µm fibre)	14000 counts (16-bit AD)/µW per ms integration time
Detector	CCD linear array, 3648 pixels
Signal/Noise	350:1
AD converter	16 bit, 1 MHz
Integration time	10 µsec - 10 min.
Interface	USB 2.0 high speed, 480 Mbps RS-232, 115.200 bps
Sample speed with onboard averaging	3.7 msec /scan
Data transfer speed	3.7 msec /scan

Table 5.2: *Important specification of Avaspec-3648 Optical Spectrometer*

The spectrometer comes with a software called Avantes AvaSoft for post-processing the data. This software was used to analyse the wavelength spectrum of the different PD signals.

5.2.3 Selection Of Optical Fibre

The light emitted during PD activity should reach the Charge Coupled Device (CCD) detector of the spectrophotometer to obtain the optical spectrum of PD. So a medium that could transmit the PD optical to CCD is required. The medium's wavelength should also match the wavelength range of the optical spectrometer and should be in the range of PD's wavelength. Hence, a fibre optical cable 'FC-UVIR600-2' from Avantes, which has a wavelength range of 200nm-2500nm having a core size of 600μm and terminated with SMA connectors, was utilised. Another fibre optic patch cable from Thorlabs having a wavelength range of 200nm-1200nm (figure 5.4) with eight cores and a size of 200μm was also used.

Figure 5.4: *200nm- 1200nm fibre optic cable utilised for the experiment*

5.2.4 The layout of Optical Test Setup

The optical test setup should be precisely adjusted as the PD light source is a point source. Figure 5.5 shows the layout of the optical arrangement. This arrangement consists of a collecting lens, a precisely adjustable work board, lens holders and fibre optic cable. The fibre optic cable and lens holders can be moved on the rail to position the PD source to the detector accurately. The lens's position calculations and details are mentioned in the next section.

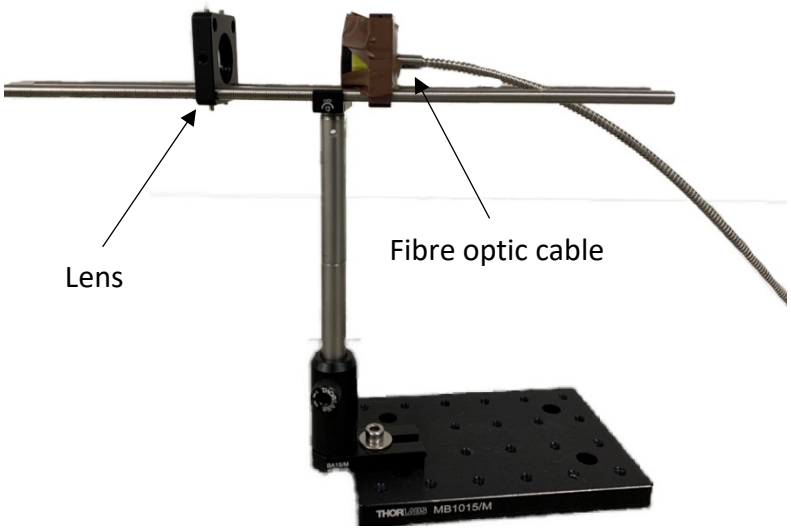

Figure 5.5: *optical test setup*

5.2.5 Lens Positionality and Directionality Calculation

The lens alignment must be done correctly so that the maximum amount of light may fall on the small area of the fibre from the source(which, in this case, is an area causing PD). Some simple calculations and trial testing are required to align the lens at the correct distance between the fibre and the PD source. As a result, the lens and magnification formulas indicated below were utilized:

$$\frac{1}{S_1}+\frac{1}{S_2}=\frac{1}{f} \qquad \textit{Eq. 5.4}$$

$$M=-\frac{S_2}{S_1}=\frac{f}{f-S_1} \qquad \textit{Eq. 5.5}$$

$$M=\frac{h_o}{h_i}=\frac{f}{(S_2-f)} \qquad \textit{Eq. 5.6}$$

Where,

S_1: Distance from PD source to lens

S_2: Distance from the sensor to fibre

h_i: height of the active area of fibre

h_o: height of PD source area

M: Magnification factor

Following multiple trials and error testing, an achromatic biconvex cylindrical lens with a focal length of 50 mm was selected. An achromatic lens is used to correct the chromatic aberration. A failure of a lens to focus all wavelengths in the same place is referred to as chromatic aberration or spherochromatism. Moreover, the lens should be able to collect the wavelength of our interest without any attenuation. The drawing of the lens is presented in Appendix C.

A cosine corrector eliminates optical interface issues associated with the light collection sampling geometry inherent in alternative sample devices such as bare fibre optics and also collects light from a 180° angle. In this case, as the fibre area is too small to collect the light and the fibre optic cables have a specific collection angle, a trial with a cosine corrector, as shown in figure 5.6, connected to the tip of the fibre cable was conducted. However, the trial failed because the cosine corrector reduced a lot of light intensity.

Figure 5.6: *Cosine Corrector*

Moreover, the rays from the PD source have to go through multiple mediums before reaching the fibre optic. The ray starts from the PD source, travels through the gas medium, then through the Plexiglass of the test cell, comes out of the plexiglass, travels through air and finally reaches the fibre optic cable. Hence, the refractive index of all the mediums must be considered. Here the absorption of rays by the mediums is neglected. Snell's law gives a relation between two refractive indexes of two mediums, the incident angle and refracted angle, as shown in the equation:

$$n_1 sin\theta_1 = n_2 sin\theta_2 \qquad \textit{Eq. 5.7}$$

Where,

n_1: incident index

n_2: refracted index

θ_1: incident angle

θ_2: refracted angle

Simulations based on this equation were done in COMSOL using optics physics. Even though the refractive index of the test gas C_4F_7N/CO_2 mixture is not known from the literature, it was assumed that the CO_2 would mainly govern the refractive index of the mixture. Based on this, simulations were done for air (~C_4F_7N/CO_2) and SF_6, as shown in figures 5.7 (a), and (b), respectively. The refractive index of the mediums at 589.29nm considered are as follows:

Air: 1.000293

CO_2: 1.00045

SF_6: 1.79883

Plexiglass: 1.466

Due to its comparatively high refractive index, it is evident that more rays will be lost when using SF_6. This could be solved by moving the lens towards the test cell, but there is a chance for flashover between the HV electrode outside the cell and the rail where the lens has been placed. The calculations aided in accurately collecting the optical PD signals. As measurements with rulers are error-prone, the PD light falling on the fibre might not be sharp. To correct this, a lamp was lit in the direction of the PD defect, and the distance of the lens (sometimes even fibre optic end) was finetuned.

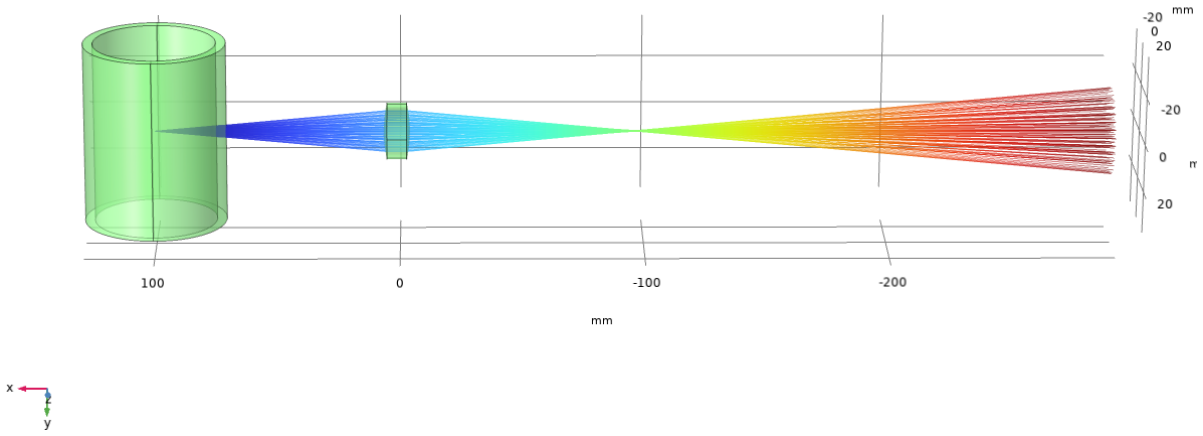

(a)

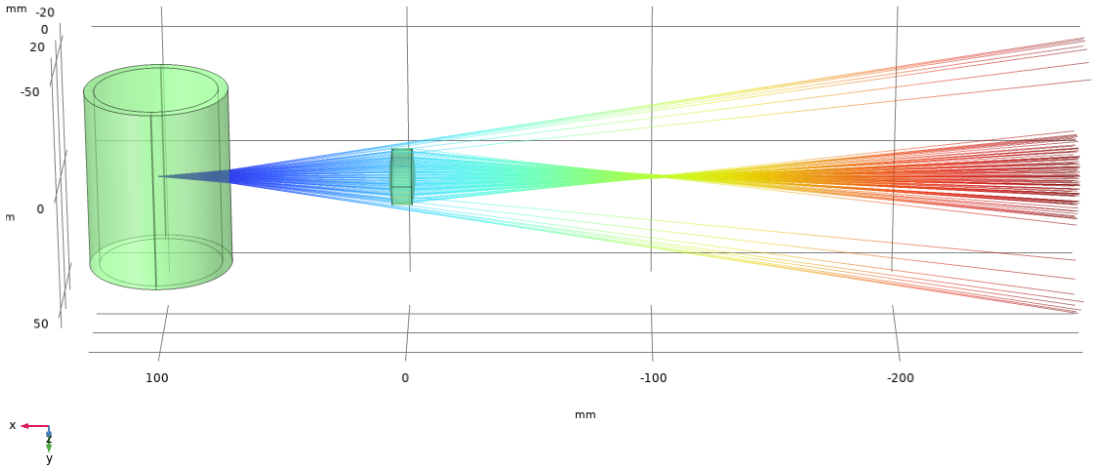

(b)

Figure 5.7: *Ray diagrams of cell with (a) air or C_4F_7N/CO_2 and (b) SF_6*

As per the calculations, a distance $S_1 = 100mm$ and $S_2 = 100mm$ was chosen with the lens focal length of 50mm.

5.2.6 Electrical PD Detection Using HFCT

A PRPD pattern obtained using an electrical method is required to reference the spectrum obtained during PD activity. In this setup, we utilise the unconventional electrical measurements of higher bandwidth using HFCT sensors. Details of the working principle are detailed in section 2.3.2.

Here, the equation that governs the gain of the HFCT is given by:

$$A = \frac{V_o}{I_{PD}} \qquad \textit{Eq. 5.8}$$

Where V_o is the output voltage across a 50Ω termination and I_{pd} is the partial discharge current as shown in figure 5.8

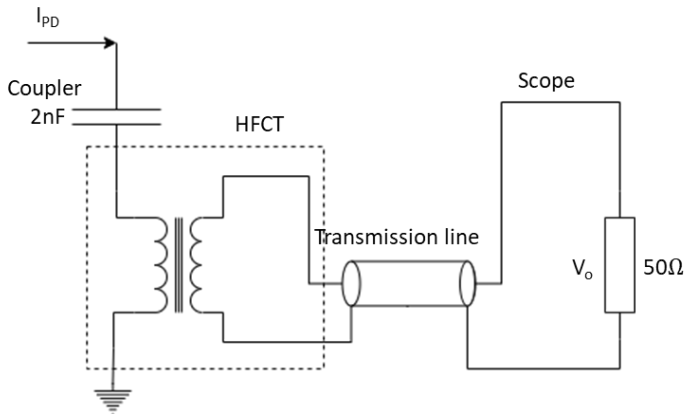

Figure 5.8: *HFCT Gain*

The gain of the HFCT sensor used in this experiment is shown in figure 5.9 and has a gain and bandwidth of 9.1mV/mA and 34.4kHz to 60MHz, respectively. This HFCT comprises five turns wound onto a TDK N30 ferrite core and is terminated with a 50Ω BNC coaxial cable in an oscilloscope. Each turn is made of a 3 mm broad flat strip evenly dispersed along the core to reduce stray capacitance in the system.

Figure 5.9: *HFCT sensor with a gain of 9.1mV/mA*

When there is a coupling of 50Hz signal due to other machines in the lab, an amplifier having a lower cut-off frequency f_{low}=30kHz, the upper cut-off frequency of f_{high}=1.23GHz, and an amplification gain of 22.7dB was utilised.

To acquire the PD signals from the HFCT, a 5GHz, 2.5GS/s PC oscilloscope from Picoscope, as shown in figure 5.10, was used. This oscilloscope is a 4 channel oscilloscope and is also used in the next experiment to collect optical signals from APD along with HFCT.

Figure 5.10: *Picoscope*

Because the signal shows each pulse, each pulse is taken separately using "Rapid Acquisition" (the number of pulses to be captured is set according to the user requirements) to acquire the PRPD pattern or undertake further analysis of PD signals. Before capturing data, the number of pulses, trigger value, time stamp, and sample frequency (at least 1.25 GS/s at ~100ns/div) can be adjusted. Once the data is collected, all trigger events and channel signals are saved as a waveform in ".wfm" format. These waveforms are used for further off-line analysis by a GUI-based software program called PDflex developed at TU Delft by the authors of [86] .

In order to acquire a PD pulse and show it in the form of a PRPD pattern and other analysis plots, the software PDflex requires a synchronization signal. Each PD pulse should be recorded along with the phase angle associated with the test voltage at which it occurred, to generate a phase resolved PD pattern. This synchronisation can be generated using a signal generator, as shown in Figure 5.11. Since the output of the single-phase HV transformer used to excite PD will be in phase with the outlet, the sawtooth signal is synchronised with the outlet and is a separate unit that is not connected to the HV end of the test transformer. This synchronisation signal is fed to channel B of the oscilloscope, as channel B is the default synchronisation channel recognised by the software.

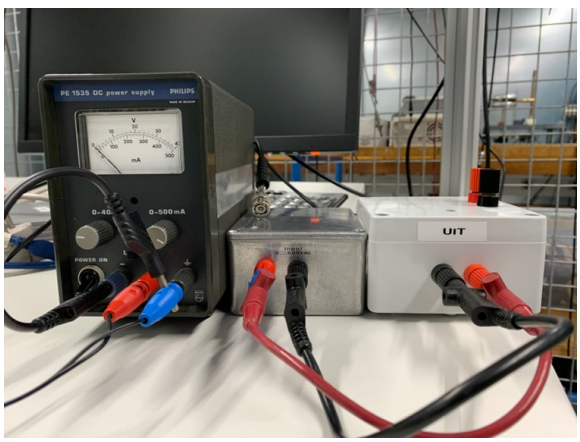

Figure 5.11: *Synchronisation Box*

The phase angle is calculated using the sawtooth signal generated by the sawtooth generator (shown in Figure 5.12), the period of which is synced with the period of the test voltage. When the amplitude of a PD pulse exceeds the trigger (set by the user), the oscilloscope records both the signal from the PD sensors and the phase signal (sawtooth). The PD pulse phase is proportional to the amplitude of the ramp voltage at which the PD pulse occurred. The sawtooth generator used in the experiment gave a voltage output of 4.52V for a whole 360° phase angle. Hence the positive half cycle is the voltage between 0V to 4.52V/2, and the negative half cycle is the voltage between 4.52V/2 to 4.52V

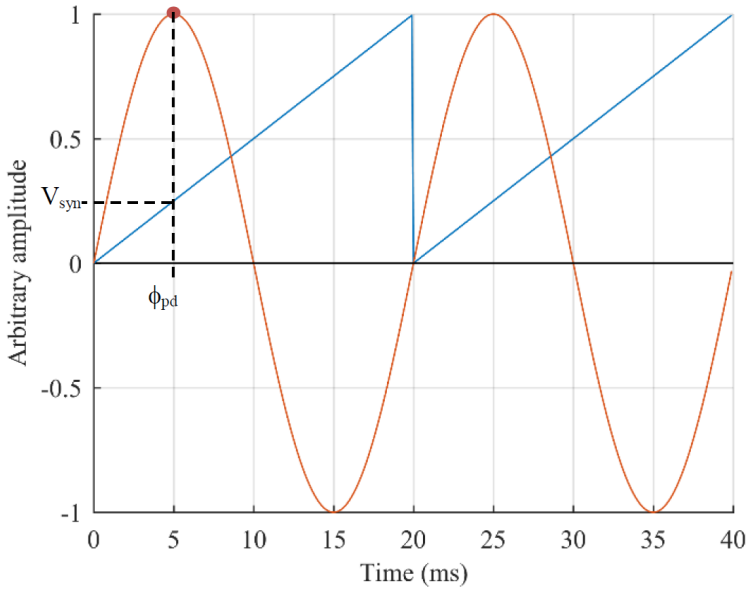

Figure 5.12: *Synchronization signal for acquiring PD*

Once the oscilloscope waveforms have been acquired, they may be examined in PDflex and analyzed individually for electrical signals. The PDflex software allows us to analyze the AT plot (time evolution representation of the current pulse of each PD pulse), the QT plot (time evolution representation of the charge of each PD pulse), the t_{rise} t_{fall} plot (cluster plot of the rise and fall time of each PD pulse), the IQE plot (cluster plot of the charge and the energy/charge ratio of each pulse), and the FW plot (cluster plot of the frequency at which the peak of the Fourier spectrum occurs and the equivalent BW). Further details of the software can be found in the documentation.

5.2.7 HFCT Output vs Charge

HFCT and APD (used in the following experiment) output a voltage corresponding to the PD charge. However, PDs are typically measured in pC. Hence, it is essential to know the relationship between the sensor's output voltage and the actual PD charge. A PD calibrator from Sietz Instrument, CAL 141, as shown in figure 5.13, was used for this purpose. The voltage equivalent to different PD charges obtained during this measurement is shown in figure 5.14.

Figure 5.13: *CAL 141 PD calibrator*

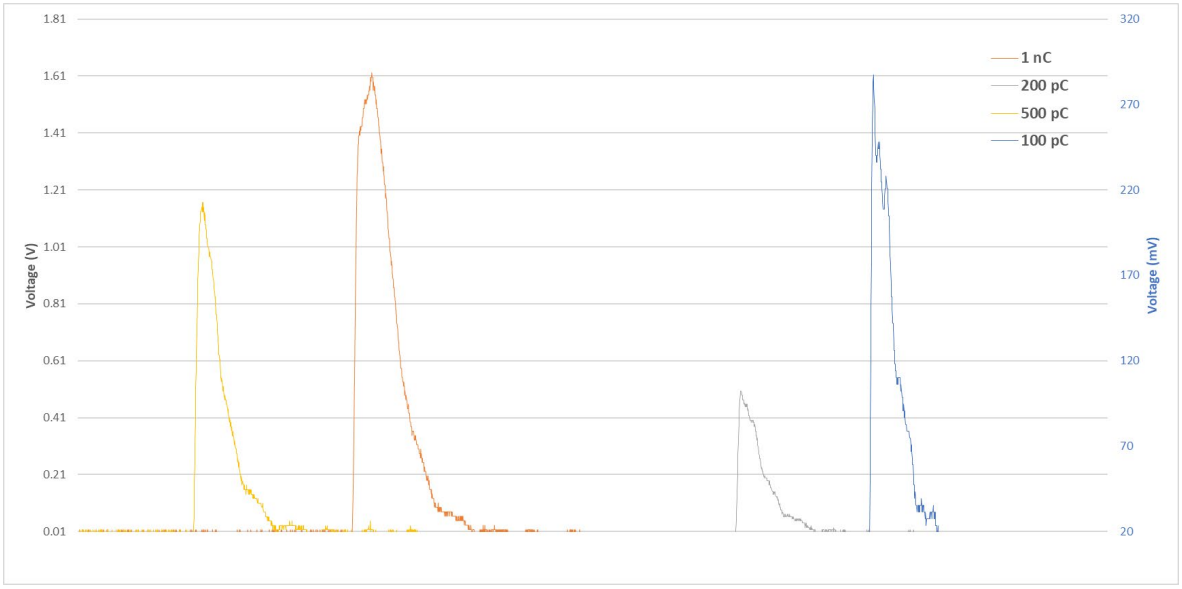

Figure 5.145: *PD pulse Voltage v/s Charge*

5.2.8 Test Setup

The schematic test setup used to measure the optical spectrum and PRPD pattern for reference is presented in figure 5.15. A 34.5kV Siemens Voltage Transformer tested to be PD-free was used to excite the PD source with voltage. The low voltage side of this transformer is connected to an autotransformer to control the HV output. To limit the current to the circuit, a protection resistor is used. A coupling capacitor provides a closed circuit for discharge displacement charge. HV probe is used to measure the voltage applied to the defect. The body of the optical breadboard is grounded to eliminate the floating potential that could occur as the rail is close to the HV electrode, which will lead to false PD detection.

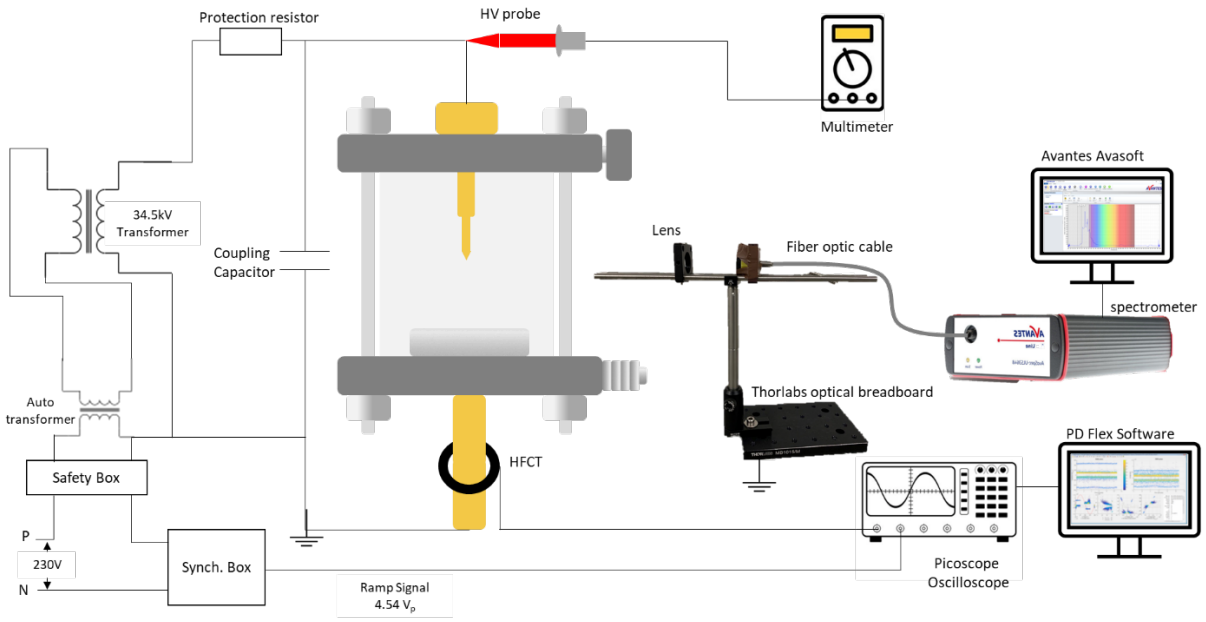

Figure 5.15: *Test setup for optical spectrum measurement with HFCT measurement*

5.3 PD Optical Spectrum Measurement

The optical spectrum of all the three defects was measured along with HFCT simultaneously. With HFCT, at least 2500 PD were collected to generate a PRPD pattern. Because the pulse duration was only a few nanoseconds, and the light emission from a single PD was very low, the transient spectrum could not be effectively evaluated within the limits of the reaction speed and sensitivity of the optical spectroscope utilized. Instead of collecting the transient spectra of a single PD, an integral spectrum of continuous PDs over several seconds was captured. This strategy can reduce the requirement for optical signal processing response rate. However, the best integral time for each PD defect is found through trial and error. Figure 5.16 presents the results for different integration times with the corona spectrum in the air.

Measurements are taken in a dark room to eliminate the background lights. Due to the spectrometer's sensitivity, it can still capture some radiation emitted from different objects in the dark room. The background light noise captured for a time integral of 30 seconds in the darkroom is shown in figure 5.17. This is saved in the system as a dark spectrum. The measured PD light is subtracted from the dark spectrum by the 'Scope – dark' option in the software to obtain an accurate PD light spectrum and not a superimposed spectrum. The dark spectrum should be saved for good results while performing with a new integration time. The lower and upper wavelength spikes, as seen in figure 5.17, are due to the noise outside the sensor's detectability range.

The spectrometer was calibrated before the experiment by the PVMD research group of TU Delft. The settings of the spectrometer were changed to recommended settings in the user manual. The obtained spectrum is saved in '.csv' format for further analysis.

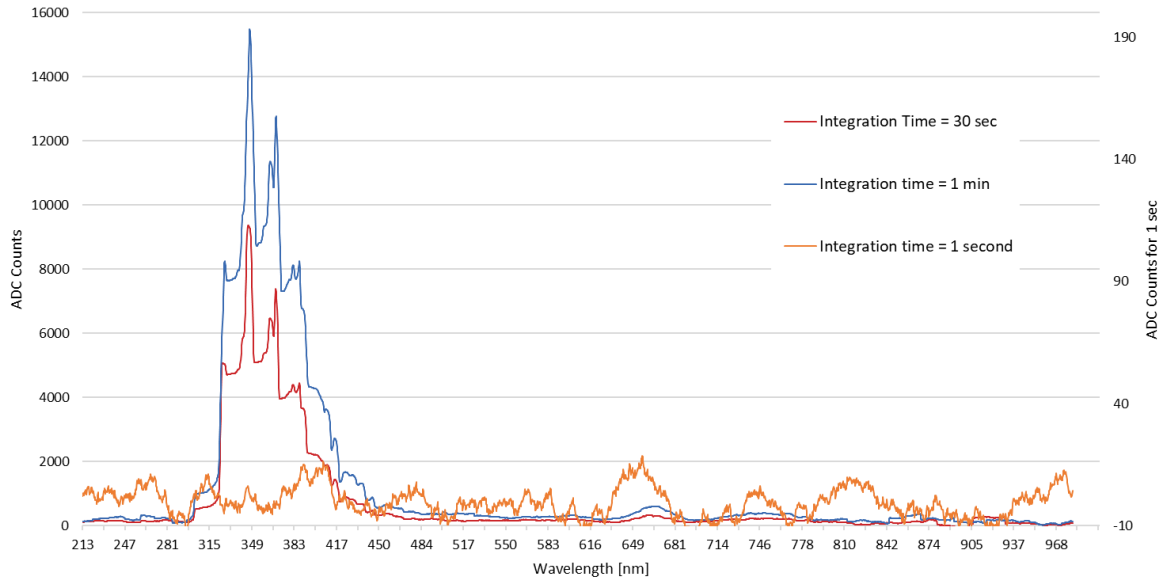

Figure 5.66: *Optical Spectrum of Corona at 14kV$_{RMS}$ with various integration time*

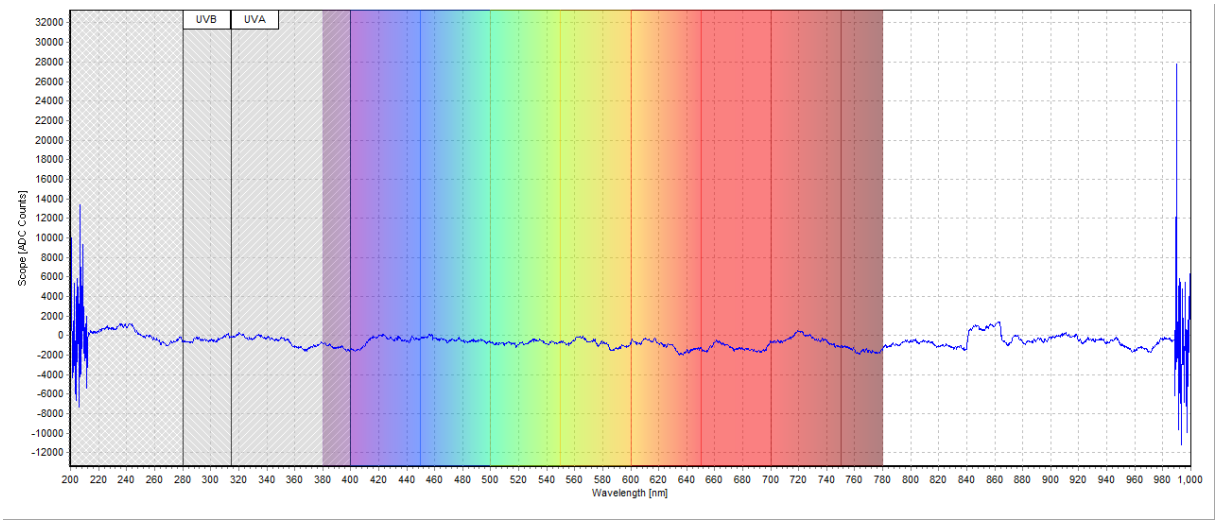

Figure 5.77: Background Noise

5.3.1 PD Optical Spectrum of Air

This section will focus on the spectrum obtained in the air during PD activity in the three defects. Tests in the air were done without the test cell to eliminate the reflection and energy loss that could occur due to the Plexiglass. Hence ambient air pressure is to be considered, and the distance between the metal protrusion and also floating electrode was almost 8cm from the ground electrode. All the voltage ratings are in kilo Volt Root Mean Square (kV_{RMS}).

- **Corona:**
  Figure 5.18 (a) shows the results of the optical spectrum obtained at 8.2kV and 14kV. Figure 5.18 (b) and (c) PRPD pattern of corona defect at 8.2kV and 14kV, respectively. Figure 5.18 (d) and (e) show the voltage pulses detected by HFCT for negative and positive corona, respectively.

  At an increasing voltage of AC, negative corona occurs first: Townsend mechanism causes feedback at relatively low field strengths since a cathode is nearby, and recurrent discharges start. With a glow discharge, a negative corona in the air fills the region around the sharp electrode across a distance of around 0.1 mm. This glow discharge is the one detected by the optical spectrometer. While the rapidly moving electrons are trapped in the air, a negative space charge forms, shielding the pointed electrode from the electric field and causing the discharge to stop.

  The rise-time of the PD pulse during negative corona is governed by the drift velocity of the electrons and is in the order of one nanosecond. When the discharge stops due to the shielding of the point electrode, the slow ions drift back and cause a subsequent current which decays in 50 to 100 ns. This current is detected by the HFCT sensor, as seen in the waveform in figure 5.18 (b). It is also to be noted that the tail time is longer when the radius is larger. If the voltage is increased, the number of discharges increases significantly in the negative cycle.

Upon increasing the voltage further, discharges occur at the positive half cycle. These discharges start at slightly higher voltages (in this case, at around 10.5kV) as no cathode is present in the region of high field strength. Hence streamers arise at the point and leave a positive space charge. The space charges shield the point from the field, the discharge halts; the positive charge drifts into space and the corona discharge re-initiates. These discharges are more irregular, with a larger wavefront and a relatively extended trough before decay sets in, as seen by the waveform in figure 5.18 (e).

Both negative and positive half cycles of the corona discharge can be detected in the optical spectrum. However, the negative corona spectrum is of lower intensity since the Townsend mechanism happens with a faint glow. The integral optical spectrum of negative corona discharges in the air shows characteristic peaks in the wavelength range of 340 to 400nm. This is attributed to emissions from traces of Nitrogen in the air, which have been reported in the literature [87]. As the voltage rises, the discharges during the positive half cycle transform into successive streamer discharges with larger PD charges and light pulses. The components in the UV area rise dramatically in the region between 315 and 450 nm, which may be attributable to additional positive point discharges.

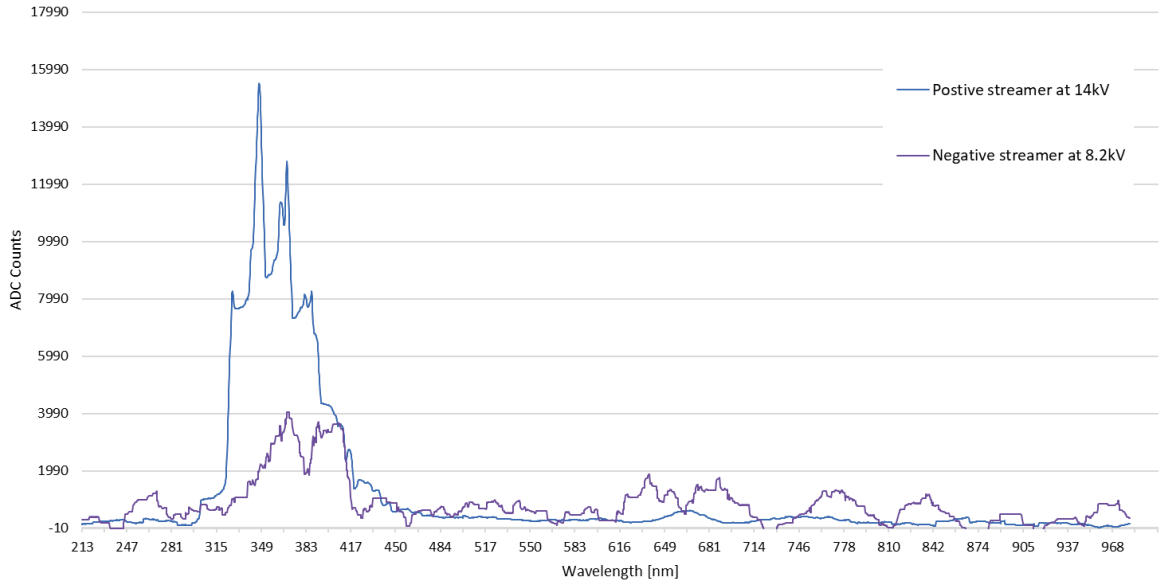

(a)

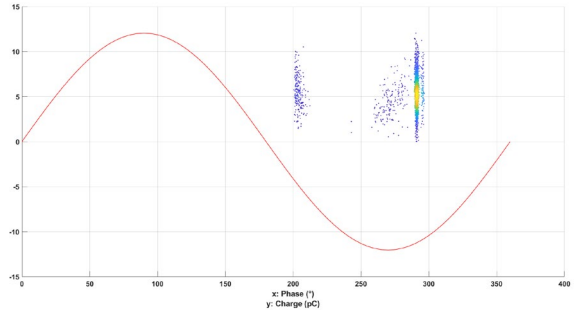

(b)

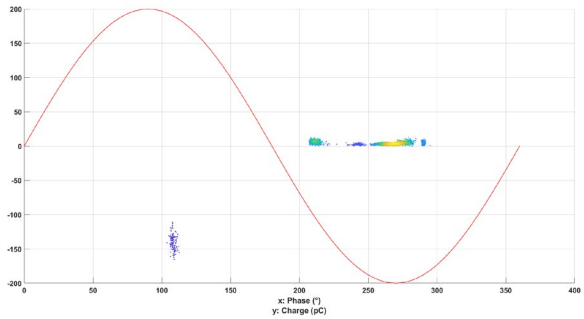

(c)

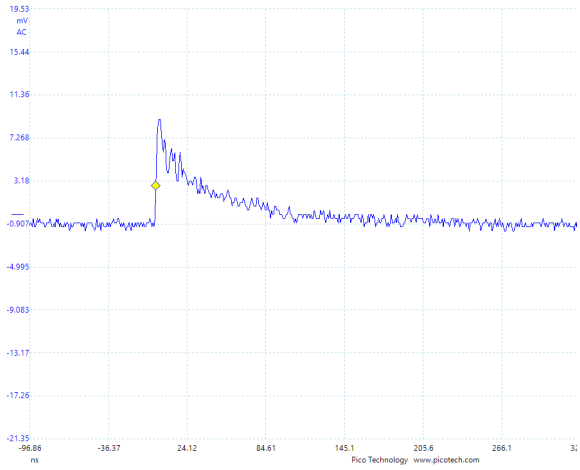

(d)

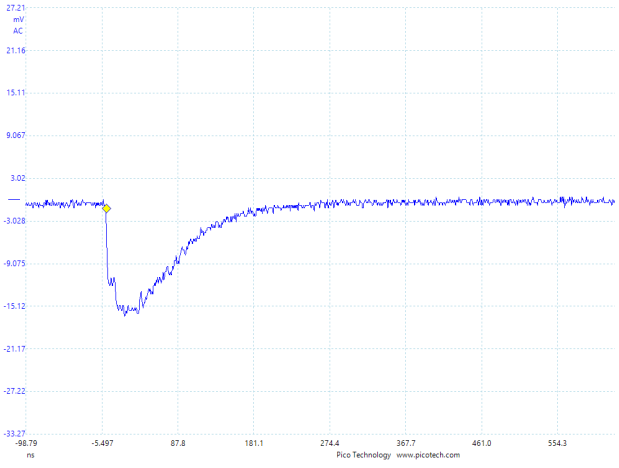

(d)

Figure 5.88: *(a) Optical Spectrum of corona, PRPD patterns of (b) IV at 8.2kV (c) positive corona at 14kV and Voltage signals captured by HFCT (d) negative corona (e) positive corona*

- **Surface Discharge:**

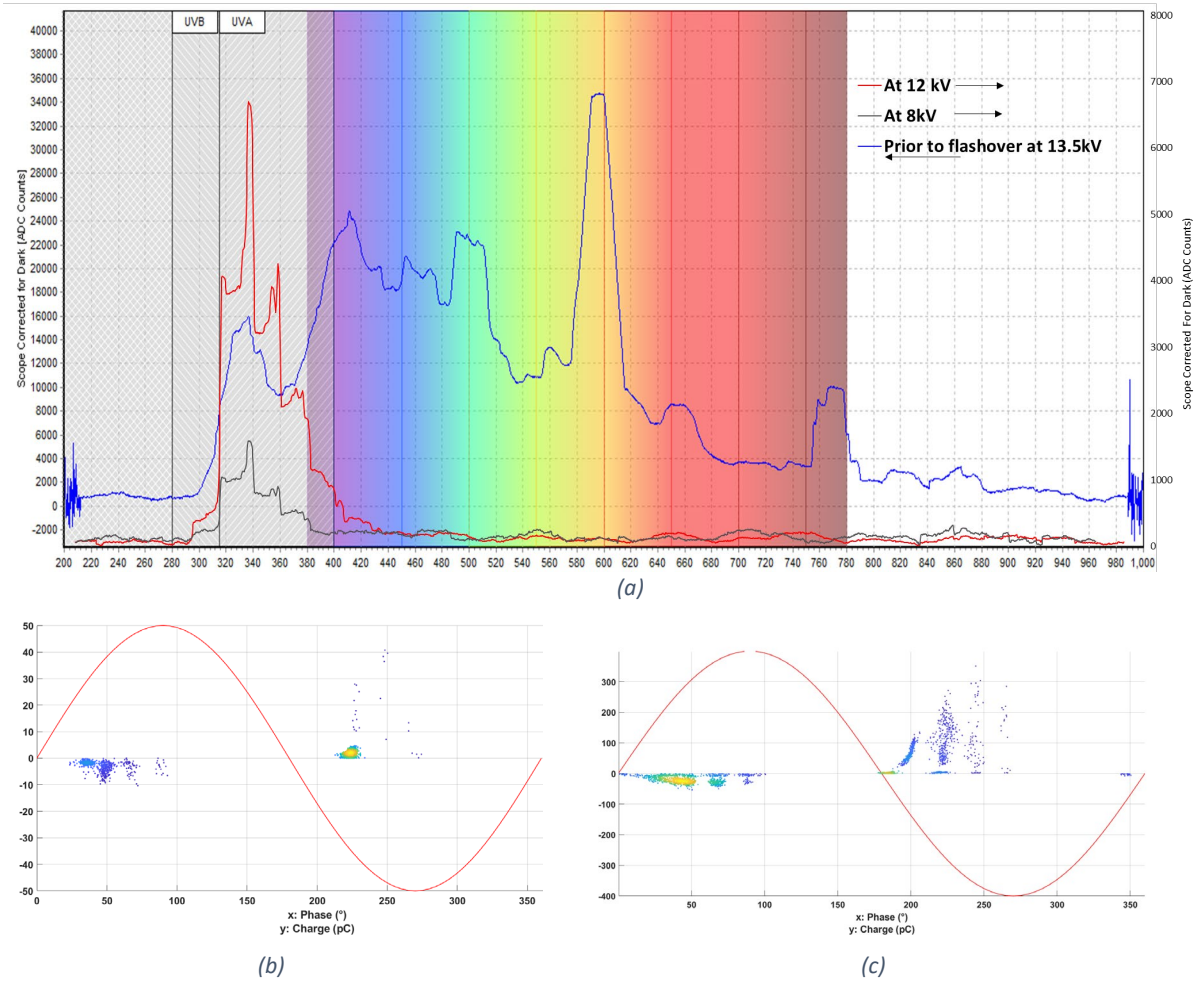

Figure 5.99: *(a) Optical Spectrum of Surface discharge at 8kV, 12kV and prior to falshover at 13.5kV and PRPD Pattern of surface discharge at (b)8kV (c)12kV*

In this case, the discharges are excited from the triple point where the insulator, electrode and air meet. Figure 5.19 shows the optical spectrum and PRPD pattern of surface discharges in air. The spectrum of surface discharges along a solid dielectric is more complicated [88] and impacted by various parameters, including insulator material, its surface condition, the composition and purity of the dielectric gas, type of electrode materials etc. In particular, electroluminescence (prior to gas ionisation) induced by electron-hole recombination and collisions triggered by energetic charge carriers in a strong electric field [89], as well as material deterioration during surface discharges, complicates the spectra.

The characteristic peaks are found to be in the UV region of wavelength 320 to 380nm. It is evident from the graph that as the electric field increases, the number of photons produced due to electron-hole recombination or by collisions of charge carriers increases.

Streamers are formed on the surface when the voltage is further increased, due to which high magnitude pulses were observed using HFCT. As can be seen from figure 5.19 (a), the wavelength of a flashover along the epoxy surface ranges from 400nm to 700nm, most of which is visible light along with some UV radiation, which is also addressed in literature [88].

By increasing voltage, the discharge increases in number and magnitudes in both the half cycles can cause treeing and might lead to insulation degradation.

- **Floating Electrode**

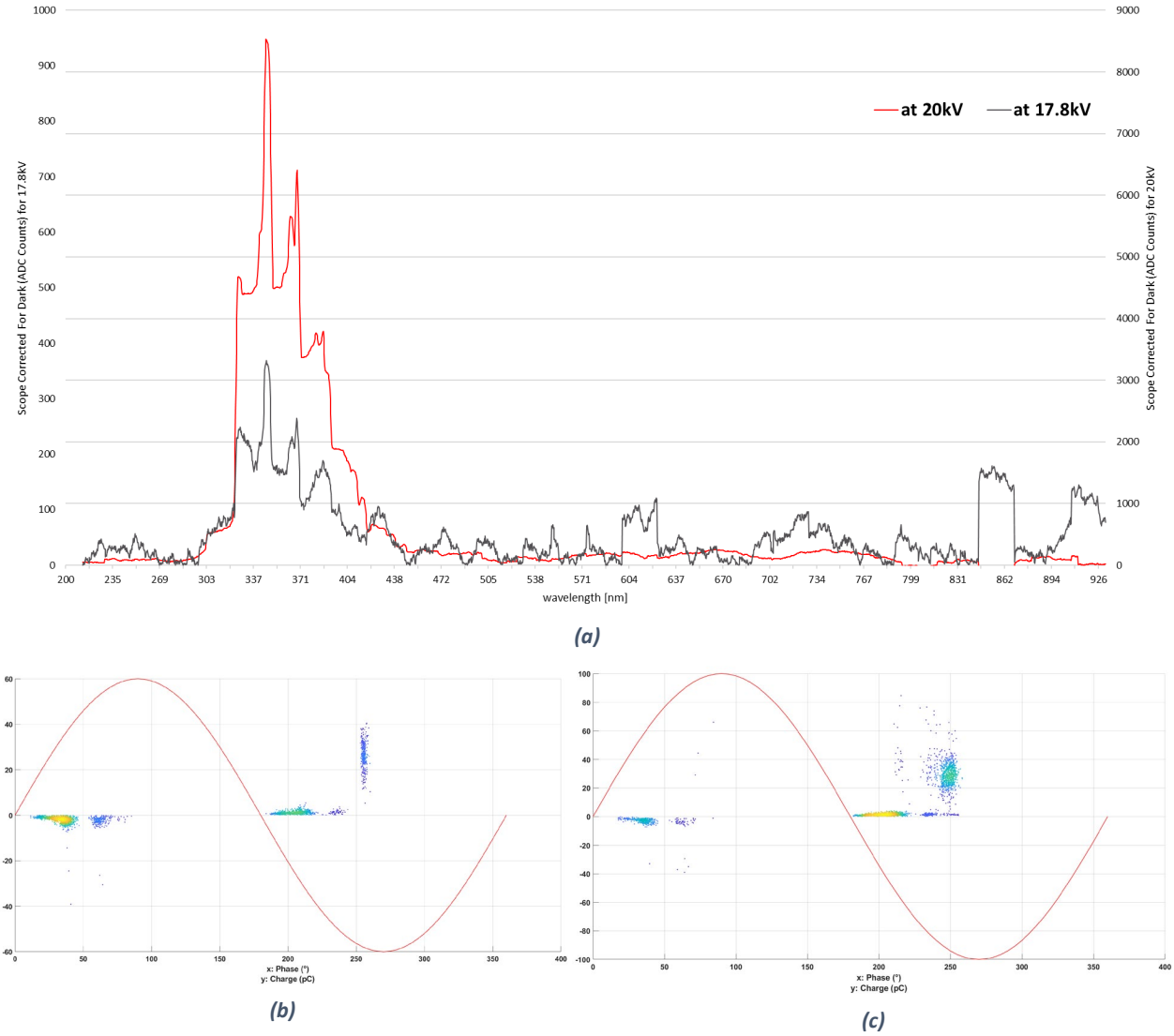

Figure 5.2010: *(a) Floating electrode discharge optical spectrum and PRPD pattern at (b)17.8kV (c) 20kV*

Figure 5.20 shows the optical spectrum and PRPD patterns obtained for a floating electrode defect in air. For discharges stimulated by a floating electrode, the PDs begin from the side of the floating electrode closest to the HV electrode at relatively low voltages, resulting in characteristics similar to corona in terms of current and light pulses, as well as the integral optical spectral distribution.

When the applied voltage is increased, the electric field along the gap between the suspended electrode and the HV electrode increases to a critical value, triggering the partial breakdown of the gap. Figures 5.20 (a) and (c) show that corona discharges transform into flare corona discharges, resulting in a higher PD charge and more intense light emission.

5.3.2 PD Optical Spectrum of C_4F_7N/CO_2 alternative gas mixture

This section summarizes the optical characteristics during partial discharges in the alternative gas mixture C_4F_7N/CO_2. Keep reminded that the mixture proportion is 5mol% C_4F_7N and 95mol% CO_2.

- **Corona**

  Figure 5.21 shows the optical spectrum. PRPD patterns, negative and positive pulse of corona discharge in the alternative gas mixture.

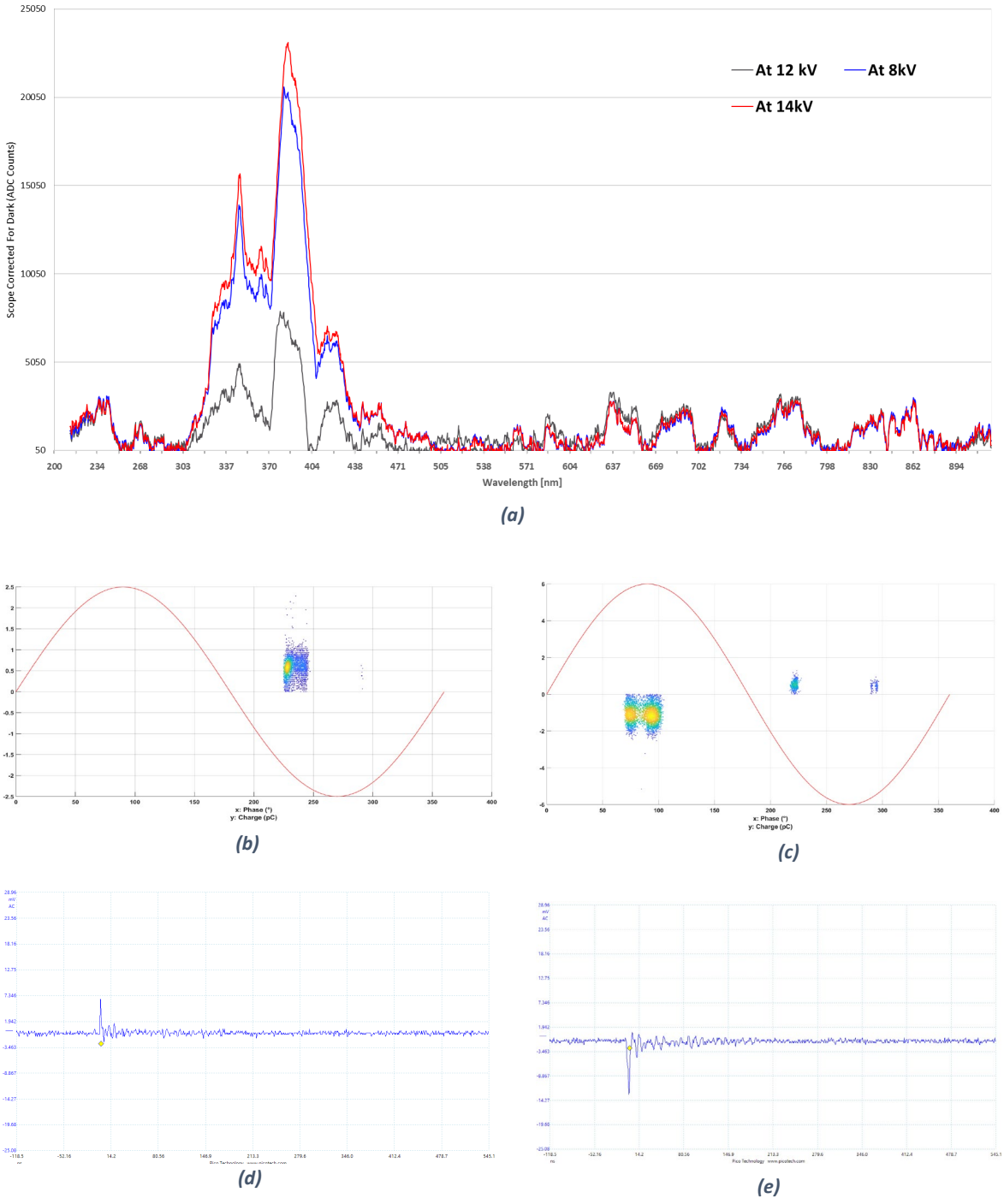

Figure 5.21: *Optical Spectrum of corona in C_4F_7N/CO_2 mixture, PRPD patterns of (b) IV at 8.2kV (c) positive corona at 14kV and Voltage signals captured by HFCT (d) negative corona (e) positive corona*

At an increasing voltage of AC, negative corona occurs; first, the Townsend mechanism takes place, and discharge starts. The low glow during this is mainly in the UV region, specifically in the 370 to 400 nm range. When the voltage is increased further, positive streamers occur due to the streamer mechanism, and more photons are released due to the de-excitation of gas molecules after the collision with the electrons. The photons' wavelength during this stage also lies in the UV region, particularly from 300nm to 400nm. These can be due to photons emitted by the excited nitrogen gas molecules in the gas mixture and the small amount of nitrogen in the air that was mixed up while filling the test cell. However, the overall spectrum in the UV region looks slightly different from air.

The discharge pulse detected by the HFCT (figure 5.21 (d) and (e) shows that the pulse width in both half cycles is very short compared to that observed in air. This is similar to the case with SF_6 and is due to the electronegative nature of the gas. As per the corona discharge mechanism described in [90], during a negative corona, the rise and fall periods of the pulse are connected to the production and dissipation of the positive-ion cloud, respectively, and the pulse duration is somewhat more than the total of the two times. The actual discharge zone in the electronegative gas or gas mixture is the critical distance from the needle electrode surface to the ionization boundary and the critical electric field. The positive ions produced by the electron avalanche will congregate at the ionization border, forming a positive-ion cloud. This can be a swift process in the case of an electronegative gas and might be the reason for pulse width to be shorter. The positive pulse is wider than the negative pulse, as can be seen in figure 5.21 (e).

Due to limitations in the test setup, a complete breakdown in the gas mixture was not performed. The emission spectrum in the VIS region that corresponds to CO_2 is expected to observe during a complete breakdown as the mixture contains more molecules of CO_2 than C_4F_7N. This is as per the knowledge obtained from [91]. However, this is to be verified by experimentation.

- **Surface Discharge**

  Figure 5.22 shows the optical spectrum and PRPD pattern of surface discharge in the C_4F_7N/CO_2 mixture. At the PDIV of 6.1kV, no distinctive optical spectrum was found. At PDIV, the photons might not have that much energy and might have been absorbed by the Plexiglass. However, upon increasing the voltage, characteristics peaks in the UV region began to form, especially in the wavelength from 315nm to 404nm. The waveform seems to be an addition of corona and surface discharge. Due to the huge electric field at the triple point, there might have been corona too. However, there is a characteristic peak in the region from 370nm to 404nm.

  Several processes for surface discharges and tree initiation have been proposed, all of which include the injection of charge carriers (electrons and/or holes) into the dielectric, especially epoxy, from a metal electrode. Electroluminescence has been proven to be connected with charge carrier movement across the dielectric, and it happens when these carriers hit with luminescence centres or trapped charges of opposite polarity (electron-hole recombination) in the polymer. A strong electric field is necessary to generate charge carriers with enough

energy to produce visible photons [89]. This can also be regarded as a reason why no photons were detected during PDIV, only at a higher electric field and discharge at 15.1kV.

Optical detection can be helpful in the following way; because charge carrier movement happens when space charge regions originate or deplete, electroluminescence may offer information on when the space charge is produced and an indirect estimate of the quantity of trapped charge [89]. This can be used in understanding the flashover characteristics in different mediums that are still not clearly understood. The authors of [71] have used this method to explain surface flashover.

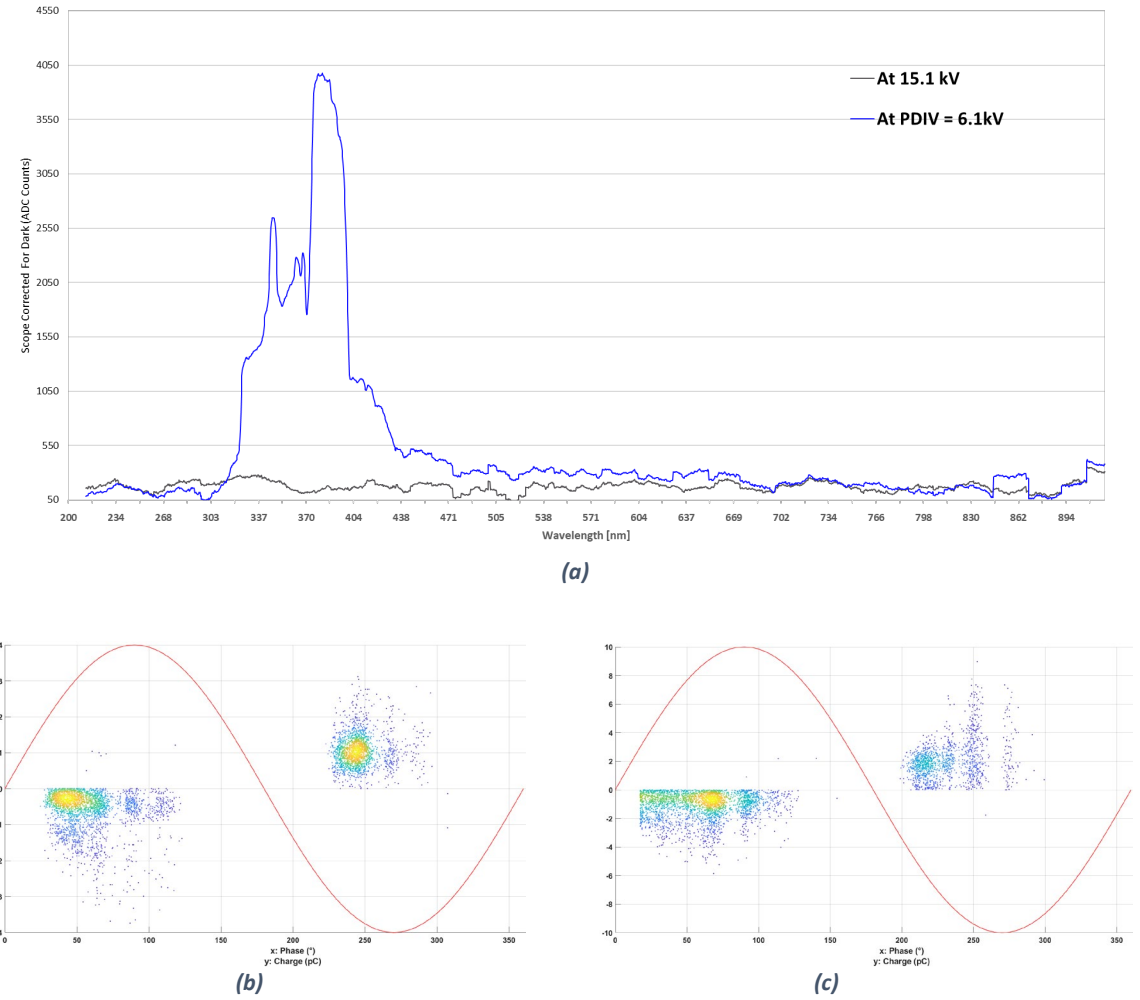

Figure 5.22: *(a)Optical Spectrum of surface discharges, and PRPD pattern of discharges at (b) PDIV=6.1kV and (c) 15.1kV*

- **Floating Electrode**

For discharges caused by a floating electrode, the PDs begin from the side of the floating electrode closest to the HV electrode at relatively low voltages as a corona discharge. When the applied voltage is increased, the electric field along the gap between the suspended

(floating) electrode and the HV electrode increases to a critical value, triggering the partial breakdown of the gap. More visible spectral lines and UV components can be observed in this case, as obtained in figure 5.23 (a). This is attributed to light emission originating from certain fluorine dissociation in C_4F_7N reactions based on the assumption that electrons involved in streamer-like discharges may have obtained energies above 14 eV to excite fluorine. This conclusion has also been disclosed in literature [81] for SF_6. Figure 5.23(b) shows the PRPD pattern at 22kV.

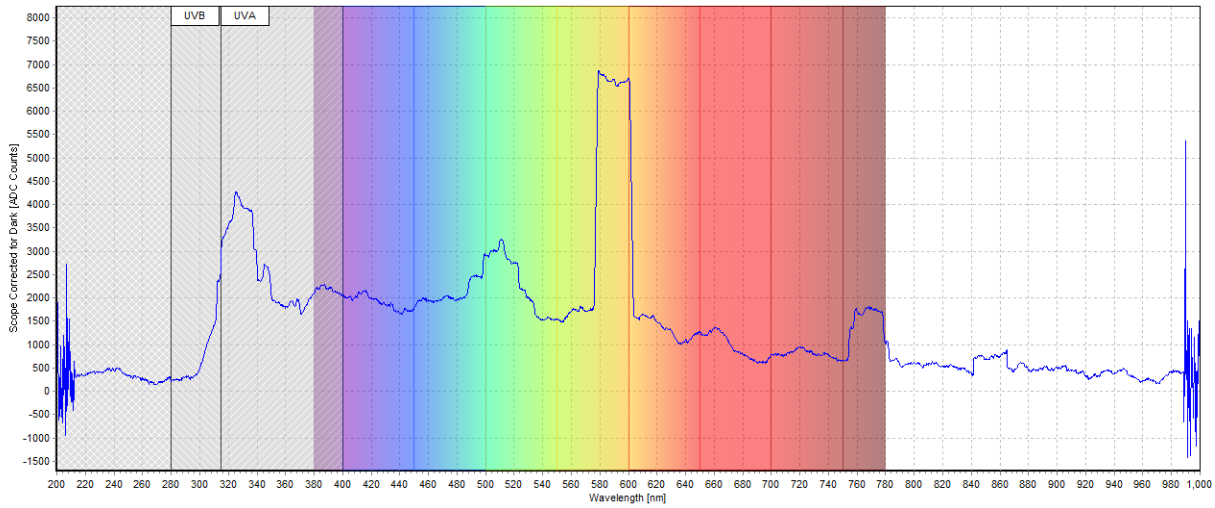

(a)

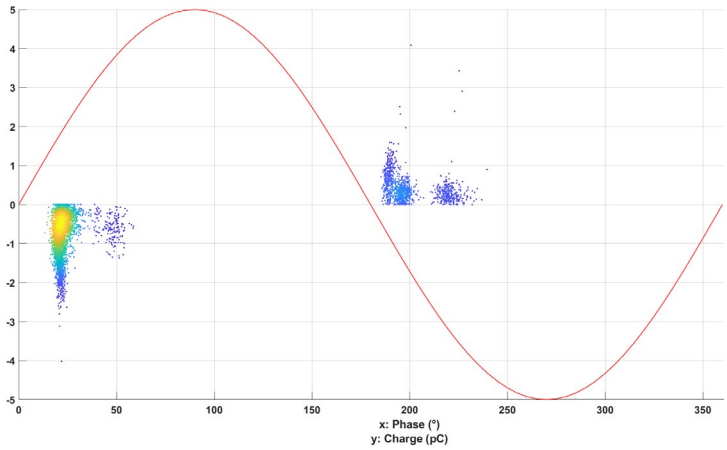

(b)

Figure 5.23: (a) *Optical spectrum obtained at 30kV and (b) PRPD pattern at 22kV*

5.3.3 Summary

With simultaneous measurement of PD activity captured through optical spectroscope and HFCT, the optical spectrum of each type of PD activity was studied. The spectrum lies mainly in the UV region for air and alternative gas. However, characteristic peaks change with respect to the medium and defect stimulated.

From this, it is understood that optical spectrum measurement of PD can also be used as a diagnostic method. If there are quite a good number of spectra for each defect and each medium, with the help of learning curve (or training curve) machine learning algorithms, it can be used as a diagnostic method. If the trend is known, even a post-processing algorithm with curve fitting and identification can be utilised to identify the PD defect and its hazard rate. However, as PDs are typically measured in pC, an understanding of the relationship between the intensity of light and charge is to be studied. It is to be noted that a direct PRPD pattern cannot be directly obtained from this type of measurement.

Spectrometer measurements can help detect the PD spectrum despite some background light. To enable this, scope–dark measurements should be available in the scope. With we can eliminate the background noise and capture only the PD.

Now, we came to know in which spectra the PD lies primarily for air and C_4F_7N; this knowledge can be utilised in selecting the sensors and have the best sensitivity.

5.4 PD measurement Using Fluorescent Fibers – Test Setup

Different forms of insulation failure cause PD at different wavelengths of the optical spectrum. As a result, detecting the signal and subsequently estimating the insulation problem using the optical effect in conjunction with PD is conceivable. This section will cover the designed fluorescent optical fibre sensing technique for detecting the PD signals in Gas Insulated Systems and the selection criteria.

5.4.1 Fluorescent Fibers- An Introduction

Fluorescent fibres are plastic fibres that produce brilliant colours from their optical fibre cores. Many fluorescence molecules are selected to produce desired fluorescent and optical characteristics.

Fluorescent optical fibre has the property of sensing a specific shimmer signal. The fluorescence molecules are excited when the external light is shined onto the optical fibre. And the fluorescence signal that meets the criterion of the total reflection is transferred down the axial direction of the optical fibre and exits the fluorescence fibre at both ends. Figure 5.24 depicts the principle of PD light transfer using fluorescent optical fibre.

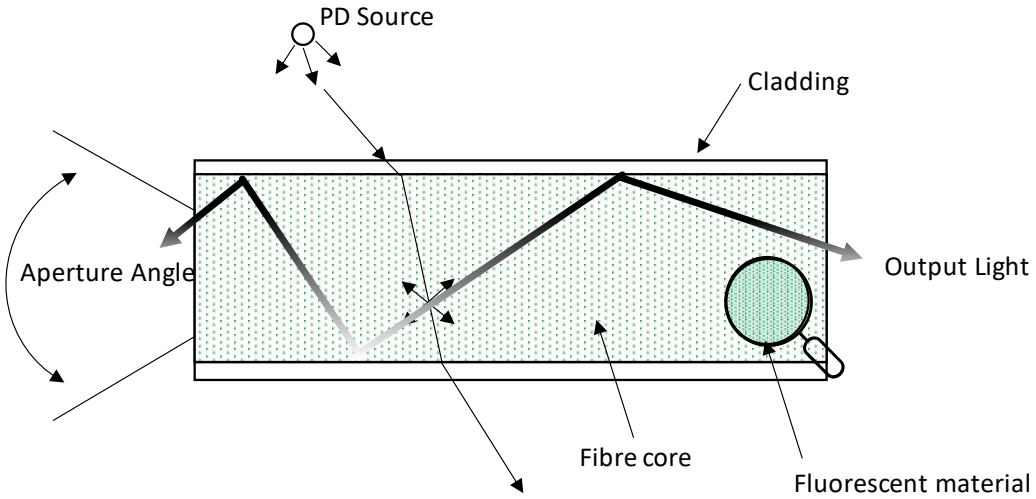

Figure 5.24: *Transition of PD light in Fluorescent fibre*

In contrast to optical communication fibre, fluorescence optical fibre lacks a numerical aperture angle. As a result, fluorescent optical fibre is more ideal for capturing PD light. Moreover, there is no use of a lens required to collect the PD light from the source to the fibre core, as in the case done for spectrum measurement.

It should be noted that during the process of stimulating and radiating the fluorescent optical fibre, the energy and wavelength of the incident light and exiting light differ; this is known as the Stokes shift. It means that there will be a 100-200 nm difference in the wavelength of the incident light and exiting light, with the wavelength of exiting light always being longer than that of incident light. This was first noticed by George Gabriel Stokes and hence the name. The origin of the Stokes shift is commonly represented in a Perrin-Jablonski diagram as an initial excitation to a higher vibrational level of the S_1 followed by a rapid non-radiative decay to the S_1's vibrational ground state (Figure 5.25), implying that the fluorescence will have less energy than the absorbed photon and thus a longer wavelength [92].

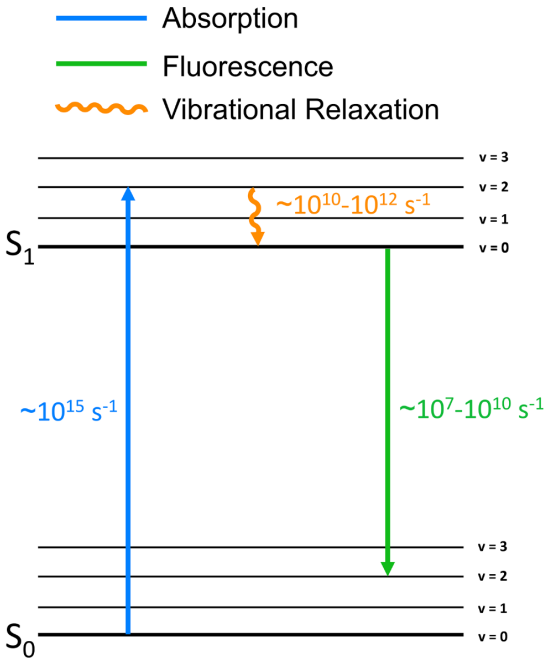

Figure 5.25: *Perrin-Jablonski shows the vibrational relaxation origin of the Stokes Shift [92].*

The fluorescent optical fibre is made of polymethyl methacrylate (PMMA), and the signal captured is photonic radiation and is entirely impervious to electromagnetic and acoustic noises. Another advantage of employing fluorescent optical fibre is that it is simple and widely applicable. When using fluorescent fibre for a PD measurement, the following also has to be considered:

- Fibre should have an excellent dielectric strength
- It should be corrosion resistant
- It should be flexible

5.4.2 Efficiency

In contrast to optical communication fibre, when a fluorescence signal transmits over a fluorescent optical fibre, there is a significant attenuation; the power generated by the attenuation may be calculated using an equation [83]:

$$A(\lambda) = \alpha(\lambda) \times L = -10 \log\left(\frac{P_o}{P_i}\right) \quad \textit{Eq. 5.9}$$

Where, $\alpha(\lambda)$: the attenuation coefficient; L: the length of the fibre; P_i: the input power; P_o: the output power. Transmission efficiency may be characterized as:

$$\eta = \frac{P_o}{P_i} \quad \textit{Eq. 5.10}$$

When $\alpha(\lambda) = 0.3dB/m$, the relationship between fluorescent fibre's length and transmission efficiency is depicted in figure 5.26 [83].

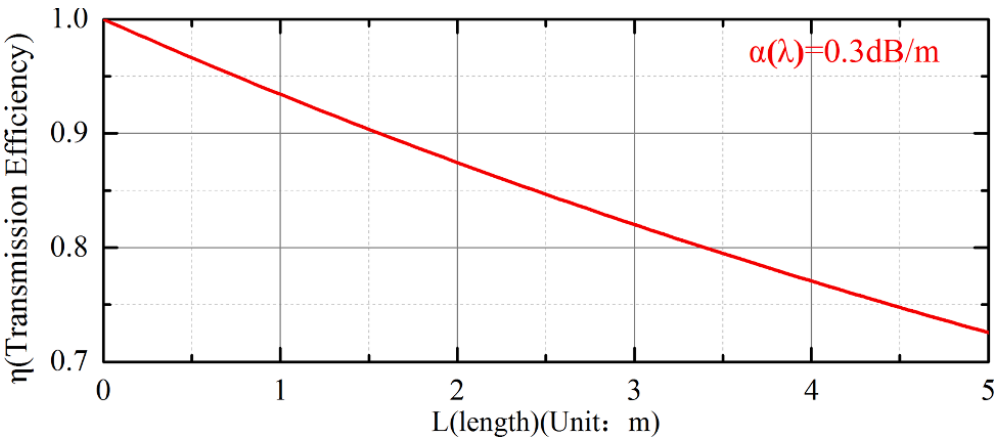

Figure 5.26: *Relationship between fluorescent fibre's length and transmission efficiency*

When the length is 5 m, the transmission efficiency is only approximately 0.73, indicating that we cannot use too much fluorescent optical fibre to enable PD detection. Specifically, if we want a transmission efficiency greater than 0.8, we must keep the length of the fluorescent optical fibre less than 3m. Hence, in this experiment, we have used a length of 2.5m that could give a transmission efficiency of 0.85.

5.4.3 Absorption and Emission Spectrum

Each fluorescent fibre has its absorption and emission spectra. Hence, for high efficiency of detecting PD, the following has to be considered:

- The absorption spectrum of the fluorescent fibre is to be in the emission spectrum of PD
- The emission spectrum of the fluorescent fibre should be in the detectability range of the photodetector.

The fluorescent fibre for this study was obtained from the manufacturer Pollinaire Fiber Optics. The absorption and emission spectra of different fluorescent fibres are shown in Table 5.3.

Colour	Violet	Blue	Green	Yellow	Orange	Red
Absorption spectra (nm)	294-410	315-410	299-477	388-511	441-545	493-580
Emission spectra (nm)	406-453	407-455	471-511	484-537	533-581	567-655
Maximum at (nm)	424	427	493	520	542	625

Table 5.3: *Optical Characteristics of the fluorescent fibres*

The other optical characteristics of the fibre are as follows:

- The refraction index of the core: 1.592
- The refraction index of the cladding: 1.416
- Numerical aperture: 0.73
- Acceptance angle: 93°

The previous optical spectrometer study shows that the PD emission spectrum lies mainly in the UV region; hence, the fluorescent fibre absorption spectra are selected to be 299nm - 477nm. The emission spectra 471nm -511nm are in the detectability range of the APD utilised. This belongs to the green fluorescent fibre, and in this study, a 0.5mm thickness fibre was used.

The fluorescent fibre was terminated using an SMA fibre optic connector to connect with the APD.

5.4.4 Selection Of Photon Detection Device

In order to convert the photons excited during a PD activity to a measurable electrical quantity, we need a photon detection device. This section outlines several critical characteristics used to choose the optical sensor for the PD detection application in this thesis. The following selection criteria should be considered:

1. **The spectral range of the light source:** The light source generates light radiation of a specific wavelength. Here, the light source of the sensor is the fluorescent fibre. Knowing the wavelength of the emission spectrum of the fibre is thus essential.

2. **Quantum Efficiency (QE):** It is also known as photon detection efficiency. A detector cannot catch all the photons released by the light source and convert them to electron-hole pairs. Quantum efficiency is thus defined as the number of electrons created per incoming photon and is commonly given as a percentage [48]:

$$QE = \eta = \frac{Number\ of\ electrons\ produced}{Number\ of\ incident\ photons} \times 100\%$$

3. **Electrical bandwidth**: The bandwidth across which the optical sensor will perform electrical signal measurements. It has been mentioned how PD measurements occur at various frequency ranges based on the type of sensor employed in electrical detection, which goes from narrow to broad and then to ultra-high frequency range.

As a result, the optical sensor's bandwidth should range from DC to MHz or maybe even higher, depending on the nature of the PD.

4. **Gain**: The majority of optical sensors output in terms of current. The observed light is of low intensity and must be amplified before reaching the measuring instrument. It is computed differently for each optical sensor [48]. It is commonly stated as a ratio of the sensor's output current to its input current. This also reflects the sensor's sensitivity, defined as the output signal's ratio to the measured characteristic. A high sensitivity sensor is to be used.
5. **Signal to Noise Ratio (SNR):** When utilized for PD measurements, the SNR ratio is the most crucial characteristic of an optical sensor. Noise is a significant PD detection disruption and is often reduced or avoided. This is produced due to the dark current produced by photo-cathode thermionic emission and the shot noise produced by the signal current.

Apart from this, cross talk, after pulse, and jitter are some parameters to be considered.

5.4.5 Sensor Types

The preceding sections explained the considerations when selecting an optical sensor for this PD detection application. Good spectral range, electrical measurement bandwidth, high quantum efficiency, good SNR, and no optical noise such as crosstalk, after pulse, and jitter are all required. There are several sensors on the market, and the three sensors mentioned here are the most appropriate based on previous and current research. Table 5.4 summarises the three sensors: PMT, SiPM and APD. The working details are well explained in the thesis [48].

Photomultiplier Tube (PMT)	Silicon Photomultiplier (SiPM)	Avalanche Photodiode (APD)
• Not immune to magnetic interference	• Immune against magnetic interface	• Highly immune to magnetic interference
• Output BW: DC to 60MHz	• Output BW: DC to MHz	• Output BW: DC to GHz
• Large size	• Small size	• Small size
• Moderate spectrum range	• Moderate spectrum range	• Large spectrum range
• Lower quantum efficiency	• Moderate quantum efficiency	• High quantum efficiency than PMT
• Highly sensitive	• Low sensitive than PMT	• Low sensitivity than PMT
• Prone to damage by ambient light exposure	• No damage by ambient light exposure	• No damage by ambient light exposure

Table 5.4: *Comparison of PMT, SiPM and APD*

Due to the High immunity to magnetic interference, high output BW, extensive spectrum range, high quantum efficiency, and no damage by ambient light exposure, the detector APD can be chosen.

5.4.6 APD130A2 – Specification and Characteristics

The ThorLabs APD sensor, APD130A2/M Si Avalanche Photodetector, as shown in Figure 5.27, was used for measurements in this thesis.

The temperature-adjusted avalanche photodetector APD130A2/M sensor combines a high sensitivity Si avalanche photodiode with a specifically developed ultra-low noise amplifier for detecting optical signals ranging from DC to 50 MHz. This sensor's very low noise is accomplished using an active low pass filter that effectively suppresses out-of-band noise.

The APD130A2 has an extremely low noise equivalent power, making it perfect for many quick low-level light detection applications. APD may readily replace PMT in many applications due to its high sensitivity. APD is unaffected by undesired ambient light, which is crucial for many PMT and SiPM sensors.

Figure 5.117: *APD sensor from Thorlabs used for the experiment*

APDs operate with a substantially greater reverse bias than standard PIN diodes. The amplification is determined by the reverse bias voltage, also known as the M (multiplication) factor. The multiplication factor is temperature dependent due to an intrinsic mechanism. As a result, with a constant bias voltage, the multiplication factor varies with temperature. The multiplication factor value decreases as temperature rises, but the multiplication factor value rises as temperature falls. This sensor, on the other hand, is temperature adjusted.

It comprises a thermistor within the sensor's housing that monitors temperature and adjusts the applied APD reverse bias voltage in response to temperature change using a unique electronic circuit. Because the multiplication factor depends on the applied reverse voltage, the temperature dependency of the factor may be greatly lowered with a thermistor.

The technical specifications of the used APD130A2 sensor are shown in Table 5.5. The light input beam should be aligned with the detector for accurate diagnosis. In the case of fluorescent fibres, we can utilise fibre adapters with SMA female part to which the fluorescent fibre terminated with SMA male connector can be connected. The output voltage (V_{out}) of

APD130A2 is a function of incident light power (P_{opt}), detector responsivity (R_M) at a specific wavelength and (Multiplication/amplification) factor M, and trans-impedance gain (G) given by the equation:

$$V_{out} = P_{opt} \cdot R_M(\lambda) \cdot G \qquad \textit{Eq. 5.11}$$

Parameters	Values
Detector	UV enhanced Silicon APD
Optical BW	200nm – 1000nm
Active area	1mm in diameter
Electrical BW	DC – 50MHz
Max. APD responsivity	25 A/W at 600 nm, M=50
Max. conversion gain	2.5× 10^6 V/W
Max. voltage output	3.6 V (High impedance load) 1.8 V (50Ω)
Electrical power requirements	±12V, 200mA
Weight	<0.1kg

Table 5.5: *Specification of Thorlabs APD 130A2/M*

The M factor for this APD is factory set to 50 at 23°C ambient temperature and cannot be tuned manually. Figure 5.28 presents the spectral distribution of the PD, optical BW of the APD sensor, and absorption and emission spectra of the fluorescent fibre.

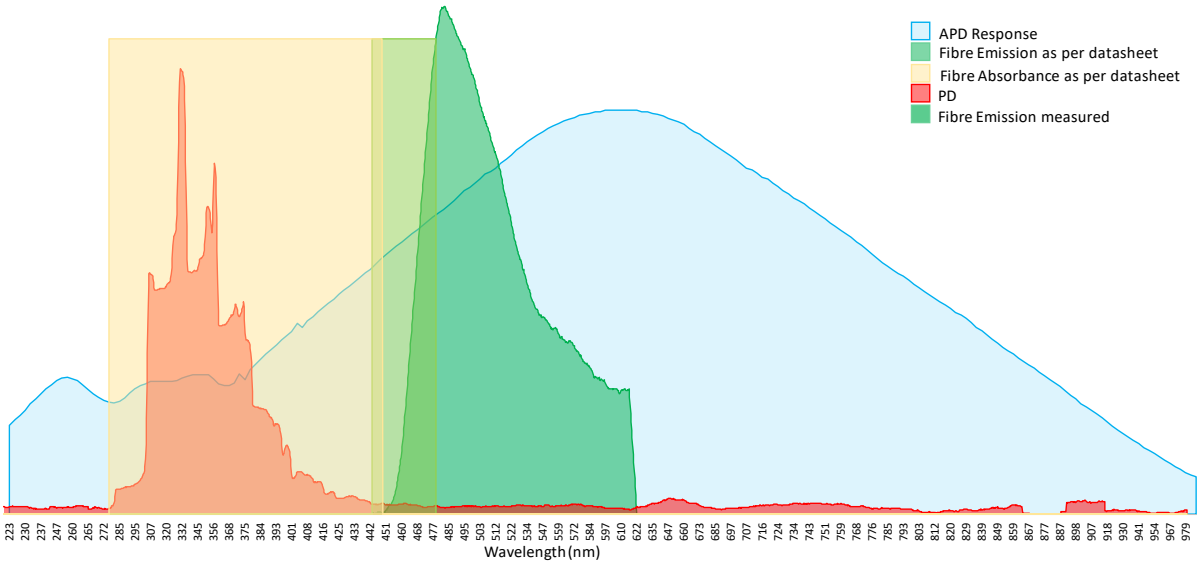

Figure 5.128: *Spectral Distribution of the components used*

5.4.7 Test Setup

The test setup used is similar to the spectrum measurement of PD except for the optical part, as shown in 5.29. The fluorescent fibre is wound along the inner side of the plexiglass. This

allows more PD photons to be collected. The fluorescent fibre is connected to the APD sensor via an SMA connector, and the electrical output is connected via a bandpass amplifier to the picoscope using a coaxial cable. The amplifier had a gain of 22.7dB, and lower and upper cutoff frequency of 30kHz and 1.23GHz, respectively. This eliminated the noise that couples with the electrical circuitry of the APD sensor and also amplified the electrical output. Both the HFCT and APD sensor signals were collected as in the previous setup and post-processed in PDFlex.

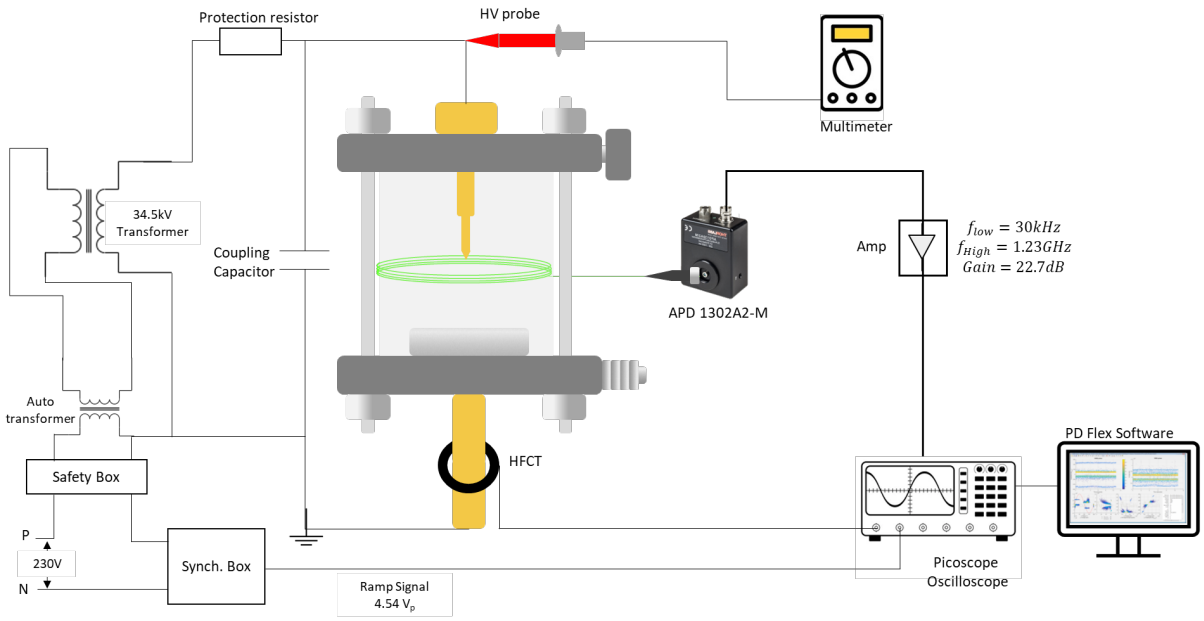

Figure 5.139: Test Setup for combined electrical and optical PD measurement

5.5 Results Of PD Optical Detection Using Fluorescent Fibres

This section comprises the results obtained from optical detection of PD measurement in both air and C_4F_7N/CO_2 alternative gas mixture.

5.5.1 Typical HFCT And Optical PD Pulse Output

The primary attribute obtained when detecting partial discharges is the PD pulse. This is the first thing we notice when measuring PD before proceeding with further analysis. Hence, preliminary tests were done to ensure the setup worked as expected. A corona set up in the air was utilised for the same. Figure 5.30 shows the signals captured simultaneously from both HFCT and fluorescent fibre-connected APD sensor for positive corona at $7kV_{RMS}$. This setup did not utilise an amplifier. From the figure, it is also evident that there will be no shift in the phase from the APD sensor as in HFCT due to the fact that the APD sensor captures the intensity of the photons falling on the sensor, and light does not have polarity. With the increase in PD charge, the number of photons increases; hence, the APD outputs higher voltages relative to the intensity of the light. The PD pulse recorded by the APD optical sensor only indicates the presence of light due to PD but does not help to categorize the kind of PD; hence post-processing is required.

A certain amount of such pulses from both APD and HFCT simultaneously are captured by setting the trigger on the HFCT signal. In the following experiments, at least 2500 samples of such HFCT and APD signals are captured and saved for plotting PRPD and other post analyses. Post-processing is mainly done by the software PDFlex mentioned in section 5.2.6.

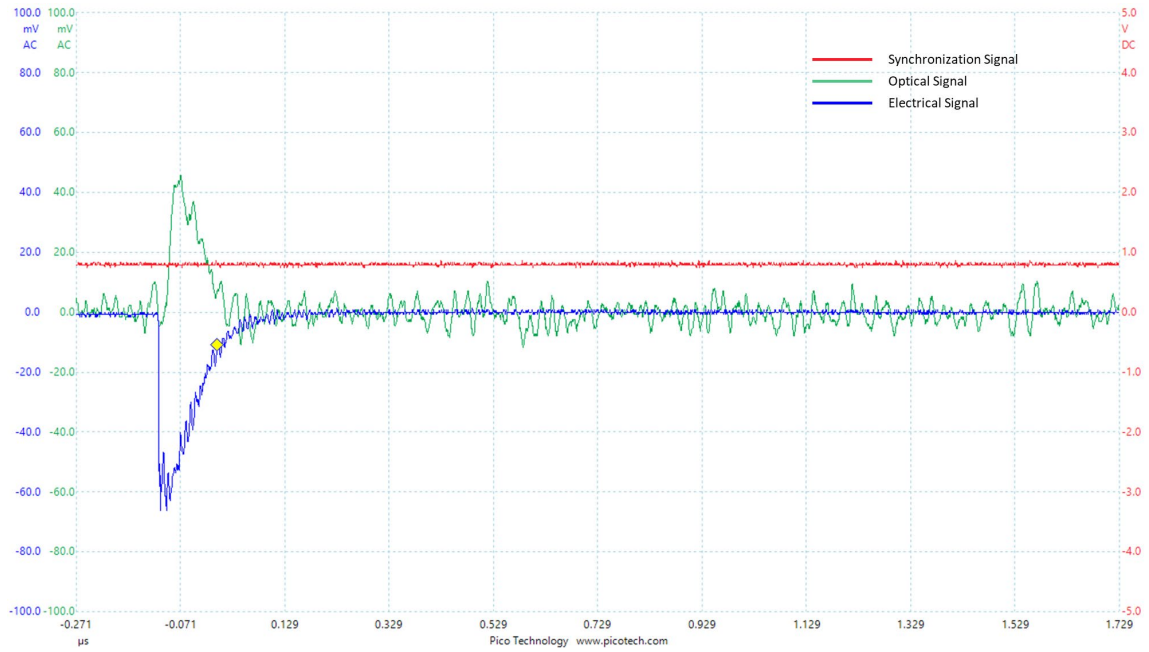

Figure 5.14: Electrical and the optical signal obtained for positive corona in air

5.5.2 Electromagnetic Immunity

The key argument for utilising optical PD detection of HV equipment is the optical sensor's high interference immunity. Unlike PMT optical sensors, the solid-state silicon-based APD units in the APD sensor employed in this study are insensitive to magnetic fields, resulting in a low level of device noise in the actual PD detection, especially in strong electromagnetic noise environments. Moreover, fluorescent fibres do not couple with any interference because the operating domains (fibre – optical, noise – EM) are different. Figure 5.31 compares signals collected from the HFCT and APD sensors simultaneously under high noise conditions. This noisy condition was caused by the breakdown experiments that were taking place in another area of the lab. Even though the breakdown experiments were taking place far away from PD measurement, the electrical sensor in the PD detection circuit was influenced. However, no similar effect was observed in the signals received from the APD sensor. Remember that coaxial cables are also used in the setup, and a high-quality coaxial cable free from defects is required to resist electromagnetic interference in PD detection.

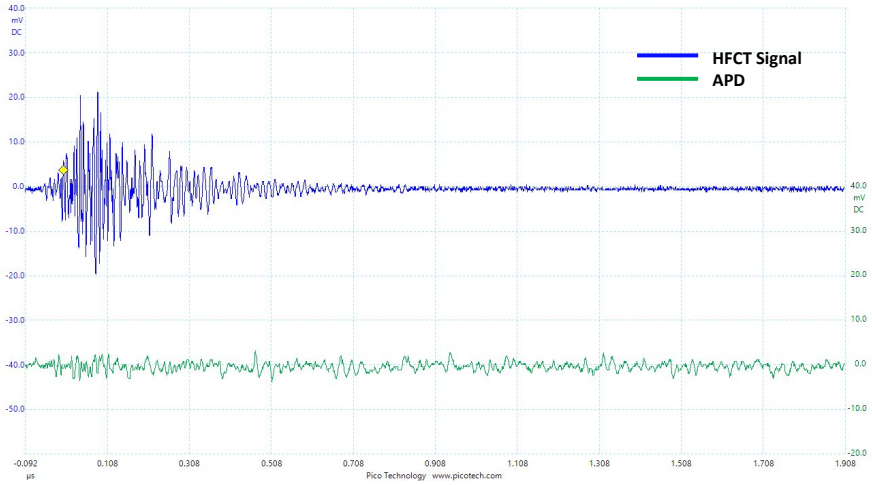

Figure 5.31: Noise Captured by HFCT and APD signal in EM noise enviroment

5.5.3 PRPD Patterns

The PD activities vary in time lag and amplitude periodically when an AC voltage is applied, which is why the phase resolved partial discharge (PRPD) pattern is recommended for PD diagnosis and defect-recognition in insulation systems under AC. In a PRPD pattern, the PD data from a specified number of applied voltage cycles is shown on the phase axis in one voltage cycle. This subsection summarises the insights from the PRPD pattern collected from the HFCT and fluorescent-connected APD sensor.

The negative corona was unable to be measured using the green fluorescent fibre. This could be because negative coronas are weak glows in the VIS or IR wavelength region, and due to their low intensity, no characteristic peaks were observed during optical spectrum measurements performed in section 5.3. This was the case for both C_4F_7N/CO_2 gas and the air. When an orange (absorption spectrum in the VIS region) optical fibre's termination with a thickness of 0.5mm was kept close to the corona PD source, as shown in figure 5.32, it could pick up the negative corona in the air. Negative corona was unable to detect when the fibre was wound. This could be due to transmission loss in the fibre as it was thinner and longer. The thinner the fibre, the less area to capture PD light, and if we use a longer length to compensate collection area, it will lead to transmission losses. From this, it was understood that a tradeoff between the length and thickness of the fibre is required to collect the PD light effectively. Table 5.9 shows some of the PRPD patterns obtained by electrical and optical measurements for corona and surface discharge.

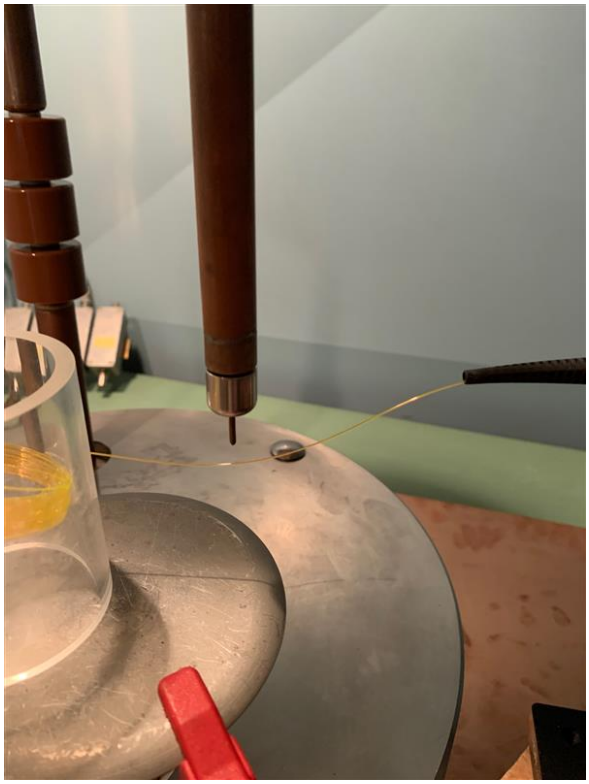

Figure 5.32: *Orange fibre used to measure negative corona*

PD	Electrical Measurement	Optical Measurement
Negative Corona (air)	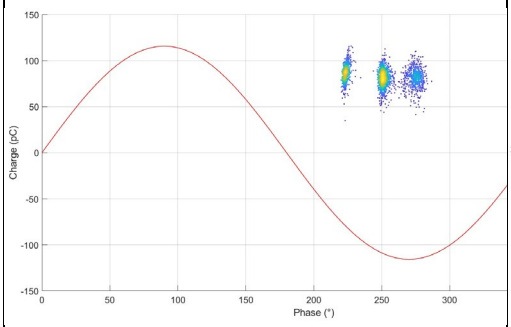	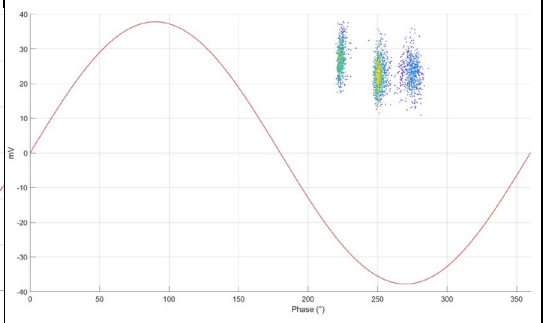
Positive corona (C_4F_7N/CO_2)	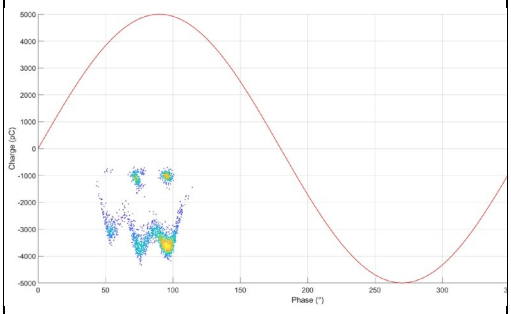	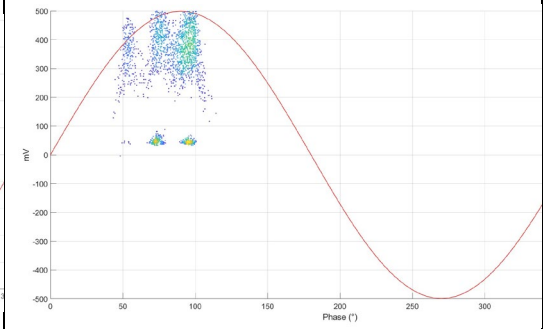
Surface Discharge (C_4F_7N/CO_2)	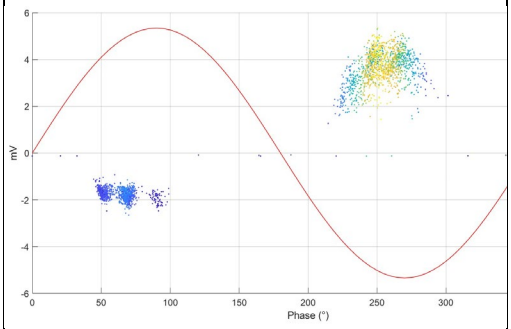	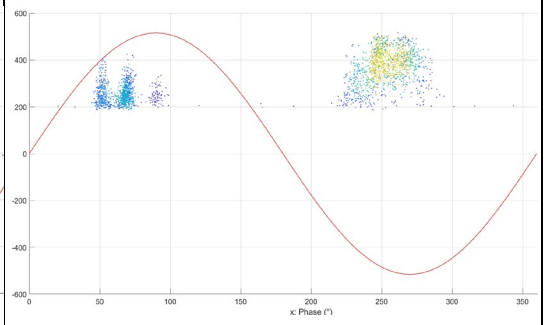

Table 5.3: *PRPD patterns obtained using Fluorescent fibres*

The PRPD pattern gives further information about the discharge's physical parameters and stochastic behaviour. The PRPD pattern can also be used to analyze stochastic light pulses [49]. By comparing the PRPD pattern in Table 5.9, it is clear that the findings of HFCT and fluorescent-connected APD tests are highly compatible in profile and distribution intensity. The shift in phase, orientation, and occurrence of the PD are similar for both the electrical and optical tests, with clear information on the type of discharge. As a result, the PRPD pattern obtained from the optical signal can provide a clear indicator of the type of discharge occurring in the setup.

5.5.4 Electrical & Optical Output Correlation

The foundation for developing a measurement system is a monotonic relationship between the signal response and the strength of a physical object [48]. The intensity of the light released by the partial discharge is proportional to the amount of PD charge and is determined

by the probabilistic cross-sections of excitation, ionization, recombination, and attachment during the entire discharge process [49]. The most popular electrical PD detection method yields results in the form of a charge or current pulse. The relationship between the intensity of the voltage (received from the APD sensor) and the severity of the PD is unknown in this setup. As a result, this section will concentrate on any potential relationship that may be established between the output of the HFCT and the APD sensor.

Figure 5.33 and 5.35 shows the plots in which the charge from the electrical sensor (HFCT) is plotted against the peak voltage of optical measurement for negative and positive corona discharges, respectively. Figure 5.34 and 5.36 shows the graph between the peak of the current pulse from HFCT against the peak voltage pulse from optical measurement.

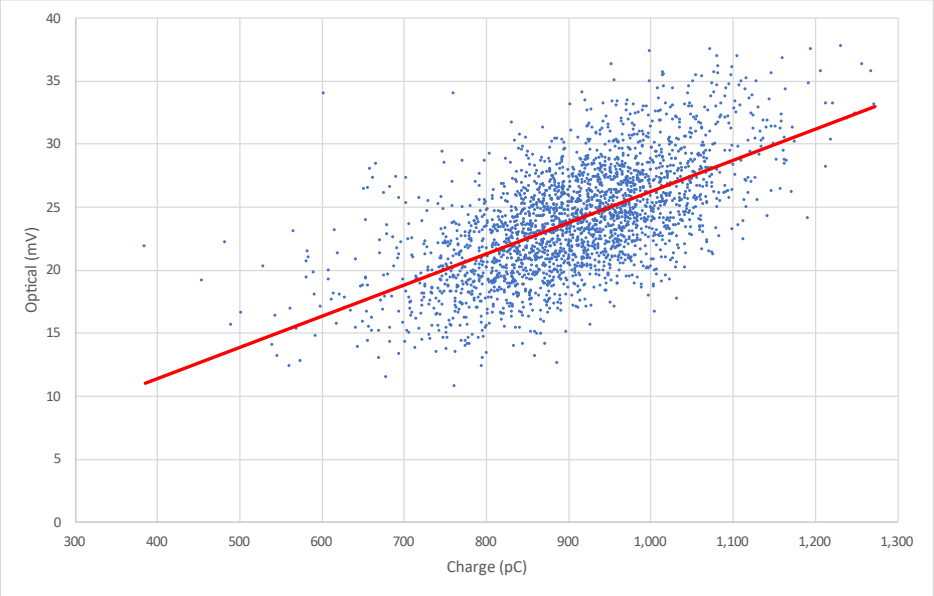

Figure 5.33: *Plot of Voltage pulse detected by fluorescent fibre connected APD sensor v/s Apparent charge PD magnitude captured by HFCT sensor for negative corona in air*

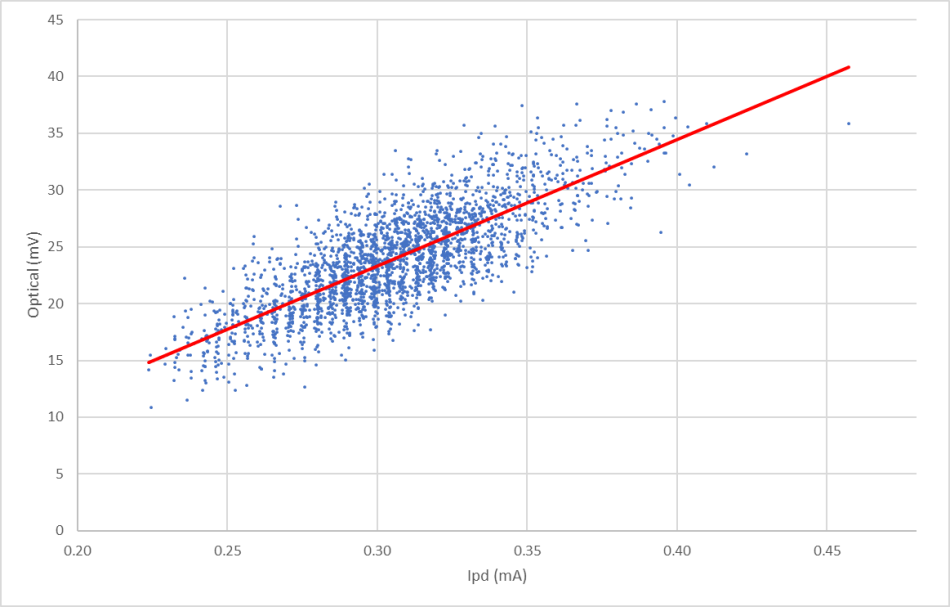

Figure 5.34*: Plot of Voltage pulse detected by fluorescent fibre connected APD sensor v/s +ve peak current pulse captured by HFCT sensor for negative corona in air*

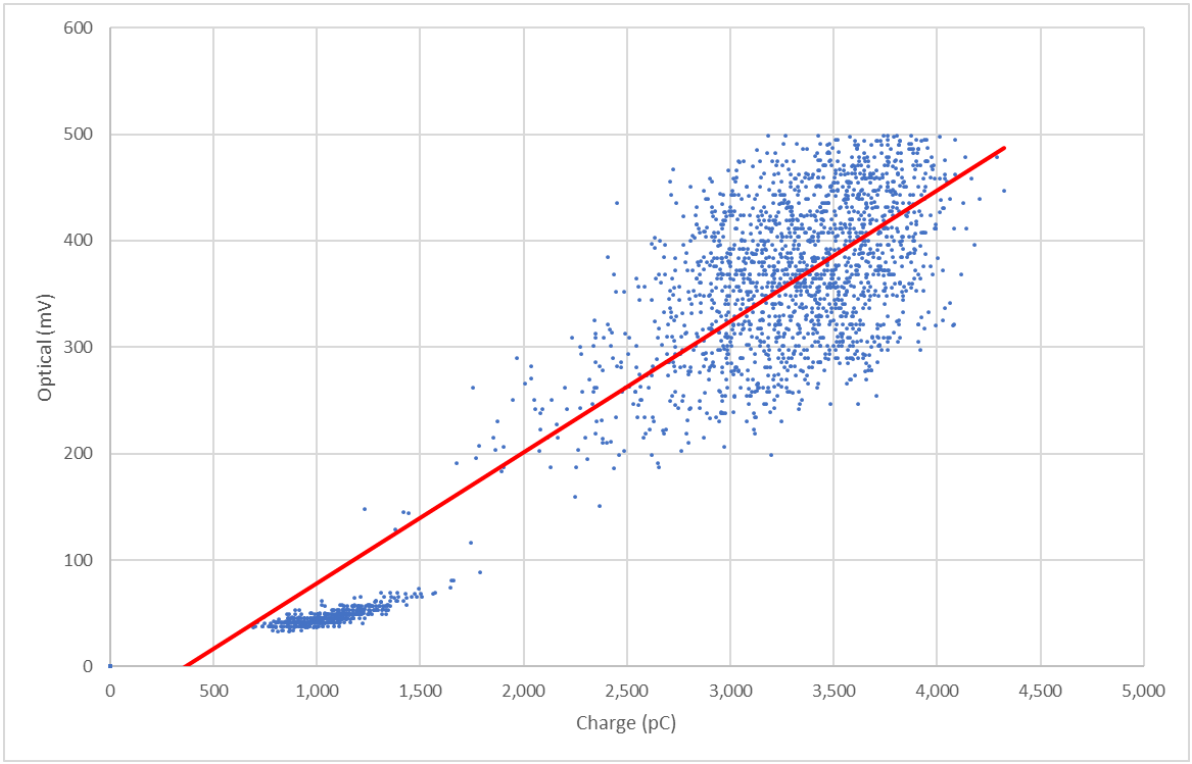

Figure 5.35: *Plot of Voltage pulse detected by fluorescent fibre connected APD sensor v/s Apparent charge PD magnitude captured by HFCT sensor for positive corona in C_4F_7N/CO_2*

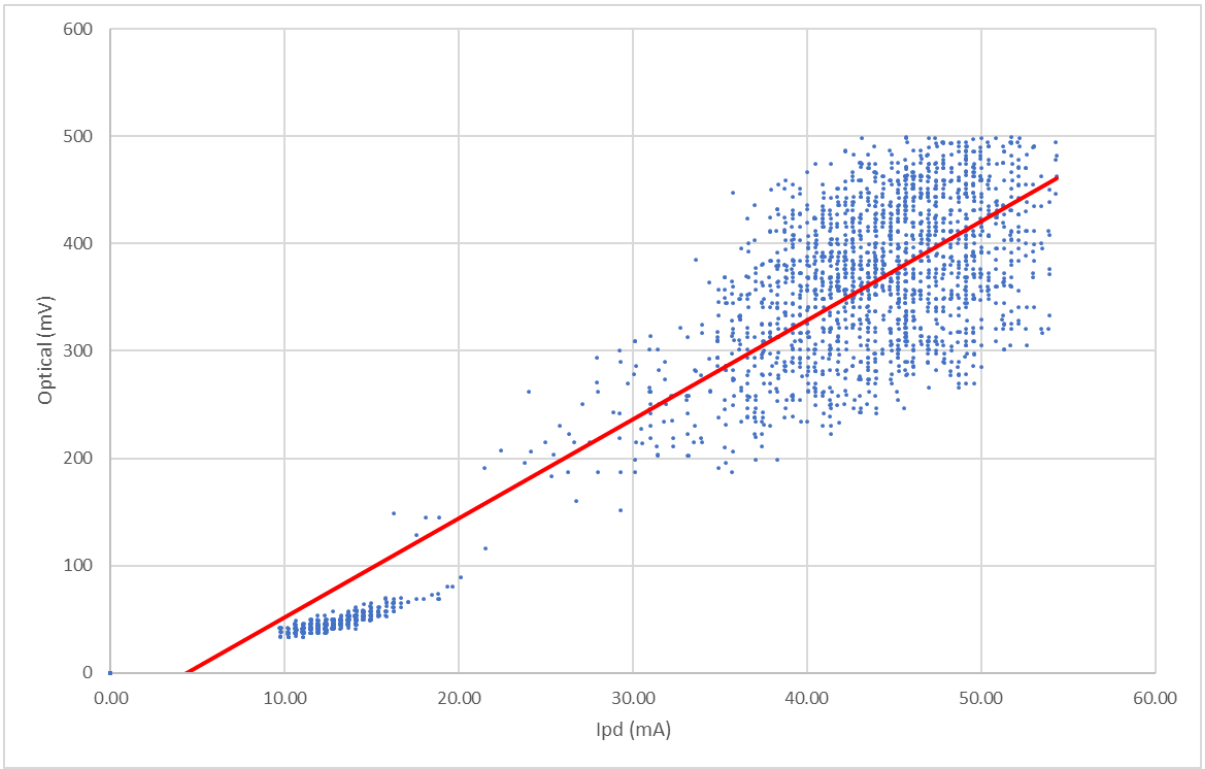

Figure 5.36: *Plot of Voltage pulse detected by fluorescent fibre connected APD sensor v/s -ve peak current pulse captured by HFCT sensor for positive corona in C_4F_7N/CO_2*

As we can see from the graphs that there is a linear growth of APD output voltage with an increase in PD current. If scattering and outliners are ignored, the relationship between light intensity (in terms of voltage pulse) and apparent PD magnitude can be approximated linear, as illustrated in equation 5.12. The equation holds for all data obtained concurrently from the optical and electrical sensors for different PD defects measured.

$$Light\ Intensity\ (mV) = A \cdot PD\ magnitude\ (mA\ or\ pC) + B \qquad Eq.\ 5.12$$

Where A is the slope and B is the constant of the linear fit line.

The relationship between optical and electrical can also be correlated using the correlation factor as follows:

$$CC = \frac{\sum x_i \cdot y_i - \sum x_i \cdot \sum \frac{y_i}{n}}{\sqrt{\sum x_i^2 - \frac{(\sum x_i)^2}{n} \cdot \sum y_i^2 - \frac{(\sum y_i)^2}{n}}} \qquad Eq.\ 5.13$$

Where x is the charge or peak current obtained from HFCT and y is the peak voltage obtained from the APD sensor. The correlation coefficient indicates how closely related the two values are. If the CC is greater than 0.8, the correlation is strong; if it is less than 0.8, the correlation is average; and if it is less than 0.5, the correlation is weak [48]. Table 5.6 gives the correlation factor of corona and surface discharges.

PD Type	Correlation Coefficient			
	Positive Cycle		Negative Cycle	
	Charge (HFCT) v/s V_{peak} (APD)	I_{peak} (HFCT) v/s V_{peak} (APD)	Charge v/s V_{peak}	I_{peak} v/s V_{peak}
Corona in air	0.9	0.8	0.62	0.78
Corona in C_4F_7N/CO_2	0.94	0.94	N/A	N/A
Surface discharge in C_4F_7N/CO_2	0.72	0.99	0.80	0.97

Table 5.6: *Correlation Coefficient of different discharges*

5.5.5 Bottlenecks

The relation between PD charge and light intensity is known as of now. However, some bottlenecks were understood throughout the experimental stages:

- Inverse Square law of light:
  The inverse square law defines light intensity at various distances from a light source. Each light source is unique, but the intensity varies similarly. Light intensity is inversely proportional to the square of the distance. This applies to all wavelengths of light.

While utilising fluorescent fibres for PD detection, it is essential to consider this to capture the weak light.

- The transmission loss of fluorescent fibre:
  Transmission loss occurs in fluorescent fibre with an increase in length. To eliminate this to a great extent, we can use thicker fibre with a short distance to obtain more PD coverage area.

5.6 Summary

Optical spectrum measurement of PD and applying its results to PD detection using fluorescent fibre was the goal of this chapter. The optical spectrum of PD in a gaseous medium varied with defects and the gas itself. However, it was found that most of the optical PD characteristics of both air and alternative gas C_4F_7N/CO_2 lie in the UV and VIS regions. With this result, the required fluorescent fibre was selected and successfully utilised for PD detection using an APD sensor. All the results were compared to electrical measurements using the HFCT sensor. The PD pulse obtained from the optical sensor does not reveal the type of discharge but merely the magnitude of light intensity. The PRPD pattern comparison revealed that the optical sensor is highly comparable to the electrical sensor in terms of phase and orientation of PD occurrence. The correlation plot demonstrated significant dispersion but also the linear behaviour of optical sensor output compared to the electrical sensor output. A similar analysis was undertaken in other literature, demonstrating a disparity in correlation graphs for different defects. The strong immunity against interference was also tested under harsh conditions, where the APD sensor outperforms the HFCT sensor in terms of noise. These analyses set the groundwork for using fluorescent fibres connected to APD sensors for PD detection.

6. Alternative Gases For Network Components Testing

This chapter comprises of author's work at the R&D Department of Prysmian Group Delft. First, an introduction to HV cable network components and the study strategy is explained. In the initial study of all the cable network components developed by the Prysmian Group, the components that undergo testing in SF_6 and the different tests and the test setup are studied in detail. Then non-homogeneity factor or Schweiger factor is introduced along with electrical field calculations of all the network components. Based on the study, verification test results of synthetic air used for testing two important network components are presented. Finally, test results of air from 2 compressors are studied for reference. Please note that all the voltages are stated in RMS.

Please note that due to Prysmian's confidentiality policies, specific details and component figures are obscured or modified.

6.1 Network Components – Introduction, Research Questions & Research Strategy

Before sliding to the research questions, it is essential to know the different HV network components used in the grid.

6.1.1 Introduction to Prysmian's HV Cable Network Components

Cable components are the bridging blocks that connect two separate equipment or places. The reliability and performance of a cable circuit are heavily influenced by the design of the cable and network components, as well as the expertise and experience of the person assembling the component. Moreover, Choosing an accessory design that is perfectly appropriate to the specific cable type and service application is critical. Hence, these components are given primary importance in electricity transmission and distribution.

High Voltage accessories based on prefabricated mouldings are a very reliable solution that is regarded as a critical asset in the safe functioning of a High Voltage cable system. The Click-Fit® concept is a one-of-a-kind "plug-system" developed by Prysmian for connecting (E)HV extruded cables ranging from 72 kV to 550 kV. Prysmian provides a wide range of network components in this portfolio. The important ones used in this study are as follows:

1. **Cable Joint:**
   A cable joint is the fully insulated and protected joining between two extruded high voltage cables. It is a rubber joint insulator. Figure 6.1 represents Prysmian's Cable joint. The following are the basic requirements of a joint:
   - It meets the exact performance requirements as the cable.
   - A high current connection that allows short-circuit current to flow between the two cable sheaths or screen wires.
   - Water ingress prevention for the joint and cable insulation

- Corrosion prevention for the joint metal work.

Figure 6.1: *Joint Insultor from Prysmian*

2. Transition Joint:

The transition joint joins two cables of various sorts, such as a polymeric extruded cable and an oil-filled self-contained cable. Sometimes transition joints are used to link cables of the same kind but of differing conductor sizes. They are intended to sustain unbalanced conductor thermomechanical force in the latter application. The most commonly used transition joints are:

- 'Polymeric extruded cable to mass impregnated cable' Transition Joint
- 'Polymeric extruded cable to oil-filled paper cable' Transition Joint
- 'Polymeric extruded cable to gas pressured paper cable' Transition Joint

Figure 6.2 shows a cut section of Prysmian's XLPE to oil-filled paper cable Transition Joint.

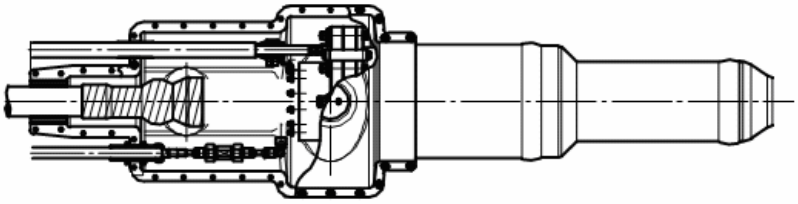

Figure 6.2: *Transition Joint from Prysmian*

3. Y-Joint:

The primary function of the Y-joint is to link three cables properly. These are mainly used to connect wind turbines. Figure 6.3 presents Y-joint from Prysmian [93].

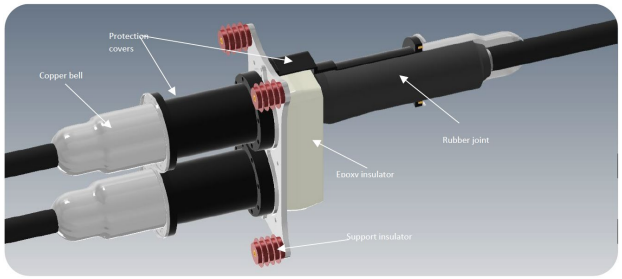

Figure 6.3: Prysmians Y-joint

4. GIS-Cable Termination

This cable termination connects to a busbar within a GIS. The bus bar is typically connected to the switchgear. A GIS cable termination model from Prysmian is as shown in figure 6.4. The following are the essential characteristics of a cable termination:

- A high-current connection is made between the cable conductor and an external busbar.
- Insulation that meets the exact performance requirements of the cable.
- Provision of cable support.
- Resistance to cable thermomechanical loads and external forces such as busbar loading.
- A high current connection that allows short circuit current to pass from the cable metallic sheath or shield wires to the system ground through a bonding lead.
- An electrically insulated connection to the cable metallic sheath or earth wires that matches the insulating quality of the cable oversheath.
- Protection for the cable insulation and sheath against atmospheric water intrusion as well as pressured dielectric gas incursion from neighbouring metal-clad busbar trunking.

Figure 6.4: GIS-cable termination

5. Stress Cone

A stress cone is a shaped insulating component having an electric stress control profile. It is used to regulate stress at the end of a low voltage insulating screen or a high voltage electrode. It is often made of moulded or machined polymer, elastomer, or

thermoset resin. This is also termed a ‘deflector cone’. It is typically used in oil-filled cable termination, as shown in figure 6.5.

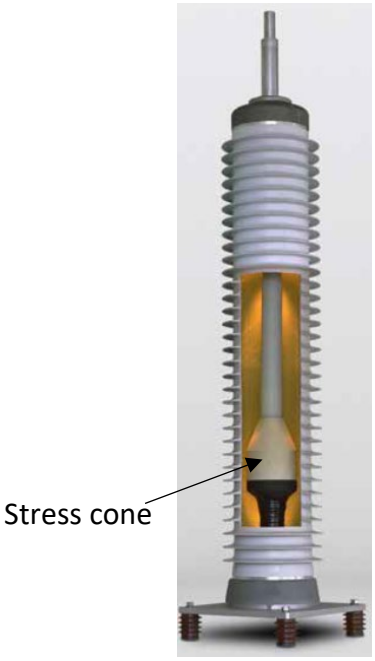

Figure 6.5: *Oil filled termination*

6.1.2 Research Questions

With XLPE technology, the dependability of cables has increased dramatically, particularly among manufacturers with strong quality control. As a result, it appears that a considerable majority of cable failures in recent years have been caused by issues with network components rather than the cables themselves. During type testing, accessories are destructively tested according to established standards using samples picked randomly from the manufacturing line to guarantee that the results represent an evaluation of a 'typical' product. They also aid in confirming that both the design and production processes are satisfactory.

Apart from this, each cable accessory undergoes routine testing or acceptance testing to verify that each piece of equipment is manufactured well and has no defects. Furthermore, because cable accessories are susceptible to installation mistakes or other difficulties in the field, the entire cable system is subjected to on-site commissioning testing, which becomes especially necessary at higher voltage levels.

From a manufacturer’s point of view, every test is of utmost importance, primarily type testing and routine testing, to ensure that the product meets the customers' expectations. Being the world leader in manufacturing (E)HV cables and network components, Prysmian ensures that all components that leave the factory are ready for the site through regressive testing.

However, most of these cable network components tested in Prysmian utilise SF_6 as an insulation medium. In the framework of sustainability policies, the organisation aims to eliminate the usage of SF_6 gas from their HV testing laboratories. Hence, it was the authors' task to deliver an alternative SF_6 solution within the scope of testing at Prysmian's HV lab in

Delft. The use of an alternative insulating medium was to be examined for the range of (E)HV products tested at Prysmian Delft and the range of voltage levels utilised for testing.

6.1.3 Study Strategy

A study strategy was proposed to answer the research topic, as presented in figure 6.6.

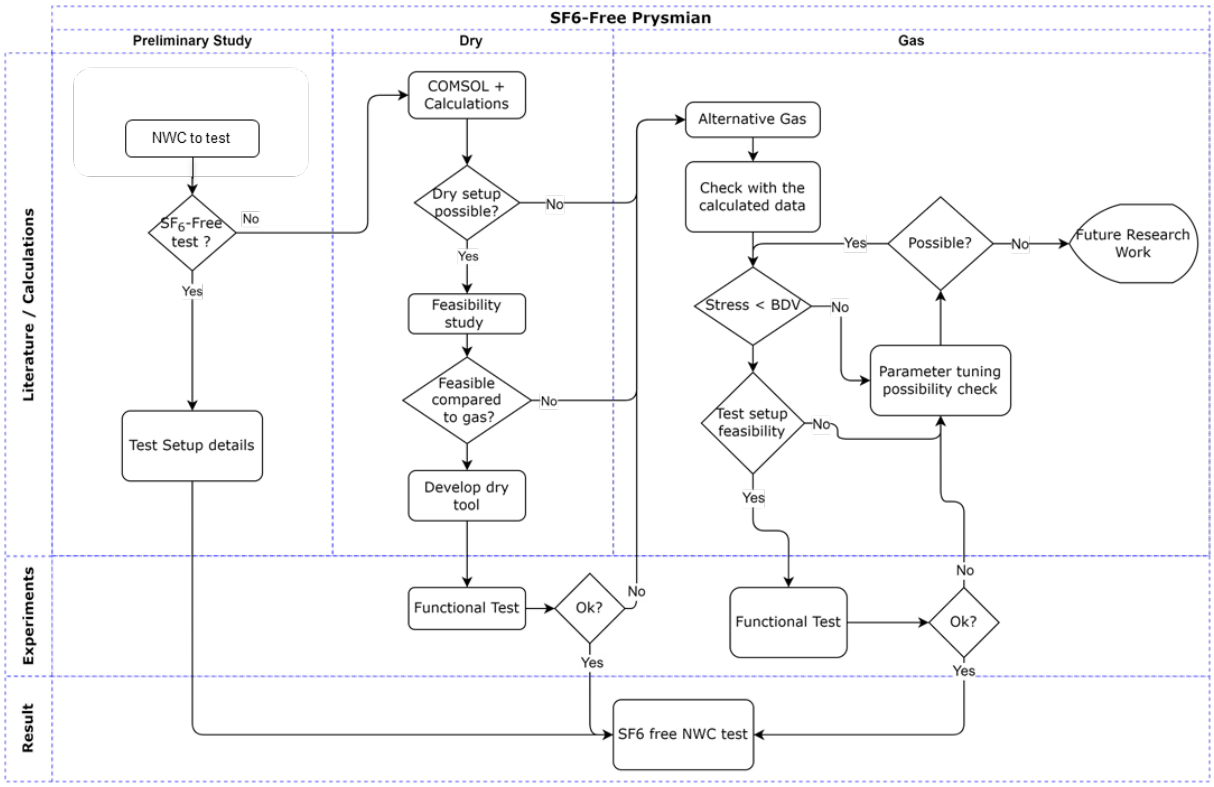

Figure 6.6: Study Strategy for SF_6 free Network Component Testing

The study was divided into three different units. Literature study and calculation were used to understand the different network components used, their testing setups, test voltages, and the possibility of a dry-type test setup. The experimental unit covers the preliminary test based on the calculations and simulations. Finally, the results of test results and test conditions are published.

The preceding sections will cover each step in detail.

6.2 Preliminary Study

The different network components were studied in detail in the preliminary study, along with the current test setups and testing voltages. Moreover, the fast-moving and demanding network components were considered and prioritised. This gave a clear understanding of which component more effort should be put on.

6.2.1 Network Component Types, Voltage Class, Test Voltages & SF_6 Free Check

Listed in table 6.1 are the different network component types, their voltage class, and test voltages produced by Prysmian Delft.

Type	Voltage Class	Routine Test			TT/PQ Test	SF_6 Free?
		AC Test 30 min.	PD Test	AC 1 min.	LI	
Joint Insulator	72	100	80			No
	123	220	174			No
	145	130	90			No
	170	130	90			No
	300	318	220			No
	420	460	330			No
	550	580	435			No
Termination Joint	72	100	80			Yes
	100	130	90			Yes
	170	130	90			Yes
	300	317	220			Yes
	420	580	435			Yes
	500					Yes
Y-Joint	72	100	80			No
Stress cone	72	100	80			Yes
	145	190	152			Yes
	170	220	174			Yes
	300	318	220			Yes
	420	460	330			Yes
	550	580	435			Yes
GIS-Cable termination	72/100	140	140	185		Yes
	170	220	325	350		Yes
	245	318	220	380		Yes
	420	580	435			Yes
	500					Yes
Single phase Transition joint Insulator	170	220	325	350		Yes
Dry-type termination	170	220	174			No
Three-phase Transition Joint Insulator	72	100	80			Yes
	170	240	174			Yes

Table 6.1: *List of Network Components, Its Voltage Class and Test Voltages*

Termination joint is a Click-Fit® solution that couples the terminations such as dry type termination and GIS-Cable termination to the cable end.

On analysing the different components, it can be seen that most components have a wide range of voltage classes and thereby different test voltages, leading to different electrical test stresses. The different types of tests to which the component is subjected and the test voltages are as per the standards. Apart from the routine testing, the component faces more stress than operating stresses during type tests or prequalification tests such as lightning Impulse. Moreover, in some cases, the components are subjected to voltage stresses requested by the clients. At Prysmian, type testing and routine testing happen in two different HV laboratories.

It is evident that five out of eight component types undergo testing in SF_6, which has to be eliminated using an alternative medium. The use of SF_6 for testing mainly arises from the test setup each type of component uses.

A Joint Insulator, which is used to connect two cables of a similar type, can be tested by connecting the HV cables on both ends as it will be on the project site. This is the same case with Y-joint and dry-type termination. Hence, these components are tested purely dry that do not require any other medium for insulation. An example of testing the dry termination is shown in depicted in figure 6.7. In the case of termination, the cable side can be connected with the in-house click fit connector and apply test voltage to the termination.

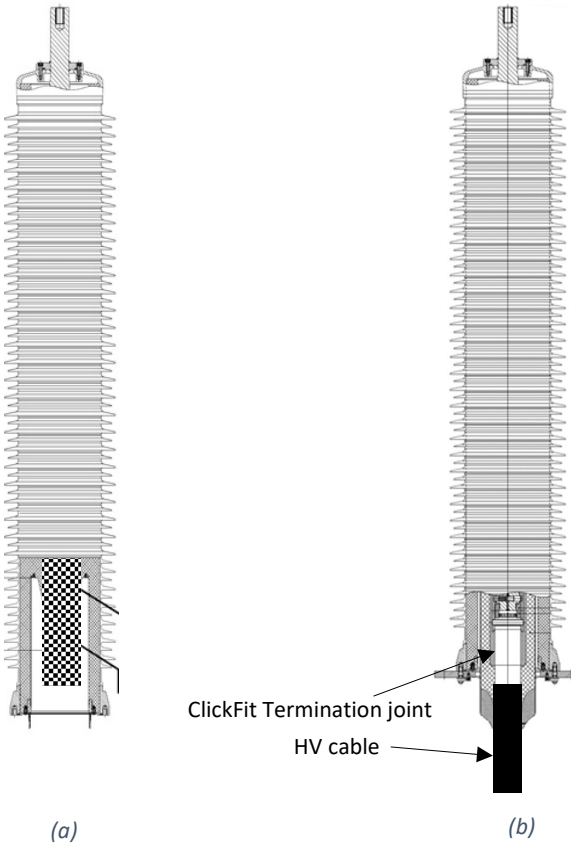

Figure 6.7: *(a) Dry type termination (b) Setup to apply HV*

To understand why SF_6 is used in the rest of the five components, we have to analyse the test setups used.

6.2.2 Test Setups

A prospective test arrangement is necessary to ensure that the network component is free of flaws and that the test voltage is administered correctly. The five components that use SF_6 one way or the other for testing and their current test setups are as follows:

- **GIS-Cable termination And Termination Joint**
  Figure 6.8 shows the test setup for the GIS-Cable Termination And Termination Joint. The test voltage is applied to the network component under test via an HV cable. As per the prevailing test setup, In order to test the termination joint, we require a GIS-cable termination and vice-versa. Here, the GIS end of the GIS-cable termination, which on-site will be connected to the switchgear busbar, is at high potential. A corona shield is placed to reduce the field strength and avoid corona at the conductor end of GIS. The whole GIS end is inserted inside a chamber filled with SF_6 at a certain pressure to eliminate flashover.

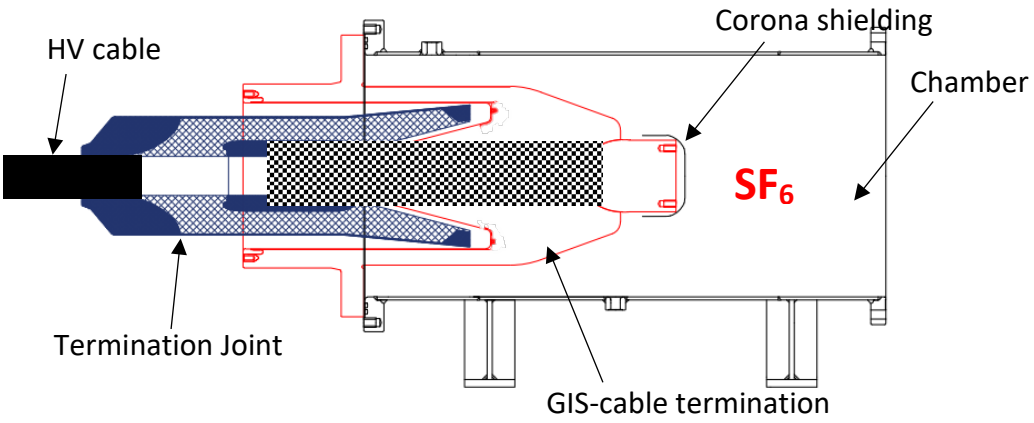

Figure 6.8: GIS-Cable Termination and Termination Join Test Setup

- **Stress Cone:**
  The test setup for the stress cones is shown in figure 6.9. This setup is also known as a back-to-back test setup, as two stress cones of the same or different sizes could be tested simultaneously. The stress cones are attached to cables with high precision and are inserted into a housing chamber filled with SF_6 at a specific pressure. This is done to attach the cable straight and effectively during testing. Using SF_6 eliminates the chances of flashover and cable damage in the highly stressed electric field regions. The region apart from the stress cone chamber is also filled with SF_6 to eliminate flashovers to the grounded chamber. Voltages are applied via the HV cable, and the required tests are conducted per the norms.

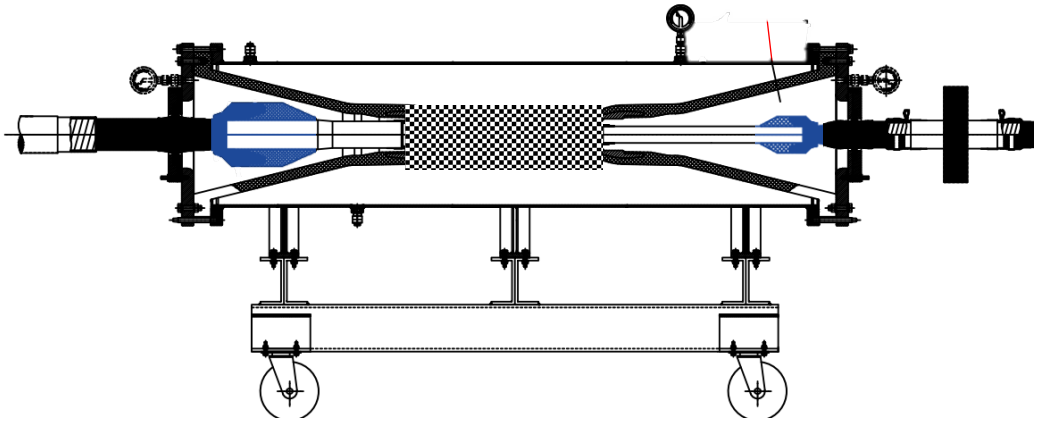

Figure 6.9: Stress cone test setup

- **Single phase Transition Joint Insulator**
  The test setup to test single phase transition joint insulator is shown in figure 6.10. A termination joint is connected to one end through which HV energizes the component. The other end of the transition joint is sealed with a flange and filled with SF_6 during the test.

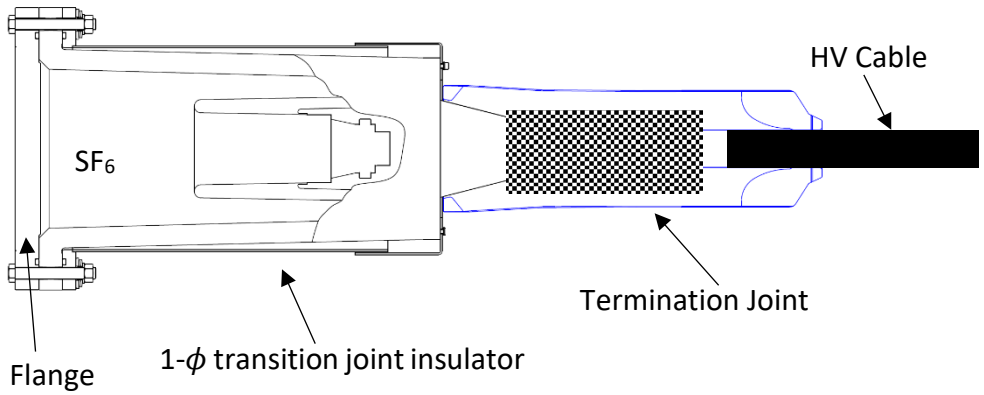

Figure 6.10: 1ϕ transition joint insulator test setup

- **Three Phase Transition Joint Insulator**
  Here, one phase of the three-phase joint insulator is only tested at a time. Figure 6.11 shows the test setup. A stress cone is compressed to the transition joint with a corona

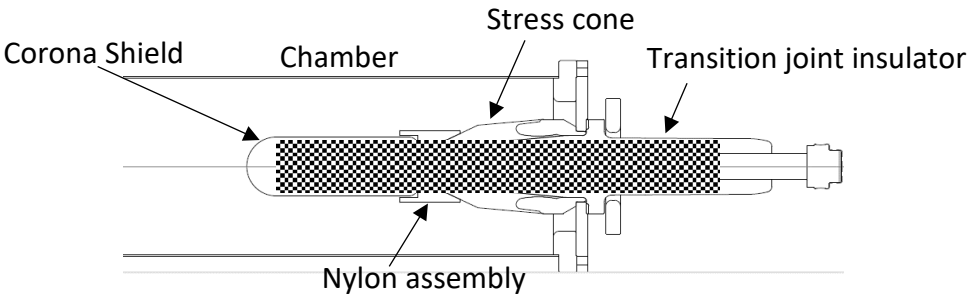

Figure 6.11: Three phase transition joint insulator

shield and nylon assembly. The whole assembly is then inserted into a chamber filled with SF_6.

6.3 Electric Field Analysis

The test setups provide a rigid and easy-to-operate environment for the test engineers and operators. However, SF_6 is used while testing these network components to eliminate flashover during testing from the component to be tested and to terminate it properly. To develop an insulating medium alternative to SF_6, the initial step will be to analyze the stresses during various tests in the area where SF_6 is filled. Electrical field analysis using COMSOL® electrostatic physics is carried out at the test voltages. This section summarises the stresses each component is subjected to.

6.3.1 GIS-Cable termination Insulator

The gaseous medium SF_6 is in contact with the electrode and epoxy housing. The field configuration with the maximum stress points is as shown in figure 6.12.

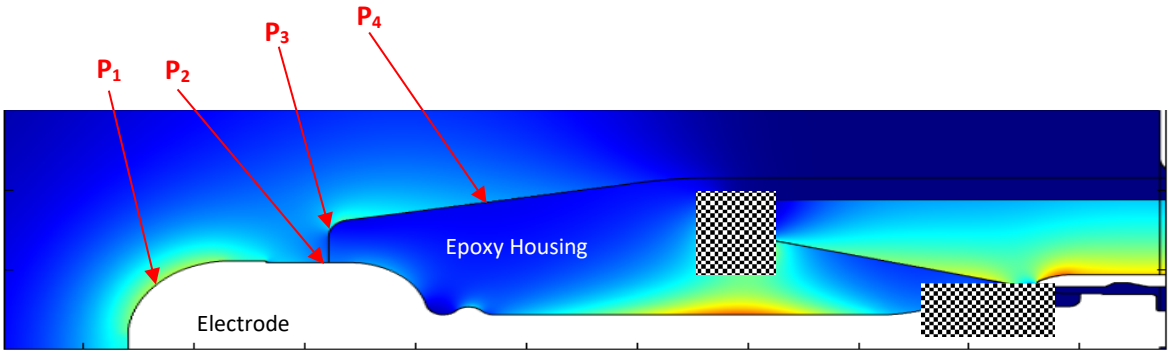

Figure 6.12: *GIS-cable termination test setup and points of maximum stresses in gas medium*

Sl.No	Voltage class	P_1 norm.	P_2 norm.	P_3 norm.	P_3 tan.	P_4 tan.	P_4 norm.	Test Voltage	Test
		(kV/mm)						(kV)	
1	72	3.71	2.12	3.10	1.21	1.3	1.66	140	AC
		4.90	2.80	4.10	1.61	1.82	2.19	185	AC 1min
		11.92	6.82	9.99	3.91	4.44	5.33	450	LI
2	170	5.78	2.51	4.97	1.58	1.32	3.05	220	AC
		9.20	4.00	7.92	2.51	2.10	4.85	350	AC 1min
		19.71	8.58	16.97	5.39	4.51	10.39	750	LI
3	245	6.27	2.86	3.62	1.66	1.08	2.34	318	AC 30min
		7.49	3.41	4.32	1.99	1.29	2.80	380	AC 1min
		20.71	9.44	11.95	5.49	3.57		1050	LI

Table 6.2: *Electric Field Stresses of GIS-cable termination insulator test setup*

Point P_1 is the corona cap–gas interface, P_2 is the triple point where gas, epoxy and electrode meet, P_3 is the curvature of the epoxy and point P_4 is the epoxy-gas interface region. Table 6.2 presents the stresses at these points. Tests of the 72kV and 172kV voltage class insulators are done in the same test chamber. And 245kV voltage class is done in a chamber having a comparatively higher volume than the latter, as the dimensions of the insulator do not fit the chamber.

From the table, it is evident that the triple point is the highly stressed point. In the presence of a sufficiently high electric field, this is the point where electron emission is favoured. In addition to being an electron source, the triple point is commonly recognized as the area where flashover in high voltage insulation occurs and the vulnerable point from which a breakdown occurs.

6.3.2 Stress Cones

Here, the gas medium is in contact with the semiconducting deflector and rubber area. Moreover, the gas is also in contact with the peeled XLPE area of the HV cable. Since a stress cone is made of stretchable material, the stress cone of a voltage class can fit in a wide range of cables having different conductor thickness and insulation thickness, provided that the stress cone's bore diameter is smaller than the cable and is within the designed voltage class. Hence, the stresses in the stress cone vary with the cable used. Moreover, there are different bore diameter stress cones in a voltage class. Hence, the typically used cable parameters used for testing were considered during electric field evaluation. Figure 6.13 shows the surface plot of the electric field in the test setup, and table 6.3 presents the electric stresses in the test setup of stress cones.

P_1 is the interface between the rubber of the insulation and gas, P_2 is the stress cone slope-ga interface, and P_3 is the junction of the triple point where gas-rubber-XLPE meets. P_4 is the epoxy-gas interface of the isolation chamber. P_5 is the triple point where the gas-epoxy-HV electrode meets. P_6 is the gas electrode interface, and P_7 is the interface between the curved electrode side and gas.

If the stress cones and the cables used are the same on both ends of the test setup, the stresses will be the same on both ends. In the contrast case, the stresses in one end do not affect the other. During simulation, the stretch of stress cone that could occur when connected to a cable is not considered, as the deviation in dimension is negligible to affect the electric stresses.

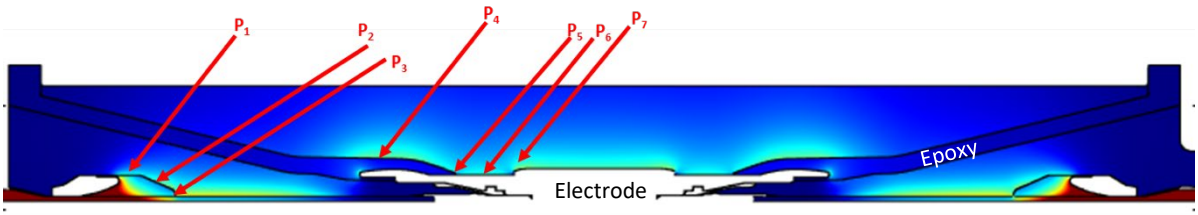

Figure 6.13: *Stress cone test setup electric field stresses*

Class	Bore Dia.	Peel Dia.	Cond. Dia	P_1 norm.	P_2 tan.	P_3 norm.	P_4 tan.	P_4 norm.	P_5 norm.	P_6 max.	P_7 max.	Test Voltage
				(kV/mm)								(kV) AC
72 kV	44.5	56.4	38.1	1.43	0.74	1.8	0.35	1.22	0.31	1.05	1.81	100
	49.5	56.4	38.1	1.23	0.66	2.10						
	52.5	59.1	38.2	1.29	0.65	1.96						
	55.5	68	50.3	1.36	0.70	1.87						
	58	68	50.3	1.4	0.71	1.85						
	60.5	68	50.3	1.44	0.71	1.62						
170 kV	49.5	59.8	26	2.15	1.89	3.8	0.77	2.69	0.73	2.31	3.99	220
	52.5	59.8	26	2.32	1.96	3.85						
	55.5	67.8	38.1	2.55	2.08	3.8						
	58	67.8	38.1	2.62	2.12	3.9						
	60.5	74.1	38.2	1.6	1.03	3.25						
	63.5	74.1	38.2	1.76	0.92	3.73						
	66.5	80.4	40.7	1.78	0.92	3.58						
	70	80.4	40.7	2.11	0.94	3.58						
	77.5	97.5	61.5	2.12	1.00	3.5						
	82	97.5	61.5	2.26	1.02	3.5						
300 kV	77.5	87.7	38.2	1.83	1.15	4.2	1.08	3.88	1.1	3.34	5.77	318
	86.5	99.2	50.3	1.83	2.48	3.8						
	91.5	103	43	1.64	3.31	3.67						
	94	107.5	56	1.83	2.45	2.88						

Table 6.3: *Electric Field Stresses in stress cone test setup*

6.3.3 Single Phase Transition Joint Insulator

The stresses expected in the gas medium in a single-phase transition joint are shown in figure 6.14, and table 6.4 presents the stresses in the insulator during testing. Here, P_1 is the interface of gas and epoxy, P_2 is the interface of epoxy curvature and gas, P_3 is the epoxy-gas interface point adjacent to the electrode curvature, and P_4 is the interface of the curvature and gas.

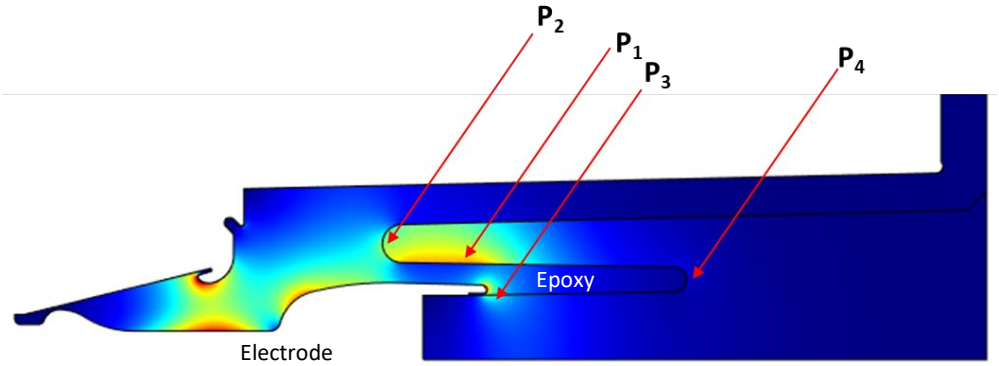

Figure 6.14: *Electric stress points of a single phase transition joint insulator*

Voltage Class	P_1 norm.	P_1 tan.	P_2 norm.	P_2 tan	P_3 norm.	P_4 norm.	Test Voltage	Test
	(kV/mm)						kV	
170	6.551	1.97	4.895	4.781	4.477	0.611	220	AC
	10.422	3.134	7.788	7.606	7.123	0.972	350	AC 1 min

Table 6.4: Electrical Stresses in 1ϕ transition joint

6.3.4 Three Phase Transition Joint Insulator

The electric stress points experienced during the testing of a three-phase transition joint insulator are shown in figure 6.15. Point P_1 is the electrode-gas interface, P_2 is the triple point where nylon fitting – gas – electrode meets, P_3 is the sharp curvature of the nylon fitting, P_4 is the junction where epoxy – gas – electrode meets, P_5 is the point of stress on the stress cone. Table 6.5 summarises the stresses for 72kV and 150kV voltage class three-phase transition joint insulator testing.

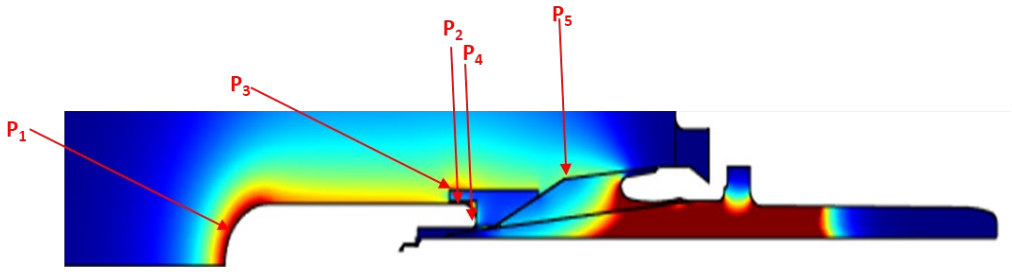

Figure 6.15: Stress points in test setup during testing in Three-phase transition Joint Insulator

Voltage Class	P_1 norm.	P_2 norm.	P_3 norm.	P_4 norm.	P_5 norm.	Test Voltage	Test
(kV)	(kV/mm)					(kV)	
72	3.88			11.45	1.12	100	AC
150	6.56	7.67	8.17	14.54	3.54	240	AC

Table 6.5: Electric Field Stresses in test setup during testing in Three-phase transition Joint Insulator

6.4 Possible Alternatives

Based on the preliminary study of the network components and its test setup, possible alternatives to SF_6 were discussed along with the R&D team of Delft. This section summarises the alternative mediums, their practicality and feasibility.

6.4.1 Solid Insulations

Solid are one of the promising solutions as an HV insulation medium. As HV tests conducted in the scope of this study do not include any huge currents that could heat the component itself (due to decreased heat dissipation), solids can be considered a promising solution in this context. However, it should be noted that, unlike gaseous medium, these insulations do not self-restore in the event of a breakdown. A context where solid insulation can be used in the cases mentioned above is during the testing of the termination joint insulator. Figure 6.16 shows a rough sketch of this. This solution brings two advantages; primarily, this setup would no longer require a GIS-cable termination insulator for testing that must be encapsulated inside a chamber with SF_6. With this setup, we indirectly eliminate the use of SF_6. The second advantage this setup could bring is that it aids in back-to-back testing of two joint insulators, which could save time.

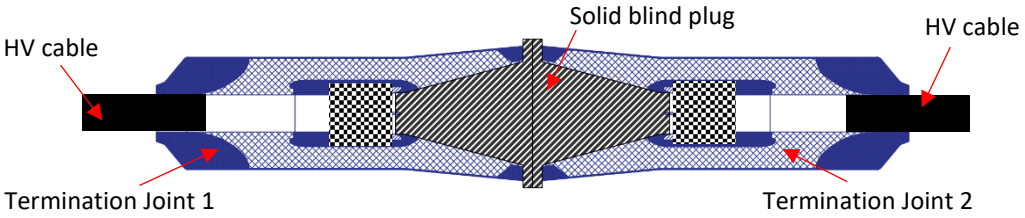

Figure 6.16: Possible Dry tool for testing termination joint

In the case of other network components, it is found that solid insulation is not a feasible solution due to many technical difficulties, such as those that could arise from the tangential electric field between the two solid interfaces.

The stresses arising in the test setup of the three-phase transition joint are due to the complex arrangement and different material permittivities. A possibility to solve this case will be to provide a solid socket-like assembly. However, this is not in the scope of study and was selected for further analysis and study.

6.4.2 Liquid Insulation

The other mode of insulation is Liquid insulation like oil. As most of the components mentioned are used as dry in practice, utilising liquid insulation during routine testing would require extra effort to clean and dry the component after testing and before handing it over to customers. Moreover, the moisture content in oil has to be maintained at a certain level to eliminate breakdowns inside the oil insulation. Even if the features of mineral oil-based liquid insulations are more significant, oils have certain drawbacks, such as environmental hazards, toxicity, and expensive disposal costs [94].

6.4.3 Alternative Gases

Using low GWP alternative gases is a solution that can help in eliminating SF_6. Recent research in the gaseous dielectric medium has resulted in a wide range of gases for HV insulations. Pressurised pure air is an exciting dielectric used for HV applications. Electronegativity is the fundamental prerequisite to having high dielectric strength in the gaseous medium, by which electrons can readily attach to gas molecules and thereby withdraw from ionization. Air consisting of oxygen is slightly an electronegative gas.

To validate whether air can be used as a dielectric medium for testing network components without any change in the current setup was of interest to Prysmian, as it brings many advantages. Moreover, Air can be delivered to the test chambers that come from compressors with filters that could capture the contaminants. It will also reduce the usage of gas bottles and is readily available at any moment. Furthermore, the air has no compatibility issues with the network component materials and can be delivered to the customers without difficulties. The breakdown voltage of compressed air increases with pressure and is most effective till 15Bar. However, there is a limit of pressure that can be used, as the component, as well as the test chamber, is designed for certain pressure.

Based on this interest, the organisation also looked into utilising synthetic air, which is 80% N_2 and 20% O_2. In general, it is air in a pure form free from other contaminants and gases. This is promoted by Siemens under the name 'Clean Air' or 'Blue Gas' and has developed switch gears based on this. However, it is to be noted that the switchgear is of considerable size, and as per the manufacturers, this could bring high CO_2 footprints as it needs more materials. The breakdown strength of synthetic air is presented in figure 6.17.

As mentioned earlier, routine tests and type testing are done in different labs at Prysmian. The primary focus was to eliminate sf6 from at least one lab. Based on this, the lab that uses most sf6 is the routine testing lab. Here only AC tests along with PD measurements are carried out. Hence the focus was to eliminate sf6 from this lab and on the AC test voltage waveform. Tests with synthetic air were performed to verify whether the calculations were correct and are discussed in the next section.

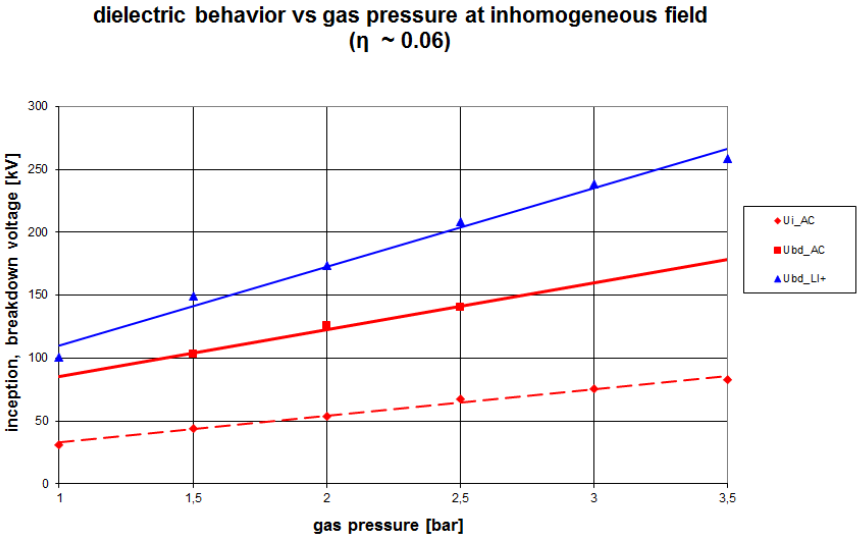

Figure 6.17: *Synthetic Air Breakdown Strength*

6.5 Functionality test with Synthetic Air

This section comprises the usage of the non-uniformity factor and pilot test results with synthetic air for two different network components.

6.5.1 η factor

The highest electric field intensity in the gap (which occurs towards the tip of the high voltage electrode) to the average electric field intensity is characterized as the electric field non-uniformity (Schweiger factor or eta factor). These parameters have been widely employed in the literature to interpret electrical insulation's electric field dependency, breakdown, and corona initiation behaviours. These factors are also computed and reported in the literature for simple geometric forms for this purpose. Geometry is said to be homogeneous if the η factor equals 1, quasi-homogeneous if the factor ranges between >1 and 5 and non-homogenous if the value is greater than 5.

To calculate eta factors for the network components, COMSOL was used to find the highest electric field strength in the geometry, and the ratio between the voltage and distance gives the average electric field.

Based on the breakdown strength results from the literature on synthetic air and based on eta factor and dielectric strength at that particular η was considered. Then a margin of almost 150% for pressure was used to ensure that the breakdown strength was above PD inception voltage.

6.5.2 Test with Stress Cone

The stress cone is one of the essential and most utilised components. The highly stressed stress cone based on table 6.3 was chosen for the test. Since stresses in the other stress cone are below this electric field stress, we can say that all other stress could be tested without any difficulty at this test pressure. A 300kV voltage class stress cone with a bore diameter of 91.5, as shown in figure 6.18, and the cable with a conductor diameter of 43mm and a peel diameter of 103 mm were used.

The stress cones were inserted into the cable. Figure 6.19 shows the stress cone used and its assembly on the cable. The cable and the stress cone were then inserted into the chamber. The chamber was vacuumed and filled with 3 bar relative synthetic air. It is to be noted that only the chamber where the stress cone was fitted was filled with synthetic air. Since all the chambers are distinctive and there is no chance of gas in the different chambers coming together, the rest were filled with SF_6. Figure 6.20 shows the application of gas in different chambers. The AC test setup consisting of PD measurement was utilised to perform the test. The test setup is as shown in figure 6.21.

***Figure 6.18**: Stress Cone utilised for the test*

Figure 6.19: *Prepared stress cone and cable prior to installation in the chamber*

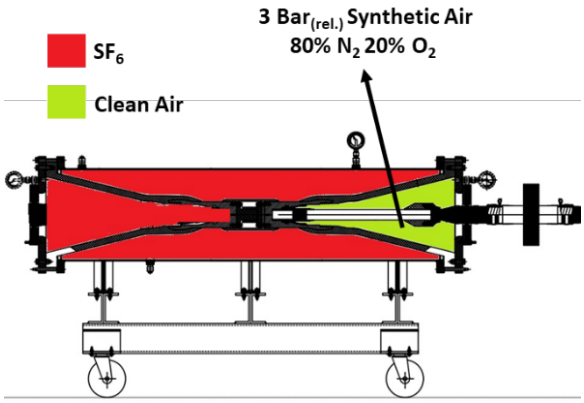

Figure 6.20: *Gases in the test chamber during testing*

Figure 6.21: *Test Setup*

The stress cone was successfully routine tested using synthetic air. It withstood AC voltage of 318kV for 30 min and was PD free at 220kV. Figure 6.22 shows the test result of PD. This result shows that all the other stress cones below this voltage class will withstand its test voltages as the stresses are comparatively low. Moreover, it was

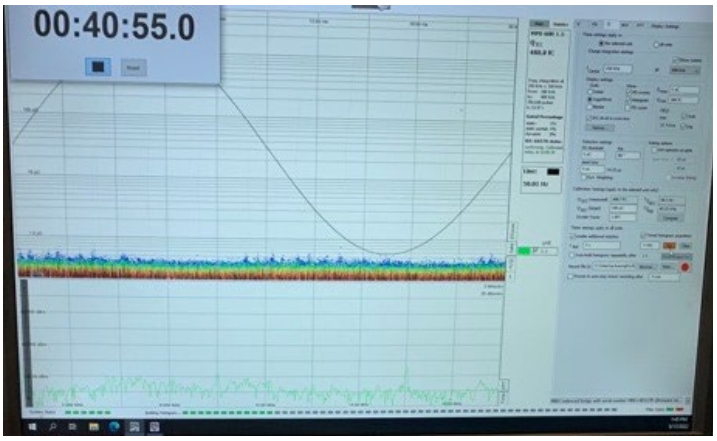

Figure 6.22: *PRPD pattern of the test at 220kV*

6.5.3 Test With GIS-Cable Termination

The GIS-cable Termination of voltage class 172kV test setup was highly stressed as per table 6.2. Hence, this product was utilised for the functionality test. Figure 6.23 shows the GIS-cable termination isolator, joint insulator, and cable connected to the test chamber. The test voltage was applied with an HV transformer to the test object via a cable termination, as shown in figure 6.24. After vacuuming to ensure no residual SF_6 and ambient air humidity were left from previous tests, synthetic air at a pressure of 6.5 Bar(rel.) was filled in the test chamber, as seen in figure 6.25. A test voltage of 261kV for 30min and 350kV for 1 min was applied to the test object. PD was measured along with the test using OMICRON PD 600.

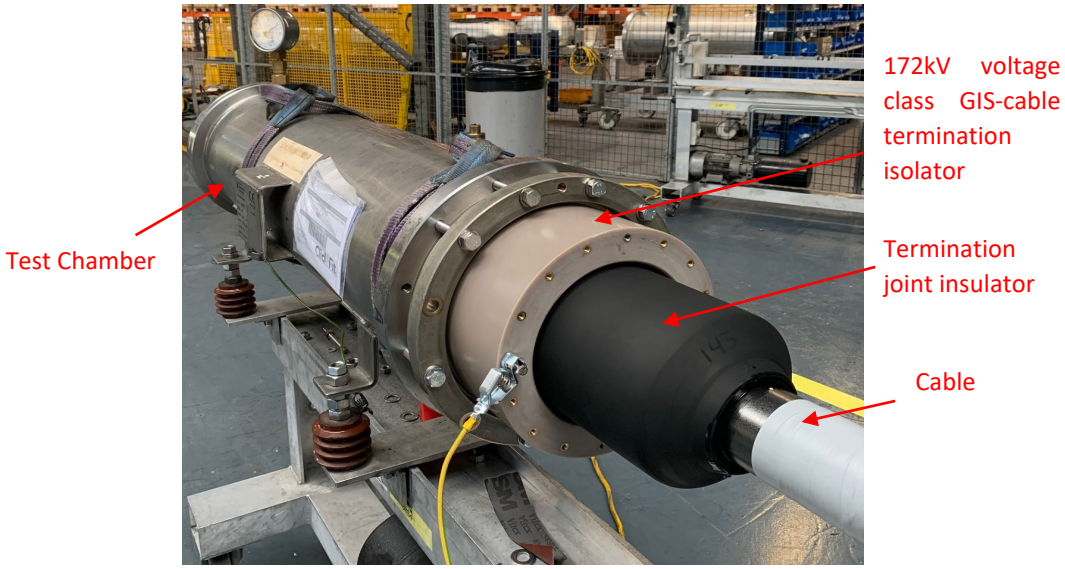

Figure 6.23: *172kV GIS-Cable termination test setup*

Figure 6.24: *Voltage application to the test object*

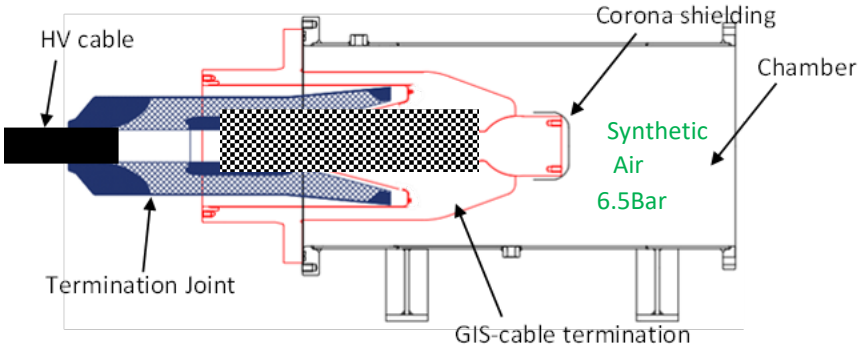

Figure 6.25: *Test Setup Internal Diagram*

Figure 6.24: *PRPD at 261kV*

Upon testing, the 172kV voltage class GIS-cable termination isolator successfully withstood AC test voltage of 261kV for 30min and 350kV for 1 min. The test also resulted in a PD-free as can be seen from figure 6.26 result which ensures that the test setup with synthetic air is corona-free from this study's point of view.

As synthetic air has less impurity compared to ambient air, and the focus is on to utilise ambient air, further analysis of breakdown strength with different η factors has to be carried out

6.6 Compressed Air Breakdown Strength

As the network component contains different eta factors and the breakdown strength varies with η factors, the breakdown strength of air has to be calculated for AC voltage for at least three different factors. This section comprises the test setup, electrode configuration, and test results of the compressed air breakdown strength.

6.6.1 Electrode Configuration

Three electrode configurations depicting homogenous, quasi-homogeneous and highly inhomogeneous configurations were used to test different η values at different pressures.

The electrode configurations used are:

1. Plane to plane configuration depicting homogenous electric field and having η factor 1, separated with a distance of 10mm as shown in figure 6.27 (a)
2. Rod to plane configuration depicting quasi homogenous electric field and having η factor 4.3, separated by a distance of 10mm as shown in figure 6.27 (b)
3. Point to plane configuration depicting a highly inhomogeneous electric field and having an η factor of 8.3, separated by a distance of 10mm, as shown in figure 6.27 (c).

All the electrodes were made of stainless steel and were polished after each test set of pressure to ensure good results. The electrodes were also cleaned with alcohol to remove any contaminants. The electrodes were placed in the test cell as shown in figure 6.28 and then vacuumed to 0.3 mBar. This ensures that the cell is humid-free and free from other gases. The cells were then filled with compressed air at the required pressure.

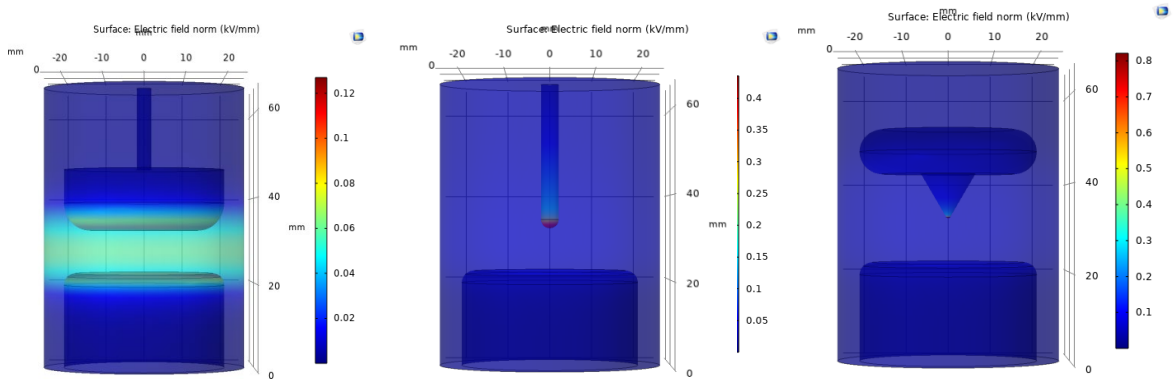

Figure 6.25: *Electrode configurations employed for the test and its electric field plot (a) Homogenous (b) Quasi homogenous (c) Inhomogenous*

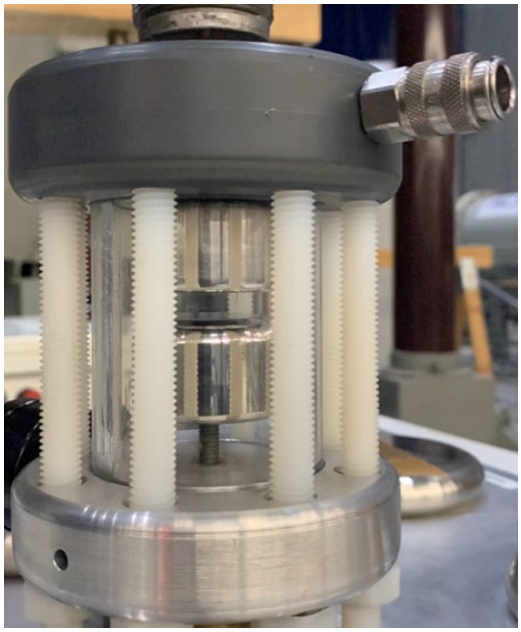

Figure 6.26: *Test cell used*

6.6.2 Test Setup

Figure 6.29 shows the test setup used for AC breakdown analysis. The test setup is similar to the one explained in section 4.4.4. Tests at each pressure were conducted at least five times to ensure good statistical results.

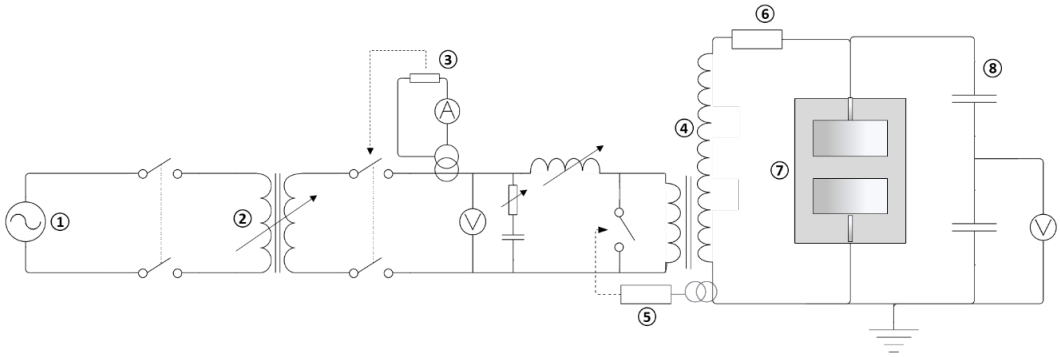

Figure 6.27: *Setup used for breakdown test 1. 220V 50Hz AC Grid; 2.Autotransformer; 3. Current Limiter; 4.HV transformer; 5.High Speed Tripping Circuit; 6. Damping Resistor; 7.Test cell; 8.Capacitive Voltage Divider*

6.6.3 Test results of air

As Prymisan is interested in moving towards the usage of compressed air, the question of how pure the air is of importance. Two compressors available at the TU Delft ESP lab were utilised for the AC breakdown voltage experiment. A 'clean air' compressor, generally used for dental purposes, and an oil-filled screw type air compressor 'Grassair SFX1500' were utilised.

The AC breakdown voltages in kV_{peak} with respect to pressure for different eta factors are presented for clean air compressors in figure 6.30.

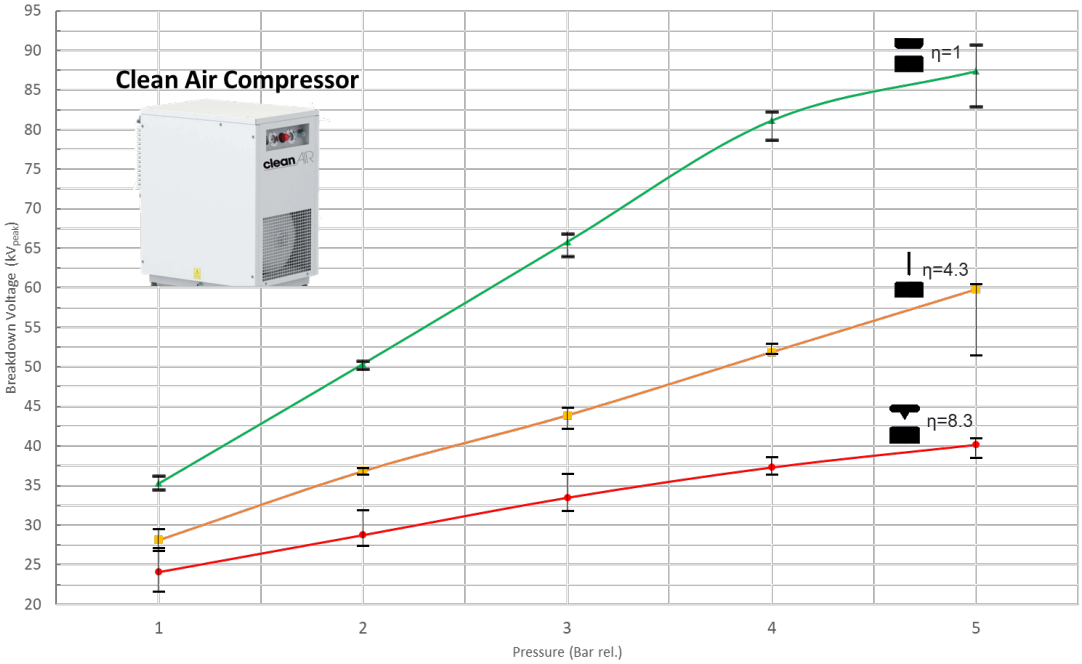

Figure 6.28: *BDV v/s Pressure for different η factors with the clean air compressor*

The breakdown mechanism in these regions is streamer as Townsend is valid only till 5 atm x 1 mm. Each geometry has attained the critical electric field for streamers to propagate and cause a breakdown. As the increase in η factor increases, the electric field concentration of the geometry increases, and breakdown follows at much lower voltages.

The curves of this result are fitted in the power equation,

$$V_{BD} = a + 18 \cdot P + b \cdot P \cdot \eta^2 + \frac{2.96 \times 10^{-8} \cdot (-49.4)^P}{\eta} + - \frac{0.924}{P^{0.233 * P * \eta}} - c \cdot P \cdot \eta \qquad \textit{Eq. 6.1}$$

Where $a = 21.22$

$b = 0.179$

$c = 3.18$

P is relative pressure in Bar, and η is the non-uniformity factor.

R^2 (goodness of fit) = 0.98

Max error = 0.53

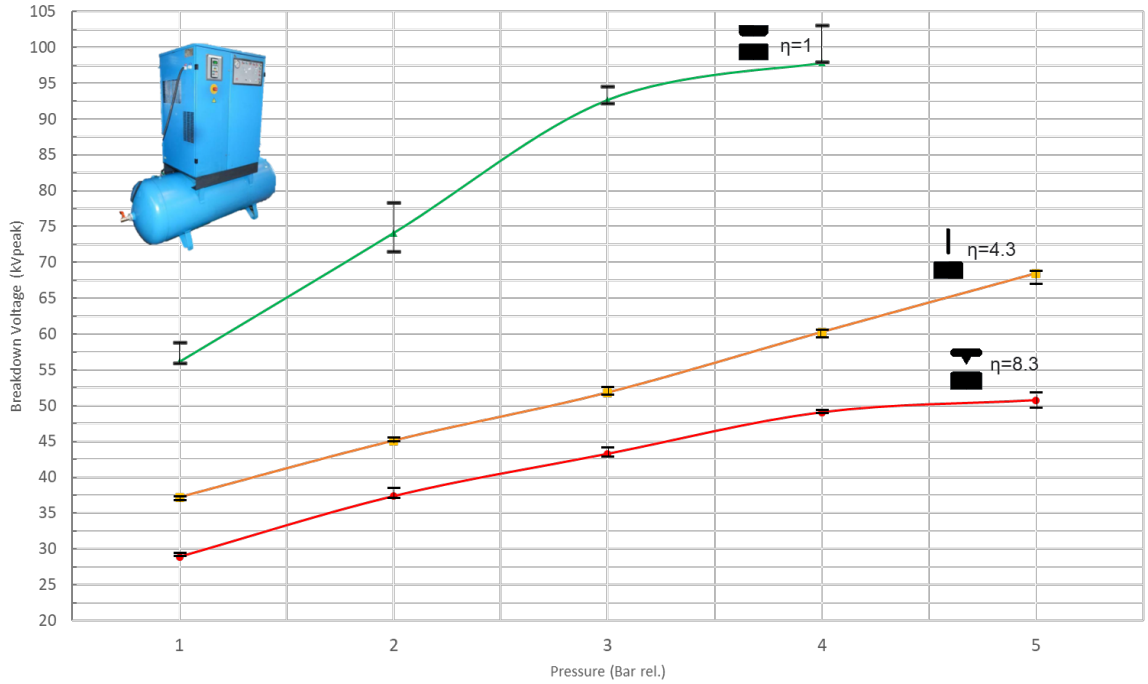

Figure 6.29: *BDV v/s Pressure for different η factors with Grassair SFX1500*

Figure 6.31 shows the results of the breakdown voltage for air from the compressor 'Grassair SFX1500'. The test results can be fitted in the equation below:

$$V_{BD} = 33.8 + 31P + 0.593P\eta^2 - \eta - 7.94P\eta - 1.8 \cdot 10^4\, \eta^2 (2.55 \cdot 10^{-5} P^3 m^2)^m \qquad \textit{Eq. 6.2}$$

P is relative pressure in Bar, and η is the non-uniformity factor.

R^2 (goodness of fit) = 0.98

Max error = 2.4

The test results show that the breakdown voltage for the same geometry is higher than the clean air compressor. Hence the details of the compressors are to be investigated for purity levels, humidity etc.

6.7 Summary

Prysmian's sustainability policies, along with the EU regulation on eliminating GWP gases from the test laboratories of Prysmian, introduced the research question of finding an alternative to the network components testing. A methodological study strategy was proposed toward the goal with the R&D team. All the network components with different voltage classes that use SF_6 were identified, and their test setups were studied in detail. The electrical stresses that could occur during the test setup were analysed using COMSOL. Based on the calculations, possible solutions were discovered. However, it was found that using gaseous dielectric is more convenient. Hence, a functional test with synthetic air was carried out based on calculations. The tests were successful. Breakdown tests were carried out to understand

further whether compressed air can be utilised for this purpose. This will provide a reference for the further steps of using compressed air for testing.

7. Conclusion And Future Scope

Chapter 7 covers all of the observations from previous chapters to address the research questions set in Chapter 1, Section 1.3. It also introduces the research's future scope and the limitations faced.

7.1 Conclusions

The research questions have been answered, and the findings and explanations are detailed in the respective chapters. The answers to the research questions are summarised as follows:

1. What is the compatibility of the novel alternative gas C_4F_7N/CO_2 mixture and epoxy with different fillers, and is retrofitting a solution from this point of view?

   The novel alternative gas C_4F_7N/CO_2 and epoxies with different fillers should be subject to thermally accelerated ageing to analyse the long-term compatibility. Since there are no specific standards for accelerated ageing of alternative gases at this point in time, the recommendation from CIGRE was taken into account. For the alternative gas mixture C_4F_7N/CO_2, an ageing temperature of 100°C and a duration of 4-8 weeks were derived optimum by CIGRE, based on the standards prevailing for SF_6. These parameters were considered for ageing with a pressure of 6 Bar absolute, as this is the average pressure used in pilot projects.

   Upon ageing, the Al_2O_3-filled epoxy was found to be yellowing, and this was due to the thermo-oxidation reaction of epoxy with the gas. Since the epoxy surface is more prone to morphological changes during ageing, flashover voltage tests of AC and LI^+ waveforms were carried out. The results show that the Al_2O_3-filled epoxy did not change the flashover characteristics. However, Quartz filled epoxy show improved flashover characteristics. As per the works of literature, this might be due to the migration of SiO_2 filler to the epoxy surface, which could create traps and cause the flashover voltage to increase. Another possibility is that the band gap of the epoxy was altered due to the crystalline defects caused during the ageing process. This reasoning has to be verified with further investigations. The breakdown strength of the gas is not altered by the interaction of epoxy or the filler. This means that the gas is highly stable with epoxies. However, further research is required to analyse the decomposition of the gas and whether the decomposed products could cause compatibility issues.

   From the retrofitting and dielectric point of view, the gas is suitable for retrofitting the GIS at this pressure. More studies are recommended to analyse the effect of pressure and C_4F_7N concentration in the mixture.

2. What are the optical PD characteristics of the C_4F_7N/CO_2 mixture considering different defects in a gas-insulated system?

   The metal protrusion, floating electrode, and surface defects, which are prominent in Gas-Insulated HV systems such as GIS and GIL, were considered for the study. Optical PD characteristics were measured using an optical spectrometer. The alternative gas mixture C_4F_7N/CO_2 results were compared with air for reference.

   Results show that each insulating gas and each defect have its own optical PD characteristics. However, for both the insulating gases, the PD mainly occurs in the UV region, which is attributed to the emission from N_2. Surface discharges at higher voltages produce photons in the VIS region due to streamer propagation along the surface. Floating electrodes in C_4F_7N/CO_2 at higher field strengths also produce emissions in the visible region owing to fluorine disassociation.

   Once the optical spectrum of the gases was understood, the research question was further extended to investigate how PD could be measured using fluorescent fibres and APD sensors. Experimental results were compared to electrical measurements using the HFCT sensor. The PD pulse obtained from the optical sensor does not reveal the type of discharge but merely the magnitude of light intensity. The PRPD pattern comparison revealed that the optical sensor is highly comparable to the electrical sensor in terms of phase and orientation of PD occurrence. The correlation plot demonstrated significant dispersion and the linear behaviour of optical sensor output compared to the electrical sensor output. The strong immunity against interference was also tested under harsh conditions, where the APD sensor outperforms the HFCT sensor in terms of noise. These analyses set the groundwork for using fluorescent fibres connected to APD sensors for PD detection.

3. Is it technically feasible to use Siemens clean air (80% N_2 + 20% O_2) and dry air for network components HV routine testing?

   A thorough understanding of the different HV cable network components, test setups, and test voltage waveforms paved the path to solving the research question efficiently. At Prysmian, SF_6 is used as an insulation medium while testing network components. A study plan was proposed to solve the research question. Electric field simulations were performed to identify the stresses in the test setup. The possibility of using dry-type, liquid, and gaseous mediums was investigated upon analysing the stresses. However, retrofitting the current test setup with an alternative gaseous dielectric was found to be the most efficient solution. Hence, the focus was on alternative gaseous dielectrics, primarily synthetic and compressed air.

   Based on analysing the non-uniformity factor and comparing the breakdown field strength of synthetic air, functionality tests on actual network components were carried out in the HV laboratories of Prysmian. All the tests were successful and led to

further analysis of compressed air usage for testing. For further analysis, breakdown strengths in geometries representing different non-uniformity factors were carried out in two different compressed air.

7.2 Recommendation and Future Scope

The thesis covers a wide range of research topics; however, there is still scope for more research in the future.

- Compatibility of C_4F_7N/CO_2 and epoxy
  The matrix of tests that can be done in this domain is countless; however, the following will give a good understanding of the novel gas interaction with materials.
  1. Accelerated ageing under various gas pressure, the content of C_4F_7N in the mixture and ageing temperatures near to glass transition temperature of the epoxy is recommended to simulate the worst-case conditions that could occur.
  2. Thermal ageing to simulate mixed interaction of multiple components of GIS will yield an actual case of the GIS
  3. Arrhenius-based thermal stresses on an entire compartment of GIS or GIL can give an idea of the lifetime expectance of the GIS or GIL using this novel gas.
  4. Gas Chromatography can be utilised to understand the decomposition of the gas upon ageing. Scanning Electron Microscopy (SEM) could give an idea of the surface characteristics of epoxy. Dielectric spectroscopy in the GHz range could give more information at the molecular level of the epoxy.
  5. The research focused here was on accelerated thermal ageing. To fully understand whether there is any effect on the combined effect of electrical stresses and thermal stress, ageing under accelerated electro-thermal ageing is recommended.
  6. The compatibility of decomposed gas (due to PD or heavy arcing) with different components of the GIS materials is recommended.

- Optical PD Characteristics of the Alternative Gas
  1. Optical PD characteristics, even though does not yield in PRPD patterns, can still be utilised to identify PD defects based on the characteristic peaks obtained. Studying the multiple spectra with the help of a learning curve (or training curve) machine learning algorithms can help diagnose PD. However, some techniques should be identified to eliminate the requirement of focusing the detector on PD defects.
  2. Using fluorescent fibres for PD detection brings out several difficulties, such as transmission loss due to the length and area of light coverage. This makes it challenging to use in real GIS or GIL units. An idea to overcome this will be using fluorescent painting on the walls of a GIS and terminating at several points. A figure of a draft idea is presented in figure 7.1.

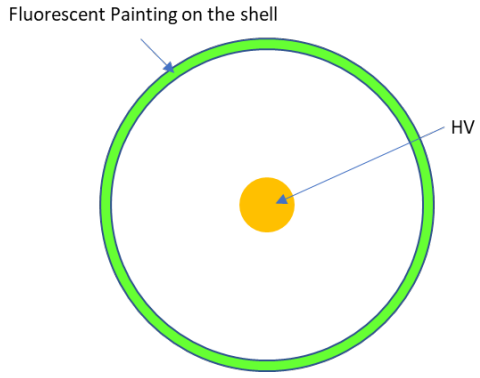

Figure 7.1: *Illustration of possible setup*

- Alternative Gases for Network Components Testing
    1. Experiments to investigate compressed air to test network component is to be carried out in real network components.
    2. The possibility of using a mixture of air with other electronegative gas has to be investigated

7.3 Scientific Challenges and Limitations

Taking on a project of this magnitude was sure to present obstacles, yet, this became an opportunity for increased learning and development for the researcher. This section presents the possible challenges that future researchers in this domain should oversee:

1. Test Setup: The test setup used in this research was time-consuming to operate. For example, it was only possible to test only a few samples a day as the GIS system's SF_6 recovery, filling, and air vacuuming was intense work and time-consuming. A small setup that could handle the test voltages would be optimum for this purpose.
2. Time: The wealth of time is the only wealth that is more valuable than human resources. More tests and a more in-depth understanding of this novel gas would have been possible with time. Always keep a clock in your hand. Once you are in the experimental phase, time flies.

Appendix A

Ideal Gas Law applied to 5 mol% C_4F_7N and 95mol% CO_2

mol_C=12.011

mol_F=18.998

mol_N=14.007

mol_C4=4*mol_C+7*mol_F+mol_N

mol_CO2=44.0095

mol_C4_mix=.05*mol_C4+.95*mol_CO2

molar mass C4 = 195.04

molar mass C4 mix = 51.56

As per the bottle of gas obtained

m=3582 [g]

M=mol_C4_mix [g/mol]

V=50 [L]

T=15+273.15 [Kelvin]

R=0.0821 [L*ath/K*Mol]

n=m/M

P*V =n*R*T

From this, Pressure, Volume and Temperatures can be calculated as required. These calculations were utilised in this thesis to identify the number of bottles to be purchased, the number of tests that could be done, and the pressure at elevated ageing temperature (to make sure the chamber could withstand the pressure).

Appendix B

The following table and figures were obtained from the manufacturer of epoxy samples. The mechanical and electrical properties of the epoxy samples are tabulated in table B.1. All values shown are obtained from test samples (sample size and dimensions according to ISO).

Item	**Quartz filled epoxy**		**Al_2O_3 filled epoxy**		Unit	Measurement Standard
Resin Type	Solid epoxy resin based on Bisphenol A		Solid epoxy resin based on Bisphenol A			
Hardener	Phthalic anhydride PSA		Anhydride			
Filler	Quartz LM-10		Al_2O_3			
Processing	Conventional gravity casting process (under vacuum)					
Mechanical Properties						
	Min. Value	Typical Value	Min. Value	Typical Value		
Tensile Strength (@RT)	60	82	55	75	N/mm^2	ISO/R 527
Tensile Strength (@75°C)	55				N/mm^2	ISO/R 527
Compressive Strength	160		170		N/mm^2	ISO/R 604
Flexural Strength	100	135	115	133	N/mm^2	ISO/R 178
Deflection	3.0 - 3.5		2-2.5		mm	ISO/R 178
Elasticity Modulus	10 - 12	10.5	8-10	8.5	kN/mm^2	ISO/R 527
Impact Strength	9	10.8	10	20	KJ/m^2	ISO/R 179
Density	1.75-1.85	1.79	2.0-2.2	2.1	g/cm^3	DIN 53479
Water Absorption	0.15-0.25		0.15-0.25		%	ISO/R 62
Thermal Conductivity	0.8 - 0.9		0.8-0.9		W/mK	DIN 53612
Glasspoint with DSC-method	112 - 129	121	115	122	$°C\ [T_1/2, g]$	ISO 11357-2
Coeff. of linear Thermal Expansion	30 - 35		32-38		$10^{-6}\ mm/mm°C$	VSM 77110

Electrical						
Dielectric Constant (25°C 50 Hz)	Refer to fig B.1 (a)			4.99	ϵ_r	IEC 60250/DIN 53483
Loss Tangent tan δ (25°C)	Refer to fig B.1 (a)			0.5-0.7		IEC 60250/DIN 53483
Volume Resistivity	Refer to fig B.1 (b)			$3.2 \cdot 10^{13}$	Ω/cm	IEC 60093/DIN 53482
Electric Strength	23	25		25	KV/mm	IEC 243
Surface Resistance				$54 \cdot 10^{13}$	Ω	IEC 60093

Table B. 1: *Mechanical and electrical properties of the epoxy samples*

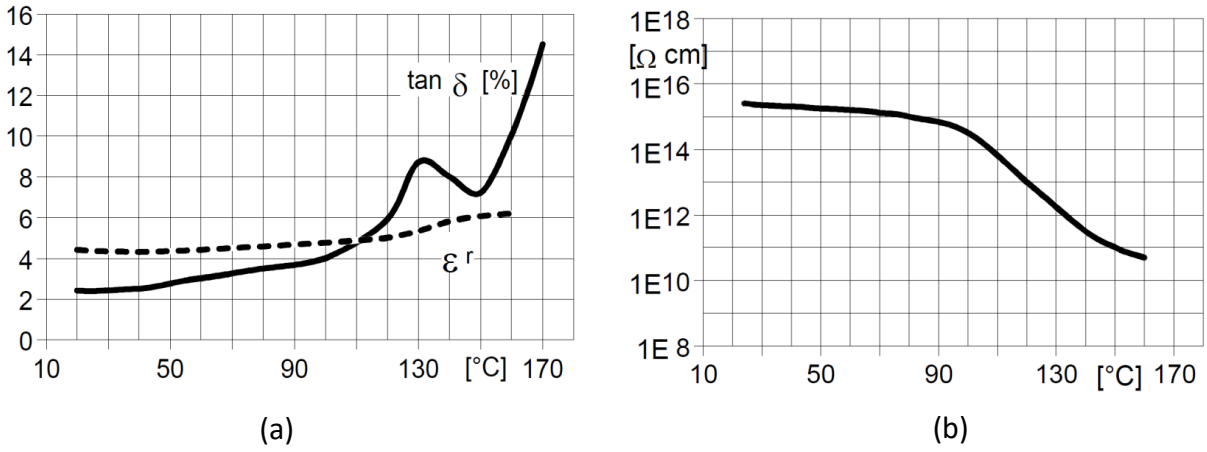

*Figure **B.1:** (i) Loss factor (tan δ) and Dielectric constant(ϵ_r) as a function of temperature (measurement frequency: 50 Hz) (IEC 60250/DIN 53483) (ii) Volume resistivity (ρ) as a function of temperature (measurement voltage: 1000V) (IEC 60093/DIN 53482)*

Analysis details of the Al_2O_3 filler that was used in the epoxy are shown in Table B.2 [95]. The market name for this is MARTOXID® MDLS-6.

Component	**Unit**	**Value**
Al_2O_3	%	≈ 99.8
Na_2O soluble	%	≈ 0.03
Na_2O total	%	≤ 0.02
CaO	%	≈ 0.03
Fe_2O_3	%	≈ 0.03
SiO_2	%	≈ 0.06
α-Al_2O_3	%	≥ 95
Loss on ignition	%	≤ 0.1

Specific Surface Area (BET)	m^2/g	0.5-1.4
Primary Crystal	μm	≈ 4
Bulk density	kg/m^3	≥ 800
Electrical conductivity (25% in H_2O)	$\mu S/cm$	≤ 100
Particle size distribution:		
d_{10}	μm	0.5-2.5
d_{50}	μm	3.0-4.0
d_{90}	μm	7-14
> 45	μm	≤ 1

Table B.2: *Typical analysis details of MATRXID® MDLS-6*

	ITEM	MATERIAL
1	BLACK ANODIZED MOUNTING RING	6061-T6 ALUMINUM
2	ACHROMATIC CYLINDRICAL DOUBLET	N-BK7
3		N-SF10

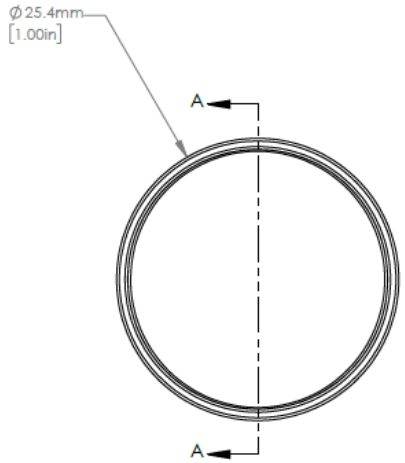

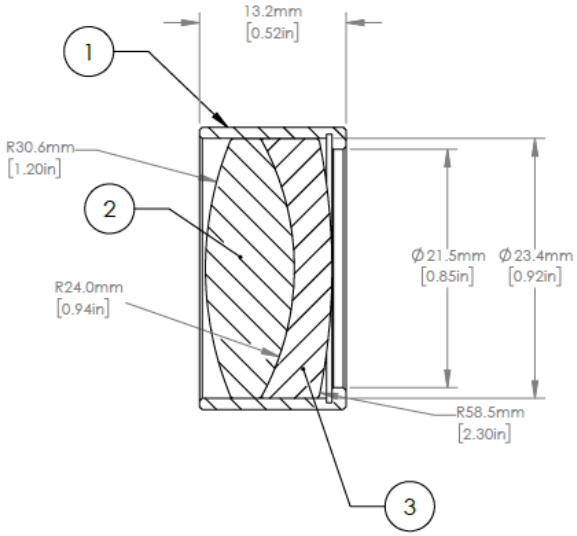

NOTES/SPECIFICATIONS:

1. FOCAL LENGTH: 50.0mm ±1.0%
2. BACK FOCAL LENGTH: 44.7mm
3. DESIGN WAVELENGTH: 587.6nm
4. CLEAR APERTURE: >Ø22.86mm
5. SURFACE QUALITY: 40-20 SCRATCH-DIG
6. CENTRATION: <5arcmin
7. COATING: BBAR Ravg <0.5% FROM 400-700nm, 0° AOI, ON OUTER OPTICAL SURFACES

FOR INFORMATION ONLY
NOT FOR MANUFACTURING PURPOSES

DRAWING PROJECTION		
	NAME	DATE
DRAWN	KMR	20/SEP/16
APPROVAL	DD	26/SEP/16

VALUES IN PARENTHESIS ARE CALCULATED AND MAY CONTAIN ROUNDOFF ERRORS

THORLABS
www.thorlabs.com

MOUNTED ACHROMATIC CYLINDRICAL LENS
Ø25.4mm, f=50.0mm, -A COAT

MATERIAL	REV
SEE TABLE	B

ITEM #	APPROX WEIGHT
ACY254-050-A	15.1 g

References

[1] Working Group III, "Climate Change 2014 Mitigation of Climate Change - Working Group III Contribution to the Fifth Assessment Report of the Intergovernmental Panel on Climate Change," Cambridge University Press, USA, 2014.

[2] WG D1.67, "Electric Performance of new non-SF6 gases and gas mixtures for gas-insulated systems," CIGRE, 2021.

[3] Michael Eves, "A Literature Review on SF6 Gas Alternatives for use on the Distribution Network," Western Power Distribution , 2018.

[4] S. Kosse and T. Hammer, "Future Proof and Low Carbon Footprint Insulation for Switchgear," in *XXIst Symposium on Physics of Switching Arc*, Nove Mesto na Morave, Czech Republic, Sep 07-11, 2015.

[5] WG B3.45, "Application of non-SF6 gases or gas mixtures in medium and high voltage gas-insulated switchgear," CIGRE, 2020.

[6] Association, Energy Networks, "Engineering Recommendation G69: Guidance on working with Sulphur Hexafluoride," in *Energy Networks Association*, London, 2013.

[7] Environmental Protection Agency, "Global Mitigation of Non-CO2 Greenhouse Gases: 2010 - 2030," in *Environmental Protection Agency*, Washington, 2013.

[8] "Regulation (EU) No 517/2014 of the European parliament and of the council of 16 April 2014".

[9] European Commission, "Report from the commission assessing the availability of alternatives to fluorinated greenhouse gases in switchgear and related equipment, including medium voltage secondary switchgear," 2020.

[10] European Commission , "EU legislation to control F-gases," 2022. [Online]. Available: https://ec.europa.eu/clima/eu-action/fluorinated-greenhouse-gases/eu-legislation-control-f-gases_en.

[11] Y. Kieffel, A. Girodet, F. Biquez, Ph. Ponchon, J. Owens, M. Costello, M. Bulinski, R. Van San, K. Werner , "Sf6 Alternative Development For High Voltage Switchgears," in *CIGRE*, Paris, 2014.

[12] M. Seeger, R. Smeets, J. Yan, H. Ito, M. Claessens, E. Dullni, C. M. Franck, F. Gentils, W. Hartmann, Y. Kieffel, S. Jia, G. Jones, J. Mantilla, S. Pawar, M. Rabie, P. Robin-Jouan, H. Schellekens, J. Spencer, T. Uchii, X. Lia and S. Yanabu, "Recent development of alternative gases to SF6 for switching applications," in *CIGRE*, Paris, 2017.

[13] Myriam Koch, "Prediction of Breakdown Voltages in Novel Gases for High Voltage Insulation," ETH Zurich, Zurich, 2015.

[14] Christophorou L G, Olthoff J K, and Green D S., "Gases for electrical insulation and arc interruption: possible present and future alternatives to pure SF6," in *NIST Technical Note 1425*, Washington DC, 1997.

[15] M. H. L. a. R. G. Richard, "Gaseous Dielectrics with Low Global Warming Potentials". US Patent US 7,807,704 B2, 05 10 2010.

[16] Mohamed Rabie and Christian M. Franck, "Assessment of Eco-friendly Gases for Electrical Insulation to Replace the Most Potent Industrial Greenhouse Gas SF6," Environmental Science & Technology, 2018.

[17] Yannick Kieffel, "Characteristics of g3 – An Alternative to SF6," IEEE, 2016.

[18] C. Preve, D. Piccoz and R. Maladen, "Validation Methods of SF6 Alternative Gas," in *CIRED - 23rd International Conference on Electricty Distribution*, Lyon, France, 2015.

[19] Zhiguo Chen, Hui Zhang, Yan Shang, Qingguo Chen, Baozhong Han, and Zesheng Li, "Theoretical study of OCCHCN as a potential alternative insulation gas for SF6," *AIP Publishing ,* vol. 7, 2017.

[20] L. G. Christophorou, J. K. Olthoff and D. S. Green, "Gases for Electrical Insulation and Arc Interruption: Possible Present and Future Alternatives to Pure SF6," USA Department of Commerce , 1997.

[21] C. Preve, R. Maladen, G. Lahaye, T. Penelon, M. Richaud and S. Galas, "Hazard Study of MV Switchgear with SF6 Alternative Gas in Electrical Room," in *IRED 24th International Conference on Electricity Distribution*, Glasgow, 2017.

[22] Y. Kieffel, T. Irwin, P. Ponchon and J. Owens, "Green Gas to Replace SF6 in Electrical Grids," *IEEE Power and Energy Magazine,* vol. 14, no. 2, pp. 32-39, 2016.

[23] T. Uchii, Y. Hoshina, T. Mori, H. Kawano, T. Nakamoto & H. Mizoguchi , "Investigations on SF6-Free Gas Circuit Breaker Adopting CO2 Gas as an Alternative Arc-Quenching and Insulating Medium," *Gaseous Dielectrics X. Springer,* p. 205–210.

[24] Loucas G. Christophorou, James K. Olthoff, David S. Green, "Gases for Electrical Insulation and Arc Interruption: Possible Present and Future Alternatives to Pure SF6," United Ststes Department of Commerce Technology Administration, 1997.

[25] J. D. Mantilla, N. Gariboldi, S. Grob and M. Claessens, "Investigation of the insulation performance of a new gas mixture with extremely low GWP," in *2014 IEEE Electrical Insulation Conference (EIC)*, 2014 .

[26] 3M, "3M™ Novec™ 5110 Insulating Gas," 2017. [Online]. Available: https://multimedia.3m.com/mws/media/1132123O/3m-novec-5110-insulating-gas.pdf. [Accessed 02 02 2022].

[27] 3M, "3M™ Novec™ 4710 Insulating Gas Data Sheet," 2017. [Online]. Available: Available: https://multimedia.3m.com/mws/media/1132124O/3m-novec-4710-insulating-gas.pdf. [Accessed 03 02 2022].

[28] Christophe Preve, Daniel Piccoz, Romain Maladen, "Application of hfo1234zee in mv switchgear as SF6 alternative gas," in *24th International Conference on Electricity Distribution* , Glasgow, 2017.

[29] J.-L. Bessede, "Eco-Design in Electrical Engineering: Eco-friendly Methodologies, Solutions, and Example for Application to Electrical Engineering," *Springer,* 2017.

[30] S. Kosse, P.G Nikolic and G. Kachelriess, "Holistic evaluation of the performance of today's SF6 alternative proposals," in *Holistic evaluation of the performance of today's SF6 alternative proposals*, Glasgow, 2017.

[31] Dr. Sebastian Glomb, Martin Göppel, Peter Pilzecker, ""“Alternative Gases” and Gas Mixtures," DILO.

[32] ABB, "Gas-insulated ring main unit SafeRing AirPlus," ABB, [Online]. Available: https://new.abb.com/medium-voltage/switchgear/gas-insulated-switchgear/iec-gis-rmu-for-secondary-distribution/iec-gas-insulated-ring-main-unit-safering-airplus. [Accessed 13 02 2022].

[33] Martin Kristoffersen, Thor Endre, Magne Saxegaard, Maik Hyrenbach, Per Arne Wang, Denny Harmsen, Theo Van Rijn, Robert Vosse, "RMU With Eco-Efficient Gas Mixtures: Field Experience," in *24th International Conference on Electricity Distribution*, Glasgow, 2017.

[34] Siemens, "Blue-high Voltage products," Siemens, [Online]. Available: https://www.siemens-energy.com/global/en/offerings/power-transmission/innovation/blue-high-voltage-products.html. [Accessed 03 02 2022].

[35] H. Nechmi, A. Beroual, A. Girodet, P. Vinson, "Effective ionization coefficients and limiting field strength of Fluoronitriles-CO2 mixtures," *IEEE Transactions on Dielectrics and Electrical Insulation,* vol. 24, no. 2, pp. 886-892, 2017.

[36] Tianran Zhang, Wenjun Zhou, Yu Zheng and Jianhui Yu, "Insulation Properties of C4F7N/CO2 Mixtures under Non-uniform Electric Field," *IEEE Transactions on Dielectrics and Electrical Insulation,* vol. 26, no. 6, pp. 1747 - 1754, 2019.

[37] Tianran Zhang, Wenjun Zhou and Jianhui Yu, "Insulation Properties of C4F7N/CO2 Mixtures under Lightning Impulse," *IEEE Transactions on Dielectrics and Electrical Insulation,* vol. 27, no. 1, pp. 181-188, 2020.

[38] IEC 62271-200, "High-voltage switchgear and controlgear - Part 200: AC metal-enclosed switchgear and controlgear for rated voltages above 1 kV and up to and including 52 kV," IEC, Switzerland, 2011.

[39] Douglas C. Montgomery, Design and Analysis of Experiments, John Wiley and Sons, 1997.

[40] M. Ren, M. Dong, Z. Ren, H. Peng and A. Qiu, "Transient Earth Voltage Measurement in PD Detection of Artificial Defect Models in SF6," *IEEE Transactions on Plasma Science,* pp. 2002-2008, Aug 2012.

[41] M. Muhr, R. Schwarz, "Experience with optical partial discharge detection," *Materials Science-Poland,* vol. 27, no. 4/2, 2009.

[42] Di-bo Wang, Ju Tang, Ran Zhuo, Jun-yi Lin, Jian-rong Wu and Xiao-xing Zhang, "SA-SVM incremental algorithm for GIS PD pattern recognition," in *2012 International Conference on High Voltage Engineering and Application*, 2012.

[43] Fuping Zeng, Ju Tang, Xiaoxing Zhang, Siyuan Zhou and Cheng Pan, "Typical Internal Defects of Gas-Insulated Switchgear and Partial Discharge Characteristics," in *Simulation and Modelling of Electrical Insulation Weaknesses in Electrical Equipment*, 2018, p. 214.

[44] F.H Kreuger, "Partial Discharge," in *Industrial High Voltage Volume 2*, Delft university Press, 1992, pp. 117-157.

[45] I.A. Metwally, "Status review on partial discharge measurement techniques in gas-insulated switchgear/lines," *Elsevier,* 2003.

[46] A. Rodrigo Mor, L.C. Heredia, and F.A. Muñoz, "Clustering Plots for the separation of partial discharge sources based on amplitude, charge and energy of PD pulses," in *INSUCON 2017 13th International Electrical Insulation Conference*, Birmingham, UK, 2017.

[47] R. Cselko, Z. A. Tamus, A. Szabo and I. Berta, "Comparison of Acoustic and Electrical Partial Discahrge Measurements on Cable Terminations",," in *IEEE Conference*, 2010.

[48] Sweta Kumari, "[Thesis] Feasibility study for usage of optical partial discharge detection in HV Cable termination," TU Delft, Delft, 2018.

[49] M. Ren, J. Zhou, B. Song, C. Zhang, M. Dong and R. Albarracin, "Towards Optical Partial Discharge with Micro Silicon Photomultiplier," *MDPI Sensors,* 2017.

[50] R. Schwarz, M. Muhr and S. Pack, "Evaluation of partial discharge impulses with optical and conventional detection systems," in *XIVth International Symposium on High Voltage Engineering*, Beijing, China, August 2005.

[51] Yiming Zang, Yong Qian, Xiaoli Zhou, Antian Xu, Gehao Sheng, Xiuchen Jiang, "Application of a partial discharge method based on the novel multispectral array sensor and GMM in different insulating gases".

[52] R. Schwarz and M. Muhr, "Modern Technologies in Optical Partial Discharge Detection," in *Annual Report Conference on Electrical Insulation and Dielectric Phenomena*, 2007.

[53] R. Schwarz, M. Muhr and S. Pack, "artial discharge detection in oil with optical methods," August 2005.

[54] Tao Jiagui, Yang Jinggang, Ye Gaoxiang, Tang Ju, "A System Using Fluorescent Fiber for Partial Discharge Detection in Transformer," 2016.

[55] Yiming Zang, Mohamad Ghaffarian Niasar, Yong Qian, Xiaoli Zhou, Gehao Sheng, Xiuchen Jiang, Peter Vaessen,, "Optical Detection Method for Partial Discharge of Printed Circuit Boards in Electrified Aircraft under Various Pressures and Voltages," *IEEE Transactions on Transportation Electrification,* 2022.

[56] L. E. Lundgaard, "Partial Discahrge- Part XIII: acoustic Partial Discharge Detection fundamental," *IEEE Electrical Insulation Magazine,* vol. 8, 1992.

[57] R. Schwarz and M. Muhr, "Partial discharge measurement as a Diagnostic Tool for HV-Equipments," in *IEEE Conference*, 2006.

[58] M. M. Yaacob, M. A. Alsaedi, J. R. Rashed, A. M. Dakhil and S. F. Atyah, "Review on Partial discahrge detection technique Related to High Voltage power Equipment using Different Sensors," *Photonics sensors,* vol. 4, 2014.

[59] Prysmian Group, "Sustainablity Report 2021".

[60] G. Petraconi, H. S. Maciel, R. S. Pessoa, G. Murakami, M. Massi, C. Otani, W. M. I. Uruchi, and B.N. Sismanoglu, "Longitudinal Magnetic Field Effect on the Electrical Breakdown in Low Pressure Gases," 2004.

[61] Lee, Hyung-Seok & Kim, Cheol & Kwon, Young-Doo & Doh, Jaehyeok, "Long-term life prediction of polyacrylate rubber (ACM) gasket with chlorine cure sites using the four-parameter recovery model," in *Institution of Mechanical Engineers, Part D: Journal of Automobile Engineering*.

[62] Z. Zheng, , H. Li, W. Zhou, J. Yu, H. Wang, J. Zhang, Y. Jiang, J. Zhao, L. Yang, Y. Zhou , "Compatibility between C4F7N and the Sealing Material EPDM Used in GIL," in *IEEE Conference on Electrical Insulation and Dielectric Phenomena*, Washington - USA, 2019.

[63] Yi Li, Xiaoxing Zhang, Yalong Li, Dachang Chen, Zhaolun Cui, Wei Liu, and Ju Tang, "Interaction Mechanism between the C4F7N−CO2 Gas Mixture and the EPDM Seal Ring," *ACS OMEGA,* 2020.

[64] Xiaoxing Zhang, Peng Wu, Lin Cheng, and Sicong Liang, "Compatibility and Interaction Mechanism between EPDM Rubber and a SF6 Alternative Gas - C4F7N/CO2/O2," *ACS OMEGA,* 2021.

[65] YI LI , XIAOXING ZHANG , JI ZHANG, QI CHEN, YALONG LI, SONG XIAO, ZHAOLUN CUI, AND JU TANG, "Thermal Compatibility Between Perfluoroisobutyronitrile-CO2 Gas Mixture With Copper and Aluminum Switchgear," *IEEE Access,* vol. 7, pp. 19792-19800, 2019.

[66] Zhichuang Li, Weidong Ding, Yishu Liu, Yue Li, Zhongbo Zheng, Wei Liu, Keli Gao, "Surface Flashover Characteristics of Epoxy Insulator in C4F7N/CO2 Mixtures in a Uniform Field under AC Voltage," *IEEE Transactions on Dielectrics and Electrical Insulation,* vol. 26, no. 4, p. 1065, 2019.

[67] John Owens, Ang Xiao , Jason Bonk , Michael DeLorme and Agnes Zhang , "Recent Development of Two Alternative Gases to SF6 for High Voltage Electrical Power Applications," *Energies,* vol. 5051, p. 14, 2021.

[68] Andrey E. Krauklis and Andreas T. Echtermeyer, "Mechanism of Yellowing: Carbonyl Formation during Hygrothermal Aging in a Common Amine Epoxy," *Polymers MDPI,* 2018.

[69] T. S. Sudarshan and, R. A. Dougal, "Mechanisms of Surface Flashover Along Solid Dielectrics in Compressed Gases: a Review," *IEEE Transaction Dielectric Electrical Insulation,* vol. 21, no. 5, pp. 727-746, 1986.

[70] A. H. Cookson, "Review of high-voltage gas breakdown and insulators in compressed gases," *IEEE Proceedings A,* vol. 128, no. 4, pp. 303-312, 1981.

[71] Yang Meng, Haorui Xuan, Zichen Deng, Zhichuang Li, Weidong Ding, and Wen Liu, "The surface flashover process under positive lightning impulse voltage: initial stage and evolution," *Journal of Physics D: Applied Physics,* vol. 55, 2022.

[72] ASTM, "Standard Test Method For Dielectric Breakdown Voltage and Dielectric Strength of Solid Electrical Insulating Materials at Commercial Power Frequencies".

[73] Andreas Putro Purnomoadi, Asset health index and risk assessment models for high voltage gas-insulated switchgear operating in tropical enviroment, Delft: TU Delft, 2020.

[74] H. C. Miller, "Surface flashover of insulators," *IEEE Transactions on Electrical Insulation,* vol. 24, no. 5, pp. 765-786, 1989.

[75] Anderson R A, "XIV Int. Symp. on Discharges and Electrical Insulation in Vacuum," 1990.

[76] F.H Kreuger, "Compressed Gas Insulation," in *Industrial High Voltage*, Delft, Delft University Press, 1991, p. 86.

[77] IEC 60060-1-ed.03, "High-Voltage Test Techniques – Part 1: General definitions and test requirements," 2010.

[78] Purnomoadi, Andreas, "Asset Health Index and Risk Assessment Models for High Voltage Gas-Insulated Switchgear Operating in Tropical Environment," TU Delft.

[79] A. Pedersen, "Evaluation of the effect of surface defects on breakdown in strongly electronagative gases or gas mixture," *Gaseous Dielectric II,* pp. 201-290, 1980.

[80] R. Yuan, H.LI, W.Zhou, J.Yu, G.Jin, "Compatibility between C3F7CN and epoxy rei at high temperature," in *IEEE conference on electrical insulation and dielectric phenomena*, Washington, 2019.

[81] Ming Ren, Bo Song, Tianxin Zhuang, Shujing Yang, "Optical partial discharge diagnostic in SF6 gas insulated system via multi-spectral detection," *ISA Transactions,* vol. 75, pp. 247-257, 2018.

[82] Yiming Zang, Yong Qian , Xiaoli Zhou , Mohamad Ghaffarian Niasar, Gehao Sheng, Xiuchen Jiang, "Optical Characteristics and Fault Diagnosis of Partial Discharge in C4F7N/CO2 Gas Mixture and SF6 Based on Novel Multispectral Microarray Detection," *IEEE Transactions On Dielectrics And Electrical Insulation,* vol. 29, no. 3, p. 1079, 2022.

[83] Hongtu Cheng, Xiaoxing Zhang, Ju Tang, Song Xiao, Tingting Wang, Bing Luo, Shuangshuang Tian, "The application of fluorescent optical fiber in partial discharge detection of Ring Main Unit," *Measurement,* vol. 174, 2021.

[84] X.J. Cai, X. Wang, X.B. Zou, et al., "Properties of streamer discharges in different gases at atmospheric pressure," *Gaodianya Jishu/High Voltage Engineering,* vol. 41, no. 6, pp. 2047-2053, 2015.

[85] Avantes, "AvaSpec3648 Fiber Optic Spectrometer," Avantes, [Online]. Available: https://www.avantes.ru/en/spectrometer/tec/avaspec3648.php.

[86] A. Rodrigo Mor, , L.C. Castro Heredia, D.A. Harmsen, F.A. Muñoz, A new design of a test platform for testing multiple partial discharge sources.

[87] Kiyoshi Fujii, Mamoru Yamada , Akira Tanaka , Kiyoshi Kurosawa , "Emission spectrum of partial discharge light in SF6 gas," in *1992 IEEE International Symposium on Electrical Insulation,*, Baltimore, USA, 1992.

[88] CHEN G., YANG X., MING Y., XIAOLONG C., CHANGRONG Q.,, "Comparison between optical and electrical methods for PD measurement," in *The 6th International Conference on Properties and Applications of Dielectric Materials*, Xian, June 2000.

[89] G. C. Stone, R. G. Van Heeswijk and R. Bartnikas, "Electroluminescence in Epoxy Insulation," in *IEEE transactions on Electrical Insulation*, 1992.

[90] Yanliang He, Anbang Sun, Xing Zhang, et al., "Effect of trace SF6 characteristics in SF6/N2 gas mixtures under DC voltages," *AIP Advances 10,* vol. 085303, no. 10, 2020.

[91] T. Billoux, V. Boretskij, Y. Cressault, A. Gleizes, Ph. Teulet, A. Veklich, "Emission spectrum of the electric arc discharge in CO2 between copper electrodes".

[92] Edinburgh Insruments, "What is the Stokes Shift?," Edinburgh Insruments, [Online]. Available: https://www.edinst.com/.

[93] Panagiotis Tsakonas, Design and development of a 72 kV cable Y-joint with integrated PD sensor for offshore wind turbine grid connections, TU Delft, 2016.

[94] S. Senthil Kumar, Dr. M. Willjuice Iruthayarajan, M. Bakrutheen, "Analysis of Vegetable Liquid Insulating Medium for Applications in High Voltage Transformers," in *International Conference on Science, Engineering and Management Research*, 2014.

[95] "martinswerk," martinswerk, [Online]. Available: https://www.martinswerk.de/fileadmin/produkte/Martoxid_MDLS-6.pdf.

[96] Yin Zhang , Xiaoxing Zhang, Chang Liu, Yi Li, Zhaolun Cui, and Mingli Fu, "Ultraviolet Spectral Analysis and Quantitative Detection of Heptafluoroisobutyronitrile (C4F7N) in a C4F7N–Carbon Dioxide (CO2) Gas Mixture," *Applied Spectroscopy .*

[97] "Halocarbons and other Atmospheric Trace Gases," Earth System Research Laboratory, Global Monitoring Division, [Online]. Available: https://www.esrl.noaa.gov/gmd/hats/combined/SF6.html.